A STUDY OF ADVANCED IGNITION SYSTEMS FOR SPARK IGNITED INTERNAL COMBUSTION ENGINES

By

Bryce Charles Thelen

A DISSERTATION

Submitted to
Michigan State University
in partial fulfillment of the requirements
for the degree of

Mechanical Engineering – Doctor of Philosophy

2024

ABSTRACT

Research into technologies directed towards the improvement in the efficiency of the internal combustion engine has been motivated over the past several years by the regulation of the United States automotive market to more stringent standards for fuel economy and emissions. Lean burn operation of spark-ignited (SI) internal combustion engines may have the potential to help meet the high fuel economy goals of the future decade by improving the efficiency of SI engines at partial loads. Although gains in efficiency are found for engines operating with diluted mixtures, these mixtures present difficulties that manifest themselves through the slow flame speeds and poor ignitability associated with lean or diluted air-fuel mixtures. Two types of ignition systems are examined here that attempt to mitigate these negative effects. They are a radio-frequency plasma-enhanced ignition system and a pre-chamber-initiated ignition system called Turbulent Jet Ignition.

First, the effects of a plasma-enhanced ignition system on the performance of a small, single-cylinder, four-stroke gasoline engine are examined. Dynamometer testing of the 33.5 cm3 engine at various operating speeds was performed with both the engine's stock coil ignition system and a radio frequency plasma ignition system. The radio frequency system is designed to provide a quasi-non-equilibrium plasma discharge that features a high-voltage pulsar that provides 400 mJ of energy for each discharge and voltages of up to 30 kV. Tests show improvement in the engine's combustion stability at all operating conditions and the extension of the engine's lean flammability limit with the radio frequency system. Particular attention is given to the improvements that the radio frequency system provides while burning lean air-fuel mixtures. Additionally, analysis of the 33.5 cm3 engine's exhaust and high-speed images of the radio frequency system taken in a separate 0.4-liter optical engine are also presented.

Second, fully three-dimensional computational fluid dynamic simulations with detailed chemistry of a single-orifice turbulent jet ignition device installed in a rapid compression machine are presented. The simulations were performed using the computational fluid dynamics software CONVERGE and its RANS turbulence models. Simulations of propane fueled combustion are compared to data collected in the optically accessible rapid compression machine that the model's geometry is based on to establish the validity and limitations of the simulations and to compare the behavior of the different air-fuel ratios that are used in the simulations. In addition to being compared to a companion experimental study, investigations into the effect of TJI orifice size and pre-chamber spark location are performed. The data generated in the simulations is analyzed and insights into the processes that make up the operation of the TJI are given. Finally, CFD analysis tools are applied to the early development and design of a TJI system intended for a heavy-duty diesel engine being converted to run on natural gas.

For my lovely wife, Courtney
I love you with all my heart, darling

ACKNOWLEDGMENTS

I want to thank my advisor, Dr. Elisa Toulson. I cannot express enough gratitude for all you have done for me, starting with giving me a research home when I was orphaned, so to speak; for your guidance and support of my research pursuits; and your near infinite patience with me as I muddled my way to the finish line. Thank you for not giving up on me.

I would also like to thank my committee members, Dr. Harold Schock, Dr. Indrek Wichman, and Dr. Jason Nicholas. Much like Dr. Toulson, I owe you each a deep gratitude for sticking it out with me. I appreciate your positive encouragement throughout these years, even when I did not think I deserved it.

I owe thanks to Dr. Criag Somerton, who sadly passed away in May of 2015, for encouraging me to return to school and for starting this whole escapade.

I owe a great deal of thanks to many others who are or were affiliated with the Energy and Automotive Research Laboratories. In particular, I need to thank Tom Stuecken, Kevin Moran, Jeff Higel, Brian Rowley, and Gary Keanny, whose last name I am not sure I spelled correctly. Without Jeff, Brian, and Gary's help in the machine shop and Tom and Kevin's help and advice, the work with the small engine covered in this document could have veered into disaster. More importantly, however, you are all wonderful individuals with whom I always enjoyed being around. Thank you, guys, for making our wing of the engineering complex the best place on campus.

I must thank the Air Force Office of Scientific Research, a major funding source for the research documented here, and Olson Ecologic, which partnered with Omnitek, for coming to Dr. Toulson for consultation on their TJI engine project.

For the simulation work, there are also many to thank, starting with Convergent Science for

allowing free use of their software. Of particular note, I must thank Shawn Givler of Convergent, who came to MSU to teach me how to use the software and continued to provide support over the years, and Hannah Leystra for her kind and friendly support to academic users like myself. I must also thank the people at Michigan State's Institute of Cyber-Enable Research. I was helped immensely many times by visiting their open office hours, and of course, I would not have been able to complete most of my research without their platform.

I must also thank Dr. Tonghun Lee and his graduate students, Dr. Stephen Hammock and Dr. Casey Allen. Thank you, Dr. Lee, for allowing me to join your research team along with some pretty incredible stories. For Stephen, thank you for welcoming me into the group, and Casey, thank you for setting the example for all of us in the second wave to follow.

I also want to acknowledge the students with whom I worked most closely. First on the list chronologically is Daekeun Chun, my first officemate. Daekeun, it was a great pleasure getting to know you and paling around with you those first couple of years of grad school together. Also, thank you to Dr. Gerald Gentz and Dr. Masumeh Gholamisheeri, with whom I collaborated and spent the most time with in classes or the lab. The two of you are both amazing people. I cannot come to campus without being nostalgic about our time together.

And, of course, where would I be without my family? First and foremost, my wife, Courtney. Thank you for supporting me through all of this and for your patience. Thank you to my children, Paige and Elias; while you two didn't help me at all with this, everything I will do in my life will be for you guys. Thank you for the inspiration and for making me the best thing that I can ever hope to become, your dad. Thank you to my parents, James and Mary; your love, support, and friendship are unmatched in this world. Thank you to my brother, Austen. I wouldn't pick anyone else to grow up with. I love you, man.

Finally, I want to thank a companion who has been by my side every day since my second year. Gus, I have loved you since we met that day in Georgia. You are the type of dog men write novels about. Thank you for always being my good boy.

TABLE OF CONTENTS

LIST OF ABBREVIATIONS

ε	Dissipation
λ	Relative Air-to-Fuel Ratio: Actual/Stoichiometric
AF	Air-Fuel
AFR	Air-Fuel Ratio
AMR	Adaptive Mesh Refinement
bmep	Brake Mean Effective Pressure
CAD	Crank Angle Degrees
CAD	Computer Aided Design (distinguished from previous by context)
CAFÉ	Corporate Average Fuel Economy
CAS	Combustion Analysis System
CFD	Computational Fluid Dynamics
CFL	Courant-Friedrichs-Lewy Condition
COV_{IMEP}	Coefficient of Variation of IMEP
DAQ	Data Acquisition
EGR	Exhaust Gas Recirculation
FTP	Federal Test Procedure
GDI	Gasoline Direct Injection
GDP	Gross Domestic Product
GM	General Motors
h	Height of location of an ignition source in TJI pre-chamber from orifice
H	Total height of the TJI pre-chamber
HAJI	Hydrogen Assisted Jet Ignition

HC	Hydrocarbon Emissions
HCCI	Homogenous Charge Compression Ignition
IMEP	Indicated Mean Effective Pressure
IMEPn	Net Indicated Mean Effective Pressure
k	Turbulent Kinetic Energy
k	Ratio of specific heat (Chapter 1 only)
LAG	Russian acronym for avalanche activated combustion
MBT	Maximum Brake Torque
MFB	Mass Fraction Burn
MSU	Michigan State University
NEDC	New European Driving Cycle
NI	National Instruments
NOx	Nitric Oxides
PCIC	Pre-chamber Initiated Combustion
PISO	Pressure Implicit with Splitting Operators
ppm	Parts per Million
r	Compression Ratio
RANS	Reynolds Averaged Naiver-Stokes Equations
RF	Radio Frequency
RNG	Renormalized Group Theory
Rpm	Revolutions per Minute
SAE	Society of Automotive Engineers
SI	Spark Ignition

SOR	Successive Over Relaxation
TDC	Top Dead Center
TJI	Turbulent Jet Ignition
TTL	Transistor-Transistor Logic
U.S.	United States
UCSD	University of California San Diego
VVT	Variable Valve Train
y	Normalized height location of ignition source in pre-chamber

CHAPTER 1: INTRODUCTION AND BACKGROUND

Despite the growth in the development and availability in the marketplace of automobiles with all-electric powertrains, projections for the year 2050 estimate that four out of every five new vehicles sold in the United States (U.S.) will contain an internal combustion (IC) engine [1]. It should be expected, therefore, that IC engines will continue to be the predominant source of propulsion for ground transportation in this country for the next three decades and beyond. Accordingly, improvements in the efficiency of internal combustion engines will continue to be of interest to engine developers, academic researchers, and government agencies and laboratories [2-4]. In addition to improving their products, motivation for continued improvement in engine efficiency must also be pursued in response to government legislation that dictates fleet-wide fuel economy targets. Standards for either fuel economy and/or carbon dioxide emissions are common in some form in nearly all major markets globally [5]. In the U.S., fuel economy standards are applied to the fleets of new cars manufacturers sell each year in the domestic market. These standards are known as the Corporate Average Fuel Economy (CAFE) standards. Before the recently passed, effective June 2020, Safer, Affordable, Fuel-Efficient (SAFE) legislation, CAFE standards were set to require a yearly increase of 5% through 2025. The new legislation, however, lowers expectations down to 1.5% [6]. Motivation for improving fuel economy remains strong despite these revised targets as governments at the individual state level are expected to push back against the legislation. Already, California, along with a subset of automotive manufacturers, has taken steps to commit to fuel economy standards that are more stringent than those required by SAFE [7].

Engine efficiency improvements are among the many solutions being proposed and investigated to increase fuel economy [8]. One method to improve engine efficiency is to operate an engine using highly dilute mixtures, using either excess air or recirculated exhaust gas, to

deliver higher thermal efficiencies and reduce the pumping work of the engine. While this is common practice in diesel powertrains, spark-ignited (SI) engines, which accounted for 75% of the on-highway fuel burned in the U.S. in 2018 [9], currently operate with stoichiometric air-fuel mixtures. Operating an engine using lean or highly dilute mixtures is not straightforward. As mixtures become leaner, flame temperatures and propagation speeds are reduced, resulting in slower burn rates, which can negatively affect combustion stability. Attention to engine-out emissions is also important for lean-burn engines as common after-treatment systems, the three-way catalyst, for SI engines are unable to process nitric oxide (NOx) emissions in the presence of excess oxygen [10]. Enhanced ignition strategies have been proposed as a means to overcome the negative impacts of slower flame speeds. These strategies increase burn rates in one or more of the following ways: they increase the supplied ignition energy, they supply the ignition energy in unique ways, they distribute the sources of ignition throughout the combustion chamber, and/or they enhance the mixing rate within the combustion chamber through the addition of turbulence [11]. The research efforts covered below focus on two enhanced ignition strategies that facilitate lean-burn operation. Turbulent jet ignition (TJI) utilizes a jet of hot combustion gases as the ignition source for the bulk of the combustible mixture within an engine, whereas plasma-enhanced ignition attempts to utilize the non-equilibrium effects of certain plasmas to enhance the rate of combustion.

1.1 Current and Future Automotive Technologies

The significant increase in fuel economy that is required over the next decade will require improvements to almost every component that goes into a vehicle. While the introduction of alternative fuels and electric hybrid powertrains have recently received a great deal of attention in attempts to address fuel economy, 91.5% of the energy consumed for transportation was derived from petroleum in 2014 [12]. In addition, spark-ignited gasoline engines are currently the most

predominant engine type in automotive powertrains and are expected to remain so in the foreseeable future [8]. As a result, there is currently intensive research into developing more efficient strategies for these types of engines, such as low-temperature combustion (LTC) technologies and enhanced ignition technologies to enable lean or dilute combustion. Several of these ignition and combustion strategies have been investigated in the past with the goal of achieving lean burn engine operation. These methods include strategies such as homogenous charge compression ignition (HCCI) [13-18], stratified charge combustion using direct injection [19-23], plasma-enhanced ignition [24-26], and pre-chamber-initiated combustion [27-29]. The following describes an investigation of two types of enhanced ignition systems, a plasma-enhanced system and a pre-chamber-initiated system called the Turbulent Jet Ignition, for use in spark-ignited internal combustion engines.

The automotive industry has already responded to the more stringent regulations by introducing several new technologies, as shown in Figure 1-1, published originally by Lutsey [30], that are already being implemented in production vehicles. During the development of the 2012 CAFE standards, the three major American automotive manufacturers publicized several technologies they planned to invest in developing to meet the increased efficiency standards. These include improvements to transmissions, vehicle weight reduction, and several engine technologies like gasoline direct injection, variable valve timing, turbocharging, cylinder deactivation, and perhaps ambitiously for General Motors HCCI [8, 30]. All three manufacturers also expressed commitment to alternative fuel vehicles and electric hybrid vehicles [30].

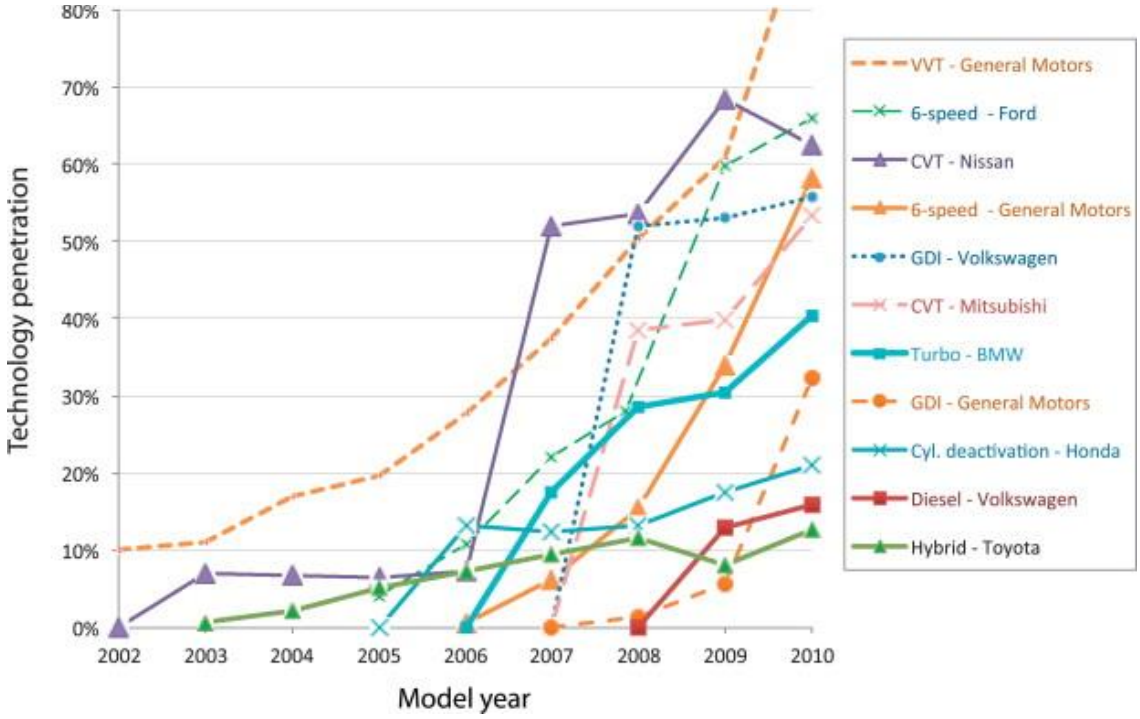

Figure 1-1 Penetration of improved technologies to address fuel economy by various automakers for model years 2002-2010 from [30] (VVT: Variable Valve Timing, CVT: Continuously Variable Transmission, GDI: Gasoline Direct Injection)

1.2 Lean Burn for Improved Engine Efficiency

For spark-ignited internal combustion engines, operating an engine with fuel-lean mixtures can provide increased engine efficiencies. Two sources of efficiency gains can be achieved with an engine that is capable of operating with lean or diluted mixtures. First, the engine's output can be controlled by controlling the amount of fuel provided to the engine, decoupling load control from the amount of air ingested by the engine. If the lean limit of the engine is tolerant enough, this can result in the elimination or at least a significant reduction in the throttling of the engine's intake, similar to what is achieved in diesel combustion, significantly reducing the pumping losses. The second improvement comes as a result of the thermodynamic properties of mixtures with excess air as they are subjected to the standard Otto cycle. The benefits of lean combustion can be seen in the example provided by Bradley [31], shown in Figure 1-2. This figure shows various thermal efficiencies for ideal Otto cycles using several different strategies for load control. For these

calculations, isentropic compressions and expansions are assumed along with constant volume combustion. The thermodynamic properties of the gas after combustion are those of the equilibrium products of combustion. The relevant data for discussion are sets (a), (b), (c), and (d). Each case is for a naturally aspirated engine with a compression ratio of 10.5.

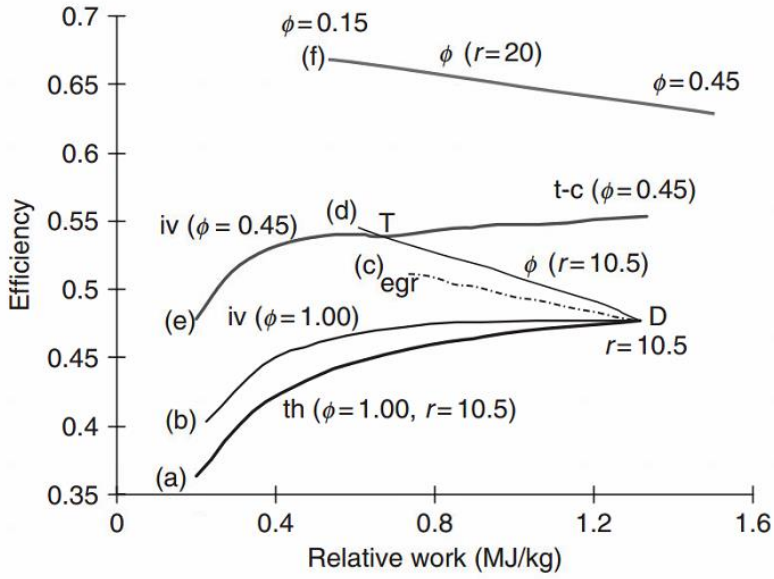

Figure 1-2 Otto Cycle Thermal Efficiencies generated using different engine strategies from [31]; (a) Stoichiometric air-fuel (AF) mixture, throttled intake, (b) Stoichiometric mixture, no throttle, variable intake valve timing, (c) Stoichiometric AF mixture using exhaust gas as a diluent, (d) Variable AF mixture

The data set labeled (a) is for a standard spark ignition engine with a stoichiometric mixture. As a result, the load is controlled by the use of throttling to limit air intake at lower loads, which negatively affects engine efficiency at low loads. Set (b) also uses a stoichiometric mixture, but instead of using a throttle to limit the intake, the amount of air ingested is controlled by varying the timing used for the inlet valve closing. Set (d) is for an engine that controls output by varying the equivalence ratio of its mixture operating in the absence of any throttling or special valve timing. To achieve its lowest output, the mixture is made lean to an equivalence ratio of 0.45. Output is increased by increasing the equivalency. Finally, the data set labeled (c) shows

efficiencies achieved using a strategy similar to that used in (d) but using recirculated exhaust gases to dilute the mixture in the engine rather than fresh air. This leads to slightly lower efficiencies but may facilitate using a three-way catalyst for exhaust treatment. Regardless of the strategy, all four curves converge at the same point with the highest load. This is because, for each strategy, this high load condition corresponds to a stoichiometric mixture and wide-open throttle.

1.3 Research Questions

- Will replacing a standard inductive coil ignition system with a plasma-enhanced ignition system extend the lean operating limit of a spark-ignited internal combustion engine?
- What effects does the plasma-enhanced ignition system have on engine-out emissions?
- How well can the operation of a Turbulent Jet Ignition system be modeled using RANS CFD modeling and detailed chemistry?
- What is the effect of orifice size on the TJI combustion process?
- How does pre-chamber spark location affect the TJI combustion process?
- What additional insights into the TJI can be gained from the three-dimensional field data generated from the simulation that is absent from data generated experimentally?
- What are the parameters of the TJI nozzle and pre-chamber that most affect pre-chamber mixing?

1.4 Experimental Objectives

- Construct a small engine dynamometer test stand to the requirements stipulated by the Air Force Office of Scientific Research Office, the funding source for the plasma-enhanced ignition study.
- Develop data acquisition capabilities and data analysis routines for the dynamometer test stand.

- Mount a Fuji Imvac-34EI single-cylinder engine with the necessary instrumentation for engine testing and combustion analysis to the dynamometer.
- Integrate a radio-frequency plasma ignition system with the Fuji Imvac-34EI engine.
- Integrate a radio-frequency plasma ignition system in an optical access engine.
- Perform comparison studies of the lean operating limits for both the small and optical engines.

1.5 Modeling Objectives

- Using CONVERGE CFD software, set up three-dimensional computational fluid dynamic simulations of the Michigan State University Rapid Compression Machine with a Turbulent Jet Ignition.
- Develop the framework for efficiently implementing CONVERGE software at Michigan State University High-Performance Computing Center.
- Perform simulations with detailed combustion chemistry of the RCM with an unfueled TJI using propane fuel.
- Develop post-processing tools to aid in the task of analyzing CFD-generated data.
- Identify the appropriate balance between model accuracy and computational cost for the CFD simulations.
- Compare simulation results to experiments and identify sources of error in the model.
- Perform a parameter study to examine the effect of the TJI orifice size.
- Perform a parameter study to examine the effect of pre-chamber spark location.
- Build a single-cylinder engine model of an Omnitek natural gas-refitted Detroit Diesel Series 50 engine.
- Perform cold flow analysis to assess the pre-chamber mixing performance of TJI nozzle

and pre-chamber designs.

CHAPTER 2: LITERATURE REVIEW

2.1 Lean Burn Combustion in Internal Combustion Engines

For a gasoline spark-ignited engine, operating the engine while at partial loads with lean equivalence ratio mixtures offers a means to improve fuel economy by reducing pumping losses and improving the maximum theoretical thermal efficiency of the Otto cycle. Addressing the thermodynamic efficiency first, equation (1) below expresses the ideal Otto cycle's thermal efficiency [32].

$$\eta = 1 - \frac{1}{r^{k-1}} \tag{1}$$

In the equation above, *r* is the compression ratio of the engine, and *k* is the ratio of specific heats of the working fluid within the cylinder. It is evident that increasing the compression ratio is an effective means of increasing the efficiency of the cycle. Still, the degree to which this can be done is limited by the onset of knock in SI engines. The efficiency can also be improved by increasing the ratio of specific heats of the working fluid within the cylinder. This can be accomplished by burning lean air-fuel mixtures as increasing the amount of air relative to fuel increases the ratio of specific heats in the mixture.

Second, with the ability to burn lean mixtures, engine load can be controlled to an extent by adjusting the air-fuel ratio (AFR) within the engine. The output of the engine is directly related to the amount of energy released during combustion. This, of course, is directly related to the amount of fuel provided each cycle. Since a typical SI engine runs at stoichiometric AFR conditions, the amount of air taken into the engine must be matched with a prescribed ratio to the amount of fuel provided. So to operate at a partial engine load, the amount of air must be restricted to accommodate a lower amount of fuel. This is typically accomplished with a throttling valve located in the engine's intake. While this effectively reduces the load by limiting the amount of fuel that

enters each cylinder, it comes at a price, as the engine must exert work to intake air past the valve. Figure 2-1 below is a breakdown of the mechanical losses experienced by a 1.6-liter four-cylinder engine in terms of mean effective pressure (MEP), which is work divided by engine displacement.

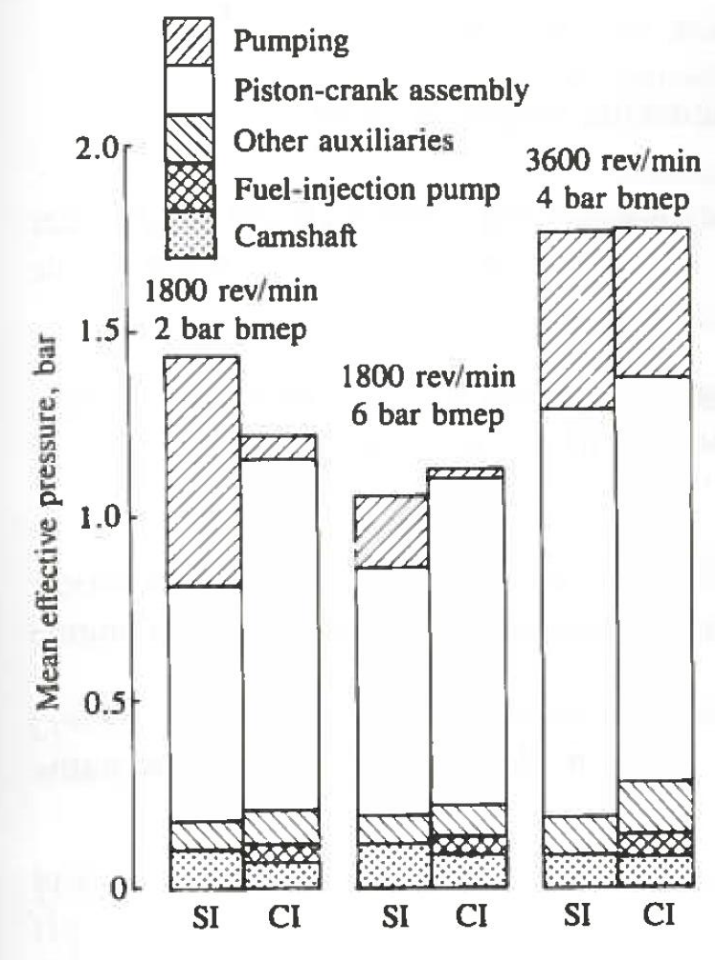

Figure 2-1 A Comparison of the major categories of friction losses at different engine loads and speeds for 1.6-liter four-cylinder overhead-cam automotive spark-ignition and compression-ignition engines [33]

The figure breaks down the mechanical losses into five separate categories. In the case of the SI engine, the two largest contributors to losses are the friction in the piston crank assembly and the work performed by the engine pumping air and exhaust in and out of the engine. The first two load speed conditions for the SI engine displayed in the figure are both for engine speeds of 1800 rev/min and at different loads of 2 and 6 bar brake mean effective pressures (BMEP), which is a

measure of the power reaching the driveshaft of the engine. Since the engine is running at the same speed in both cases, the losses from categories other than pumping are fairly identical, although the higher load does increase the friction in the piston-crank assembly slightly. It is here that the ability to burn lean AFR mixtures can improve engine efficiency. Instead of throttling the engine intake to match a reduced fuel input, a lean burn engine allows for an amount of air to enter the engine at the lower load, similar to the amount of air that enters at the higher load point. The reduced amount of fuel will still limit the load, but the pumping work will be greatly reduced.

Using the data provided for the engine in Figure 2-1 above, a specific idea of the improvement that can be made by reducing or eliminating the need for throttling can be quantified. To produce 2 bar BMEP using a throttled intake, the engine must produce an indicated mean effective pressure (IMEPn), the total work divided by displacement generated by the engine over the entire cycle, of about 3.4 bar. 2 bar of this load makes it to the drive shaft while 1.4 bar is lost. If the throttling of the intake is eliminated or reduced, the pumping losses could be reduced to a level closer to what is experienced at the 6-bar BMEP load. If this were the case, the engine would need to produce only an IMEPn of about 3.1 bar to achieve the same brake output, a reduction of almost 9%, which is a significant amount.

Another benefit of lean combustion is its potential to reduce the nitric oxide (NOx) emissions that result from combustion. There are four mechanisms by which NOx is formed during combustion reactions. The most quantified of these is the Zeldovich or thermal NO mechanism that requires high temperatures similar to those generated in near stoichiometric combustion to achieve the high activation energy of the mechanism rate limiting elementary reaction step involving the dissociation of N_2 atoms that collide with O radicals. The second mechanism is the prompt or Fenimore mechanism, which relies on CH radicals to dissociate N_2 atoms. The third

mechanism is the nitrous oxide mechanism. This is similar to the Zeldovich mechanism in that it involves O radicals attacking N_2, but it requires a third body and only becomes an issue at high pressure. The final NOx emissions source comes from fuel-bound nitrogen fuels [34].

The Fenimore and Zeldovich mechanisms are the two major concerns in premixed spark-ignited engines. Burning in lean regimes helps to mitigate the effects of both of these two mechanisms. As the AFR becomes more lean, flame temperatures decline; so the peak temperatures within the engine are lower, resulting in fewer NOx emissions from the Zeldovich mechanism, which become insignificant at temperatures below 1700 K. The Fenimore mechanism is more active in rich combustion, and so it too becomes insignificant for lean mixtures $\lambda > 1.4$ [35]. As shown in the following reviews, several ignition concepts that permit engines to operate at lean conditions produce negligible NOx emissions.

Despite the benefits of lean burn combustion, several drawbacks have limited its practical implementation. One major hurdle is that flame speeds are reduced in leaner mixtures and are more difficult to ignite. As a result of slower flame speeds, high variability of combustion from cycle to cycle in an engine becomes a significant issue. Gasoline, in particular, has a low tolerance for lean combustion with a lean limit of λ (λ is the inverse of equivalence ratio) of about 1.4 [36], [11]. Another hindrance to lean burn technology is the problems it creates with the three-way-catalytic converter common to the exhaust system of most automobiles. The efficiency at which the catalysis converts the three major types of emissions, hydrocarbons (HC), carbon monoxide (CO), and NOx, as a function of the engine's AFR is shown in Figure 2-2 below. As can be seen, the catalyst's performance degrades rapidly when the AFR deviates from stoichiometric conditions. While both HC and CO emissions can be cared for by the catalyst in the presence of excess oxygen in the exhaust, it becomes very difficult to remove NOx [37]. So despite lean mixtures producing

less NOx emissions, the inability of standard after-treatment solutions to operate with excess oxygen means that to be used in engines without special considerations, an engine must burn lean enough to eliminate NOx on its own.

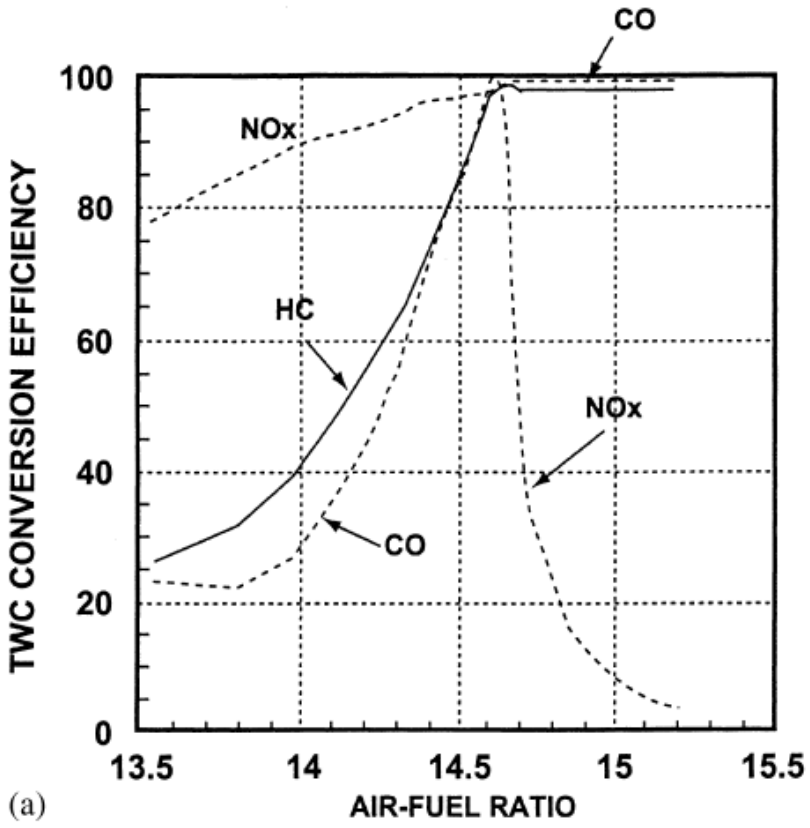

Figure 2-2 Typical Three-Way-Catalyst efficiency plot vs. air-fuel ratio (note: typical stoichiometric AFR for pump gasoline is about 14.6) [37]

To assist in the discussion of the lean-burn operation of gasoline engines, some of the results generated in a study performed by the authors Tully and Heywood [36] are included below. The data included in Figure 2-3 to Figure 2-4 were collected in a study examining the effects of adding hydrogen to a lean air-fuel mixture SI gasoline engine. The study's premise was to test a proposed strategy of adding hydrogen produced by reforming a portion of the engine's gasoline fuel with a plasmatron. While the plasmatron and the process of fuel reforming are beyond the scope of this work, the experiments produced a set of lean λ sweeps of the test engine that was used. Particular

attention should be paid to the baseline test data of gasoline fuel with no hydrogen enhancement in order to see the effects that the lean mixtures have on the engine performance and the limitations it puts on a standard SI engine.

The testing in [36] was performed on a modern 4-valve single-cylinder test engine at an operating speed of 1500 rev/min and a load of 350 kPa IMEPn with maximum brake torque (MBT) spark timing. Figure 2-3 presents some of the data generated for the λ sweep performed in [36]. This data demonstrates the effects of operating at lean conditions on engine performance. As the mixtures become leaner, the following occurs. Variation in the quality of combustion becomes greater, which is reflected by increased values of COV_{IMEP}; 0-10% mass fraction burn durations become longer, which indicates slower flame speeds; and HC emission increases due to incomplete combustion. NOx emissions are reduced as a result of lower flame temperatures. Meanwhile, Figure 2-4 serves to demonstrate the entire point of burning lean as the engine efficiency was found to peak at around λ values of 1.5 in the study.

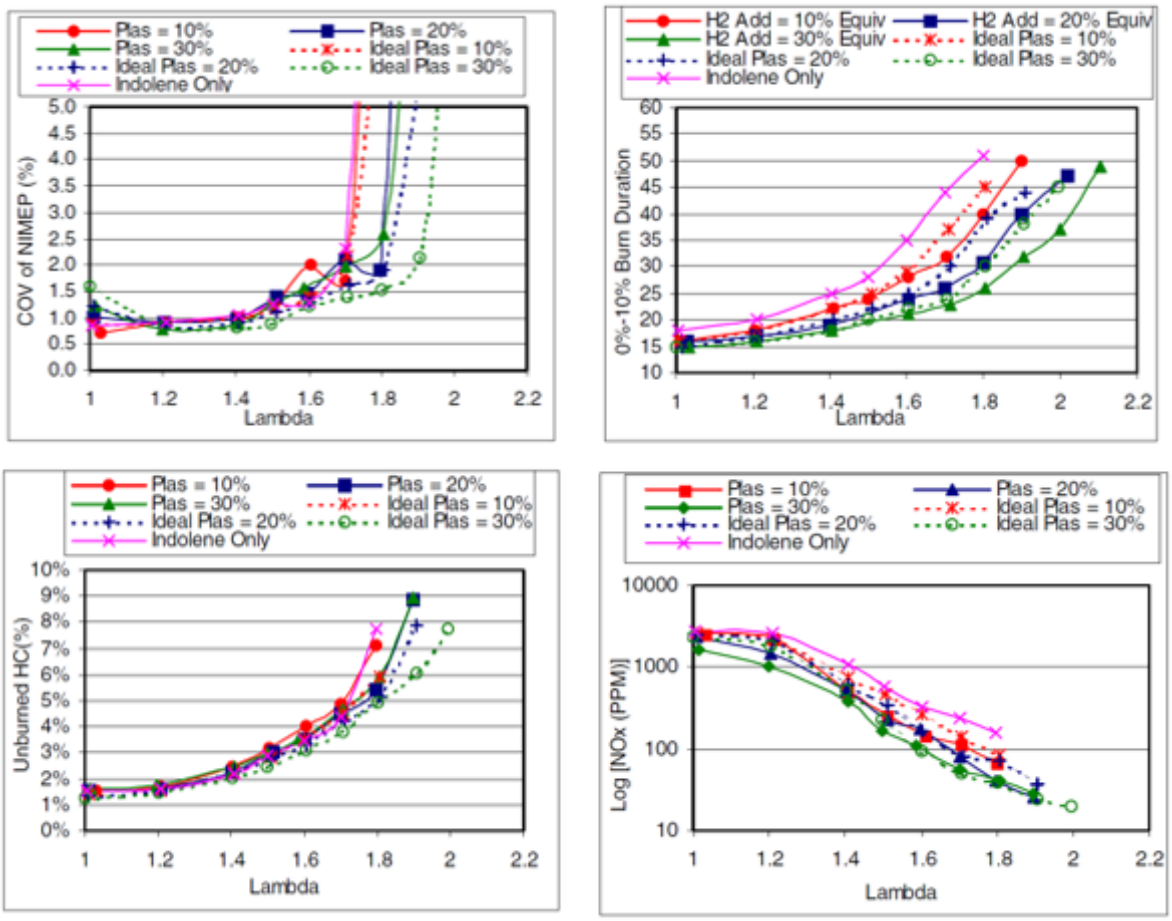

Figure 2-3 Data from a λ sweep performed in [36] (top left) COV_{IMEP} (top right) 0-10% mass fraction burn, (bottom left) HC Emissions, (bottom right) NOx emissions

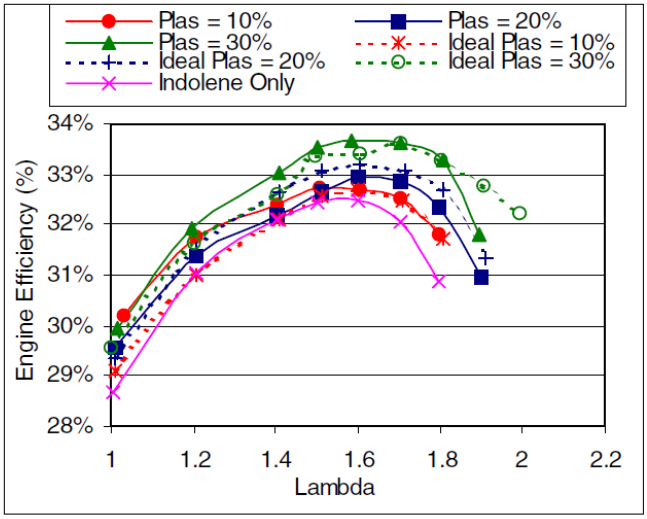

Figure 2-4 Engine-only efficiency as a function of λ [36]

To summarize, the advantages of lean burn combustion are as follows:

- Combustion with excess air leads to higher theoretical thermal efficiencies for the Otto cycle.
- The ability to burn lean allows engine load to be controlled by varying λ mitigating pumping losses.
- Burning lean lowers the maximum temperatures experienced during the combustion process, suppressing the formation of nitric oxides.

Meanwhile, the disadvantages are as follows:

- Flame speed is decreased in lean mixtures; this causes higher variability between engine cycles and difficulty completely burning fuel during the combustion portion of the engine cycle.
- Despite suppressing nitric oxide formation, operating at lean λ is incompatible with current mainstream exhaust after-treatment systems; so either special exhaust treatment is required or any ignition strategy must produce negligible amounts of NOx.

2.2 Ignition Systems for Lean Burn Engines

The traditional means of initiating combustion simply by using a spark discharge to generate a small flame kernel that initiates a flame front that subsequently propagates through an engine's combustion chamber is inadequately suited to take full advantage of lean burn combustion due to the reduced speed at which flames propagate in lean mixtures. As a result, enhanced methods of ignition are an ongoing area of research in the engine community in the hopes of facilitating the use of lean burn engines. These ignition methods include but are not limited to, stratified charge combustion, homogenous charge compression ignition (HCCI), plasma-enhanced ignition systems, and pre-chamber-initiated combustion systems such as Turbulent Jet Ignition (TJI).

Stratified charge combustion is a method of achieving lean burn operation by strategically preparing the air-fuel mixture in the combustion chamber. Essentially, the goal of the strategy is to produce two distinct zones of gas within the combustion chamber, one with a stoichiometric air-fuel ratio and the other comprised of diluent gas [38]. Normal combustion can then take place in the stoichiometric zone, taking advantage of the favorable mixture conditions, while the cycle can reap the thermal efficiency benefits that an overall lean mixture provides. The major drawbacks to this strategy, however, are that despite the addition of a diluent gas, whether composed of recirculated exhaust gas or air, combustion is still occurring at flame temperatures typical of stoichiometric combustion. This leads to elevated levels of NOx produced in the flame even when the overall air-fuel ratio is very lean. Because thermal production of NOx is not adequately mitigated in this strategy, inert exhaust gases are required to dilute the overall mixture since typical exhaust catalysts have difficulty processing NOx in the presence of excess oxygen that would result if air were used as the diluent. This limits the thermal efficiency due to the fact that air cannot be used as the diluent [38].

HCCI is a hybrid concept between spark ignition and compression ignition engines. HCCI is a technique that allows an engine to burn lean. The goal of HCCI is to trigger autoignition in the bulk of the combustion chamber. Ignition is achieved without a spark. Rather, ignition is triggered when the concentration of hydrogen peroxide atoms that have been built up during the engine's compression stroke decompose into hydroxyl radicals. Once these radicals form, the temperature of the mixture increases, and a high-temperature chain branching sequence takes over. Hydrogen peroxide begins to decompose at around 1050-1100 K, which is the temperature that is characteristic of HCCI combustion [34]. The dispersed nature of the autoignition that occurs in an HCCI engine helps to alleviate the difficulties of slow flame speeds resulting from lean mixtures

since it minimizes the distance any flames in the combustion chamber must travel to consume the reactive mixture. While HCCI yields promising potential as a method to achieve engine efficiencies associated with lean burn [39], control strategies to properly control the timing of autoignition remain an area of heavy and active research, which includes means of actively controlling valve timing and even compression ratio.

Since the experimental work and modeling focus on a plasma-enhanced ignition system and Turbulent Jet Ignition, respectively, separate sections discussing the literature pertaining to each follow.

2.3 Plasma-Assisted Combustion and Ignition Systems

The advantages of combining electromagnetic radiation with combustion include faster and more intense combustion, increased stability near the lean flammability limit, reduction of toxic combustion byproducts by the alteration of oxidation chemistry, improved fuel efficiency resulting from more complete combustion, fuel reformation, and more reliable and rapid ignition [40-44].

Investigation of the coupling of electrical energy with combustion has a history of more than a century, with plasma discharges emerging as a source for enhancing combustion over the last four decades. Earlier studies improved combustion by applying an electric field [45, 46], which was not strong enough to generate a plasma but altered the chemistry, flame stability, and flame propagation speeds. The first studies using a plasma discharge involved a thermal plasma jet to increase the flame speed and flammability limit of premixed flames [47-49]. While these new ignition systems proved to be much more effective than conventional spark plugs, the cost and complexity limited widespread use as an ignition source.

Various studies have been conducted to incorporate plasmas in flames for enhanced combustion. These studies have examined the following: pre-treatment of the fuel or reactants into hydrogen-rich syngas prior to combustion [50, 51], enhanced ignition of hydrocarbon fuels [44,

49, 52], increased stability of combustion at atmospheric pressure [43, 53-55], and enhanced combustion efficiency [24]. In particular, plasmas have shown great promise in improving the stability of high-speed ignition and combustion for supersonic propulsion systems [40, 42, 56-59], allowing such systems to operate with greater efficiency, stability, and power over a broad range of supersonic velocities. Plasmas can also alter reaction mechanisms by the decomposition of the fuel gas from larger to smaller hydrocarbon molecules and radicals via elevated electron temperatures; radiation-induced electron excitation [56]; increased adiabatic flame temperature that increases the rates of reaction and transport; and the impact of increased ion/electrons on key radical initiation and propagation reactions. More recently, plasmas have been identified as a main contributor for in-situ fuel reforming (resulting in syngas, H_2 and CO), which can greatly enhance flame stability [25]. When plasma energy is coupled into the reaction zone of a flame, a dramatic increase of electrons and ions impacts the reaction pathways and increases the rate of chemical energy conversion.

Quasi Non-Equilibrium Effects

The plasmas that are typically used in plasma-assisted combustion are classified as either equilibrium or non-equilibrium plasmas [60], [61]. The ignition system presented here attempts to provide what is initially a non-equilibrium plasma discharge that is allowed to eventually equilibrate. The advantage of incorporating a non-equilibrium plasma is that it allows for efficient energy transfer during ignition. Equilibrium plasmas (i.e., thermal arc, spark, etc.) have the disadvantage that the main mode of energy transfer to the reactive mixture is via the deposition of heat. In comparison, a non-equilibrium plasma is characterized by internal energy modes (i.e., rotational, vibrational, and electronic temperatures) that deviate from a Boltzmann distribution and differ from the neutral gas temperature [62, 63]. Temperatures of certain modes can be extremely high (thousands of K) while the rest of the system remains relatively cool (< 1000 K). In

comparison, the energy modes of typical combustion gases are in thermal equilibrium, meaning that the electrons, ions, radicals, and background gases are all at a similar temperature. Thus, non-equilibrium plasmas have the potential to efficiently target energy transfer to specific degrees of freedom in the flame that may accelerate branching reactions and subsequently increase flame speeds. Practical ignition systems for internal combustion engines are projected to be quasi-non-equilibrium systems where both benefits of ohmic heating and non-equilibrium kinetic effects combine to enhance the ignition process.

Studies of non-equilibrium plasma ignition systems in reciprocating piston internal combustion engines have demonstrated the positive effects that non-equilibrium plasmas can have on engine performance and combustion. The authors of [26] demonstrated improvement of lean burn combustion in a 0.55 L single-cylinder gasoline engine using a high voltage nanosecond pulse ignition system. A direct comparison of another non-equilibrium system with a standard spark ignition system is presented in [64], containing results from testing both systems in a four-cylinder passenger vehicle. Improvements in fuel efficiency and hydrocarbon emissions were both reported with the non-equilibrium plasma system. Finally, [65] presents testing of an RF plasma system in a four-cylinder turbocharged gasoline engine. Incorporation of the plasma system improved combustion stability at all operating conditions and extended the lean limit of combustion for the engine while also causing an increase in nitric oxide emissions. Much like these studies, the application of the RF plasma system presented below is expected to improve the performance of the small engine primarily when the engine is run in lean air-fuel ratio conditions. Unlike these previous studies, however, the ignition system is incorporated into a very small displacement engine, which adds to the challenge of producing reliable and complete combustion.

2.4 Turbulent Jet Ignition

The problem of slow flame propagation in lean air-fuel mixtures is overcome in HCCI systems

by auto-igniting a large volume of the mixture dispersed throughout the combustion chamber. In contrast, stratified charge combustion attempts to segregate a favorably combustible mixture from excess gasses in the engine cylinder. Pre-chamber initiated combustion (PCIC) operates in a manner that reflects both strategies. As the name indicates, PCIC engines have two combustion chambers. Combustion is initiated in the pre-chamber, the smaller of the two chambers, by a typical spark ignition. Then based on the particulars of the system, a flame will either propagate through or be quenched within a nozzle or orifice(s) connecting the pre-chamber to the main combustion chamber. Whether or not the flame is extinguished as it traverses through the passages connecting the two chambers, pressure in the pre-chamber forces its contents out into the main chamber in the form of a torch or a jet, entraining fluid and adding turbulence to the main chamber. The process is designed to initiate combustion in the main chamber in a number of widely dispersed areas associated with the jets emitted from the pre-chamber. Thus, this system lends itself well to use in lean burn engine applications as the dispersed ignition sites minimize the distance the lean flames must travel in the combustion chamber, and the added turbulence from the jets enhances propagation speeds.

The history of PCIC engines dates back to the 2-stroke Ricardo Dolphin engine [66] developed in the early part of the 20th century. Toulson, Attard, and Schock published a comprehensive review article on these types of ignition systems in 2010 [11]. This work summarizes the evolution of PCIC from the Ricardo Dolphin engine to the work performed on the Turbulent Jet Ignition (TJI) system developed and tested at MAHLE powertrain by Attard and colleagues [67-69]. The TJI system is very similar to the hardware currently being tested in the combustion laboratory at Michigan State University. As such, the majority of this section will be devoted to the published work generated by engine testing performed by MAHLE with this system, which began about the

time the review article referenced above was published.

Several of the past works highlighted in Toulson's review warrant attention as they pertain to important aspects of the operational theory of the TJI and similar systems. The earliest published works that stand out as having significance are those of L.A. Gussak of the Institute of Chemical Physics at the Academy of Sciences of the USSR published by the Society of Automotive Engineers (SAE) in the mid to late 1970s. In [27], Gussak introduces what he has coined the LAG-process. LAG is a Russian acronym that translates to avalanche-activated combustion. The LAG-process begins with the ignition of a rich air-fuel mixture in a small pre-chamber by means of a spark. As the flame propagates in the pre-chamber, it is eventually forced through several orifices that connect the pre-chamber to the main combustion chamber. During this process, the incomplete combustion products are expelled out into the main chamber in a torch or jet-like form. Turbulent flame kernels begin to form in the wake of the torch, and combustion is initiated in a distributed fashion throughout the main chamber, rapidly consuming the charge.

Perhaps the most significant contribution Gussak makes is that he identifies that combustion is enhanced in the main combustion chamber due to the addition of incomplete combustion products. In particular, he concludes that atomic hydrogen radicals present in the torches emitted from the pre-chamber play a key role in accelerating the combustion in the main chamber. Gussak would also publish a second paper through SAE that reported on testing of the LAG process in an automotive engine in which he demonstrates an increase in stable operation of lean mixtures, improved fuel consumption, and a lower octane requirement [70].

The next important work reviewed in Toulson's article is the work of Yamaguchi et al. at the Nagoya Institute of Technology in Japan [71]. In their study of the LAG-process they identified four modes of operation for the pre-chamber ignition system described by Gussak based on the

behavior of the ignition that was related to the size of the orifices connecting the pre-chamber to the main chamber. These four modes are as follows:

Well-dispersed burning: Results from a small orifice diameter characterized by a long ignition delay followed by rapid combustion, which is considered to be the result of chemical rather than thermal ignition.

Composite Ignition: The orifice for this mode of operation is larger than that of a) with flame kernels promoting main chamber burning. The ignition is considered to have occurred because of a combination of thermal and chemical effects.

Flame Kernel Torch Ignition: The diameter of the orifice is again increased. A turbulent jet is issued from the pre-chamber, but in this case, ignition is only attributed to the flame kernels generated by the jet.

Flame Front Torch Ignition: The orifice in this case is large enough that the pre-chamber flame passes through the orifice as an intact flame front that results in normal flame propagation in the main chamber.

This work further supports the theory put forward by Gussak that chemically active species from the pre-chamber can be used to enhance combustion in the main chamber. It also demonstrated that the composite ignition regime was the most effective at burning lean main chamber mixtures.

Finally, getting to the most recent work performed by MAHLE with their TJI device, it should be noted that the hardware and concept of the TJI grew out of the work performed at the University of Melbourne on Hydrogen Assisted Jet Ignition (HAJI) examples of literature produced from the research are given as references [72] and [73]. The TJI hardware tested by MAHLE is shown below in Figure 2-5 with a schematic of the system installed in the head of an automotive engine

in Figure 2-6.

The TJI testing conducted by MAHLE was performed using a single cylinder 0.6 liter, four-stroke, naturally aspirated, port fuel injected, water-cooled, four overhead valve engine modified from a GM Ecotec LE5 four-cylinder engine. The TJI's pre-chamber volume is 1.3 cm^3 and is designed to be 2% of the clearance volume of the test engine. As can be seen in Figure 2-6, the pre-chamber is centrally located overhead in the cylinder head. The pre-chamber's nozzle contains six orifice holes which are equally spaced with diameters of 1.25 mm with passage lengths of 3 mm. The pre-chamber is supplied with a separate fueling source via a direct injector installed in the pre-chamber housing. Much like the other pre-chamber ignition systems reviewed in [11]. The TJI is designed to operate with a favorable, if not rich, air-fuel mixture in its pre-chamber and a separate, perhaps even lean, mixture in the engine's main combustion chamber.

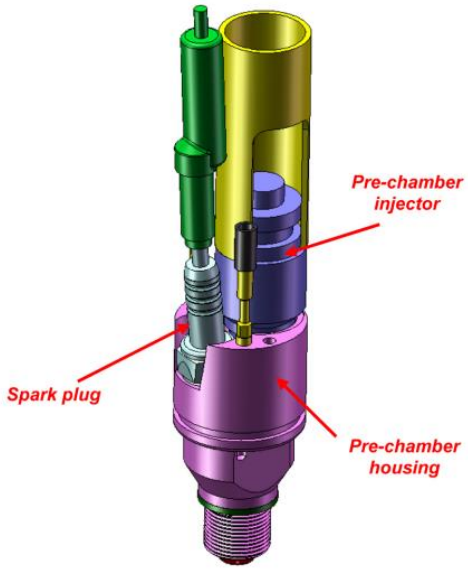

Figure 2-5 Model of the MAHLE turbulent jet ignition showing the pre-chamber housing, fuel injector and spark plug [67]

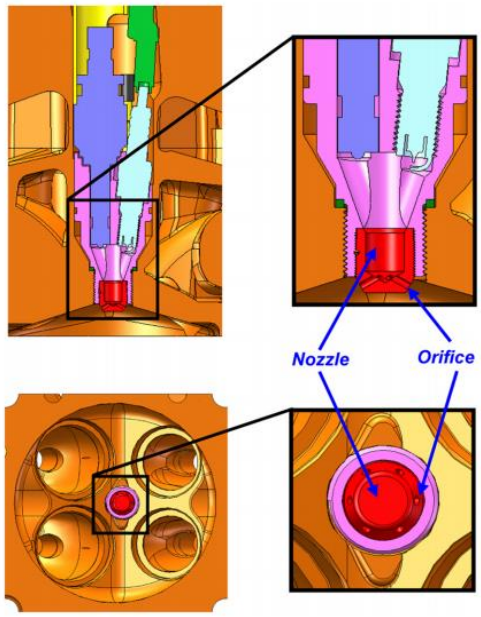

Figure 2-6 Schematic of the MAHLE turbulent jet ignition installed in the head of an automotive engine [67]

In total, eight publications were produced pertaining to the research generated from this hardware. The first published studies all report on test results generated using a duel fueling strategy wherein the main chamber was fueled by the gasoline port fuel injector and the pre-chamber was supplemented with propane fuel. This duel fueling is a result of the fact that only a small mass of fuel is needed to provide a stoichiometric or richer mixture in the TJI pre-chamber. Since there are very few if any applications for extremely low flow rate fuel injectors, a fuel in a gaseous state such as propane was necessary for its ability to be injected in a low density form [67].

In [67], the TJI hardware is introduced and lean and rich limits for the test engine using both a standard spark ignition system are reported for the engine at 3.3 bar IMEPn and 1500 rev/min. The results demonstrate an extension of the lean operating limit for the engine with the use of the TJI system as shown below in Figure 2-7. Tests were also performed with the engine at wide open throttle with air-fuel ratio varied to measure the output. The results of these sweeps for the TJI and

standard SI system are shown below in Figure 2-8. As should be expected, greatly diminished NOx emissions were reported for the engine operating at conditions leaner than $\lambda = 1.8$. Stable combustion (IMEPn < 2%) was also reported with the TJI system up to $\lambda = 2$.

The important takeaway from the results in [67] is that the engine can operate with very lean overall air-fuel mixtures, and that load can be controlled by controlling the amount of fuel injected into the system with very little or no throttling. Thus, the TJI demonstrates the ability to stably combust lean mixtures while also showing the potential for reduced dependence on throttling for load control.

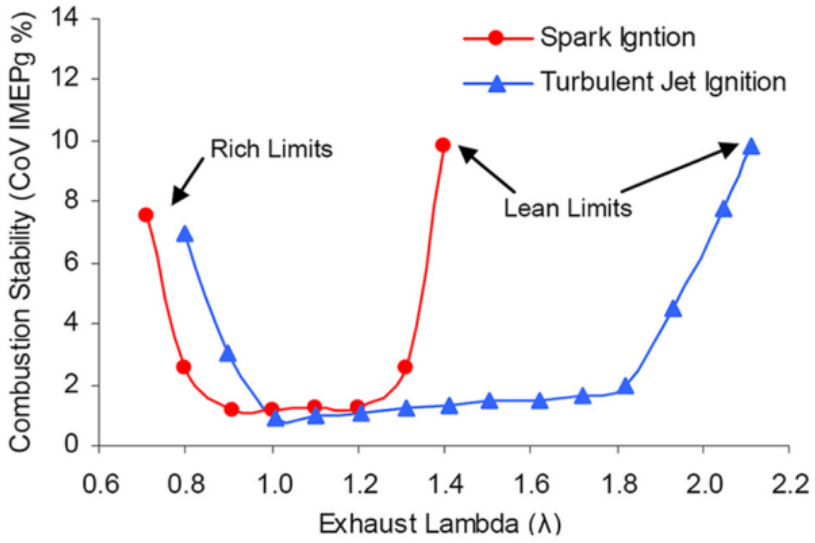

Figure 2-7 Air-fuel ratio sweep of MAHLE TJI compared to standard spark ignition [67]

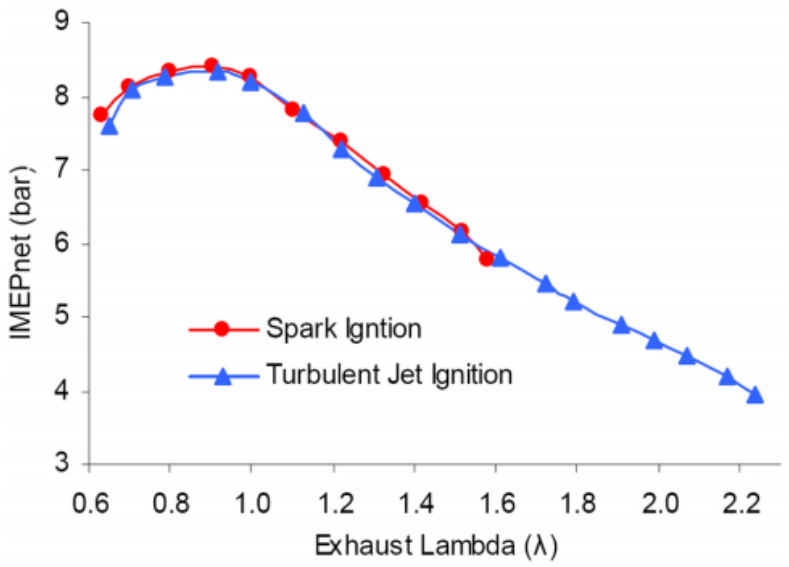

Figure 2-8 Engine loads produced by varying air-fuel ratio with the engine operating at WOT and 1500 rev/min [67]

The publications that follow [67] further examine details of the TJI system. In [74] and [75] the effects of ignition energy, spark plug orientation, and spark position within the pre-chamber are examined and show minimal effect on the performance of the system except in the case that the spark plug recessed too far in the pre-chamber. In [68], a mapping of the engine with the TJI system is performed. The map is then subsequently used in conjunction with a simulated drive cycle, and fuel economy performance is compared to that of the standard SI performance of the engine to find that the use of the TJI system provides a 13% improvement in fuel economy for both the NEDC and FTP-75 drive cycles. In [69], the issue of using duel fuels in previous works is addressed. A fuel injector's nozzle was heavily modified to allow the low flow rate required for liquid gasoline to be used as the pre-chamber fuel. The results demonstrate that there is only a minor drop in the performance of the system when gasoline is used as the sole fuel in the system. Knock extension is examined in [76], demonstrating a reduction of 10 in the required octane of the fuel used in the engine with the TJI. Knock extension is another benefit of pre-chamber

combustion systems, and it is also a subject of research being performed at Wright Patterson Air Force Base with an unfueled pre-chamber jet ignition system [77]. Finally, [78] and [79] examine the unthrottled operation of an engine with gasoline as the sole fuel source and a mapping of the engine's performance comparing all of the previous combinations of fuel sources, including vaporized gasoline in the pre-chamber.

The MSU Dual-Mode Turbulent Jet Ignition

Despite this document's publication date, most of the research covered here was conducted between 2011 and 2016. As such, the literature review up to this point has covered content that was current when the original research documented here was conducted. While research on the topic of pre-chamber-initiated combustion has continued in these intervening years [80-82], the research group at Michigan State University led by Dr. Harold Schock has continued working on the development of a TJI system for gasoline spark-ignited engines that warrants discussion. For the past several years, this group has developed and tested four iterations of what they have named the Dual-Mode Turbulent Jet Ignition (DM-TJI) engine [83-85] and trademarked it as the Jetfire® Ignition.

Implementing a Turbulent Jet Ignition system in a spark-ignited engine presents multiple obstacles that must be overcome. They are: 1) to operate with very lean or otherwise highly diluted overall mixtures, the pre-chamber must be fueled to provide a readily ignitable mixture; 2) the connection between the pre-chamber and the main chamber in the TJI is necessarily very restrictive to facilitate the creation of high-velocity jets during combustion which presents difficulty purging residual gases from small volume during the gas exchange processes of the engine negatively effecting the composition and therefore the ignitability of the pre-chamber mixture; and 3) although the TJI has demonstrated that it can operate with mixtures lean enough to all but eliminate NOx formation, in a practical application an engine will have to operate at high loads sometimes

making the utilization of mixture ratios that will produce NOx necessary, which because the engine will typically be operating with excess oxygen in the exhaust typically, will not be able to use a common three-way catalyst (TWC).

The challenge of providing a fuel source to the pre-chamber is a very old problem that has been addressed in several ways for various implementations of pre-chamber-initiated combustion. Solutions range from the utilization of a second fuel type, usually a gas such as propane or hydrogen, to using only gasoline in both chambers. In the DM-TJI, a high-pressure direct injector is used to supply gasoline to the pre-chamber.

To address the difficulty of purging the pre-chamber, the DM-TJI utilizes auxiliary means to add air into the pre-chamber. In the original prototype, this was accomplished by adding another injector into the pre-chamber to supply and regulate air injected to purge the chamber. In the third iteration, the injector was replaced with a cam-actuated poppet value.

Finally, to address the difficulties with after-treatment, research was conducted using EGR instead of air as the main chamber diluent. While the thermodynamic properties of EGR diluted mixtures are less advantageous regarding the thermal efficiency of the theoretical Otto cycle, the lack of excess oxygen in the exhaust allows for a standard TWC to be used as an after-treatment solution, providing a promising pathway forward to actual on-road use of the system without the burdensome addition of a lean burn exhaust system such as an SCR system. Testing published by Atis and Schock [83] the DM-TJI III prototype demonstrated successful operation with up to 40% EGR dilution with only a slight difference in the maximum indicated thermal efficiency, reported at 38.5%, compared to the operation with the same dilution but with air instead. More recently, engine testing with the DM-TJI IV prototype, which includes a concentric camshaft that allows for the purge air valve to be controlled independently from the cylinder valves, has achieved

indicated thermal efficiencies of nearly 50% [86]. A CAD model of the fourth generation Jetfire® is shown in Figure 2-9.

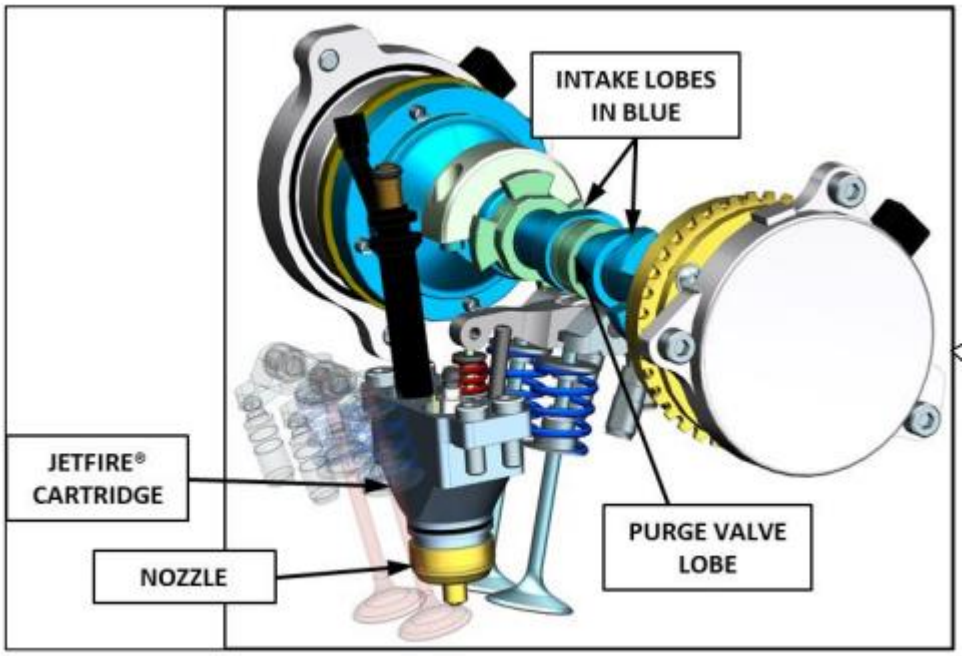

Figure 2-9 The Fourth generation Jetfire® with cam purge valve actuation, independent control from intake valves using the concentric camshaft design (Thyssenkrupp – Jetfire® Concept) [86]

2.5 Computational Modeling of the Turbulent Jet Ignition System in a Rapid Compression Machine

Simulations of the turbulent jet ignition system in an RCM are not isolated to the research presented in this dissertation. Additional simulations of TJI systems in the MSU RCM were published that examine the use of methane fuel and fuel enrichment in the pre-chamber. In Gholamisherri et al. [87], large-eddy simulations (LES) with detailed chemistry are run using Converge CFD software, the same software used in this work. They are presented in comparison to physical RCM experiments. An additional simulation using Reynolds Averaged Navier-Stokes (RANS) equations turbulence modeling is also presented and is compared to one of the experimental test cases and its corresponding LES simulation. These comparisons showed that both the LES and RANS simulations overpredicted the peak pressure generated in the RCM,

indicative of higher total heat release, and are shown in Figure 2-10. This is true of the simulations presented in subsequent chapters here as well. The LES simulation also matches the experimental trace better of the course of main chamber combustion than the RANS simulation. Figure 2-11, reproduced from [87], displays the flame front development within the pre-chamber from one of the LES simulations. Unlike the RANS simulations presented here, the larger length scales of turbulence are persevered, producing the undulated surface in Figure 2-11.

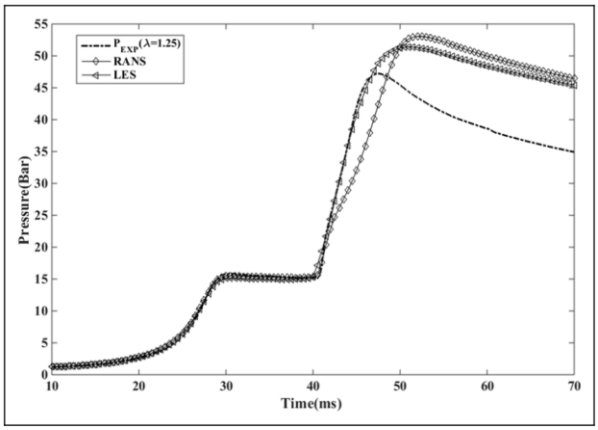

Figure 2-10 A plot of RCM combustion chamber pressure from [87] comparing experimental results to LES and RANS simulations

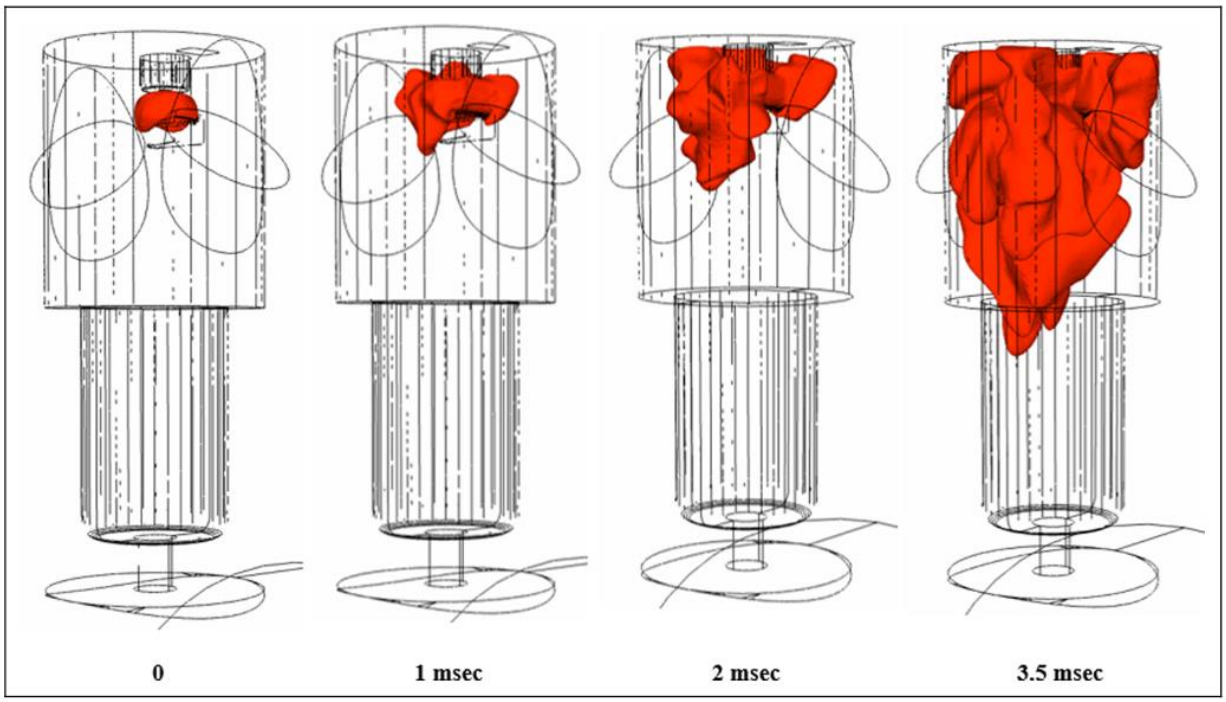

Figure 2-11 An example of flame front propagation in the TJI pre-chamber for an LES simulation taken from [87]

Validi et al. [88] present simulations of the same TJI setup that was used in [87] but with greater geometric simplifications made while transitioning the physical geometry to the computational model to allow for a more computationally efficient geometric grid to be used to discretize the domain. In the simulations presented, a hybrid Eulerian-Lagrangian large eddy simulation/filtered mass density function (LES/FMDF) computational model is used. While the modeling of turbulence and heat and mass transfer is more detailed than what was used in [87], the chemical mechanism used to model combustion contains only two reactions. Similar to [87], the simulations over-predict peak pressures, and the comparison of combustion chamber pressures to experimental data, shown in Figure 2-12, qualitatively does not look as accurate as the LES simulation in [87]. In all likelihood, this is a consequence of the simplified chemistry model being used in the LES/FMDF simulations. Figure 2-13 is also included to show a comparison of the simulation to optical images collected from a physical experiment.

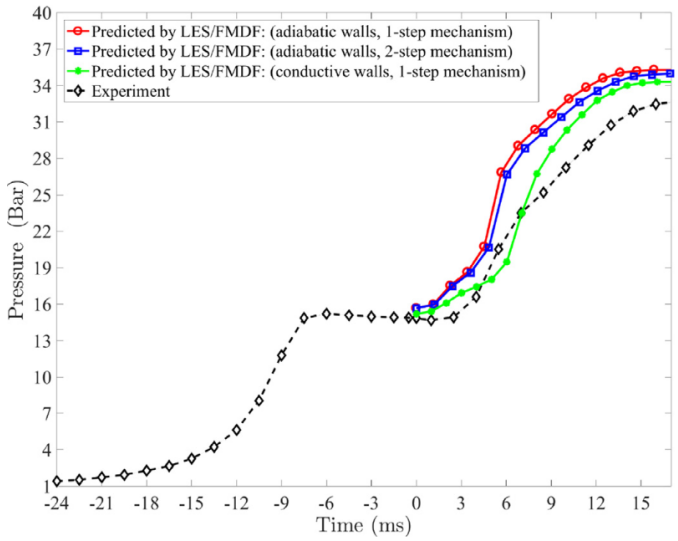

Figure 2-12 RCM combustion chamber pressure trace plot comparing LES/FMDF simulations with experimental data from [88]

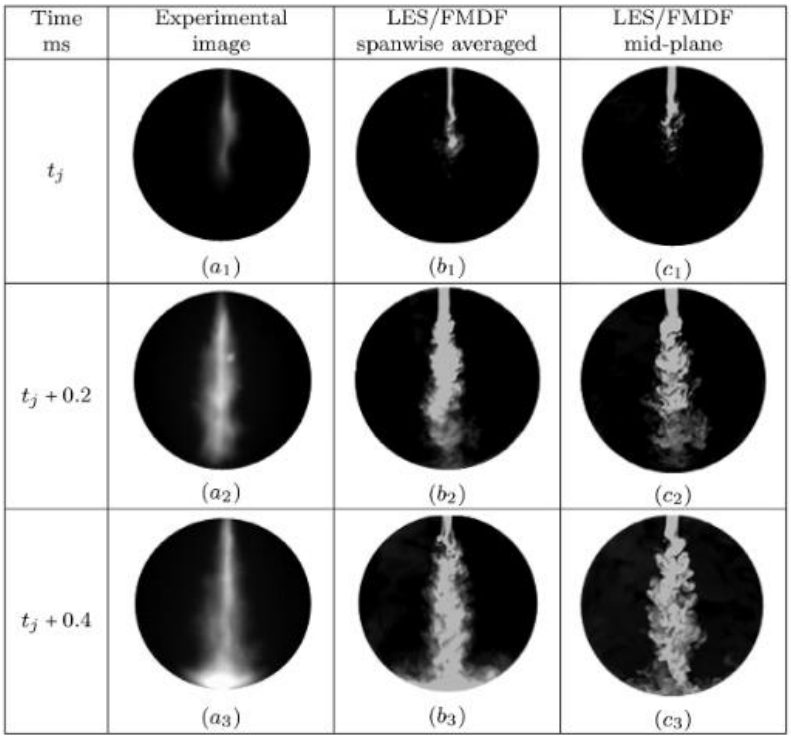

Figure 2-13 Comparison of simulated temperature data to optical images captured during an experiment from [88]

The authors of [88] also perform a parametric study similar to the one presented in Chapter 8 below, examining the effect of moving the location of the ignition source along the centerline of

the pre-chamber has on the overall combustion of the system. While the effected behavior on the combustion process is similar in both Chapter 8 and [88], the authors of [88] draw the opposite conclusion than what is presented below. In [88], the authors state that the best location for the ignition source is near the orifice of the pre-chamber. Meanwhile, Chapter 8 will espouse the opposite: the ignition source should be placed as far away from the pre-chamber exit as possible. The reason for this contradiction is that [88] is evaluating a different metric than what is evaluated in Chapter 8. In [88], the considered metric is the time between the initial ignition event in the pre-chamber and complete burn for the entire system. Meanwhile, the simulations in Chapter 8 evaluate the performance of the burn durations of the main chamber independently from the pre-chamber as the combustion in the main chamber is of primary concern in a reciprocating piston engine. It is assumed that spark timing will be set to account for the delay between the spark and the emergence of the hot turbulent jet in any engine application.

CHAPTER 3: PLASMA ENHANCED IGNITION SYSTEMS EXPERIMENTAL APPARATUSES

3.1 Plasma Ignition Systems

The main focus of this study was to examine the effects that a radio frequency (RF) plasma discharge system designed at Michigan State University had on the performance of internal combustion engines. The main component of the RF plasma system is a high-voltage pulse generator. This pulsar provides a maximum voltage of 30 kV and is current-limited at 200 mA. When firing, the generator pulses at a rate of 20 kHz, which is within the range of what is considered low radio frequency. These output pulses form a train composed of alternating high (30 kV) and low (0 V) voltage square waves of 25 μs width each. The voltage rise duration at 30 kV is 20 ns for each high-voltage pulse. The maximum pulse train duration is limited to 1.2 ms. At this pulse train duration, the maximum amount of energy the RF system provides is 400 mJ compared to the no more than the 50 mJ provided by the small engine's standard coil. The generator was controlled using a 5 V TTL signal, firing during the duration of a low signal. The system utilized the standard resistor spark plug (NGK CMR6A) that comes installed in both the Fuji and Subaru engines. The generator connects to the spark plug using a non-inductive spark plug wire. It is worth noting that pulsar generates a problematic amount of electrical noise when it fires. The steep slopes of the voltage rises generated by the device caused voltage spikes on inadequately shielded electronics. Significant adaptations to the test stand's ignition timing control, the processing of acquired data, and special shielding of the input devices on the data acquisition computer were required during testing.

The steep rising high voltage potential applied across the engine's spark plug by the RF system is designed to provide an elevated electric field strong enough to cause electron impact disassociation reactions, which generate active radical species such as O, H, and OH that are

typically produced in the branching reactions of hydrocarbon combustion. Radical propagation will be enhanced through electron or ion impact reactions, which can alternatively dissociate nitrogen or oxygen at higher rates and produce alternative species, such as singlet delta oxygen $O_2(a^1\Delta_g)$, which can dramatically impact the overall chemistry [89].

The efficiencies of these disassociation reactions peak in a gas when its reduced electric field is on the order of 10^{-15} $V \cdot cm^2$ [90]. The additional presence of radicals and other energetically active species created by electron disassociation in air-fuel mixtures has been shown to both cause ignition at gas temperatures below a mixture's autoignition temperature, non-thermal ignition, and to improve flame propagation speed in regions of active combustion [91]. While the initial application of the electric field is expected to transfer energy to electrons much faster than to the heavier ions and neutral molecules in the discharge, creating a non-equilibrium discharge, because the voltage is applied for a rather long duration, breakdown eventually occurs in the spark plug gap resulting in a high-temperature arc. The classification of the RF system as a quasi-non-equilibrium plasma is a consequence of the fact that the thermal equilibrium plasma arc is allowed to form while many non-equilibrium ignition strategies attempt to avoid the energy-expensive Joule heating associated with thermal plasmas to focus energy input to lower energy electronic modes of energy [41].

Improvement in the combustion performance of the automotive engines tested with the plasma system compared to that of a standard ignition coil at identical conditions is observed with the plasma system while operating the engines with lean air-fuel mixtures that are both more difficult to ignite and exhibit slower flame propagation speeds. Generally, the advantage of a non-equilibrium discharge is mitigated in stoichiometric conditions where a typical spark plug adequately initiates combustion. As the mixture becomes leaner, the positive impact of a non-

equilibrium plasma becomes more pronounced, and fuel oxidation efficiency is increased [24].

The benefits of the RF systems can be attributed to a number of reasons. Since the energy required to produce electronically excited species in a non-equilibrium plasma is much less than the energy required to heat the gas in the discharge [41], the initial non-equilibrium portion of the RF system's discharge is likely more voluminous compared to the small channel of the thermal arc that subsequently appears in the spark plug gap. Even if the concentrations of active radicals generated by the non-equilibrium phase of a voltage pulse are not large enough to cause non-thermal ignition of the air-fuel mixture on its own, the remaining pulses in the train provide electronically excited radicals within the volume of the initiating flame kernel contributing to an improvement in the rate of the combustion in the fledging development of the flame front. Additionally, the increased O_2 content in lean mixtures will generate a high pool of reactive oxygen molecules in excited states, which are less prone to quenching. The improvement in the ignitability and enhancement of initial flame propagation provided by the RF system plasma helps to stabilize cycle-to-cycle variation in the engine's combustion, ultimately leading to improved engine power output at lean conditions.

3.2 Small Engine Dynamometer

The Test Engine

The engine used in this study is a Fuji Imvac-34EI single-cylinder, four-stroke gasoline engine. The engine is sold for large-scale model airplane applications that are popular with hobby enthusiasts. The engine has a 33.5 cm^3 displacement, a compression ratio of 8.6, and a bore and stroke of 39 x 28 mm. The engine has an advertised maximum power output of 1.49 kW (2.0 hp), a maximum torque of 1.962 N·m, and a maximum operating speed of 7500 rev/min. The engine has a single intake and a single exhaust valve. Fuel delivery for the engine is provided by a Walboro carburetor with high and low-speed needle valve adjustments for tuning the air-fuel ratio

of the intake mixture. The engine is air-cooled, and forced air is provided by the exhaust of a blower fan mounted on the engine test stand. The engine uses an electronically controlled ignition system, called the EIS by Fuji, which utilizes a standard ignition coil powered by a 4.8 V battery. The system uses a single electronic pulse per engine revolution to control the triggering of the coil. The system adjusts ignition timing with engine speed, retarding the timing significantly at low speeds near idle but fires the system concurrent with the pulse signal at higher engine speeds. The same basic engine with different peripherals is also sold in a package marketed for power equipment applications such as leaf blowers, weed trimmers, or fluid pumps as the Subaru/Robin EH035.

Small Engine Test Stand

Engine testing was performed using a small engine dynamometer test rig that accommodates internal combustion engines with up to 7.0 kW of power output. The test stand, shown in Figure 3-1, features a Magtrol ED-815 Hysteresis Dynamometer. The dynamometer has a hysteresis brake that provides a frictionless torque loading that is independent of engine speed. The resistive torque provided by the dynamometer is generated by a magnetic field produced by a reticulated pole structure that restrains the rotor when energized. The dynamometer is controlled using a Magtrol DSP6001 high-speed programmable dynamometer controller that has a built-in current-regulated power supply for energizing the dynamometer's hysteresis brake. The controller provides analog voltage outputs for both torque and speed.

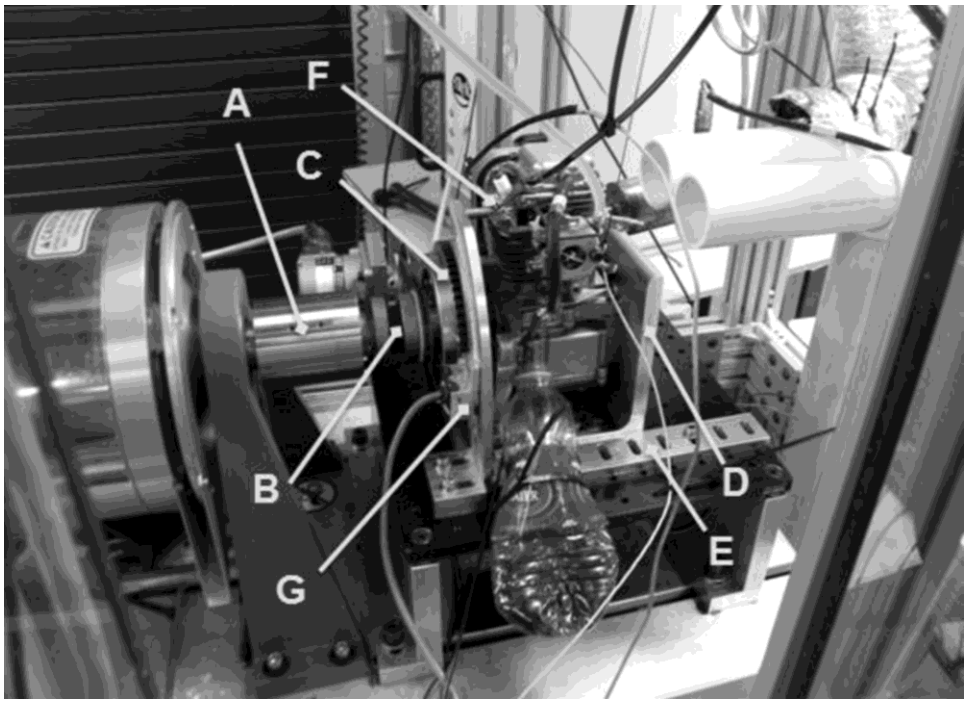

Figure 3-1 Photograph of installed engine taken from intake side: A) dynamometer shaft adapter, B) coupling, C) flywheels, D) engine mounting bracket, E) alignment block, F) in-cylinder pressure sensor, G) ignition timing Hall Effect sensor

The harsh vibrations produced by the single-cylinder engine made finding an appropriate coupling between the shafts of the engine's crankshaft and dynamometer difficult. Several couplings rated for the torque and speed that the engine was expected to operate at were initially used with the test stand, but they all failed after only a short time with the engine operating at idle with no load from the dynamometer. Eventually, a successful coupling was found. The coupling that was used for testing is a Martin Quadra-flex coupling (size 4 JEM). The coupling transmits torque through an elastomeric sleeve that engages the cavities present in the opposing metal hubs of the coupling, which are each connected to one of the two shafts. This coupling was selected for its high shaft misalignment tolerance and its torsional softness, which allows it to tolerate the harsh vibrations generated by the engine. The coupling is rated for a maximum speed of 7600 rev/min and 13.6 N·m of torque. The specified allowable parallel and angular misalignments of the coupling are 0.254 mm (0.010 inches) and 1° respectively. While the actual misalignment of the

engine setup, estimated to be at best 0.508 mm (0.020 inches), exceeded these specifications, a coupling failure never occurred during testing, and only a single coupling sleeve was replaced over the span of the test stand setup and performance of the actual engine tests.

In-cylinder pressure was measured using a Kistler Type 6052C piezoelectric pressure sensor. The sensor lacks active cooling but is relatively insensitive to thermal effects, +/- 0.5% over the temperature range expected in the engine. The pressure sensor was connected to a Kistler Type 5010B Dual Mode Amplifier. The engine's air-fuel ratio was monitored using an ECM AFRecorder 1200 system with its sensing element mounted in the engine's exhaust. The crank position was measured using a BEI H25 incremental optical encoder. The encoder is a 720-cycle per rotation resolution dual-channel quadrature encoder with a third index channel. Only a single channel and the index channel were monitored in testing yielding crank angle measurements in increments of ¼ of a degree. Engine head temperature was monitored using an Omega SA1-RTD-B resistance temperature device (RTD). The cylinder temperature was not recorded with the test rig's data acquisition system and was used only to determine that the engine had reached a steady operating temperature before data recordings were taken.

Data acquisition was performed using a personal computer with a National Instruments multifunction DAQ PCI card, part number NI PC-6143. The device is a 16-bit resolution card with 8 analog voltage inputs that can be simultaneously sampled at a rate of up to 250 kHz at voltages within the +/- 5 V range. The card is controlled using MATLAB's data acquisition toolbox and a MATLAB graphical user interface designed at Michigan State for the specific task of collecting data from the engine test stand.

3.3 Optical Engine Platform

Tests of the RF plasma system were conducted in one of Michigan State University's optical engine test cells. The RF system tests were compared to tests taken using the optical engine's

standard inductive coil with a discharge energy of 75 mJ. The setup of the testing is shown in Figure 3-2. The optical engine is a single-cylinder naturally aspirated engine adapted from a four-cylinder Chrysler engine. The bottom end of the engine utilizes a MSU modified Hatz platform [92] with a Bowditch arrangement featuring a 58 mm diameter quartz window in the piston crown [93]. The engine's single operating cylinder has a 0.4-liter displacement, four valves, direct injection, a compression ratio of 9.0, and a bore and stroke of 83 x 73.9 mm. As a result of the optical components on the engine, firing experiments were limited to only 40 cycles each due to hardware limitations and to avoid the degradation of combustion image quality. In order to ensure consistency, the engine's cooling and lubrication systems have been de-coupled from the engine's crankshaft and are externally operated and heated. This allowed the cylinder head to be preheated to a consistent temperature prior to the execution of firing experiments.

In-cylinder pressure acquisition and analysis were completed using A&D's CAS system, which enabled combustion parameters to be easily compared between tests. Imaging of the combustion was captured with a non-intensified high-speed digital video camera (Photron Fastcam APX RS), which was triggered prior to the ignition firing. The camera recorded at a rate of 10,000 images per second with a 512 by 512-pixel resolution covering an area of approximately 120 by 120 mm.

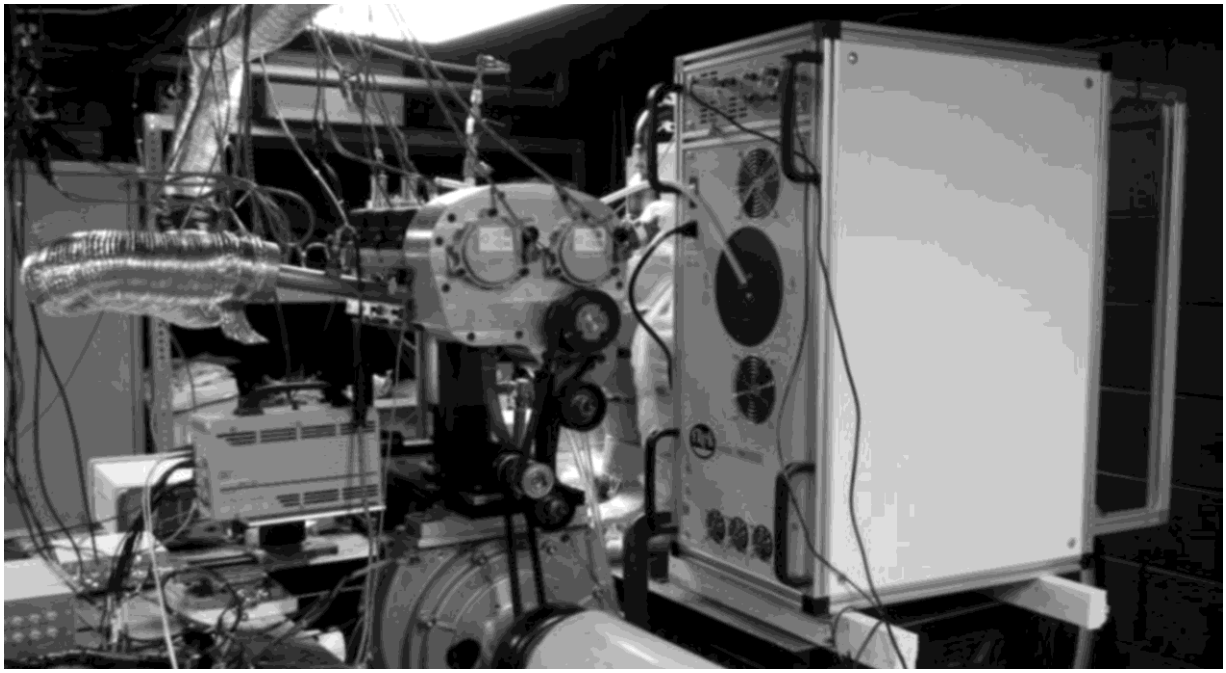

Figure 3-2 Optical Engine Setup with the high-speed camera and optical engine on the left and the RF plasma system on the right

CHAPTER 4: PLASMA IGNITION SYSTEMS TESTING

4.1 Small Engine Testing

Engine testing was performed at three engine speeds: 4000, 5000, and 6000 rev/min. Each set of data was collected with the engine operating at wide open throttle (WOT). Data collection began only once the engine's cylinder head temperature reached a steady value. A sweep of λ (relative air-fuel ratio: actual/stoichiometric) values ranging from richer than λ = 0.9 up to the limit at which the air-fuel mixture became too lean and the engine no longer could sustain the desired operating speed was stepped through by adjusting the carburetor between acquisitions. Each acquisition lasted between 4.5 to 7.5 s depending on the engine speed. These sampling time durations were chosen so that each data point collected included over 200 engine cycles. Indolene was used as the fuel in all of the testing performed.

The engine testing focused on the acquisition of the net indicated mean effective pressure (IMEP) of the engine, the coefficient of variation of IMEP (COV_{IMEP}), and the maximum pressure rise rate. This maximum pressure rise rate is indicative of the speed and intensity of combustion as faster more intense combustion will generate faster rates of pressure increase in the cylinder. In this study, a 3rd order finite difference formulation was used to compute this pressure derivative with respect to crank angle from the discrete data collected.

The ignition timing of the standard EIS provided with the Fuji engine was unaltered during testing. It was assumed that this system had been set up to run with optimal timing at near stoichiometric air-fuel mixtures. The timing for the RF system was determined for each engine speed by performing a timing sweep at λ = 1.0. This was done because the timing of the standard ignition system was not altered and adjusting the timing of the plasma systems as λ was varied such that the engine would always operate at minimum advance for best torque spark timing (MBT) would not provide a good comparison of the plasma system with the standard coil. Also,

the noise generated by the RF system prevented its ignition timing from being controlled electronically. A sensor mounted on a circular track around the axis of the engine's crankshaft was used to sense a single tooth on the engine's flywheel that triggered the RF system to begin firing its pulse train.

An OTC RG240 digital gas analyzer was used to determine the composition of the small engine's exhaust gas. The sampled gas was inducted into the analyzer through a probe line mounted in the engine's exhaust pipe. The gas analyzer recorded the measurement of nitric oxides (NOx) and hydrocarbon (HC) concentrations in ppm and oxygen, carbon dioxide, and carbon monoxide as percentages of the gas composition. Gas sampling was performed on the engine while it was running at WOT and at a speed of 5000 rev/min with several different λ values for each ignition system. The engine was run up to a steady operating temperature and air-fuel ratio and held at these steady values for at least one minute to ensure that the sampling line to the analyzer had been flushed through with exhaust gas from the operating condition of interest. Sampling was then performed for 10 seconds with the OTC gas analyzer recording gas composition once every second. These ten samples were then averaged for each test point.

4.2 Small Engine Results

The following results were collected at WOT with the engine allowed to warm up to its continuous operating temperature, as indicated by a steady reading from the temperature sensor mounted on the engine's cylinder, at these maximum loads prior to the collection of data. The RF high voltage pulsar was set to an output voltage of 30 kV with a pulse train duration of 1.2 ms. Plots displaying IMEP, COV_{IMEP}, and maximum pressure rise rate as functions of λ are shown in Figure 4-1 to Figure 4-3 for tests conducted at 4000, 5000, and 6000 rev/min, respectively. These engine speeds were chosen to fall within the anticipated operating speeds of between 4000 and 7500 rev/min for the engine as specified by its manufacturer. Finally, mass fraction burn data is

also presented for both ignition systems in Table 4-1 for data points taken at 4000 rev/min at similar loads.

While testing at WOT may not be ideal for comparing the ignition systems, it was chosen for the simplicity it provided for controlling the engine. Despite the very high engine loads, the two systems are compared at identical conditions with MBT spark timing determined for each system at $\lambda = 1.0$. While the engine load may differ between the two ignition systems at identical λ, the amount of air and fuel the engine employs is identical. Therefore, improved output and combustion stability compared to the standard ignition coil at a given air-fuel ratio indicates an improvement in the engine's combustion with the RF system.

It is evident that the plasma-enhanced system provides higher engine power output than the standard coil at identical λ. The improvement is moderate or even negligible at lower speeds and near stoichiometric conditions, but it becomes more pronounced as λ increases into the lean region of combustion and as the engine speed increases. The same pattern is observed in the comparisons of COV_{IMEP}. At identical λ, the plasma systems provide more stable, lower values of COV_{IMEP}, combustion than the standard coil. Again, as λ increases into the lean region, the difference between the systems becomes more significant. These plots indicate an enhanced ability of the engine to run using lean air-fuel mixtures with the RF plasma system.

The impact can be more fully appreciated by examining two specific data points. For example, the 6000 rev/min operating speed data set for the EIS system includes a test point at $\lambda = 0.98$ with an IMEP of 647 kPa. At the same operating speed with the RF plasma system, a point with a similar output of 639 kPa is achieved at $\lambda = 1.15$. Not only is the power output nearly identical at the leaner mixture but the COV_{IMEP} is also improved from 19.3%, an unstable operating condition, for the standard system at $\lambda = 0.98$ down to 6.0% at $\lambda = 1.15$ for the RF plasma system.

When examining the results presented here, it is important to recall that the test engine is very small and exhibits high values of COVIMEP even at ideal operating conditions. It should not be held to the same standards as larger automotive engines. So, although a COVIMEP of 6.0% may seem high, it is good for this engine since at 6000 rev/min the COV_{IMEP} is never lower than 6.0% for the standard ignition coil except for conditions of λ richer than 0.94.

Insight as to why the output of the engine is higher with the plasma systems can be gained by examining the third plot in each of the three figures that compare the maximum pressure rise rates of each system. In these plots the pressure rise rate is always higher for the plasma system than the standard coil at equivalent λ. This suggests that the rate of combustion is more rapid when the RF system is used.

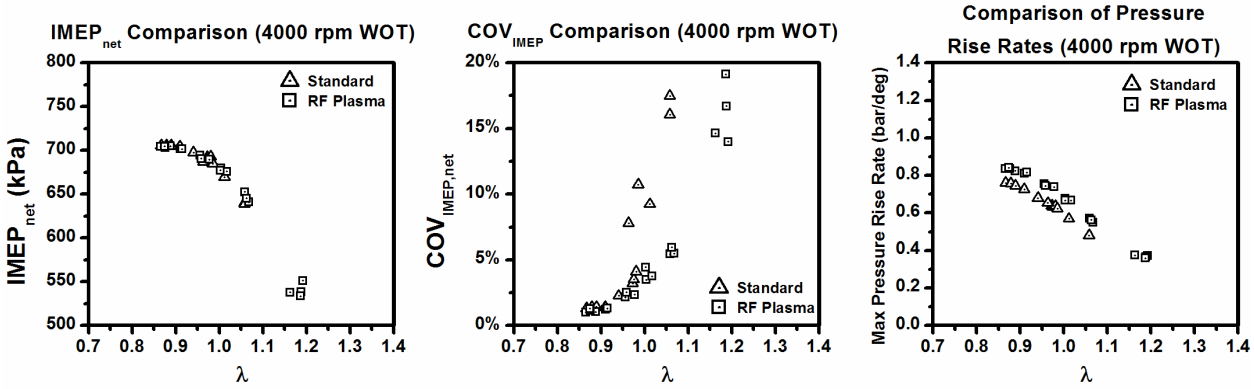

Figure 4-1 Results of Air Fuel Ratio sweep Wide Open Throttle at 4000 rev/min

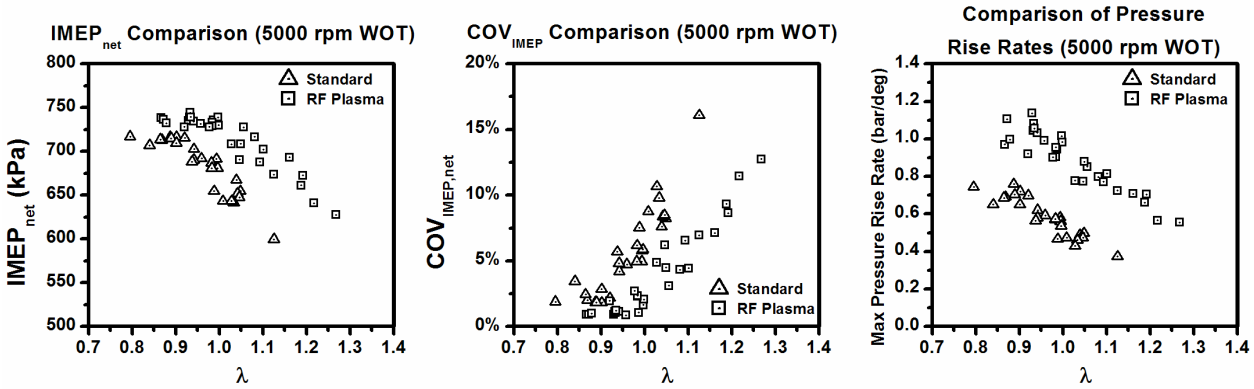

Figure 4-2 Results of Air Fuel Ratio sweep Wide Open Throttle at 5000 rev/min

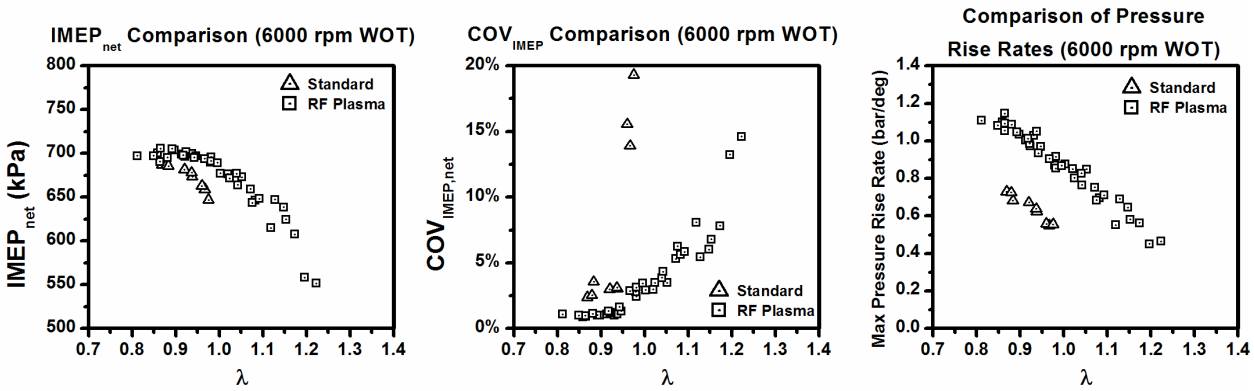

Figure 4-3 Results of Air Fuel Ratio sweep Wide Open Throttle at 6000 rev/min

While the maximum pressure rise rate difference is small at the slower speed of 4000 rpm, the difference between the two ignition systems becomes more pronounced as the engine speed increases.

Table 4-1 displays mass fraction burn data for the two ignition systems at 4000 rev/min and $\lambda = 0.98$ with spark timing set at MBT for $\lambda = 1$. Near stoichiometry, the two systems perform similarly producing identical engine loads. The burn angle durations in Table 4-1 display that the RF system produces a burn rate that is only slightly faster than the standard system. It should be noted, however, that the COV_{IMEP} is lower with the RF system. This indicates that while the RF system does not dramatically decrease the burn durations of the engine at this condition, it does provide more consistent combustion cycle to cycle, and as can be seen in Figures 4-1 to 4-3, this effect becomes greater in the more difficult-to-ignite lean air-fuel mixture regions tested.

Table 4-1 Mass fraction burn duration of the small engine at 4000 rpm

Ignition System	λ	IMEP (kPa)	COV_{IMEP}	0-10% (CAD)	10-50% (CAD)	10-90% (CAD)
Standard	0.98	690	4.1%	26.3	17.0	39.3
RF Plasma	0.98	690	2.4%	26.3	16.8	37.5

Exhaust gas composition sampled from the small engine is displayed below in Table 4-2 for

the engine operating at 5000 rev/min and WOT. The table shows higher NOx concentrations for every λ condition and a reduction in HC emissions for the stoichiometric and lean conditions presented when the RF plasma system is used. The reduction of HC emissions indicates more complete combustion occurs with the RF plasma system in these conditions. Meanwhile, an increase in NOx concentrations is expected for the RF system. The increase is likely a result of higher flame temperatures induced by the plasma system and from the fact that the effects of the plasma system may open up additional pathways for NOx formation as a result of energetic electron disassociation reactions [94]. Again, the positive effects (mainly reduction in HC emissions) of the RF plasma system become more pronounced as the air-fuel ratio in the engine becomes leaner.

Table 4-2 Small engine emissions while operating at 5000 rpm and WOT

Ignition System	λ	NOx (ppm)	CO (%)	HC (ppm)	CO_2 (%)	O_2 (%)
Standard	0.95	1148	1.64	575	14.4	0.93
	1.00	1225	1.07	712	14.4	1.43
	1.10	1074	0.40	960	13.9	2.62
RF Plasma	0.95	1851	2.11	718	15.1	0.88
	1.00	2148	1.01	651	15.3	1.25
	1.10	1394	0.14	525	13.6	2.83

Finally, the difference in the energy input of the two ignition systems being tested needs to be addressed. As stated above, the energy input for each system when it fires during a combustion cycle is 50 mJ for the small engine's standard ignition system and 400 mJ for the RF plasma system. At 6000 rev/min this corresponds to input powers to the combustion system of 5 W for the spark ignition and 40 W for the RF system. While the energy supplied by the RF system is eight times greater than that of the spark ignition, the increase in performance provided by the RF ignition system outweighs its higher power requirement as is shown in Table 4-3.

Table 4-3 compares data points obtained with the engine running at 6000 rev/min and WOT. For both the lean and stoichiometric conditions presented in the table, the RF system yields higher engine power output. While it is true that an additional 350 mJ of energy is input into the combustion chamber every engine cycle by the RF system, this amount of energy, if converted without loss to engine output, would only account for a change in IMEP of about 10.5 kPa for a 33.5 cm^3 engine. The difference between the engine output generated by the two systems in Table 4-3 far exceeds the difference in input energy between the two ignition systems and also demonstrates again that the positive effects of the plasma system are magnified at leaner λ values.

Table 4-3 Engine output comparison at 6000 rpm and WOT

λ	RF Plasma IMEP (kPa)	Standard IMEP (kPa)	RF Plasma Improvement (kPa)
1.0	677	615	62
1.1	648	525	123

No effort was made during this study to optimize the power provided by the RF plasma system. It is possible that many of the system's positive benefits could be maintained at lower power input levels by lowering the amount of energy per pulse in the RF system's pulse train or by reducing the number of pulses in each train. The effects of optimizing these parameters remain a topic of further investigation.

4.3 Optical Engine Results

Tests were run at 1500 rev/min with a targeted engine load of 4.5 bar net IMEP at λ = 1.0. The testing consisted of motoring the engine up to speed followed by the 40 engine firing cycles. At the frame rate specified above, the camera captured images every 0.9 crank angle degrees. By modifying the engine's fuel injection duration and throttle setting, λ sweeps were performed, and flammability limits (engine operating without misfires) for the two ignition systems were

determined at this 1500 rev/min speed.

Figure 4-4 contains photographs taken in the optical engine using the engine's standard ignition coil and the enhanced RF plasma system. Each column is a series of images from a separate engine test with its test conditions specified directly above it. The two left columns of images show the results of test conditions run at rich air-fuel conditions. Mass fraction burn data is given in Table 4-4 for these two tests. The right two columns of images show the optical tests run at the lean limit of each system. The leanest air-fuel mixture achieved for the standard coil was $\lambda = 1.30$, while the leanest mixture achieved without misfires was $\lambda = 1.45$ with the RF system. The results for the optical engine were similar to those of the small engine and showed that the RF system improved the engine's tolerance for lean air-fuel mixtures. The images, located on the left-hand side of Figure 4-4, of the rich combustion show a comparison of the flame propagation in the engine between the two ignition systems. Particular attention should be paid to the comparative sizes of the flame fronts at equivalent crank angles between the two tests for angles equal to or less than 32 degrees after the ignition systems were fired. The diameters of the flames shown in the RF system's column are roughly 40% larger on average than those of the standard coil at identical crank locations. It is clear from these images that the initial flame kernel produced by the RF discharge is larger, allowing the flame to propagate through the combustion chamber in a shorter amount of time. This is further confirmed by the burn angle data in Table 4-2, which shows an initial burn duration (0-10% mass fraction burn) 6 degrees shorter for the RF system than the optical engine's standard coil.

Table 4-4 Mass Fraction Burn Durations of the Optical Engine at 1500 rpm

Ignition System	λ	IMEP (bar)	0-10% (CAD)	10-50% (CAD)	10-90% (CAD)
Standard	0.94	4.4	17.0	13.0	35.0
RF Plasma	0.94	4.5	11.0	12.0	31.0

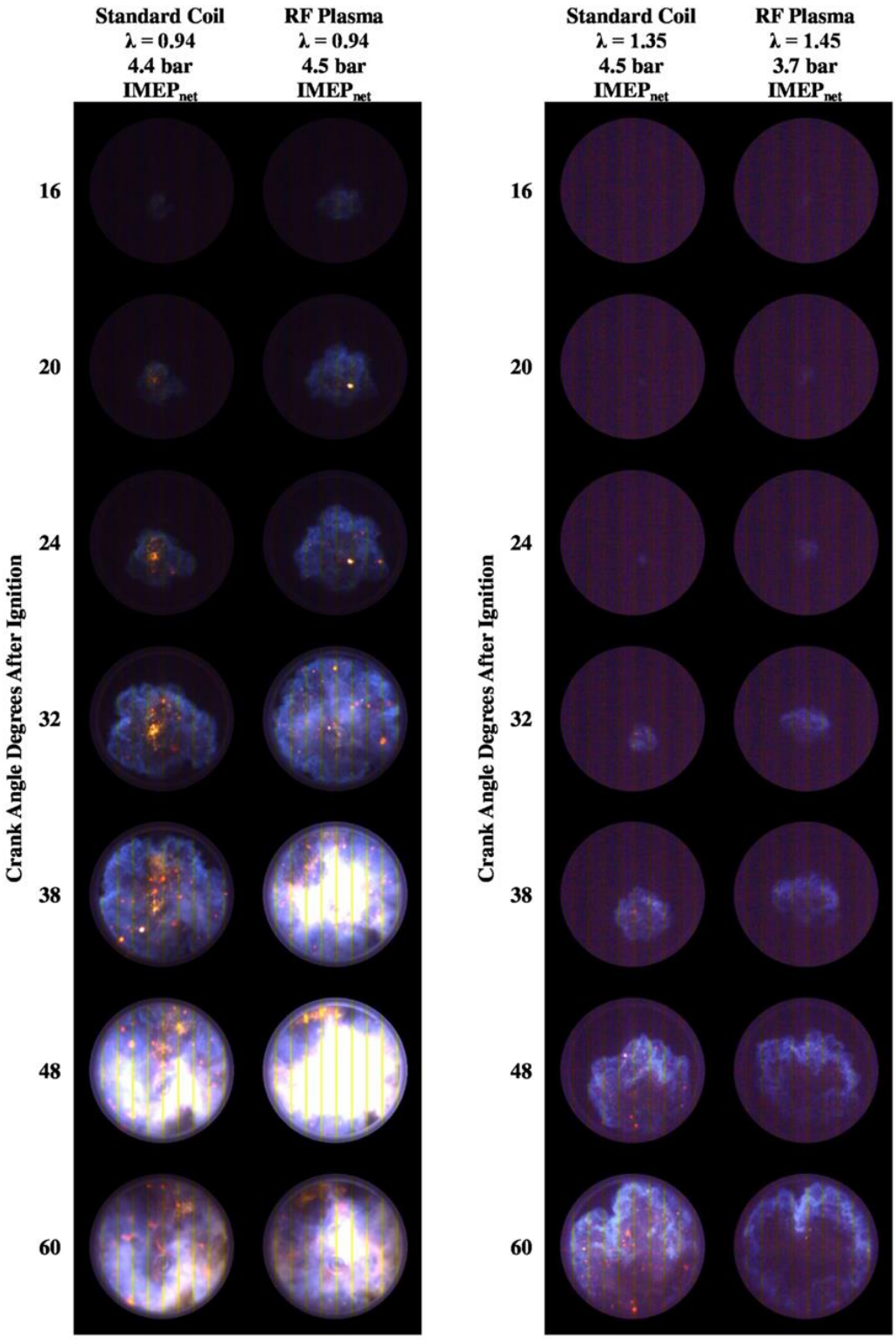

Figure 4-4 Images from the optical engine test runs, (left) rich air-fuel conditions, (right) the lean limit for each ignition system

4.4 Summary of Plasma Ignition System Testing

A radio frequency plasma system was built and successfully tested in both a small single-cylinder four-stroke gasoline engine and an automotive scale optical engine at Michigan State University. In both setups, the radio frequency system was compared to each engine's standard ignition coil in order to demonstrate the positive effects of the plasma system on the engines' performances. Particular attention was paid to the improvements that the radio frequency system provided to both engines while burning lean air-fuel mixtures.

Small engine tests were performed on a 33.5 cm^3 single-cylinder engine at wide open throttle at multiple engine speeds and air fuel ratios. The results of the testing demonstrated an improvement in cycle-to-cycle variability of the combustion (lower COV_{IMEP} values) with the radio frequency plasma system at all operating conditions, with the improvement being more pronounced while the engine operated with leaner air-fuel ratios. The power output of the small engine was also higher with the radio frequency plasma for stoichiometric and leaner air-fuel ratios. While the ignition energy of the radio frequency plasma system is 350 mJ greater than that of the engine's standard coil, the improvement in power output observed typically outweighed the additional energy required by the plasma system. Emissions data indicated improved combustion performance with lower hydrocarbon emissions for air-fuel ratios that were stoichiometric or leaner (indicating more complete combustion) and increased nitric oxide emissions that are likely generated by higher flame temperatures.

Results from the testing performed in the optical engine coincide with those obtained from the small engine. It was found that the lean flammability limit of the optical engine was extended from $\lambda = 1.35$ with the engine's standard coil to $\lambda = 1.45$ with the radio frequency system. The images collected also show a larger initial flame kernel and more advanced flame fronts at equivalent crank angles for the radio frequency system compared to the engine's standard coil.

While the radio frequency system shows improvement over both test engines' standard coils, the pulse generator creates a large amount of electrical noise. This noise created severe problems for the electronics in both test setups. This noise would have to be mitigated before a radio frequency system like the one presented here could see widespread use as an ignition source. Also, no attempt was made to optimize the ignition energy provided by the radio frequency plasma system. Further testing of the radio frequency system at lower energy inputs similar to that of the standard coil should be conducted to help quantify how much the larger ignition energy provided by the radio frequency discharge used in this study contributed to improved engine performance and whether the benefits of more stable combustion and leaner burning mixtures can be maintained at lower levels ignition energy.

CHAPTER 5: RAPID COMPRESSION MACHINE TESTING OF THE TURBULENT JET IGNITION SYSTEM

5.1 The Rapid Compression Machine Experiments

The simulations presented in chapters 7 and 8 model combustion within the rapid compression machine (RCM) at Michigan State University (MSU) with an installed TJI system. The MSU RCM is a single-firing combustion device. The RCM has a pneumatically driven piston, which, when fired, rapidly compresses gases within its combustion cylinder. At the end of compression, the piston remains stationary, leaving a constant volume combustion chamber. The MSU RCM has a cylinder diameter of 50.75 mm and variable compression ratio and stroke length. It is equipped with an optical cylinder head that accepts a 50.75 mm diameter quartz window opposite the RCM's piston that provides optical access to the combustion chamber. This optical head is also equipped with a pressure transducer to measure pressure within the combustion chamber. Heating of the RCM's chamber walls is provided by electric band heaters wrapped around the RCM's combustion cylinder. RCMs are typically used for ignition studies for compression-ignited fuels for chemical-kinetic mechanism development. Examples of such studies performed with the MSU RCM are given in [95] and [96] and include a more in-depth description of the MSU RCM.

The geometry of the TJI pre-chamber and RCM setup used in the modeling is based on testing performed with an unfueled TJI system installed in the RCM using propane fuel. The results of these experiments can be found in the works of Gentz et al. [97, 98]. The specifics of the RCM setup used in the testing in [97, 98] are used in the simulations presented here. The RCM's compression ratio is set to 8.5 with a stroke length of 203.2 mm and wall and initial gas temperatures of 353 K. The pre-chamber hardware used in the tests referenced above is shown in Figure 5-1, which was designed based on the TJI pre-chamber used in the work of Anderson et. al [77]. A diagram of the combustion cylinder of the MSU RCM with the TJI system installed is

displayed in Figure 5-2. Spark timing in the testing was also always set to after TDC was reached so that combustion took place in a constant-volume environment.

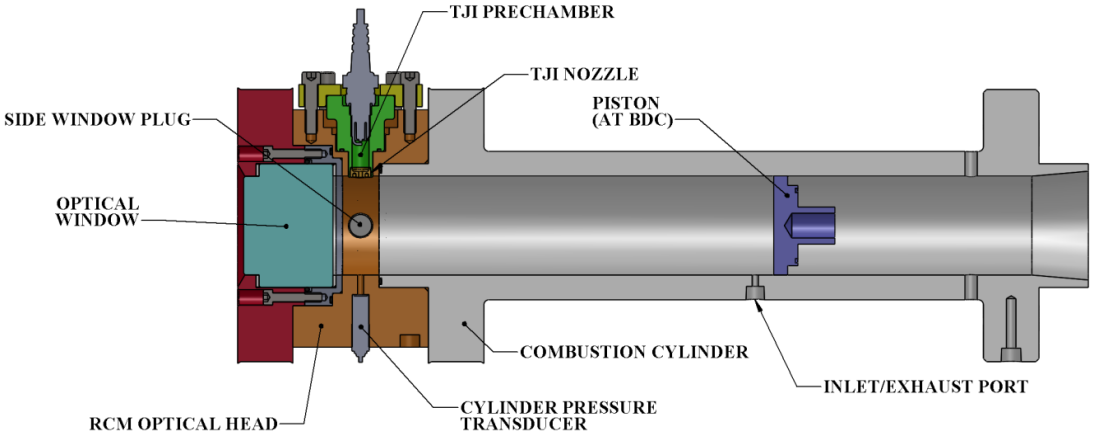

Figure 5-1 The Rapid Compression Machine's combustion cylinder with the Turbulent Jet Ignition installed

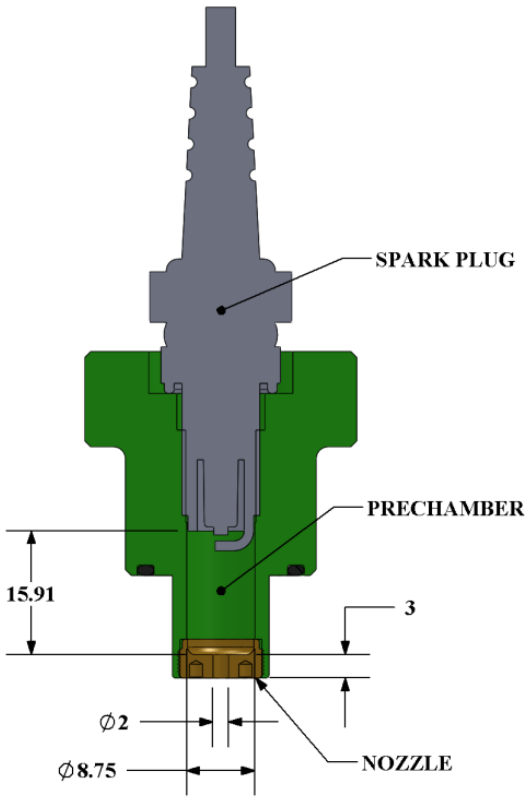

Figure 5-2 Cross section of the Turbulent Jet Ignition System

5.2 Brief Description of the Unfueled TJI System in the RCM

The Turbulent Jet Ignition (TJI) system is an ignition strategy that utilizes a standard spark ignition system to initiate combustion and two separate combustion chambers connected to each other by one or more small passageways. Typically, these passages are cylindrical orifices, and for the purposes of discussion, the following description of the TJI proceeds to describe a device that has only a single orifice connecting the two chambers. The larger of the two chambers is called the main chamber, while the smaller of the two is designated as the pre-chamber, which is about 2% of the main chamber's volume in the application discussed below. The pre-chamber volume surrounds a spark plug and is where combustion is first initiated. As combustion propagates in the pre-chamber, pressure builds within it, and a jet of pre-chamber gases is emitted through the connecting orifice into the main chamber. At first, this jet, referred to as the cold jet, is composed of unburned pre-chamber gases, but as combustion progresses through the pre-chamber, a hot jet is eventually emitted into the main chamber, producing ignition in the larger volume, which contains the majority of the fuel in the system. A schematic of the setup of a TJI system and its basic combustion process is given in Figure 5-3.

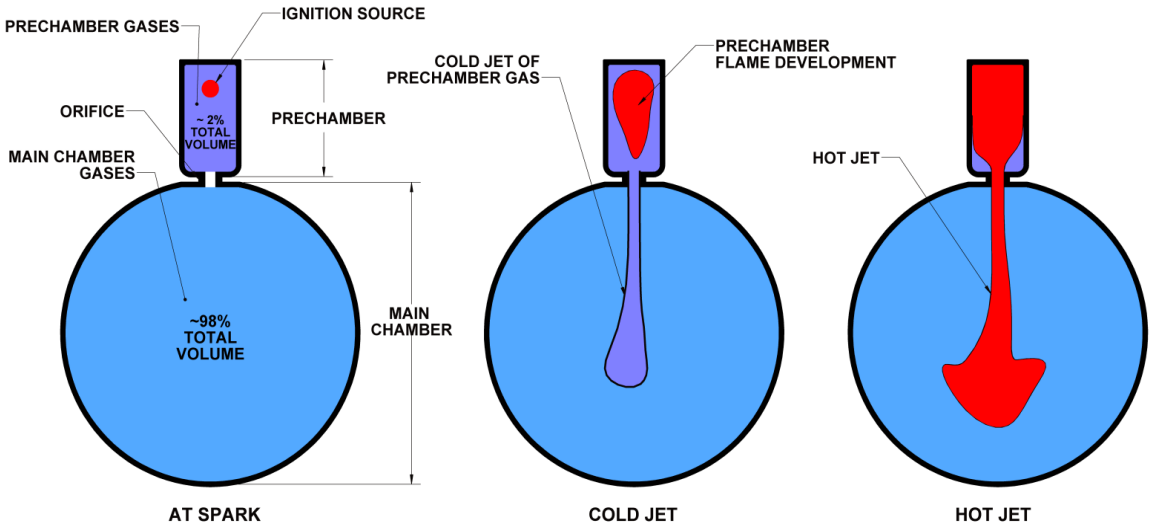

Figure 5-3 Diagram of the Turbulent Jet Ignition combustion processes starting from ignition in the pre-chamber and followed by the jet of pre-chamber gases that precedes the hot jet of gases that serve to ignite the main combustion chamber

The hot jet produced by the TJI system has two effects on the combustion in the main chamber. First, the generation of turbulence produced by the shear of the jet flow increases flame propagation speeds. Second, the jet distributes hot gases over a wide region in the main chamber, generating dispersed ignition throughout the chamber where the jet has passed. As a result of these two effects, the TJI is suited for two types of applications in spark-ignited (SI) internal combustion engines. The strategy can potentially be used to extend the knock limit of an SI engine and/or extend the engine's lean operation limit. For both applications, the TJI provides faster flame speeds due to the enhanced mixing effects of the turbulence generated by the jet and the shorter distances that the flames must propagate to consume the charge in the main chamber due to the dispersion of the ignition throughout the chamber. In the case of lean limit extension, the enhanced flame speeds and shorter propagation distances mitigate the effects that the slower flame speeds associated with lean mixtures present. From the perspective of knock limit, the enhanced flame speeds and reduced propagation distances serve to reduce the residence times of end gases in the combustion chamber.

CHAPTER 6: COMPUTATIONAL MODELLING OF THE RAPID COMPRESSION MACHINE

6.1 Computational Fluid Dynamics Software: CONVERGE

The commercially available computational fluid dynamics (CFD) software CONVERGE [99] is used to perform the simulations presented here. CONVERGE is a compressible, fully three-dimensional code with sub-models for modeling both turbulent flow and combustion. The software is purposely designed for internal combustion engine simulation, and it accommodates the types of complicated boundaries common within an engine. It also easily handles moving surfaces like those associated with a piston or valves. The presented simulations use a second-order finite-volume discretization of the equations governing fluid motion that is fully implicit in time. The SOR (Successive Over-Relaxation) technique is used to solve the governing transport equations, while the PISO (Pressure Implicit with Splitting Operators) method [100] handles the coupling of pressure and velocity. The values of field variables are co-located at the centers of the computational domain's finite-volume cells. To avoid the checkerboarding effects that may occur as a result of the co-location of velocity and pressure, Rhie-Chow interpolation is utilized [99].

The simulations use a variable simulation time step. CONVERGE uses an algorithm that determines a maximum time step based on several criteria. To start, the size of the time step is limited to an amount that is only an additional 25% that of the previously executed time step. In addition, three CFL numbers related to convection, the speed of sound, and diffusion are used to constrain the time step size when any of these CFL numbers violate their user-defined limits. Finally, if there is active combustion, the time step may be limited by the amount of temperature change occurring in any cell. With this constraint, the time step is kept small enough that no cells in the domain experience a temperature rise over the span of the time step that exceeds a user-specified value [99].

Turbulence Modeling for Momentum and Mass Transport

The simulations use the Reynolds Averaged Navier-Stokes (RANS) form of equations governing fluid motion. The two equation RNG (Renormalized Group Method) k-ε eddy-viscosity model, which is common in many CFD codes [101], is used to model the effects of turbulence on the mean flow field. With this model, a transport equation for the turbulent kinetic energy, k, and a transport equation for the turbulent dissipation, ε, are solved along with the RANS equations, which can be found in [101] , governing the mean flow field. The values of k and ε are used along with the concept of eddy-viscosity to provide closure to the Reynold's stress terms that appear in the RANS equations.

Computational Mesh

A Cartesian-cut-cell method is used for the generation of the computational mesh that is used by CONVERE for the simulations [102]. With this method, the boundaries of the simulated fluid domain are defined by surfaces composed of groups of triangles, each defined by the coordinate locations of their three vertices, which is essentially equivalent to the triangles that are used to define surfaces in STL (Stereo Lithography [103]) formatted files used by CAD systems.

The computational mesh is generated automatically prior to each simulation step in the following manner. First, the surfaces that are in motion are moved to their updated locations. Next, a base mesh, which remains unchanged step-to-step and is orthogonal, is overlaid beyond the extent of the fluid domain. The mesh, which, due to its orthogonally, may also be referred to as a grid, is then trimmed by the surface boundaries. Cells falling entirely outside the boundaries are discarded, while those completely inside are left alone. Cells that are intersected by one or more of the triangles that make up the fluid's boundaries are divided at the intersecting triangles. The portion of the cell that falls outside the fluid domain is discarded while the rest of the cell remains. After the cutting process, the mesh consists of a core of rectangular cells surrounded by irregularly

shaped cells adjacent to the boundary surfaces. The irregular cells near the boundaries remain orthogonal at their interfaces with adjacent finite-volume cells, but they have multi-faceted faces that match the boundary surfaces perfectly, at least to the accuracy of the triangles provided to represent the boundary surfaces at their interfaces with the boundaries.

An added advantage provided by the cut-cell process is how well it accommodates boundary motion. By trimming a static mesh at each simulation step, the motion of a boundary will either consume or add cells as it traverses through the fluid domain, altering the mesh only in the area very near the boundary that is in motion rather than distorting the entire grid. In the simulations presented below, the only surface motion is that of the compressing RCM piston. As the piston translates from bottom dead center (BDC) to top dead center (TDC), it proceeds to trim and remove computational cells instead of compressing the mesh in the direction of the piston motion.

Smaller cell sizes are generated throughout the domain with one of two methods. Both methods determine the smaller cell sizes by scaling the base grid. This scaling is performed by successively halving the dimensions of the base grid cells. As a result, if a 2.0 mm square base grid, which means that the grid has equal 2.0 mm spacing in each Cartesian direction, is used in the simulations, a scale level of one results in cell sizes with dimensions of 1.0 mm; a scale of 2, in sizes of 0.5 mm; a scale of 3, in sizes of 0.25 mm and so on.

One of the methods used to specify cells that receive scaling or refinement is called fixed embedding. Fixed embedding scales the cells of the computational mesh in either designated volumes within the fluid domain or along the domain boundaries. The other method used to refine the size of the computational cells is Adaptive Mesh Refinement (AMR) [99], [102]. AMR applies scaling throughout the domain to cells that are in regions with high gradients of either temperature or velocity irrespective of their location and only temporarily for the duration when these large

gradients are present in a cell. The application of AMR results in grid refinement that follows propagating flame fronts and appears within and near the jets that the TJI produces. Thus, with AMR, increased resolution is added to the mesh in areas where it is needed, while other cells that are away from any flow or combustion activity, which can be resolved on the coarse base grid, are left alone. This helps to keep the overall cell count of the simulations down while still providing the accuracy of a smaller grid where it is needed.

Combustion Modeling

Combustion is simulated using the SAGE chemistry solver [104] provided with CONVERGE along with a detailed chemical-kinetic mechanism. A multi-zone method is used in CONVERGE to reduce the computational effort required to solve the detailed chemistry. With the multi-zone method, the computational cells are mapped from three-dimensional space into a space defined by cell composition, temperature, and pressure. The cells are then subdivided within this new space into groups of like cells, each containing cells that fall within a small band of each other regarding these three parameters. The set of chemistry equations is then solved once for each group. With the updated progress of the chemistry determined, the cells are mapped back into the three-dimensional domain. This method reduces the number of times that the set of chemistry equations must be solved significantly by solving for a relatively small number of groups of cells rather than solving the set of equations for each cell individually. The detailed mechanism used in the simulations is the propane mechanism published by the Combustion Research Group at the University of California San Diego (UCSD)[105]. The UCSD mechanism consists of 235 elementary reactions and 50 species.

The SAGE model used by CONVERGE does not apply any turbulence models to the mean chemical production terms associated with the species conservation equations. The k-ε turbulence model is only applied to the governing equations for mass, momentum, and energy. As a result,

the chemistry is solved using only the mean quantities in each computational cell as though it were a zero-dimensional homogenous reactor. The argument for the absence of a model for the effects that turbulent fluctuations have on the production terms in the species conservation equation is given in Pomraning et. al. [106].

While the reader should consult Pomeraning et. al. [106] for a demonstration and detailed discussion showing the validity of using a zero-dimensional reactor within each cell, the argument made by the authors is that the turbulence models that account for the effects of turbulence on the chemistry in RANS simulations are usually incorrectly applied. The authors demonstrate that when the mean field generated in a RANS simulation is under-resolved as a result of a computational grid that is too coarse, a significant sub-grid field is present, a concept borrowed from large eddy simulation terminology which is the difference between the actual field and the field resolved on the computational grid. It is argued that when the sub-grid field is large, the effect it has on the accuracy of the simulation of the combustion chemistry far outweighs the effects generated by turbulent fluctuations. As a result, the turbulence model that should be accounting only for the effects of turbulence on the combustion process must also account for the effects of under-resolution for which the models are not intended. By adding resolution to areas in the simulation that are under-resolved, Pomeraning et al. [106] demonstrates that the errors generated by the sub-grid can be minimized, and the argument is made that the remaining effects of turbulent interaction with the combustion chemistry are on the same order of magnitude as the uncertainty associated with the parameters used to define reaction rates in typical detailed kinetic mechanisms.

Finally, in the simulations presented below, the spark ignition used by the RCM is modeled by an energy source located between the surfaces of the spark plug electrodes. The source is active for 1.0 ms and deposits a total of 30 mJ of energy at a constant rate evenly throughout the volume

of a sphere of 0.8 mm diameter by increasing the internal energy of the fluid within the sphere. The spark timing, which marks activation of the energy source, used in the simulations occurs 0.53 ms after TDC is reached by the RCM; so the combustion occurs when the RCM piston is stationary and the main chamber is at a constant volume.

6.2 CONVERGE Model of the Rapid Compression Machine

The diagram in Figure 6-1 shows the computational domain used in the simulations. The simulations begin with the piston at BDC and include the flow calculation during the compression stroke of the RCM. The simulation is initialized with a quiescent homogenous mixture of propane and air with set to a desired λ and a pressure of 1.0 bar at a temperature of 80 °C. The boundaries all have no-slip velocity and isothermal temperature conditions applied to them except for the walls of the pre-chamber, orifice, and the outer diameter of the main chamber, which have law-of-the-wall models for momentum from [107], and energy from [108] applied instead. The temperature of the model's walls is 80 °C to match the temperature the RCM is heated to for the experiments performed in Gentz et al. [97, 98]. Piston motion is input as position as a function of time. It is determined by modeling the compression process as a polytropic compression with the piston position calculated based on the pressure measured in the RCM experimental tests. While this simplification likely introduces error, the RCM does not have a sensor or other means with which to determine piston position.

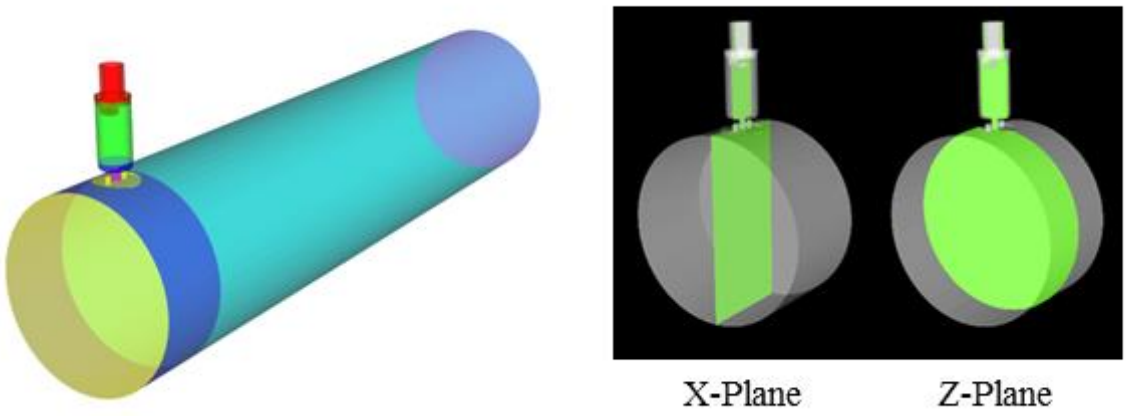

Figure 6-1 The simplified geometry used to define the fluid domain in the simulation is displayed with the piston at bottom dead center (left). Note that the spark electrode geometry is maintained in the model. The RCM geometry with the piston at top dead center with planes intersecting the domain labeled X and Z (right). The center axis of the pre-chamber cylinder and nozzle orifice lie in these planes. The two planes will serve as locations where contour data is displayed in subsequent figures

Two computational grids were utilized for each RCM simulation. A square coarse grid with a base grid dimension of 4 mm is used from the start of the simulation until just before TDC is reached, at which point the field variables of the simulation are mapped to a more refined square grid with a base dimension of 2.0 mm. The coarse grid is used to limit the overall cell count of the simulation during compression since the volume of the computational domain is significantly larger during the initial stages of the simulation, and the absence of active combustion during this phase permits the use of a larger mesh. AMR and fixed embedding are both utilized in the fine and coarse grids. In both cases, the refinement scale is typically limited to a scale level of 3, resulting in computational grid sizes of 0.5 mm and 0.25 mm for the coarse and fine grids, respectively. There are two exceptions to this scale limit. A scale level of 4 is used for the fixed embedding refinement within the orifices for the TJI configurations with orifice diameters less than 2.0 mm, resulting in grid sizes of 0.25 and 0.125 mm within the two grids, respectively. The other exception occurs in a spherical region surrounding the energy source used to initiate combustion in the

simulation. During the spark, which occurs after the simulations have transitioned to the 2 mm base grid, a scale level of 5 is utilized, resulting in a grid size of 0.0625 mm in the volume between and around the spark plug electrodes. An example of the computational mesh that results from the application of both refinement methods is shown in Figure 6-2. Since AMR is used along with the cutting and discarding of cells that result from the piston's motion, the total cell count varies over the course of the simulations, with typical total cell counts ranging from about 0.8 to 1.4 million cells.

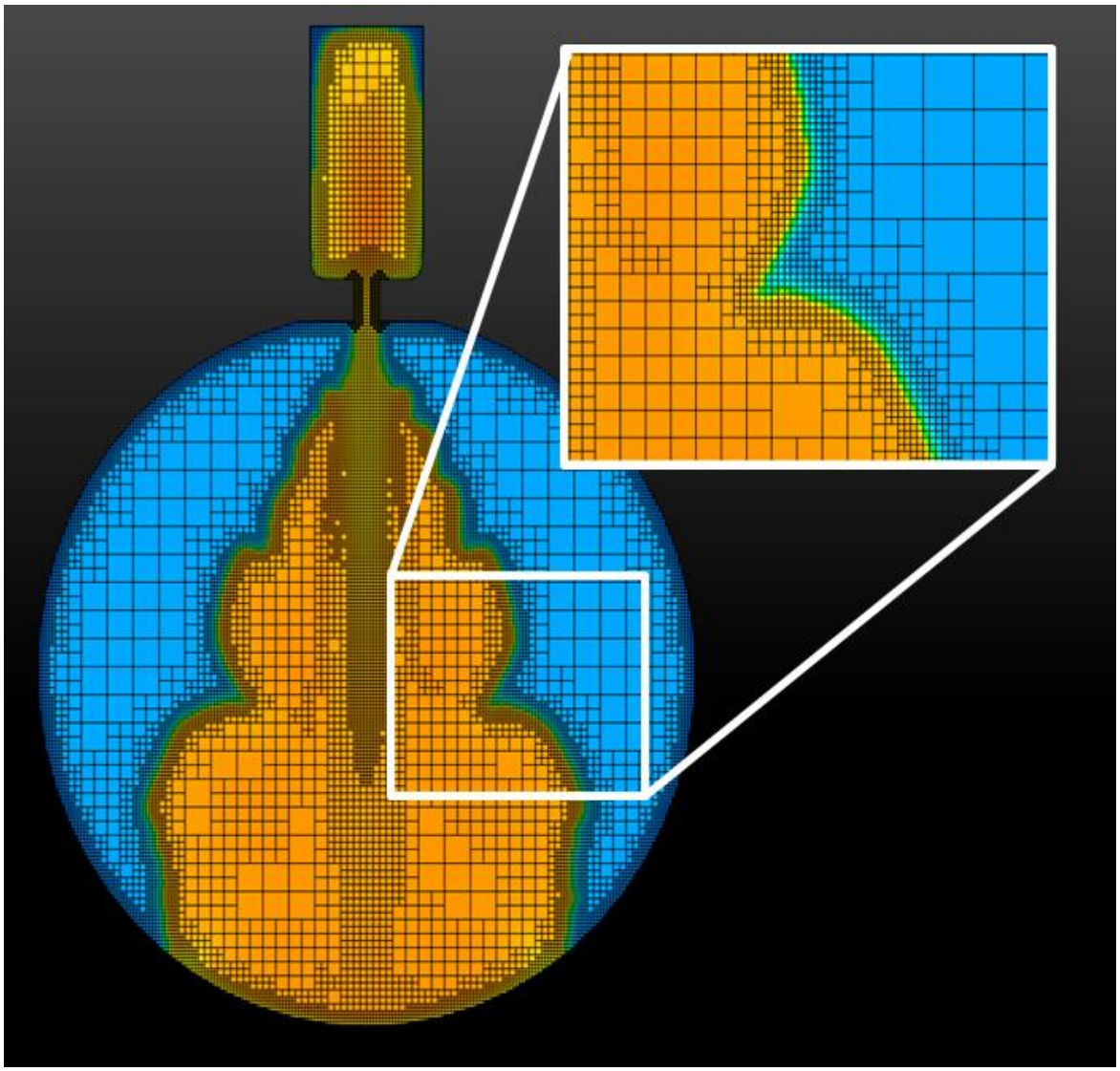

Figure 6-2 An example of an orthogonal mesh generated by CONVERGE. The mesh is overlaid on a clip plane colored based on the value of temperature in each computational cell. Note the refinement of the grid near the boundaries (fixed embedding) and in areas where a gradient in the temperature is present (adaptive mesh refinement)

CHAPTER 7: MODEL VALIDATION AND COMPARISON TO EXPERIMENTS

Three simulations are presented below, one for λ values of 1.00, 1.26, and 1.51 each. These simulations were selected to match actual RCM tests performed at MSU. All three simulations are initialized at BDC with a pressure of 1.00 bar and a temperature of 353 K to match the experiments. The base computational grid in the simulations is 2.0 x 2.0 x 2.0 mm. Adaptive mesh refinement is applied throughout the simulation based on temperature and velocity fields, along with refinement fixed to the domain's boundaries all with a maximum embedding or refinement scale of three. At this scale, the 2.0 mm base grid in a fully refined area of the computational grid has cell dimensions of 0.250 mm and volumes of less than 0.016 mm^3. The grid size was selected based on a compromise between the results of grid convergence studies like those performed in [106], which suggests base grid sizes of 2.0 mm for internal combustion engine applications and computational expense. Also, the results of a grid convergence study that was performed during the setup of the simulations presented here showed that the RCM simulations became grid-independent with the use of a 1.75 mm base grid (minimum AMR grid of 0.219 mm) and smaller. While the 2.0 mm base grid does exhibit some effects of grid dependence, the results are close enough to the 1.75 mm grid that the additional computational expense did not warrant its use.

7.1 Comparison of Simulation Results to Physical Experiments

The three plots shown in Figure 7-1 below compare the mean pressure in the simulation domain to that measured in the RCM experiments. The time datum in this figure is set to correspond to TDC as determined by the experimental pressure trace. Since spark timing is not precisely determined in the experiments, the simulation pressure is time-shifted so that the two traces match at 16 bar. Each of the three simulations exhibits similar behavior, as the simulation pressure maintains in reasonably accurate agreement with that of the experimental pressure during the early stages of combustion, but the simulation begins to deviate as the pressure in the combustion

chamber increases, with the simulation combustion rate becoming more rapid. Due to the faster combustion rate in the simulation, a peak pressure is reached sooner in the simulations than what is observed experimentally. After the end of combustion has been reached by both, the two traces decline at similar rates due to heat loss to the walls of the RCM.

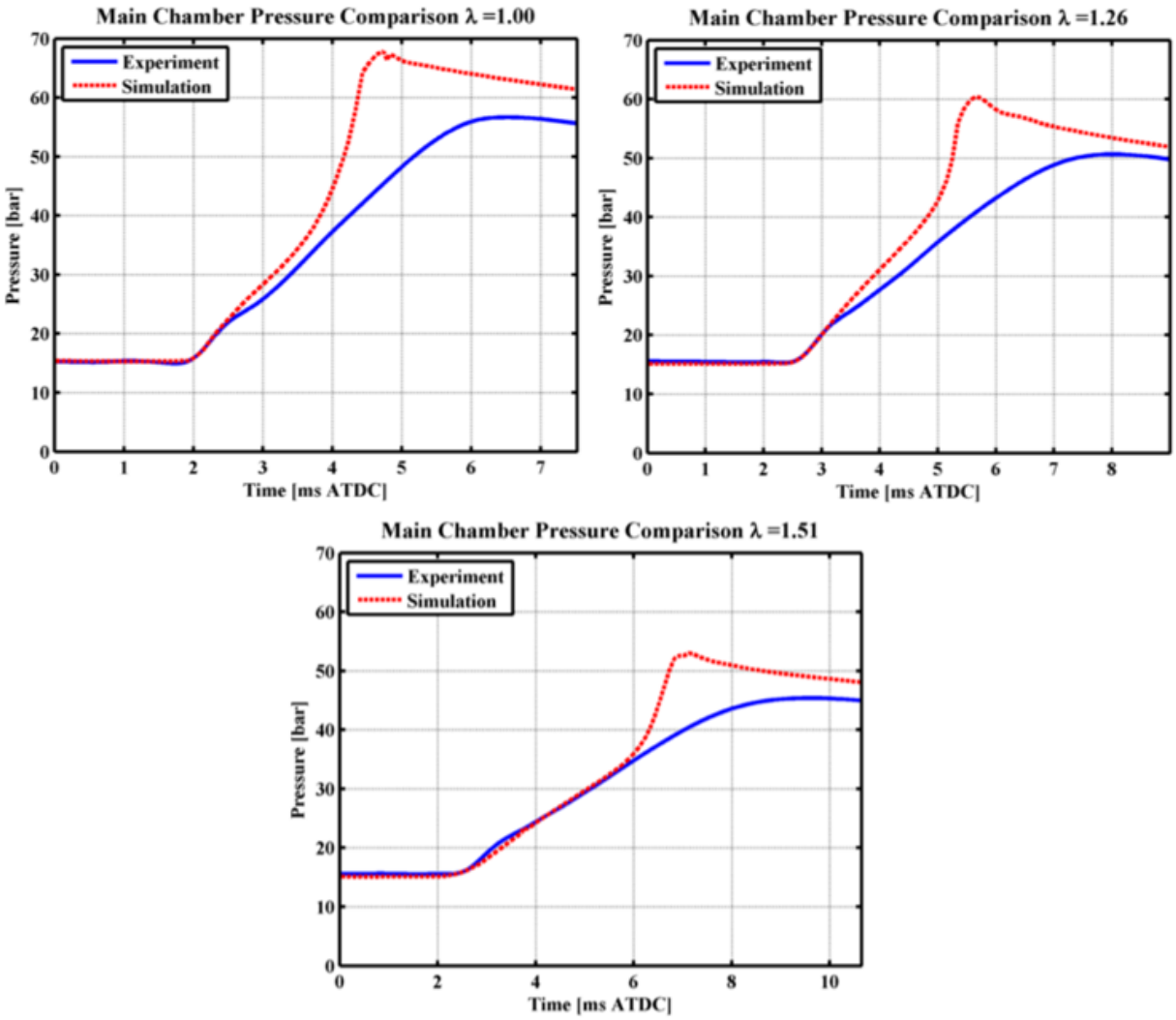

Figure 7-1 Main chamber pressure comparisons between the three simulations and data from their associated experiments

The two planes that are shown in Figure 6-1 are used in the figures that follow as the locations at which simulation data is displayed. The TJI orifice's centerline lies in both planes, with the Z-Plane parallel to the face of the RCM's piston and the X-Plane perpendicular. The time datums

used in Figures 7-2 to 7-4 are determined uniquely for each simulation and are set to coincide with the moment that hot gases first emerge from the orifice into the main chamber; so a time equal to 0 ms in the subsequent figures corresponds to the first moment that a jet would appear, albeit too faint to detect, in the optical window of the experiments. This datum is chosen to facilitate the comparison of images generated from the simulation data to the optical images captured experimentally from the RCM. It also allows for the comparison of the propagation of the three simulation jets in the main combustion chamber to one another. The datum relative to TDC is different for each of the simulations, with the delay increasing with λ as it takes longer for the flame to propagate through the pre-chamber as the mixture becomes more lean.

Figure 7-2 is a comparison of the $\lambda = 1.00$ simulation to optical images obtained from the physical experiment on which the simulation is based. The images that comprise the first row are of the visible light emitted from combustion in the experiment. The first image in this sequence is artificially enhanced to be made brighter to provide better visibility, as the light of the jet as it initially emerges from the orifice is very faint. The two remaining rows of images are contour plots of the mole fraction of the OH radical plotted from the simulation on the two planes specified above. These images are, of course, smooth looking compared to the optical images, as the turbulent structure is missing in the mean field values generated by RANS simulations.

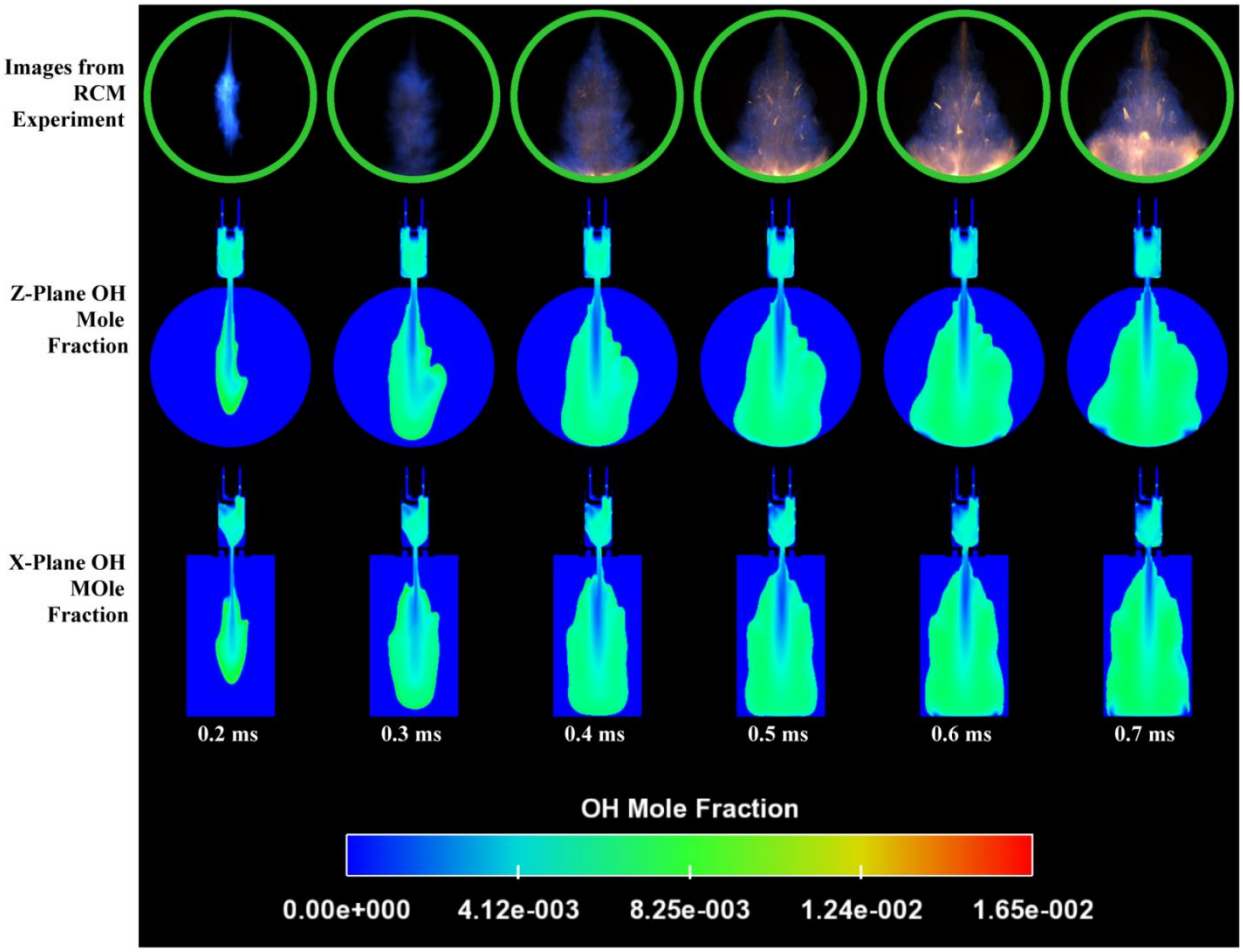

Figure 7-2 Optical images obtained for λ=1.00 experiment are compared to the contours of the OH mole fraction generated from the corresponding simulation. The time datum, 0 ms, corresponds to the time when hot gases first begin to emerge through the orifice into the main chamber of the RCM (Note: the first optical image is artificially brightened to facilitate visibility)

Figure 7-3 is a comparison of the three simulations and demonstrates the effects of the equivalence ratio on the speed with which the jet enters the main chamber, the temperature of the combustion that results, and the rate at which the fuel is consumed in the main chamber. Despite initial appearances, the third, fourth, and fifth images in the λ = 1.51 sequence are unique. The development of the jet just happens to be that slow for such a lean condition.

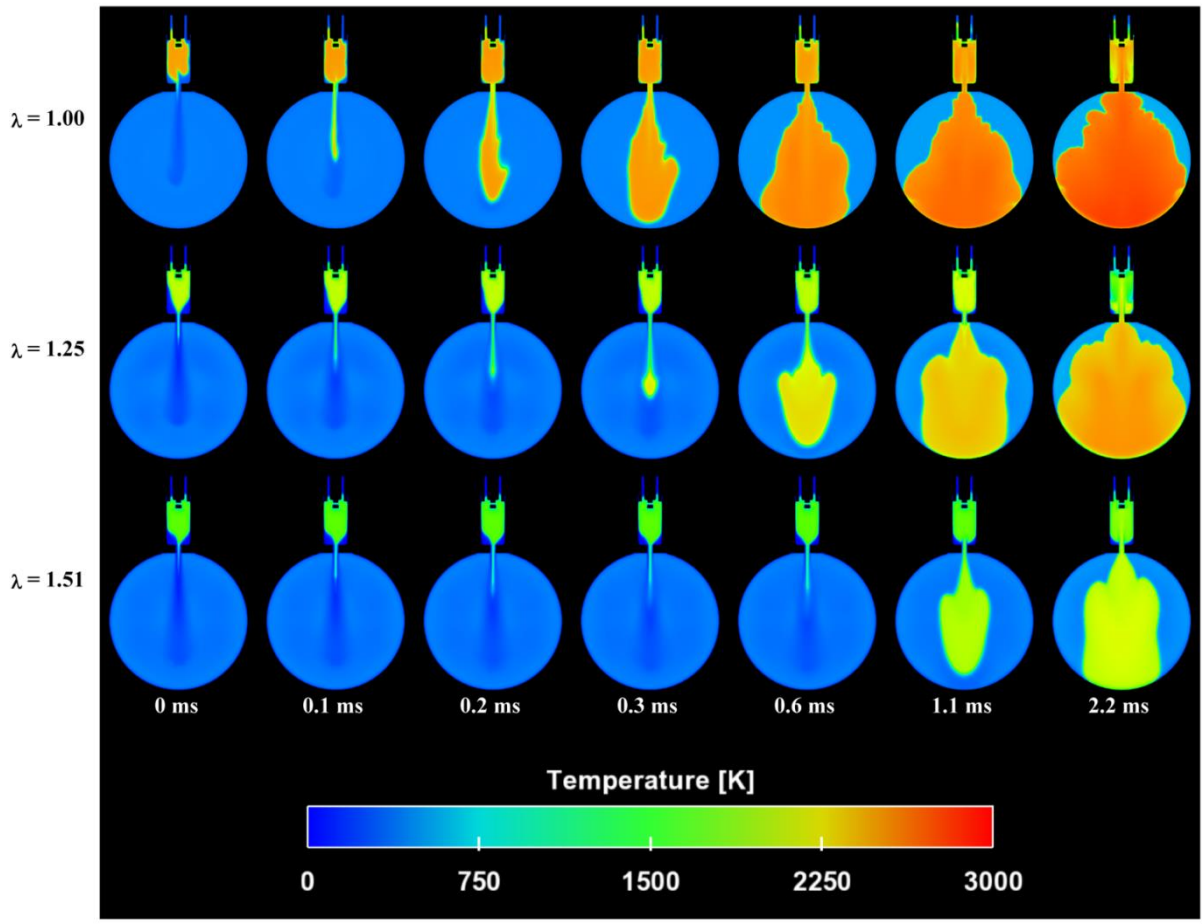

Figure 7-3 Temperature contours on the Z-plane for all three simulations. The time datum, 0 ms, is set for each simulation individually to coincide with the moment that hot gases first begin to emerge from the pre-chamber orifice into the main chamber of the RCM

Finally, Figure 7-4 consists of images generated from the λ = 1.00 simulation. The first sequence of images displays the contours of the simulation's turbulent kinetic energy, indicating areas of high turbulence. As expected, turbulence is generated by the gases that are forced out of the pre-chamber. It can also be seen that the turbulent energy has significantly dissipated in the main chamber by the time the combustion has reached its later stages. The second row of images in the figure tracks a passive scalar that was mapped to be equal to unity within the pre-chamber at TDC. The scalar is modeled with the same transport properties as the other gas species in the simulations. Its value should serve as a marker for gas initially in the pre-chamber prior to the

initialization of any combustion. Together, these two sequences demonstrate that the active jet that emerges from the pre-chamber initially enters into and propagates through a highly turbulent mixture predominantly composed of gases that were originally in the pre-chamber themselves.

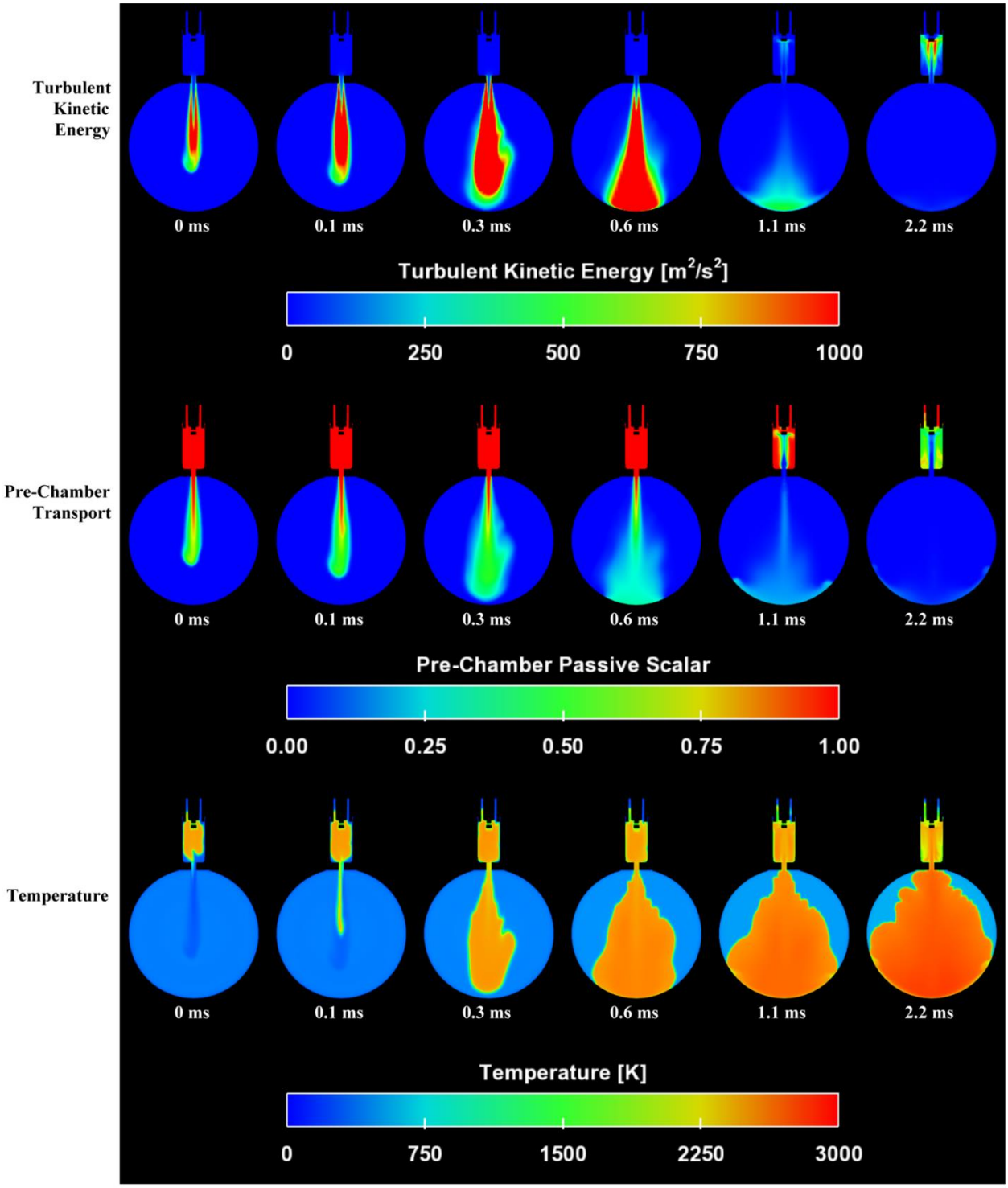

Figure 7-4 Contours of turbulent kinetic energy, a passive scalar mapped to be unity within the pre-chamber at TDC, and temperature for the λ = 1.00 simulation

7.2 Summary of Simulation Comparisons

The simulations appear to model the initial stages of the combustion process in the RCM accurately with the TJI device, as demonstrated by the figures above. There remains a significant discrepancy in the combustion rate in the latter stages of the process with the simulation overpredicting it. Common to all three cases examined is that the rate of combustion significantly accelerates when the pressure in the RCM reaches 35 to 40 bar. The discrepancy could be caused by the inadequacy of the chemical mechanism at elevated pressures or the homogenous reaction assumption made in conjunction with the SAGE combustion model used in the simulations. While the UCSD mechanism has been suggested to be appropriate for combustion up to 100 atm and has been validated using data for homogenous ignition delays generated in an RCM [33], high-pressure chemical mechanisms for fuels such as propane are presently an active area of research [34,35]; so a better-suited mechanism may exist in the future that would produce better results.

The differences in the peak pressures between the simulations and experiments also appear to be quite stark in Figure 7-1 as well. Evaluating the two peak pressures by themselves does indeed show a significant difference indicating, at first glance, a major difference in the amount of heat released in the simulations compared to the amount of heat released in the experiments. But comparing the peak pressures to each other by themselves is flawed. Since the rate of combustion in the simulation is unnaturally faster at high pressures than in the experiment, it reaches its peak pressure much sooner. Keeping in mind that both the simulation and the experiment lose heat to their surroundings, the two pressures must be compared at the same time, after the end of combustion in the experiment to examine both pressures after they have been subjected to heat loss for the same amount of time. It can be seen in Figure 7-1 that the difference in pressure is much less, at around 5 bar, at identical times after combustion has completed in the experiment. This difference is easily accounted for by pointing out that there are many crevice volumes in the

RCM in which unburned gases may become trapped during combustion and that remain unburned. These crevices are almost totally unaccounted for in the simulations. CAD models of the RCM setup used for the experiments indicate that nominally there is about 1 cm^3 crevice volume.

CHAPTER 8: RAPID COMPRESSION MACHINE MODELING RESULTS

8.1 Results from Comparison of Orifice Sizes

Four simulations are presented below for orifice diameters of 1.0, 1.5, 2.0, and 3.0 mm. The initial conditions for the four simulations are all identical and have been selected to match a single specific physical RCM test that was performed during the collection of the data presented in Gentz et al. [97, 98] with a 1.5 mm diameter orifice nozzle. Finally, the spark timing, which was not precisely controlled or measured in the experiments relative to TDC of the RCM, was estimated to occur 0.53 ms after TDC based on the presence of a noise spike on the RCM pressure transducer's signal that occurs as a result of the ignition system firing.

The RCM experimental tests of the TJI system generated optical images of the light emitted through the RCM's sapphire end window captured at 10,000 frames per second by a high-speed camera. Figure 8-1 compares contour plots on the X and Z planes displayed in Figure 6-1 of the radical species OH generated from the 1.5 mm diameter orifice simulation along with the high-speed camera images captured during the physical RCM test on which it is based. The time datum in this figure corresponds to the time when a jet is first visible in the optical window. This datum is selected for two reasons. The first is that the first optical image frame containing evidence of a flame is a natural starting point with which to reference the optical images to themselves since the preceding images up to that point are void of any visible activity. The second reason is that the entry of hot gases into the main combustion chamber signifies the beginning of the main combustion event in the TJI process where the vast majority of the fuel is consumed. In the following, this moment of hot jet entry into the main chamber is referred to as the hot jet exit, and the delay between its occurrence and the firing of the spark is called the hot jet delay, which is essentially an ignition delay between the spark and the start of combustion in the main chamber.

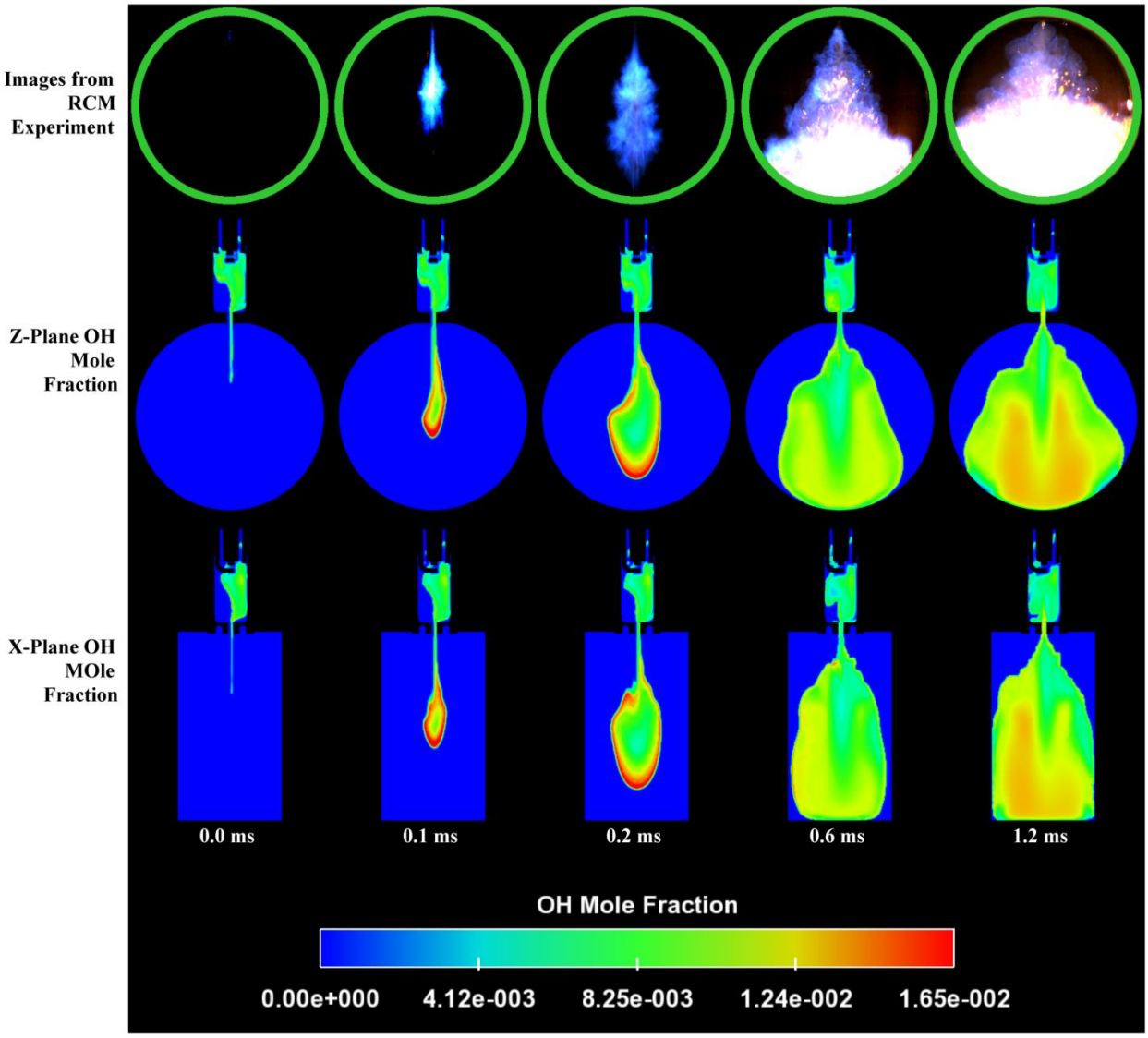

Figure 8-1 A comparison of optical images from the 1.5 mm orifice RCM experiment together with contour plots of the mole fraction of the radical species OH generated by the 1.5 mm orifice simulation at the plane locations is shown in Figure 6-1. The time datum used corresponds to the emergence of a hot jet into the pre-chamber. Also note that because of low levels of light emitted during initial jet penetration in the experiments, the first three optical images have been enhanced to facilitate the identification of the hot jet

A comparison of the pressures in both the main chambers and the pre-chambers of the simulations of the four TJI configurations is given in Figure 8-2. The time datum chosen for Figure 8-2 corresponds to the spark timing used in the simulations. This timing specifically corresponds to the start of the 1 ms energy source that models the spark ignition. Figure 8-2 demonstrates that

the orifice diameter affects the hot jet or ignition delay that roughly corresponds to the onset of the pressure rise within the main chamber. The 1.0 mm case exhibits the shortest delay, followed by the 3.0 mm case which barely precedes the 1.5 mm case. The 2.0 mm case has the longest delay which is nearly 1.5 ms longer than the 1.0 mm case. With the pre-chamber pressure included in Figure 8-2, the effects of the orifice size on the pressure within the pre-chamber as well as the interaction of the two chambers can be observed. It is clear from the figure that as the orifice becomes smaller and the flow between the two chambers is more restricted, the difference between the main chamber and pre-chamber pressures becomes more pronounced. While the difference in the two chamber pressures is the most drastic in the 1.0 mm case, the 3.0 mm case generates pressures with hardly any difference between the two chambers at all. All four of the configurations, however, exhibit the same basic behavior with the pressure differential alternating directions between the two chambers as the TJI process proceeds. This basic behavior begins with the pressure higher in the main chamber than the pre-chamber during the compression stroke as gas is forced into the pre-chamber through the orifice. After the spark has initiated combustion, the pressure in the pre-chamber overtakes that of the main chamber producing jet flow into the main chamber. Eventually as a result of combustion in the main chamber along with the near completion of combustion in the pre-chamber, the pressure in the main chamber once again becomes large driving flow back into the pre-chamber. When combustion is completed in both chambers, the two pressures begin to equilibrate as the overall pressure of the two chambers combined is reduced as a result of heat loss.

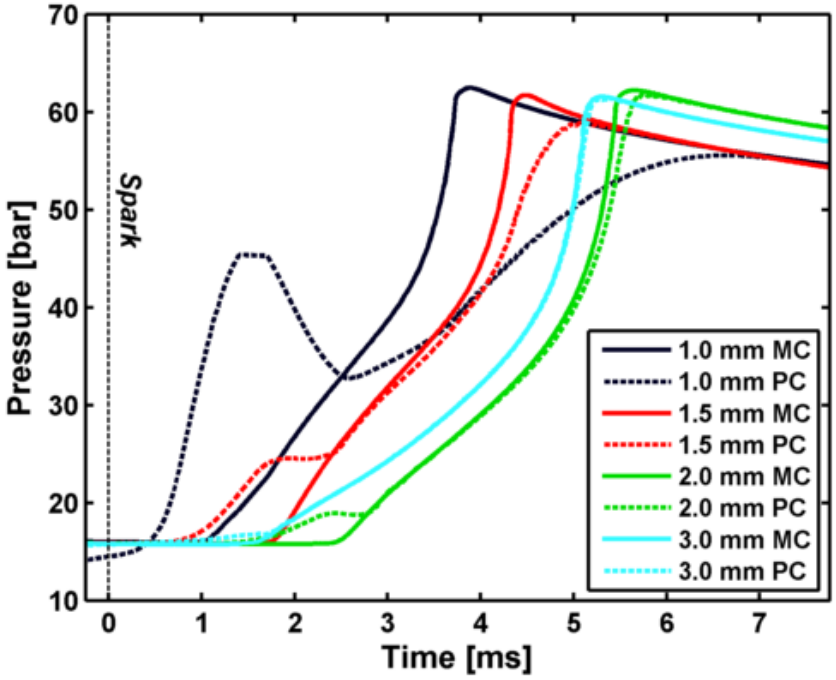

Figure 8-2 Comparison of the pressures generated in both the pre and main chambers of the four simulations. The time datum corresponds to the spark timing (the start of activity from the energy source) used in all four simulations and occurs 0.53 ms after the piston has reached top dead center

Figure 8-3 displays the pressure data generated in the main chambers of the four simulations again but without the pre-chamber pressures. Also in this figure, the time datum for each simulation corresponds to the time of the hot jet exit. The use of this time datum allows for the simulations to be compared at the start of combustion in the main chamber. Many of the following figures utilize this time datum as they are intended to compare the combustion performance of each of the nozzle configurations once each of their hot jets has entered the main combustion chamber. In an application, the combustion event in the main chamber will be of primary concern since it contains the majority of air and fuel in the system; so referring to this datum is appropriate for the comparison of the performance of the different orifice diameters. Meanwhile, it is anticipated that the hot jet delay times will be accounted for with the determination of proper spark timing in any future engine applications.

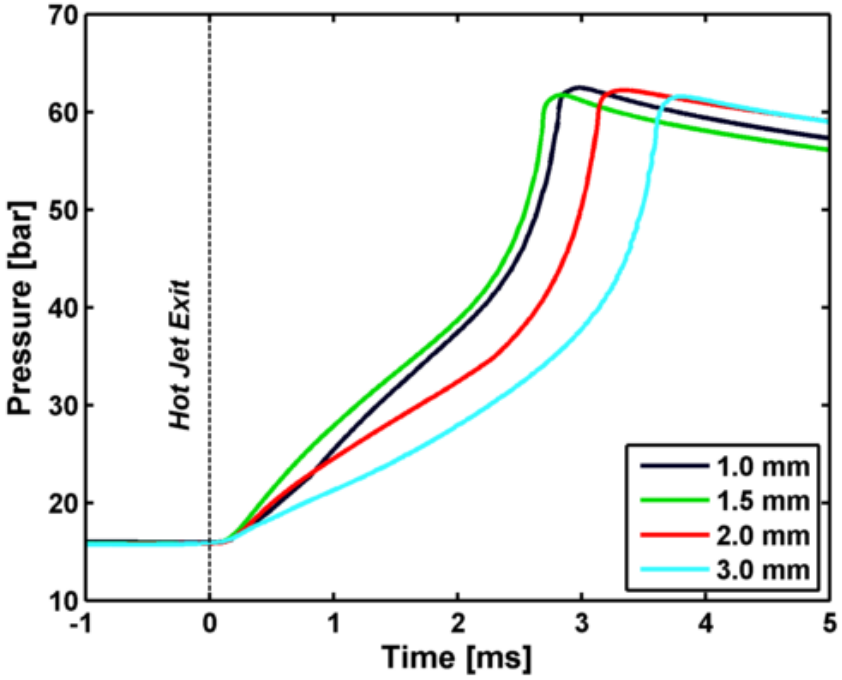

Figure 8-3 Comparison of the main chamber pressures of the four simulations with the time datum moved to coincide with the exit of the hot jet into the main chamber to compare the main chamber combustion rates. The locations of 50% mass fraction burn for each simulation are also included

The graph in Figure 8-4 displays a summary of the hot jet delay of each of the four simulations. In addition, two mass fraction burn durations, the 10-90% and the 0-10% durations, are included. For the RCM, mass fraction burn is simply defined as the percentage of the total pressure rise that has already occurred [98]. Since the piston remains stationary at TDC, changes in the volume of the combustion chamber need not be taken into account as is required in an engine application. The datum used for the 0% mass fraction burn is the hot jet exit; so the burn durations are representative of combustion in the main chamber. The 0-10% duration indicates the speed at which the hot jet ignites the contents of the main chamber while the 10-90% duration measures the speed at which the bulk of the combustion in the chamber takes place. Figure 8-4 shows that the fastest burn rates are achieved with the 1.5 mm diameter orifice. The 1.0 mm orifice generates the second shortest burn durations followed in order by the 2.0 and 3.0 orifice simulations. The

display of the hot jet delays in this figure again demonstrates what is observed in Figure 8-2 that the longest delay occurs in the 2.0 mm diameter orifice simulation with the 1.0 mm case exhibiting the shortest.

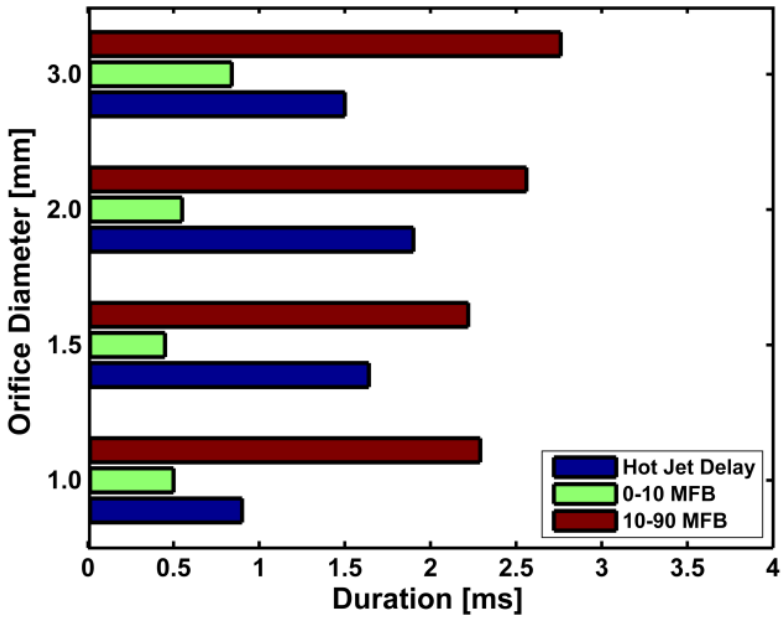

Figure 8-4 Comparison of mass fraction durations, which are referenced to the hot jet exit, and the hot jet delay, which is the time that elapses between the firing of the spark and the emergence of a hot jet into the main chamber

A comparison of the development of the jet propagation in the main chamber of the simulations is shown in Figure 8-5 with contour plots of temperature displayed at various times after the hot jet has penetrated into the main combustion chamber. One important observation from this figure is that in all of the cases except the large 3.0 mm orifice case, the pre-chamber is asymmetrically burned. This results in an initial hot jet with a mixed composition of burned and unburned gases which in turn creates an asymmetric pattern in the main chamber. Significant asymmetry similar to what is demonstrated in the figure was also observed experimentally with the asymmetry randomly displaying itself from test to test and is thought to be due to the variability in initial flame kernel formation [109]. Finally, it should also be noted how the extent of the flame propagation in Figure 8-5 corresponds appropriately to the pressure traces of Figure 8-3.

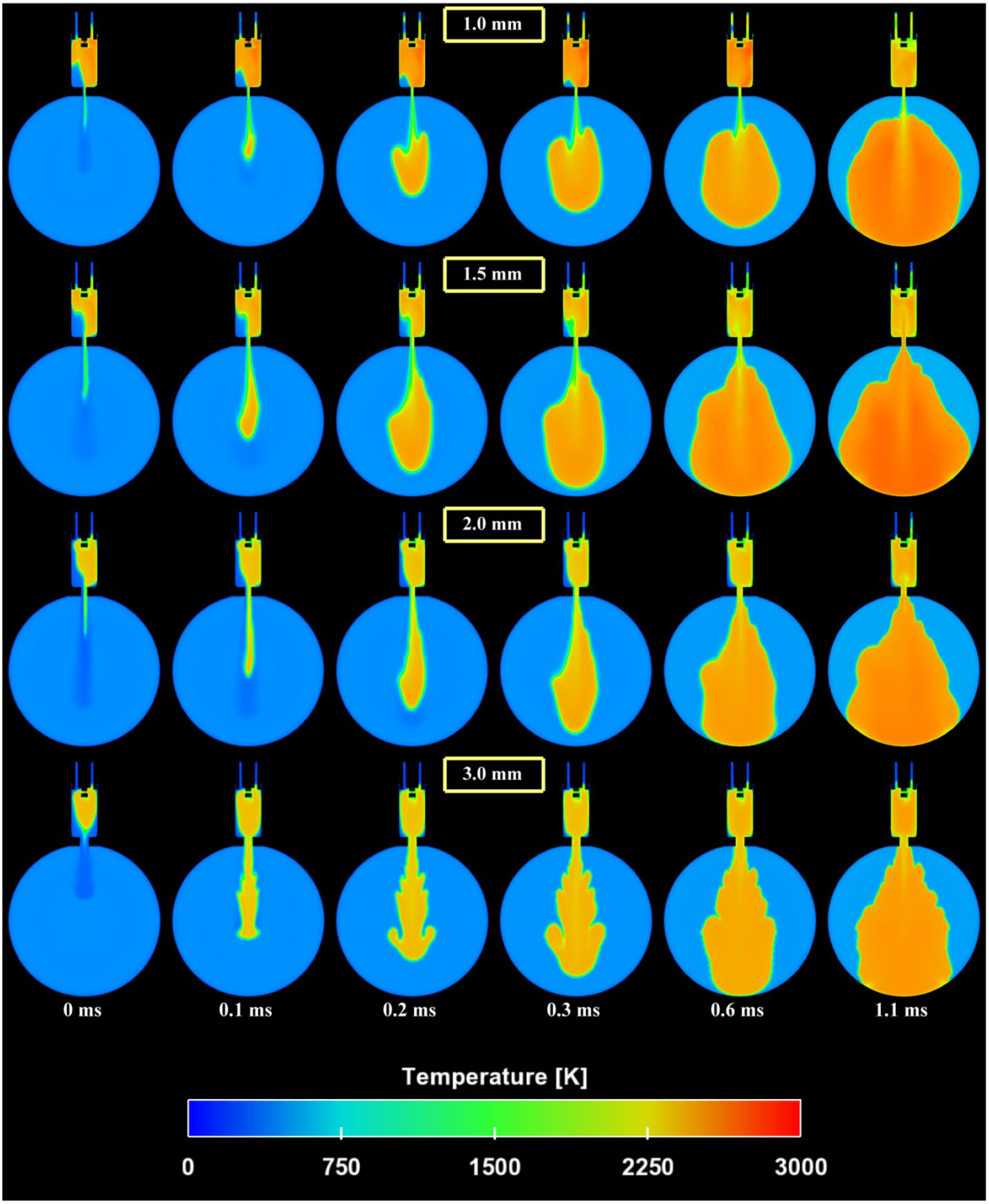

Figure 8-5 A comparison of the temperature contours on the Z-plane from Figure 6-1 for the four simulations. The time datum in this figure is set to correspond to the time of the hot jet exit into the main chamber

Thus far, the results of the simulations presented closely resemble the images captured during the physical experiments. One motivation for performing the simulations presented in this study is the three-dimensional field data that the simulations generate that cannot be easily measured experimentally. Figure 8-6 demonstrates a visualization of the flame propagation in the RCM that is not accessible experimentally. In the figure, surfaces correspond to a normalized propane mole fraction of 0.5, which is defined as the local mole fraction of propane divided by the initial premixed mole fraction of propane with a value of 1 corresponding to completely unburned gases and a value of 0 corresponding to the absence of propane. These surfaces are indicative of the locations of the propagating flame front and are presented at the same time intervals as the images in Figure 8-5. The view of the simulation domain in this figure is isometric with a wireframe denoting the boundaries of the RCM.

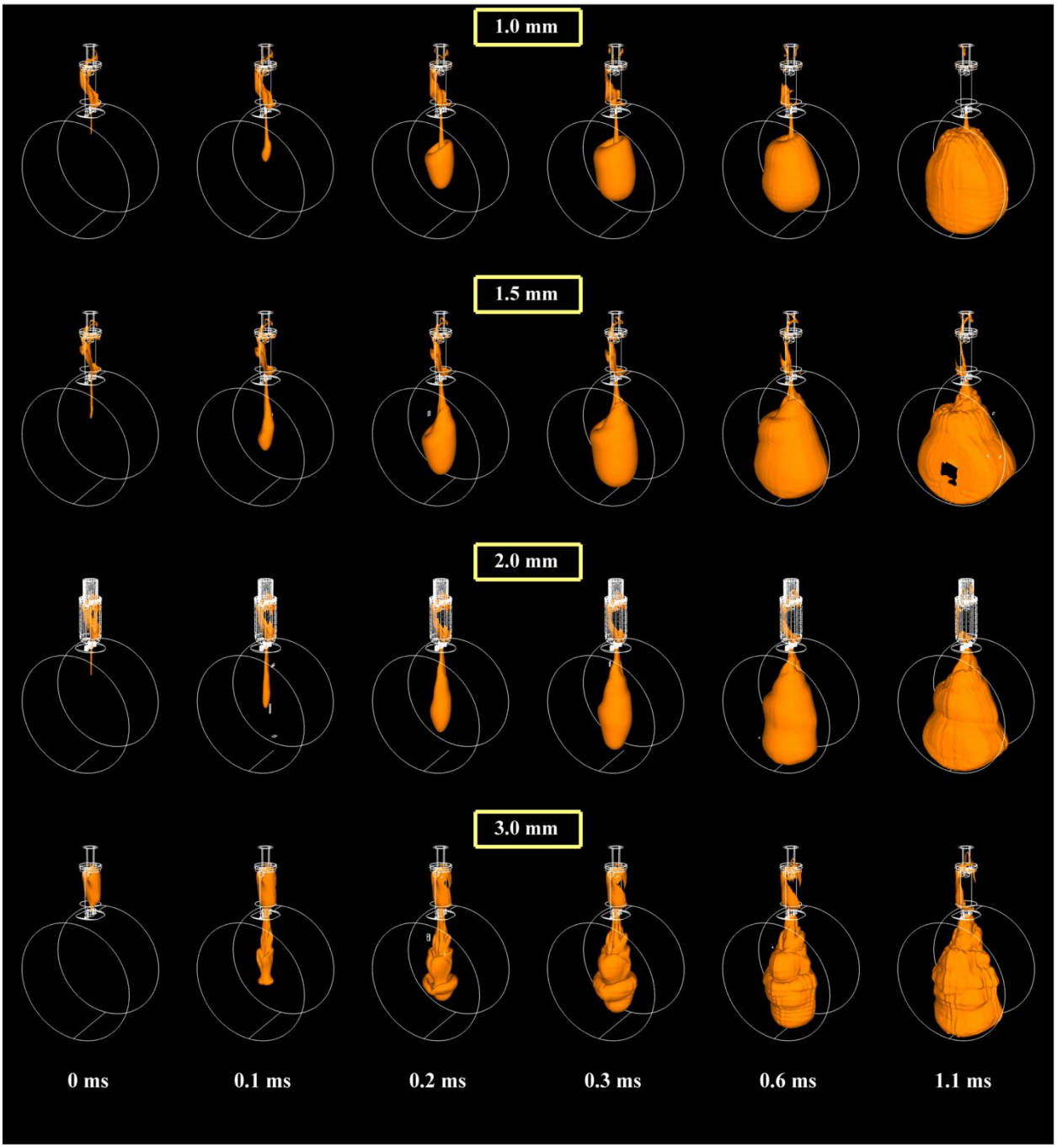

Figure 8-6 Three-dimensional views of the flame front propagation of the four simulations. The surface displayed above represents the locations in the domain with a normalized propane mole fraction of 0.5 (defined as the local propane mole fraction divided by the initial premixed propane mole fraction). The time datum in this figure is set to correspond to the time of the hot jet exit into the main chamber

Another quantity that is difficult to measure experimentally is the velocity of the turbulent jet

as it exits the nozzle orifice. Figure 8-7 displays the orifice velocity as a function of time again using the time of the hot jet exit as the datum. While the velocity in the orifice is not uniform, the velocities plotted in the figure are equivalent to the spatially uniform velocity that would result in an identical volumetric flow rate through the orifice at the given instance of time. This figure demonstrates two aspects of the behavior of the TJI system. The first is that there is a significant jet of cold pre-chamber gasses that is emitted into the main chamber prior to the emergence of the hot jet in each of the four simulations. The second aspect is that there is a flow reversal back into the pre-chamber as combustion progresses in the main chamber. Consistent with the expectation of flow through restrictive passageways, the velocities of the jets increase as the diameter of the nozzle orifice decreases.

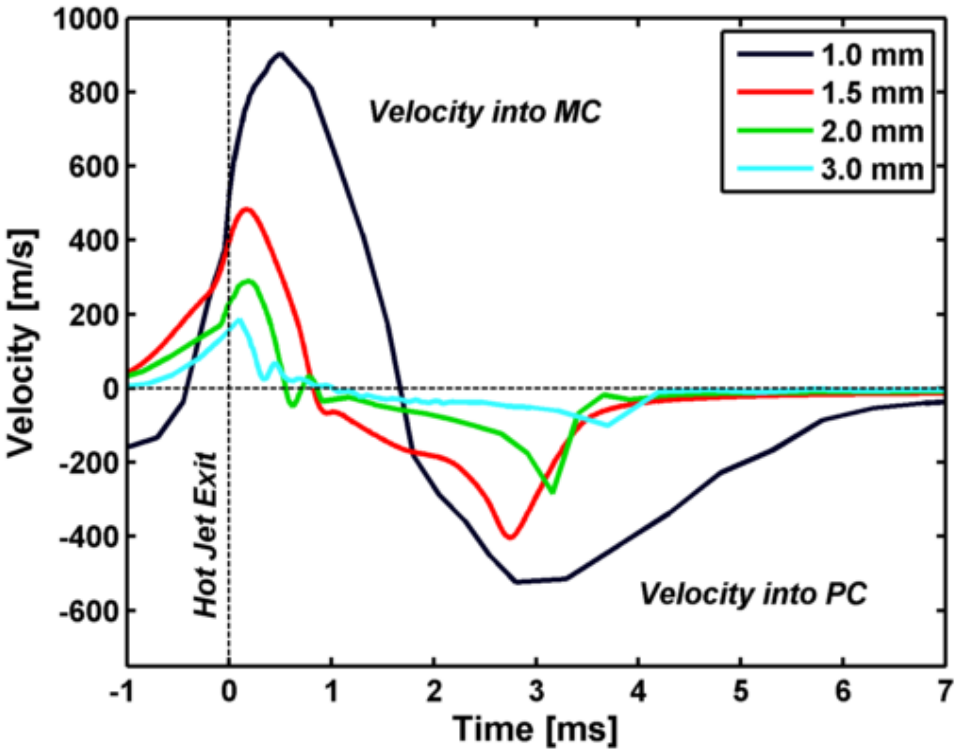

Figure 8-7 The velocities of the jets at the orifice exit into the main chamber for the four simulations. The time datum is that of the hot jet exit and the velocity is measured based on the volumetric flow rate through the orifice

One of the operating principles by which the TJI enhances the rate of combustion is through the addition of turbulence in the main chamber of the combustion device generated by the high shear flow of the jet that the pre-chamber emits. In the two-equation k-ε model utilized to model the effects turbulence has on the mean flow field, the turbulent kinetic energy is a calculated field variable that quantifies the kinetic energy of the modeled fluctuations in the flow velocity [110]. The total turbulent kinetic energy within the simulation domain as a function of time is shown in Figure 8-8. Figure 8-9 shows a comparison of contour plots of the local turbulent kinetic energy at the time steps used in Figure 8-5 and Figure 8-6. A white line is overlaid on these images denoting the location of the flame front at each instance of time. The quantity shown in Figure 8-9 is the turbulent kinetic energy per units mass, the k from the k-ε model, while the total turbulent kinetic energy that is plotted in Figure 8-8 has units of energy and is calculated by integrating the product of density and the turbulent kinetic energy per unit mass, k, over the entire volume of the simulation domain.

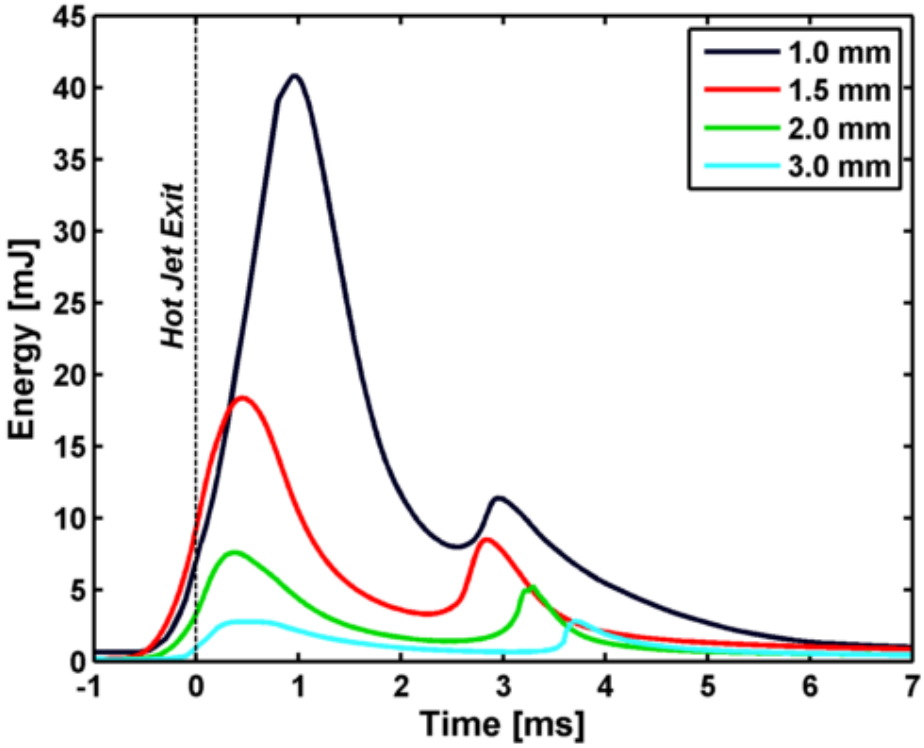

Figure 8-8 A comparison of the total turbulent kinetic energy as a function of time in the simulation domain referenced to the time of the hot jet exit. The total turbulent kinetic energy is calculated by integrating the product of density and the local specific turbulent kinetic energy over the full domain of the simulation

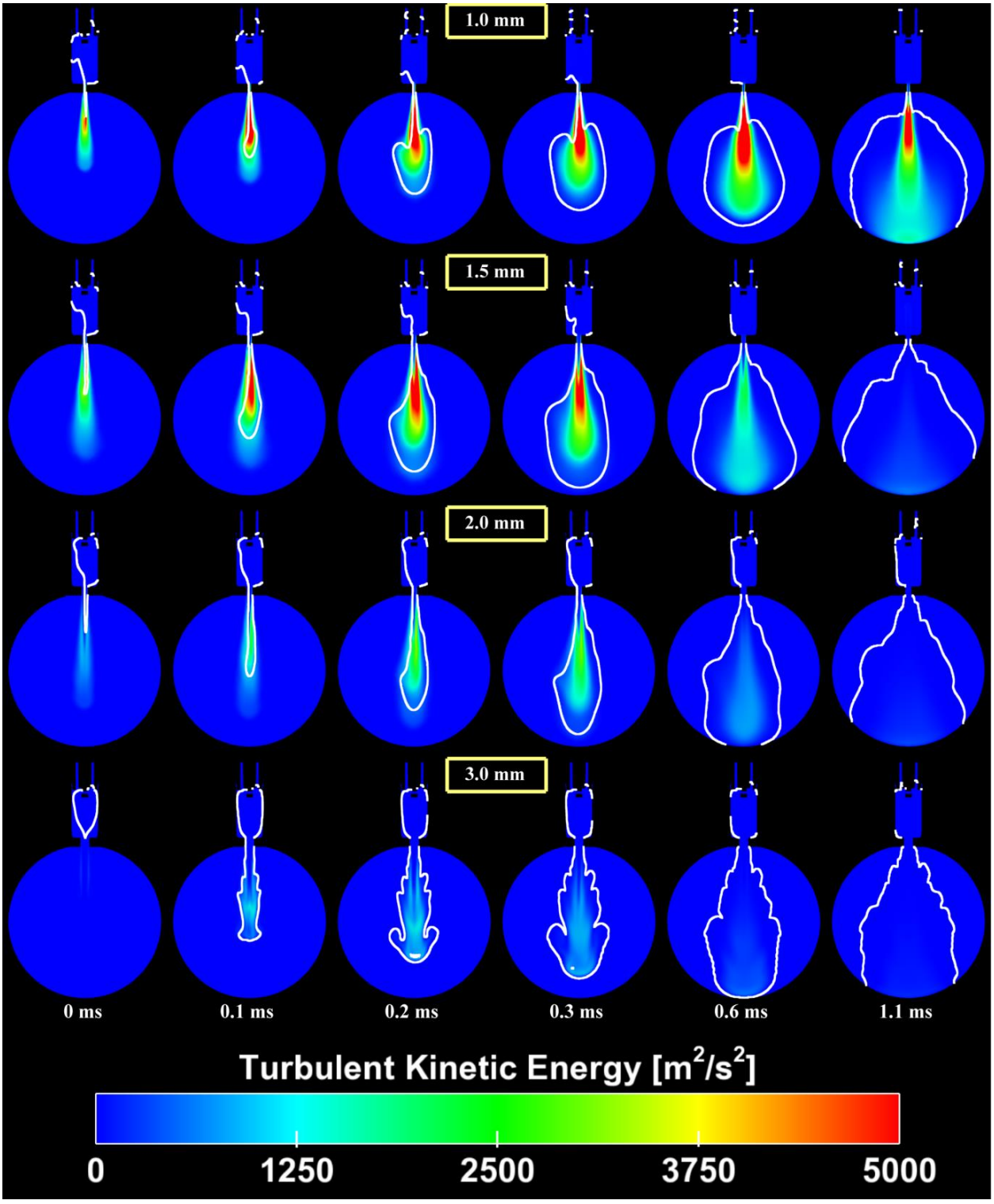

Figure 8-9 A comparison of the local turbulent kinetic energy, k, of the simulation on the Z-plane from Figure 6-1 with the time datum corresponding to the hot jet exit for each simulation. The white contour overlaying each image corresponds to the location of the 0.5 normalized propane mole fraction surface presented in Figure 8-6 representing the approximate location of the active flame front

Since higher jet velocities will cause larger mean flow velocity gradients, which provide the energy for turbulence, the trend that the total turbulent kinetic energy follows that of the orifice velocities presented in Figure 8-7 is expected. The peak in this total energy occurs just after the orifice exit velocity of the jet reaches its maximum. The energy dissipates as the pre-chamber jet velocity dwindles, depriving the turbulent kinetic energy of its main production source. Once combustion in the main chamber has progressed to the point that flow begins to reverse direction flowing back into the pre-chamber from the main chamber, the total turbulent kinetic energy again increases to a second local maximum. With increasing orifice size, both the heights of the peaks and the difference between them become smaller.

Figure 8-9 serves to visualize the locations in the flow most affected by the turbulence generated by the TJI system's hot jet. The images show turbulent kinetic energy concentrated in a plume along the centerline of the jet. With the white overlay tracing the progress of the flame front, it is evident that between the 0.3 ms and 0.6 ms time steps shown, the flame propagates outside of the regions in the main chamber where turbulence has been generated by the hot jet. The flame must then propagate without the aid of the strong turbulence generated by the hot jet for the remainder of combustion.

8.2 Discussion of Orifice Diameter Comparison

From the results presented in the previous section, there are five phases that can be identified that occur over the course of the RCM TJI process. These phases are listed in the order they occur and are named as follows: compression, pre-chamber combustion initiation, cold jet, hot jet, and flow reversal. The phases are distinguished from each other on the basis of the pressure difference between the pre-chamber and main chamber, which dictates the flow direction, the composition of the gas flowing through the orifice, and the chamber or chambers in which combustion, if it is occurring, is located. Descriptions of each phase are given below as well as being indicated in

Figure 8-10, which displays the full pressure traces from both the main chamber and pre-chamber of the 2.0 mm orifice simulation starting from the start of compression to beyond the end of combustion.

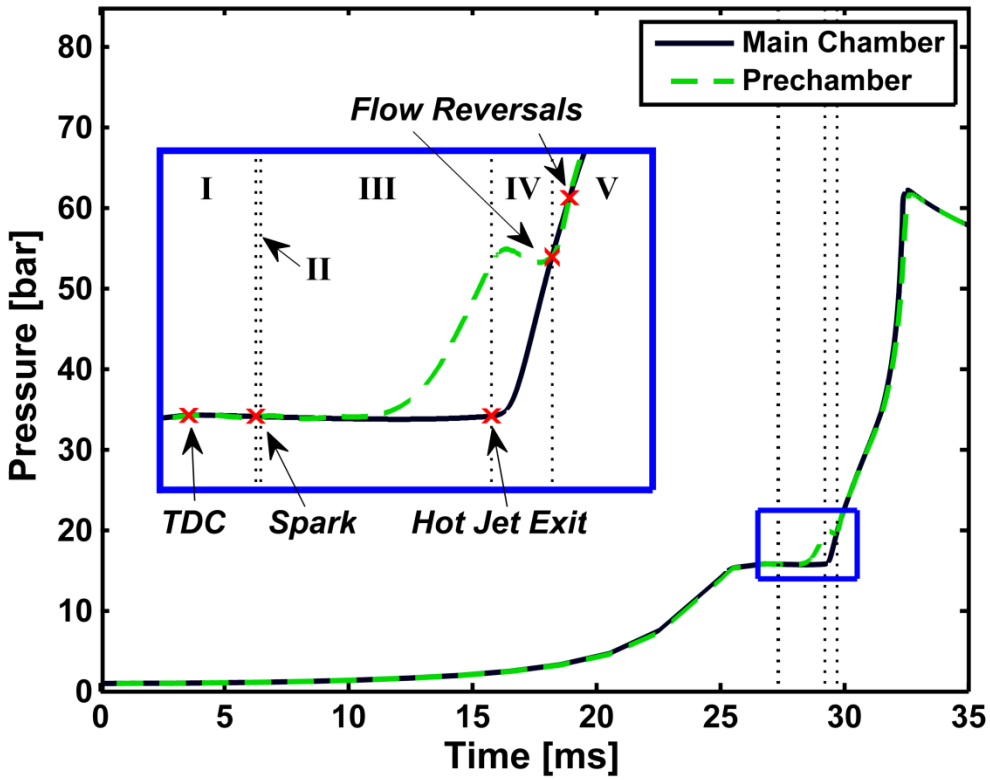

Figure 8-10 Pressure trace diagram displaying both pre-chamber and main chamber pressures generated by the 2.0 mm orifice diameter simulation with the five phases of the TJI process in the RCM indicated (I. Compression, II. Pre-chamber Combustion Initiation, III. Cold Jet, IV. Hot Jet, and V. Flow Reversal)

Phase I: Compression

The first phase of the TJI process in the RCM is the compression phase, which spans from the beginning of compression until the spark plug is fired. During this phase, the pressure in both the main chamber and pre-chamber increases as the main chamber volume is reduced as a result of the piston motion. While compression occurs, a jet of low velocity when compared to the eventual hot jet of main chamber gases flows into the pre-chamber. During this phase, the pressure in the main chamber remains greater than that of the pre-chamber due to the flow restriction of the orifice

separating the two chambers. Although this phase receives little attention in the previous section, the tail end of the compression phase is present in Figure 8-2. For the majority of the cases, the pressure difference between the two chambers is small at the end of the compression stroke, but this pressure difference can be clearly observed for the 1.0 mm case in the figure as the increased restriction of the flow between the chambers by the orifice prevents the mass flow required to equilibrate the two chambers from passing from the main chamber to the pre-chamber.

Phase II: Pre-chamber Combustion Initiation

The second phase, which is the pre-chamber combustion initiation phase, begins at the beginning of the spark energy source that initiates combustion in the pre-chamber. The duration of this phase is short and consists of the period of time it takes for the pressure in the pre-chamber to rise due to combustion to a level greater than that of the main chamber. At the beginning of this phase, it should be expected that there will still be a flow of main chamber gases into the pre-chamber unless the TJI orifice is large enough and/or the spark timing is delayed enough after TDC that the transfer of mass between the two chambers has allowed the pressure between the chambers to equilibrate before the initiation of combustion. As a result of this possibility, this phase may not always appear in some cases.

Phase III: Cold Jet

After combustion in the pre-chamber during the second phase has built the pressure in the pre-chamber up beyond that of the main chamber, the flow within the orifice will change direction flowing from the pre-chamber to the main chamber. At this stage, the combustion in the pre-chamber is only developed in the upper portion of the pre-chamber, so the jet is composed of unburned gases from the bottom of the pre-chamber. This is the cold jet phase of the TJI process. Jet velocity increases during this phase as the pressure in the pre-chamber builds due to continued combustion within it. During this phase, the mass transferred into the main chamber in the form

of the cold jet, isolated by itself, should increase the main chamber pressure, but since the main chamber is so large compared to the pre-chamber, any increase in pressure from the addition of mass from the pre-chamber is imperceptible and outweighed by the loss of heat being experienced by the gas in the main chamber to the RCM walls.

Phase IV: Hot Jet

Eventually, combustion progresses in the pre-chamber to the point that the flame front reaches the orifice, and high-temperature gases begin exiting into the main chamber with this first appearance of hot gases in the main chamber serving as the hot jet exit datum used in Figure 8-3 to Figure 8-9. This marks the beginning of the hot jet phase. During this phase, combustion occurs in both chambers. At first, the pressure in the pre-chamber is much higher than the main chamber and, in fact, as Figure 8-7 demonstrates, the pressure difference, inferred from the jet velocities of this figure, will rise to a maximum shortly after the hot jet exit. The delay between the hot jet exit and the maximum velocity increases as the nozzle orifice size decreases. Meanwhile, the speed of the jets produced by the TJI increases with decreasing orifice diameter. Soon after the peak jet velocity is reached, a combination of combustion in the main chamber initiated by the hot jet and the reduction of heat release in the pre-chamber, which has burned nearly all of the gas that remains within it, causes the pressure in the main chamber to reach that of the pre-chamber eliminating the jet and ending the hot jet phase of the TJI process.

Phase V: Flow Reversal

With the pressure in the two chambers again equal, the final phase of the TJI process begins. The description of this phase is slightly more difficult as it differs on a case-to-case basis. The 1.0 and 1.5 mm configurations provide the simplest behavior. In these cases, once the main chamber pressure overtakes that of the pre-chamber, flow in the orifice is reversed with the flow going from the main chamber into the pre-chamber for the remainder of active combustion. For the 2.0 and

3.0 mm cases, an oscillation occurs in the orifice velocity (see Figure 8-7) just after the hot jet phase ends. As a result of this oscillation, the flow direction may reverse more than once. The cause of these oscillations in the simulations appears to be the result of the composition of the gases that are forced back into the pre-chamber after the flow has been reversed Since the bulk of ignition in the main chamber is convected to its bottom half, much of the gas that remains close to the nozzle exit when flow reversal begins is unburned. This results in unburned gas from the main chamber being forced into the pre-chamber, which is itself full of hot gas, where it is quickly burned increasing the pre-chamber pressure which may cause the flow to reverse back again. Once combustion is complete in both chambers, heat losses reduce the overall pressure in the system, and flow will continue from the main chamber to the pre-chamber until the pressures match. The orifice size dictates the duration of this flow, with smaller orifices exhibiting longer durations as the restriction inhibits the mass flow into the pre-chamber, which is necessary to equilibrate the two chambers.

A table summarizing the five phases discussed above is provided in Table 8-1. The last two phases of the TJI process are of the most interest in terms of comparing the combustion performance of the various orifice-size TJI configurations examined, because it is during these two phases that combustion occurs in the main chamber and, therefore, is when the majority of energy is released. The results of the simulations show that the smaller orifices, 1.0 and 1.5 mm, produce a faster rate of combustion in the main chamber with the 1.5 mm orifice showing slightly faster burn times than the 1.0 mm. Meanwhile, the 3.0 mm orifice yielded the slowest burn times of the four as interpreted from the data presented in Figure 8-4. The two smaller orifices exhibit faster main chamber burn times because they produce the highest velocity jets (Figure 8-7) which in turn generates a greater amount of turbulence (Figure 8-8 and Figure 8-9) in the main chamber

enhancing flame propagation. That the 1.5 mm configuration outperforms the 1.0 mm is likely due to a combination of the fact that turbulent flame speeds level off (they asymptotically approach a maximum) as turbulence levels increase, at least until a level of turbulence is reached where extinction becomes a concern [111], and that the effects of the orifice size on the amount and state of the gas that is emitted from the pre-chamber may contribute negatively to the main chamber combustion performance. Somewhere between the 2.0 mm and 1.0 mm orifice diameters perhaps close to 1.5 mm, there is a point at which the turbulence generated by the higher velocity jet no longer enhances the flame speeds in the main chamber enough to offset the effects of heat transfer in the orifice and the reduction in the size of the resulting jet that it produces.

Table 8-1 Summary of the five phases of the TJI process with main chamber and pre-chamber representing main chamber and pre-chamber respectively

Phase	Chamber with Higher Pressure	Location of Combustion	Orifice Flow
Compression	Main Chamber	None	Unburned into Pre-chamber
Pre-chamber Combustion Initiation	Main Chamber	Pre-chamber	Unburned into Pre-chamber
Cold Jet	Pre-chamber	Pre-chamber	Unburned into Main Chamber
Hot Jet	Pre-chamber	Both	Burned into Main Chamber
Flow Reversal	Main Chamber	Both	Mixture of Burned and Unburned into Pre-chamber

Taken together, the duration of the second and third phases of the TJI process establish an ignition delay for the main chamber. Specifically, this delay is the amount of time that elapses between the firing of the spark and the time when the hot jet exits the orifice into the main chamber.

These times are summarized in Table 8-2 and can be observed in the main chamber pressure traces included in Figure 8-2, which uses spark timing instead of the hot jet exit as its time datum, along with the mass fraction burn duration shown in Figure 8-4. Of the four simulations, the 1.0 mm configuration exhibits the shortest delay followed by the closely grouped 3.0 and 1.5 mm cases. Finally, the 2.0 mm orifice has a delay over twice that of the 1.0 mm case. The mass of the gases and the fraction of them that is burned in the pre-chamber at the times of the hot jet exit are also included in Table 8-2. The difference in the amount of mass that is burned in the pre-chamber of each case prior to the exit of the hot jet is one of two primary factors that influence the observed delay times. In the larger orifice diameter case of 3.0 mm, there is less restriction of the flow, and a large portion of the mass originally in the pre-chamber is pushed out into the main chamber while combustion develops in the upper sections of the pre-chamber. As a result, less of the mass originally in the pre-chamber has to be burned for the flame to reach the orifice. This is why the 3.0 mm case exhibits the second shortest ignition delay. On the other hand, in the smaller orifice diameter case of 1.0 mm, the increased restriction of the flow between the two chambers yields a flow field that is more advantageous to flame propagation as a result of higher levels of turbulence in the pre-chamber since the velocity of flow induced by compression into the pre-chamber increases with decreasing orifice size. Also, the smaller orifice's advantage is the increased lag between the pre-chamber and main chamber pressures. Figure 8-2 shows that there is still a pressure differential across the orifice for the 1.0 mm case at the beginning of the spark event. This indicates that a flow remains into the pre-chamber during flame initiation to provide an energy source for turbulence. This is demonstrated in Figure 8-11, which is a plot of the average turbulent kinetic energy per unit mass, k, within the pre-chamber near the simulations' spark timing for the four TJI configurations. It is clear from this figure that there are much higher levels of turbulence

present in the pre-chamber of the 1.0 mm case during the second and third phases of the TJI process compared to the other orifice diameters, significantly contributing to its shorter hot jet delay. The balance between these two factors generates the ignition delay results shown in Table 8-2. In the longest delay case of the 2.0 mm orifice, the restriction of the orifice is enough to require that more pre-chamber mass must be burned than in the 3.0 mm case, but at the same time, the 2.0 mm orifice does not provide enough restriction to generate a flow in the pre-chamber favorable to increased flame propagation speeds like in the 1.0 mm case.

Table 8-2 Summary of main chamber ignition delay and pre-chamber contents at the time of hot jet exit

Orifice Diameter [mm]	Ignition Delay [ms]	Pre-chamber Mass at Hot Jet Exit [mg]	Pre-chamber Burn Fraction at Hot Jet Exit [ ]	Burned Mass in Pre-chamber at Hot Jet Exit [mg]
1.0	0.90	9.54	0.44	4.22
1.5	1.64	7.68	0.46	3.50
2.0	1.90	7.02	0.39	2.77
3.0	1.42	5.94	0.54	2.70

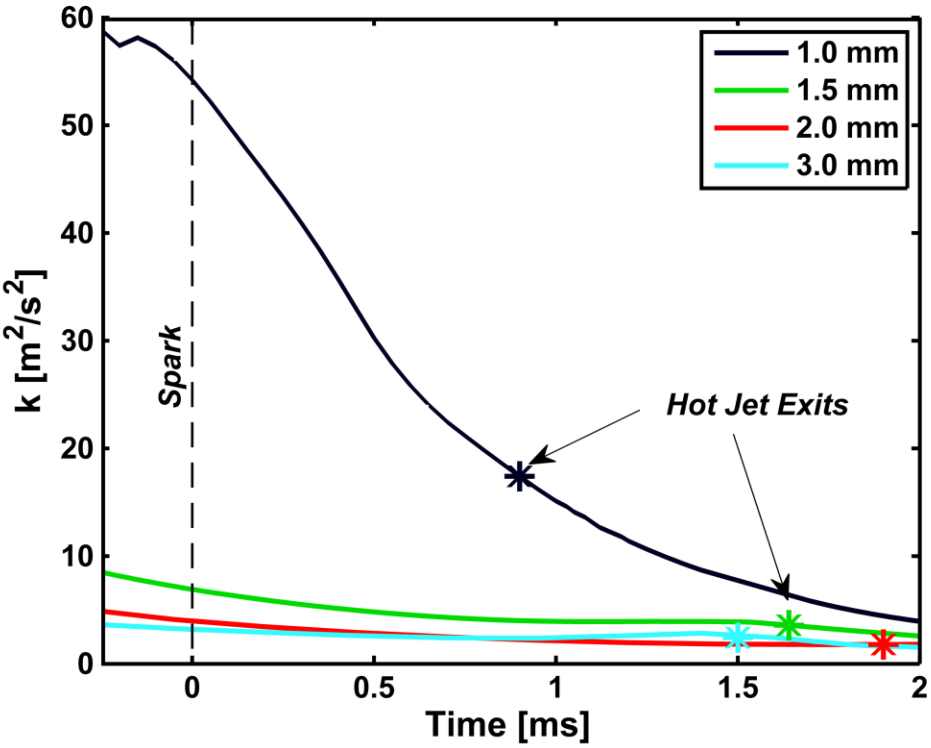

Figure 8-11 Averaged turbulent kinetic energy per unit mass, k, in the TJI pre-chamber with the spark timing as the time datum

8.3 Summary of Orifice Diameter Simulations

Four fully three-dimensional computational fluid dynamic simulations with detailed chemical kinetic combustion modeling in a Rapid Compression Machine (RCM) with an installed Turbulent Jet Ignition (TJI) system have been presented. The four simulations all have TJI pre-chambers with a single centrally located orifice with diameters of 1.0, 1.5, 2.0, and 3.0 mm, each with identical initial conditions based on the conditions of a specific experimental RCM test run with the 1.5 mm diameter orifice.

The combustion induced by the TJI system's jets in the main combustion chamber of the RCM is the main focus of the analysis and discussion of the simulations. It is found that the smaller orifices produce faster burn rates in the main combustion chamber after a hot jet is emitted from the pre-chamber. This results from the increased amount of turbulence generated by the higher

velocity jets that the smaller orifices generate. A limit, occurring around the orifice size of 1.5 mm, is approached where the additional turbulence generated by a more restrictive orifice is offset by the negative effects that result from the smaller orifice size, which may include a smaller hot jet diameter and increased heat loss in the orifice during the hot jet discharge. This is demonstrated by the 1.5 mm case, which achieves a faster main chamber burn than the 1.0 mm case despite the 1.0 mm orifice generating a higher jet velocity and increased levels of turbulent energy.

With access to flow field data for the entire duration of the TJI process in the RCM, five distinct phases of the TJI process are identified and discussed. The five phases are labeled as follows: compression, pre-chamber combustion initiation, cold jet, hot jet, and flow reversal. A description of these phases and the RCM and TJI's behavior during each of them was described. Additional phases of operation should be anticipated to arise for the TJI process in a four-stroke engine application generated by the gas exchange processes associated with intake and exhaust that are absent in the single fire tests of the RCM. Combined together with the compression phase, these gas exchange phases will be responsible for scavenging the pre-chamber. While residual gas in the pre-chamber isn’t a concern in the RCM, it will be an important factor in an engine as ignition in the pre-chamber will require an ignitable mixture around the spark plug, which a high concentration of burned gases from the previous cycle in the pre-chamber may prevent. The increased amount of lag in the pre-chamber pressure compared to that of the main chamber during compression in the RCM as the TJI orifice diameter is reduced demonstrates the effect of increased restriction on displacement-driven gas exchange between the chambers. It is, therefore, possible that while small orifices may generate better jets for the ignition and combustion in the main chamber, they may be too small to provide adequate scavenging of the pre-chamber and, thus, be inappropriate for use in an engine.

The remaining four phases from the TJI process in the RCM should also be present in an engine application with only slight differences resulting from continued piston motion throughout the process. The spark timing in an engine occurs before TDC; so the pre-chamber initiation phase will take place with a definite flow into the pre-chamber. This appears advantageous as the short hot jet delay of the 1.0 mm orifice, which still experiences an inflow into the pre-chamber when the spark is fired, indicates that the turbulence generated by flow into the pre-chamber is beneficial to fast pre-chamber combustion. The two jet phases, cold and hot, will be altered slightly by the piston motion that will continue to increase the pressure in the main chamber as combustion develops in the pre-chamber. Both jets will also be emitted into a main chamber experiencing a contraction of its volume and a more complicated flow field than what is experienced in the RCM. Finally, the flow reversal phase should remain in an engine due to the large disparity between the sizes of both chambers irrespective of the piston motion. What may be most interesting about this phase in an engine, however, is how in-cylinder motion will affect the composition of the gases that are forced back into the pre-chamber during this phase and whether or not it is disadvantageous to burn fresh gases in the pre-chamber after combustion in the main chamber has been established.

Finally, a conclusion can be drawn from the field data presented in Figure 8-5, Figure 8-6, and Figure 8-9 that increasing the number of orifices and, therefore, the number of jets that are produced by the TJI has great potential to improve the rate of combustion in the main chamber.

8.4 Results from Spark Location Comparisons

The boundary geometry used for this set of simulations is shown in Figure 8-12. The simulations include the compression stroke of the RCM and begin with the piston located at bottom dead center. Two major simplifications have been made to the geometry compared to the physical RCM and TJI system that it represents. The first is that the crevice volumes in the RCM have been ignored. In regards to the simulations and their analysis for the purposes of discussion, these

volumes are of little consequence. While estimates of the total volume of the MSU RCM's crevice volumes put them on par with the volume of the pre-chamber [112], the effect of neglecting them only leads to the simulations consuming slightly more fuel than what would be consumed in the physical experiments since there are no places for unburnt gases to escape combustion in the simulations without the crevices.

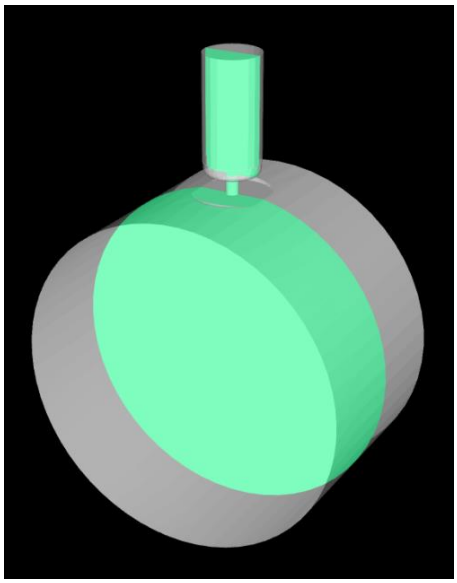

Figure 8-12 The boundary geometry for the simulations at top dead center with the domain boundaries represented by the white transparent surfaces while the green plane intersecting the centerline of the pre-chamber is the location of the clipping plane that is used in Figures 8-15 and 8-17

The pre-chamber, meanwhile, is also simplified from that of the actual TJI hardware shown in Figure 8-12. To facilitate consistent geometry between each of the four cases with different ignition source locations, the boundaries and geometry associated with the TJI system's spark plug have been removed. What remains is a pre-chamber that is a simple cylinder with a radius around its bottom end as shown in Figure 8-13. Also displayed in this figure are the four spark locations used in the simulations.

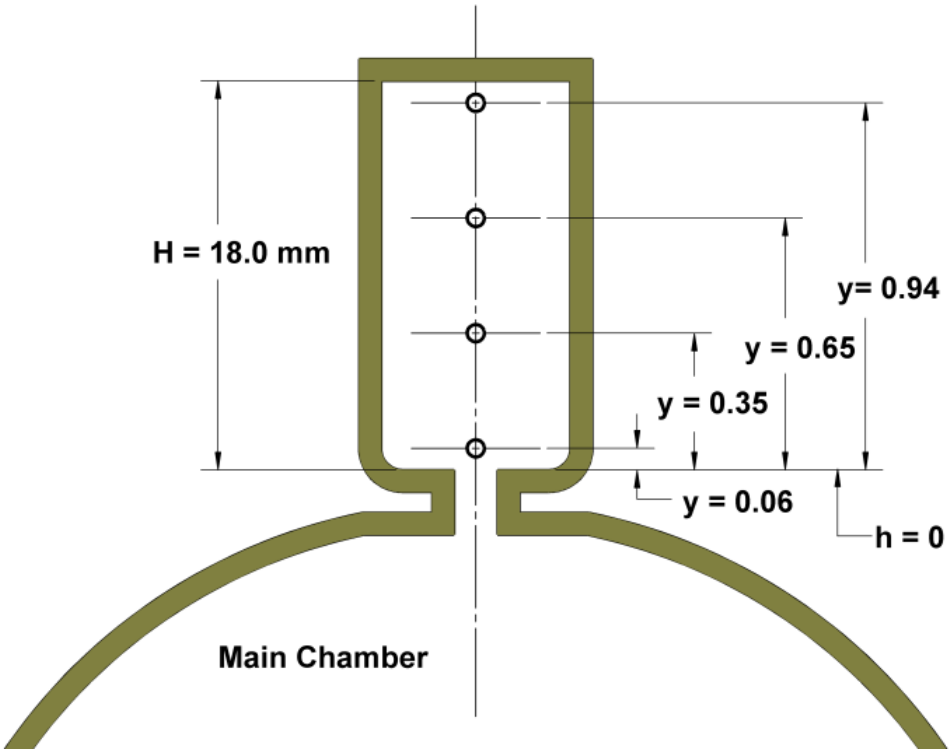

Figure 8-13 Schematic of the TJI pre-chamber showing the different source locations used in the simulations

The four spark or energy source locations all lie on the axis of the pre-chamber cylinder. The total pre-chamber height, *H*, is 18.0 mm. The source located at the top of the pre-chamber is offset 1.0 mm from the top wall of the volume. At the opposite end, the lowest source location is offset 1.0 mm from the bottom wall of the pre-chamber and the orifice opening. The remaining two locations are located to divide the 16.0 mm gap between the top and bottom locations evenly. Using the coordinate system established in Figure 8-13 leads to spark locations with heights, *h*, from the bottom of the pre-chamber of 1.0, 6.3, 11.7, and 17.0 mm. Each of these locations will be designated as a normalized value, *y*, related to the overall height of the pre-chamber as specified in equation (2), yielding values of 0.06, 0.35, 0.65, and 0.94.

$$\boldsymbol{y = \frac{h}{H}} \tag{2}$$

Other than the location of the ignition source varying from simulation to simulation, all four

simulations are identical. All four share the same computation for the compression stroke of the RCM. The initial mixture in the simulations is uniform throughout and is a mixture of dry air and propane in proportion to produce a λ of 1.27 at 353K and 1.0 bar. The boundaries are isothermal, with temperatures that are also 353 K.

Figure 8-14 contains plots of the pressure generated in the four simulations' main and pre-chambers chambers. The time datum in this figure is relative to the start of the spark energy source and the spark timing. Also displayed in this figure are markers on the main combustion chamber and pre-chamber pressure traces that signify the moments in the simulations when hot gases first enter the main combustion chambers. This moment is designated as the time of hot jet exit. It will serve as the time datum used in the evaluation of the performance of combustion in the main chamber of the RCM since it is only after this moment that combustion in the main chamber begins, which, as the larger of the two volumes, also serves as a benchmark for the performance of the entire TJI system.

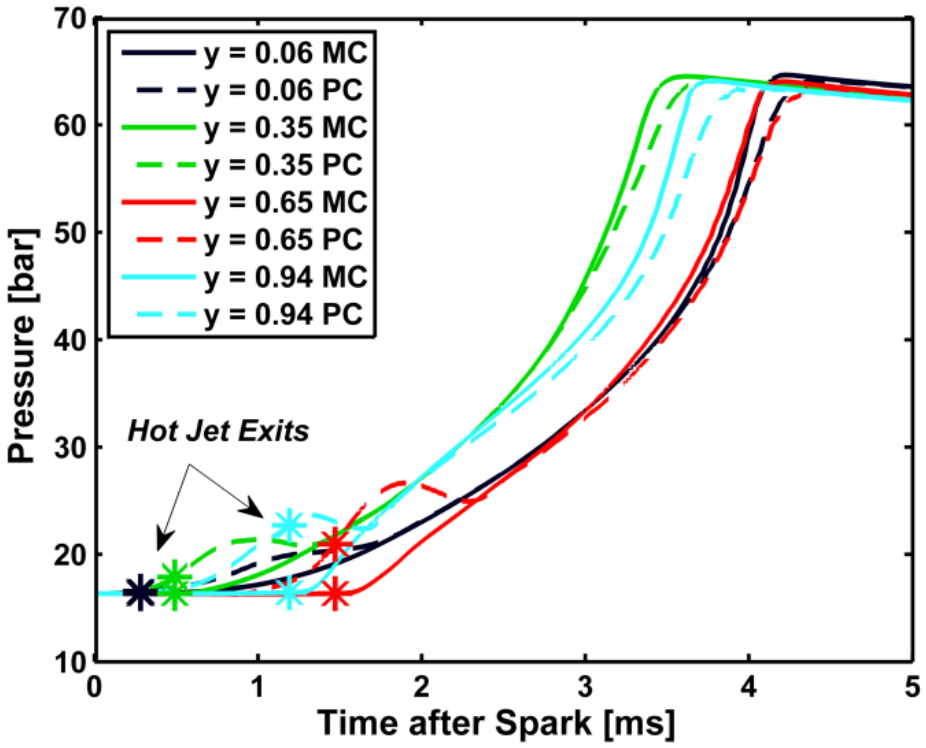

Figure 8-14 Pressure in the main and pre-chambers of the four simulations with the moment that the hot jet first exits indicated. The time datum for this data corresponds to the spark timing

The development of combustion in the simulation pre-chambers is presented in Figure 8-15. In this figure, planes intersecting the simulation domain through the center of the pre-chamber are colored by the local value of temperature. The time datum in this figure corresponds to spark timing. The first column of images shows the energy source shortly after its activation. The following columns each display the simulations at times that correspond to the hot jet exit for the simulation, highlighted with a green border. This figure not only compares initial flame development but also indicates the order in which the hot jets emerge into the main chamber relative to the spark location.

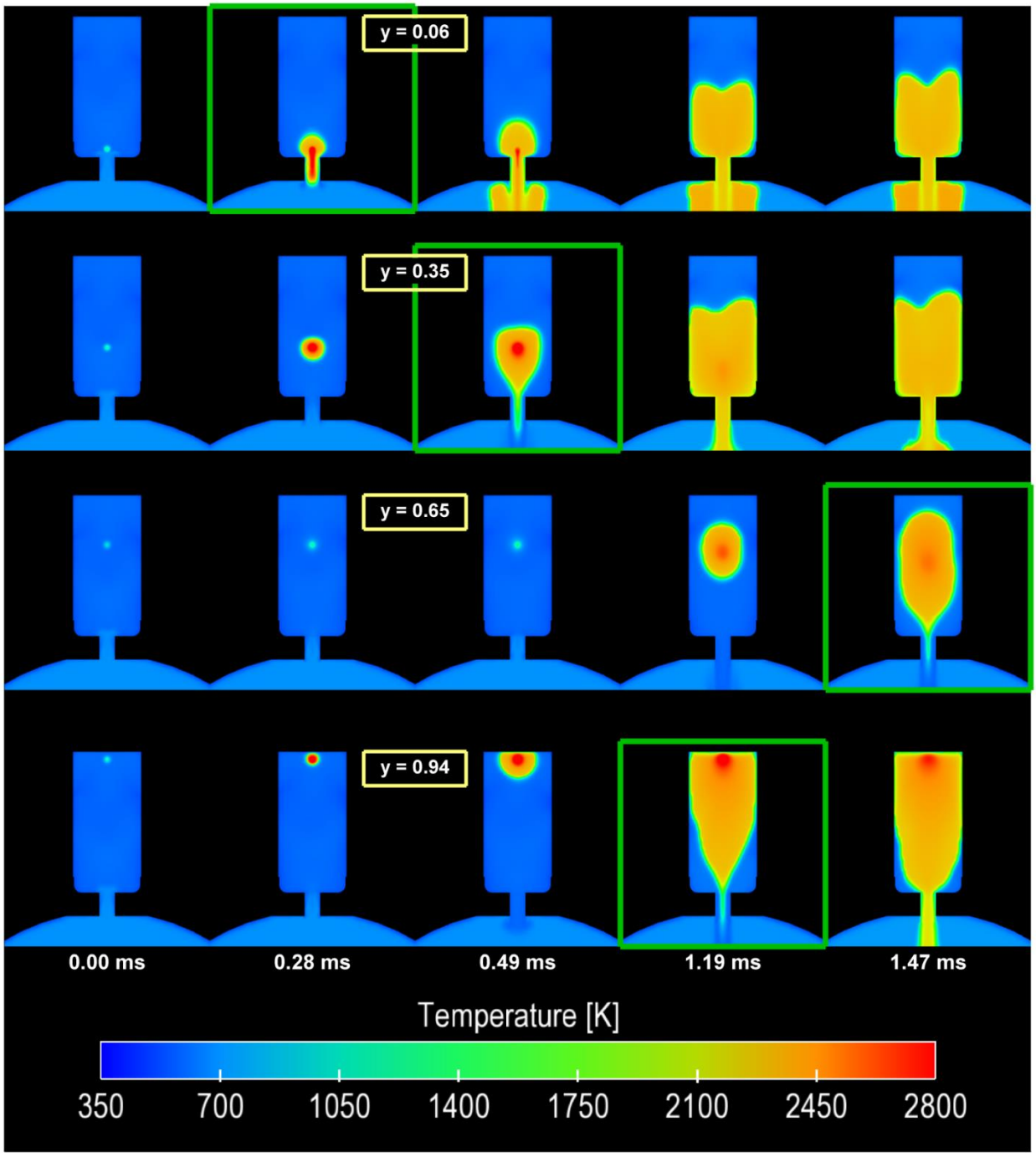

Figure 8-15 Temperature contours on the plane shown in Figure 6-1 showing the development of combustion in the pre-chambers of the four simulations. The frames highlighted with a border correspond to the time of the hot jet exit for that case. The time datum in this figure is the spark timing

Given the disparity in the hot jet exit times between the simulations, it is difficult to compare the four cases' main chamber combustion while using spark timing as a datum for time. Thus, the

main chamber pressure data from Figure 8-14 is replotted in Figure 8-16 with the time datum set to correspond to each simulation's hot jet exit time and, therefore, the beginning of combustion in the main chamber. Markers for spark timing are also provided in this figure to help connect Figures 8-14 and 8-16.

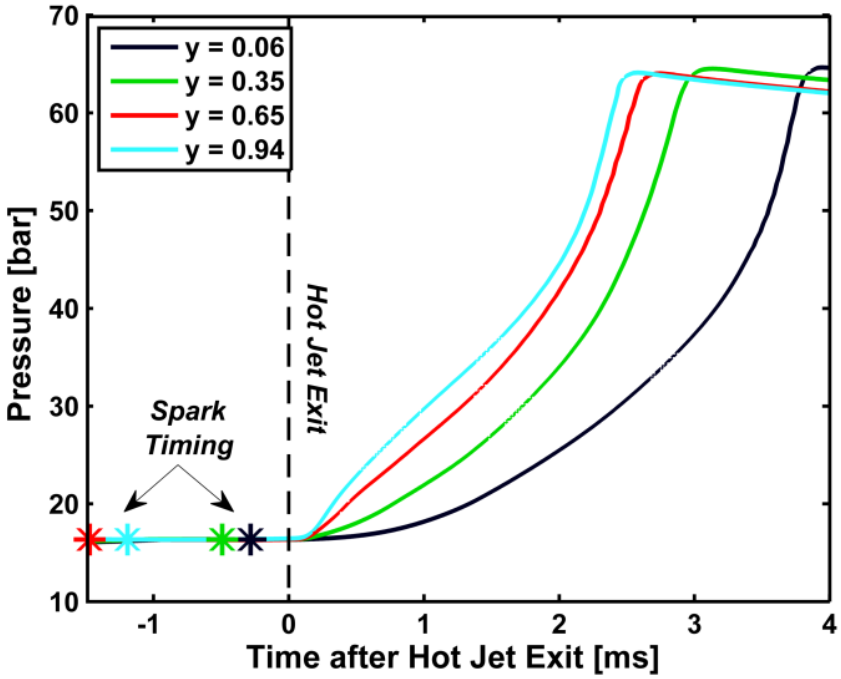

Figure 8-16 Main chamber pressures plotted with the time of hot jet exit for each simulation as the time datum with the spark timing relative to the new datum indicated

With the hot jet exit as the time datum for each simulation individually, Figure 8-17 is presented similarly to that of Figure 8-15. Each image includes only the whole main chamber. These temperature contour plots demonstrate the differences in main chamber combustion development between the four cases. Individual frames are also highlighted to indicate that they correspond to the occurrence of a 10% mass fraction burn in the main chamber.

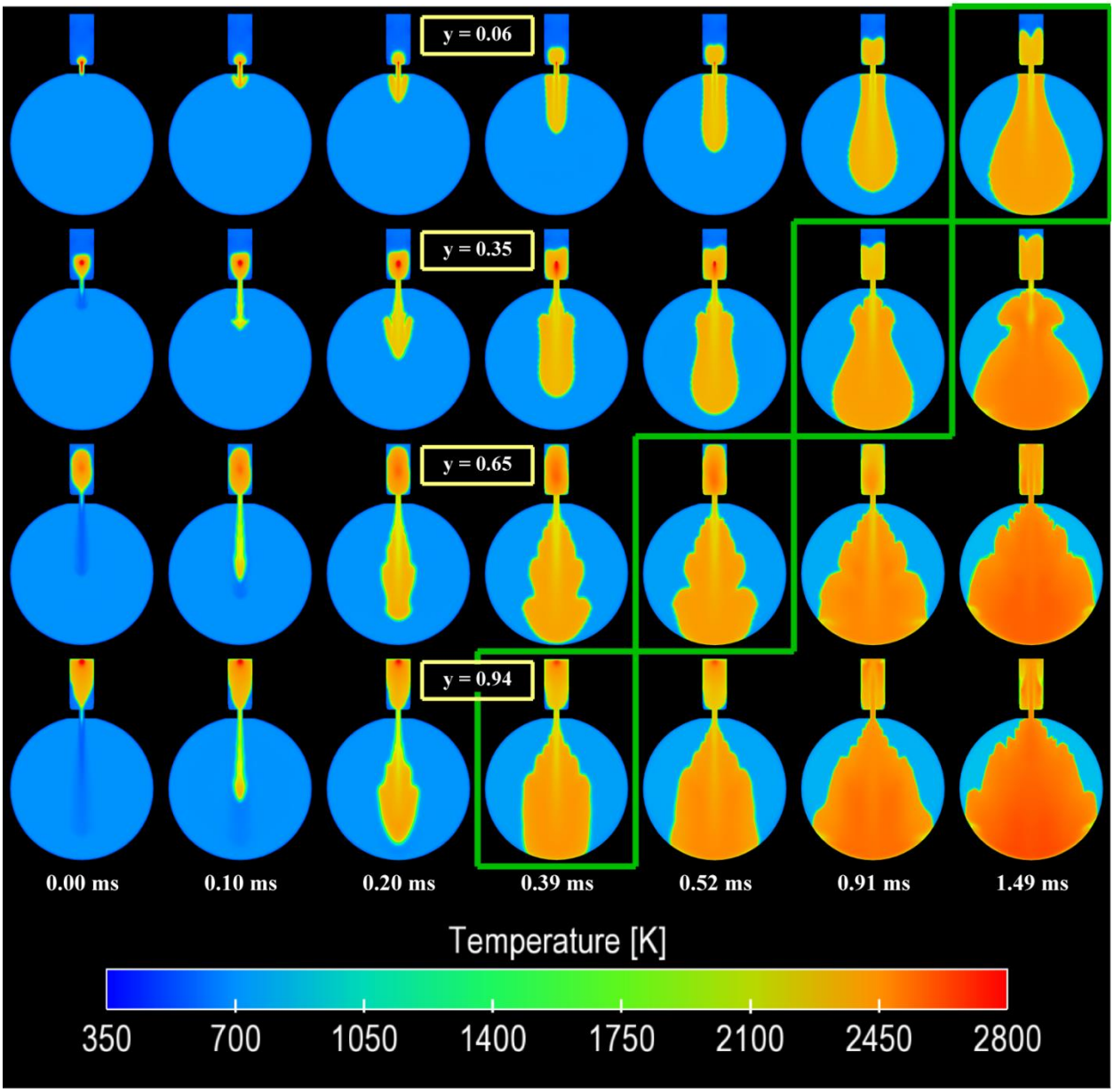

Figure 8-17 Temperature contours on the Z-plane shown in Figure 6-1 showing the development of combustion in the main chambers of the four simulations. The frames highlighted with a border correspond to when 10% of the mass fraction burn in the main chamber has been achieved. The time datum in this figure is the time of the hot jet exit for each simulation

Beyond the qualitative look that Figure 8-17 provides, calculations of mass fraction burn durations for each simulation are given for comparison in Figure 8-18. In RCM experiments, mass fraction burn is calculated directly from combustion chamber pressure without the need to correct for an expanding volume since the piston remains stationary and the spark occurs after top dead center. Thus, the mass fraction burn is simply the ratio of the current pressure rise due to combustion to the total pressure rise that will occur by the end of combustion [97].

There are a total of three parameters calculated in Figure 8-18. The first is the hot jet exit delay, which is the time that elapses between the start of the spark and the entry of hot gases into the main chamber. The other two are the 0-10 and 10-90% mass fraction burn durations in the main chamber. Here 0 corresponds to the hot jet exit of each simulation and not the spark timing; so the 0-10% mass fraction burn duration is the amount of time that elapses between the hot jet exit and 10% of the total pressure rise in the main chamber occurring.

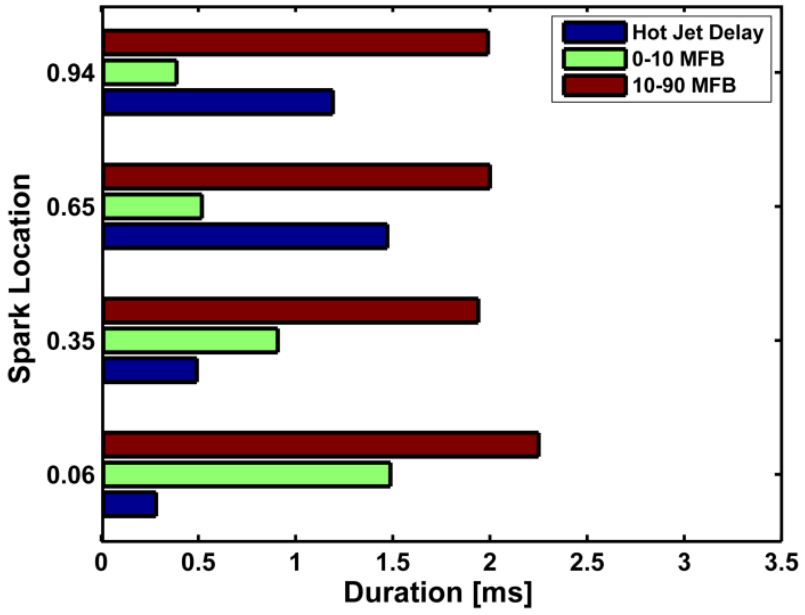

Figure 8-18 Mass fraction burn durations and the delay between the spark timing and the exit of a hot jet into the main combustion chamber

Just as indicated in Figure 8-15, Figure 8-18 demonstrates that the two lower spark locations

emit a hot jet in a shorter amount of time after the spark than the higher locations. In an engine application, this delay between the spark and the hot jet will have a direct influence on the necessary spark timing for the TJI system, but as long as the delay is not so long that it limits the speed at which the engine can operate, it is not a measure that is very important to the evaluation of the overall system performance since the small size of the pre-chamber contains only a small portion of the total fuel energy within the system. The more appropriate measures of the performance of the system configurations are the two burn durations that are included in Figure 8-18. The 0-10% mass fraction burn duration demonstrates the speed at which ignition in the main chamber takes place. This duration decreases as the height of the source location is increased. Meanwhile, the 10-90% burn durations measure the speed at which the bulk of combustion in the main chamber occurs. This duration is similar for all cases except for the lowest $y = 0.04$ case. The close similarity of this duration for the other three cases indicates that the effects of the jets generated by the pre-chamber on main chamber combustion are limited to the early stages of combustion only.

The averaged exit velocity of the jets generated in the four simulations as a function of time, with the hot jet exit time serving as the time datum, is given in Figure 8-19. This velocity is equivalent to the uniform velocity required to produce the same volumetric flow rate through the orifice occurring at each moment. This figure shows that prior to the hot jet exit, there is a jet of unburned gases, the cold jet, that are expelled from the pre-chamber. The cold jet's duration and velocity increase as the spark location is moved higher in the pre-chamber. In all four cases, the exit velocity reaches a maximum after the hot jet exit with the $y = 0.65$ location producing the highest peak exit velocity. The highest exit velocity at the beginning of the hot jet, however, is produced by the $y = 0.94$ case, with this velocity declining as the spark location is moved lower.

Following the peak velocity, the exit velocity declines as the combustion in the pre-chamber reaches completion. Eventually, the direction of the flow in the orifice is reversed, the negative values in Figure 8-19, as the pressure in the main chamber has increased due to combustion within it enough to overtake the pressure in the pre-chamber forcing main chamber gases into the smaller chamber.

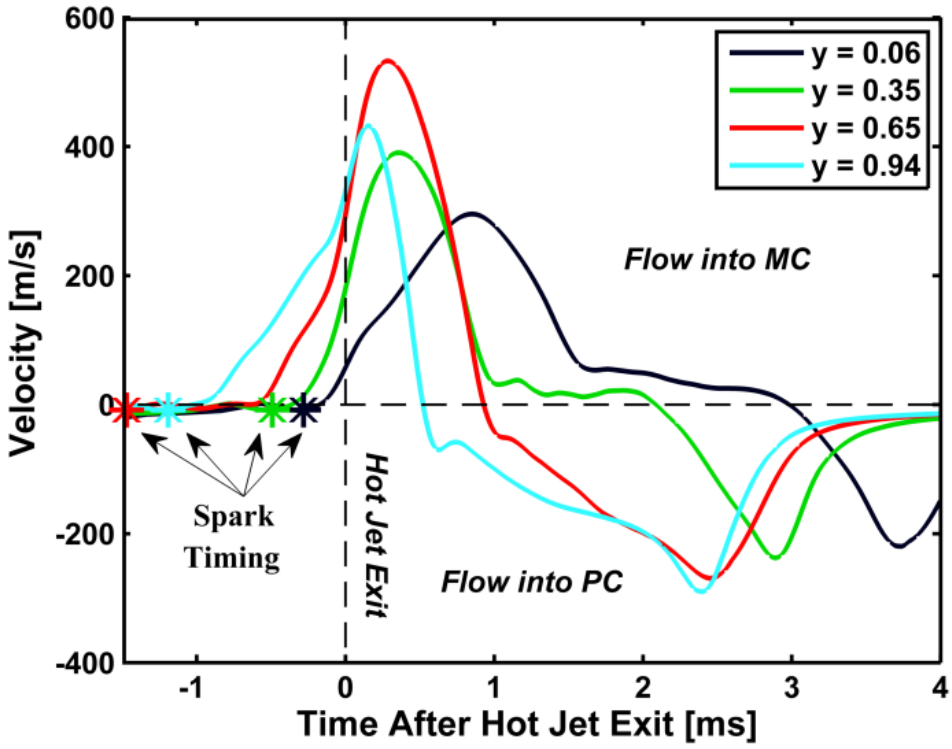

Figure 8-19 Orifice averaged exit velocities of the four simulations. The time datum is the hot jet exit for each simulation

As the schematic in Figure 5-3 indicates and the positive velocities during the negative time values in Figure 8-19 demonstrate, there is a certain amount of mass transfer that occurs from the pre-chamber to the main chamber before hot gases appear in the main combustion chamber. To demonstrate the amount of the pre-chamber contents that have been convected into the main chamber by the cold jet, a measurement of the mass contained in the pre-chamber is displayed in Figure 8-20. The data plotted in this figure is normalized to the total mass within the pre-chamber

at the spark timing. As Figure 8-19 anticipates, the cold jet that transports the most unburned mixture into the main chamber before the hot jet is produced occurs in the y = 0.94 simulation. The amount of pre-chamber mass ejected into the main chamber before the arrival of hot gas decreases as the spark location is lowered.

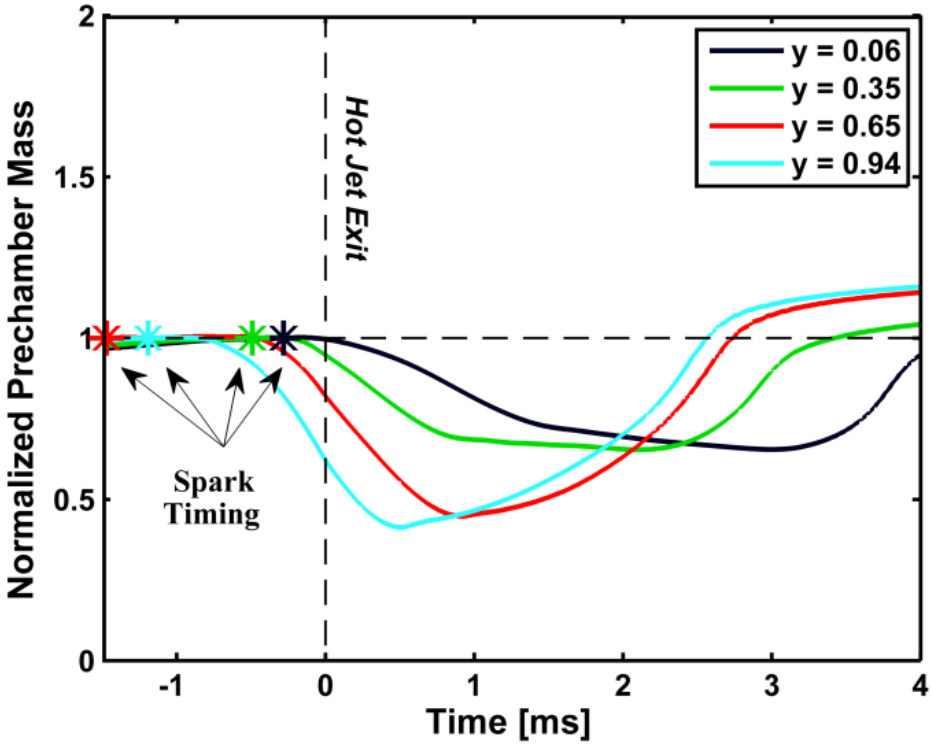

Figure 8-20 The amount of mass in the pre-chamber is normalized by the mass that is originally in the chamber at the spark timing plotted against time with the time of hot jet exit as the time datum

8.5 Summary of Spark Location Simulation Results

The results of four computational fluid dynamic simulations with active combustion using detailed chemical kinetics of a Turbulent Jet Ignition (TJI) system in a rapid compression machine with four different spark ignition locations are presented above. A comparison of the main chamber combustion performance of the four simulations demonstrated that the highest spark location within the TJI pre-chamber at y = 0.94 produced the fastest ignition in the main chamber, as

reflected in its 0-10% mass fraction burn duration. The $y = 0.65$ location follows closely behind, with the duration increasing as the spark location gets closer to the bottom of the pre-chamber. With the exception of the lowest location, $y = 0.06$, the 10-90% burn durations of the simulations are all nearly identical.

The simulations show that locating the spark high in the pre-chamber produces a jet that is more effective at quickly igniting the main chamber. Since the pre-chamber flames must propagate a greater distance through the pre-chamber to reach the orifice, more pre-chamber gas is burned, generating a higher pressure differential between the two chambers. When the flame reaches the orifice in the higher location cases, the jet has a higher velocity, penetrating the main chamber quickly and creating high levels of shear, which generates turbulence.

Conversely, the only advantage demonstrated in locating the ignition source towards the bottom of the pre-chamber is that it shortens the delay between firing the spark and having a hot jet enter the main chamber. In the $y = 0.06$ case, the hot jet emerges in a short amount of time, but it is slow at first building up as combustion continues to propagate through the remainder of the pre-chamber. Eventually, the velocity reaches a peak, but most of the jet is essentially wasted as it just emits hot gases into a core region in the main chamber that has already burned rather than coming into contact with a fresh mixture.

With the results of the simulations in mind, it is apparent that the pre-chambers of the best design in a TJI system will be the ones that burn the largest amount of their pre-chamber contents prior to the exit of hot gas into the main chamber. These pre-chambers produce hot jets with higher initial velocities, as shown above, to improve the initial combustion in the main chamber. With the pre-chamber geometry used in the simulations above, this is best achieved with the ignition source located at the top of the pre-chamber furthest away from the orifice.

While the data above suggests that the spark in a TJI pre-chamber should be located deep in the chamber, it should be noted that the $y = 0.65$ case does not perform poorly compared to the best $y = 0.94$ case. In an engine application, additional processes will occur that are absent from the RCM simulations. While the RCM simulations have a compression stroke, the device is fired with a uniform mixture of fresh gases. In an engine, the pre-chamber must be purged of exhaust gases each cycle. Due to the constriction of the orifice between the main chamber and the pre-chamber, it should be anticipated that there may be exhaust gas residuals in the pre-chamber. It is then possible that a location deep in the pre-chamber may contain a high amount of residuals, making it difficult to achieve ignition at that spot. If that is the case, then moving the spark away from that location and closer to the orifice can be done without losing much performance. Essentially, in the design of a TJI pre-chamber, the ignition source needs to be located as far away from the orifice as possible in a place that provides a consistently ignitable mixture.

CHAPTER 9: CFD MODELLING FOR THE DEVELOPMENT OF A TURBULENT JET IGNITION SYSTEM FOR A CONVERTED NATURAL GAS ENGINE

The following chapter presents CFD simulations that were performed during the early stages of the development of a Turbulent Jet Ignition system to be used in a heavy-duty engine that was to be converted from diesel fuel to natural gas. While three types of simulations are presented, most of the work focuses on a simplified analysis used to evaluate the effects of pre-chamber geometry on the mixing and scavenging behavior of the pre-chamber, which are referred to as the simplified mixing simulations. The remaining simulations attempt to incorporate more fidelity into the simulations by including additional features or geometry. The first of these is a simulation that includes the injection of gaseous auxiliary fuel into the pre-chamber. The second incorporates more of the engine's physical geometry, allowing the intake gas exchange process to be simulated. At the same time, a simplified combustion model was also used to provide a preliminary evaluation of jet propagation into the main combustion chamber.

9.1 The Engine and Conceptual Pre-Chamber Design

The converted engine is a Detroit Diesel series 50, an 8.5-liter four-cylinder heavy-duty diesel engine that was in production for a dozen years between the mid-nineties and mid-aughts [113]. A portion of a series 50 engine's cylinder head, sawn approximately down the centerline of either the first or fourth cylinder of the inline configuration engine, was provided, accompanied by technical drawings for the engine valves, by the project's development partner, Omnitek Engineering. A photograph of the cylinder head is shown in Figure 9-1. The photograph here displays the engine's extreme suitability for the TJI conversion. Its ample and centrally located cavity, originally intended to accommodate its diesel direct injector, provides a readily accessible, well-positioned location for the TJI pre-chamber. Germane to the simulations presented below is that fuel for the main combustion chamber in the engine was no longer to be provided directly

injected into the cylinder but was instead added upstream of the intake valve.

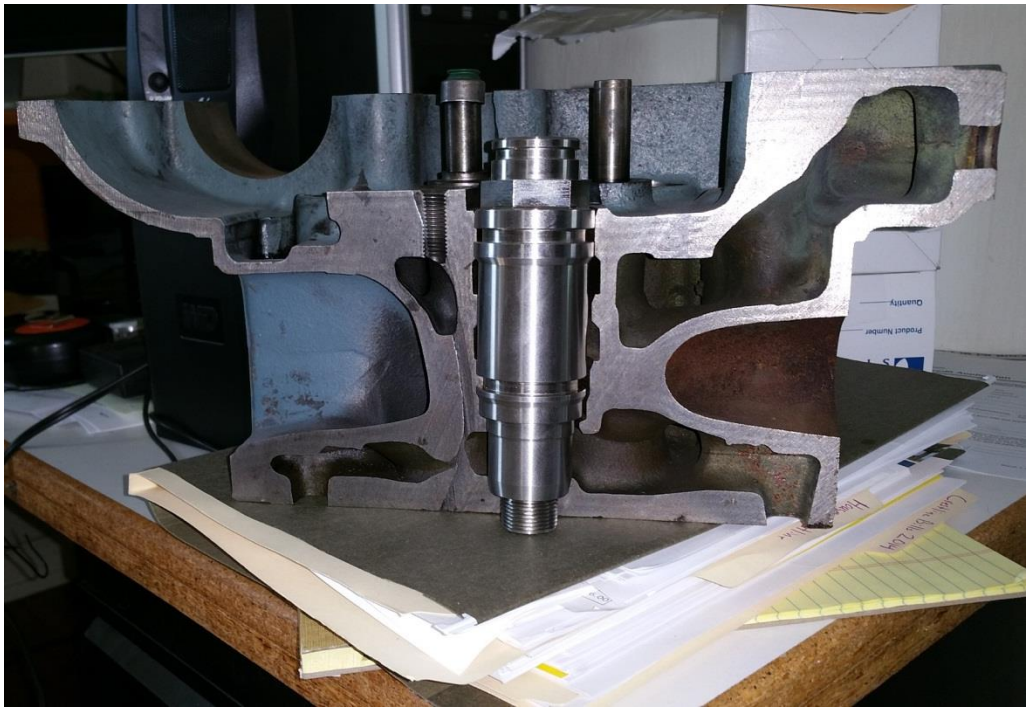

Figure 9-1 Detroit Diesel Series 50 cylinder head sawed in half showing intake port on the left, the cavity for the direct injector to be replaced with TJI centered, and the exhaust port on the right

A conceptual design for the pre-chamber was provided at the beginning of the project before CFD evaluations were run. A cross-sectioned drawing of the design is shown in Figure 9-2. The housing is a revolved body designed to fit into the injector cavity in the cylinder head. It includes a cavity and threaded thru-hole to accommodate a spark plug, a long straight hole through which fuel for the pre-chamber is intended to be supplied, a pre-chamber cavity, and a multi-orifice nozzle.

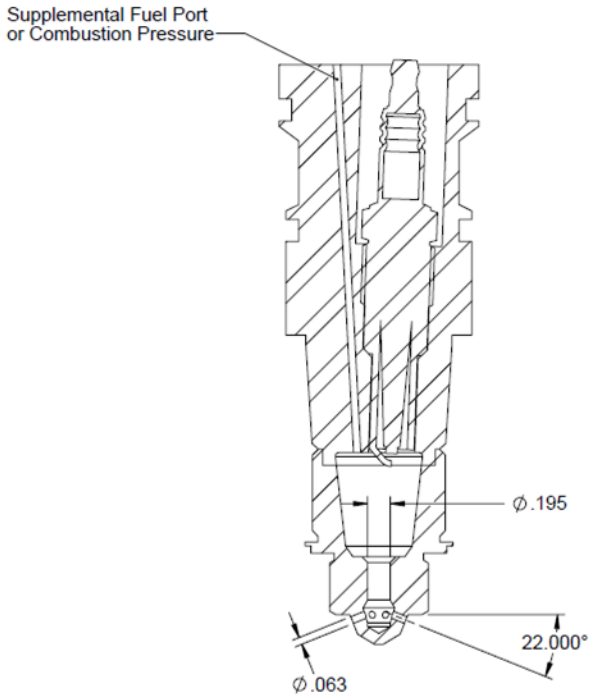

Figure 9-2 A sectioned view of the initial conceptual turbulent jet ignition pre-chamber design

Definition of the Pre-chamber Internal Geometry

Since only the internal geometry of the TJI pre-chamber that is in contact with the fluid domain is of consequence to the simulations, the conceptual design of Figure 9-2 was converted to the simplified CAD model shown in Figure 9-3. The pre-chamber cavity is an axisymmetric revolution of the profile shown in the figure except for the orifices and the spark electrodes. To facilitate discussion, regions of the pre-chamber cavity are designated in Figure 9-3 dividing the pre-chamber into a lower chamber and an upper chamber. The lower chamber is further subdivided into the neck and nozzle subregions. Specific revolved surfaces are also designated in the diagram. They are the interior nozzle surface, the exterior nozzle surface, the neck flare, the nozzle bottom, and the cylinder head, which are labeled in the detailed view on the right side of the figure. The two nozzle faces are the two surfaces through which the orifice passes. The neck flare is generated

by connecting the interior nozzle surface's top edge with the neck's bottom edge. The nozzle bottom is the circular flat at the bottom of the nozzle, and the cylinder head is the underside surface of the cylinder head or the top of the main combustion chamber. Finally, the geometry in Figure 9-3 also includes a hole in the bottom surface of the nozzle that is absent in Figure 9-2. This hole was designated as the "breather" hole as its potential inclusion targeted improving the performance of the pre-chamber in regard to scavenging by providing a path for incoming air that is in line with the direction of the piston's motion. The inclusion or omission of this feature is evaluated using a subset of the simulations detailed below.

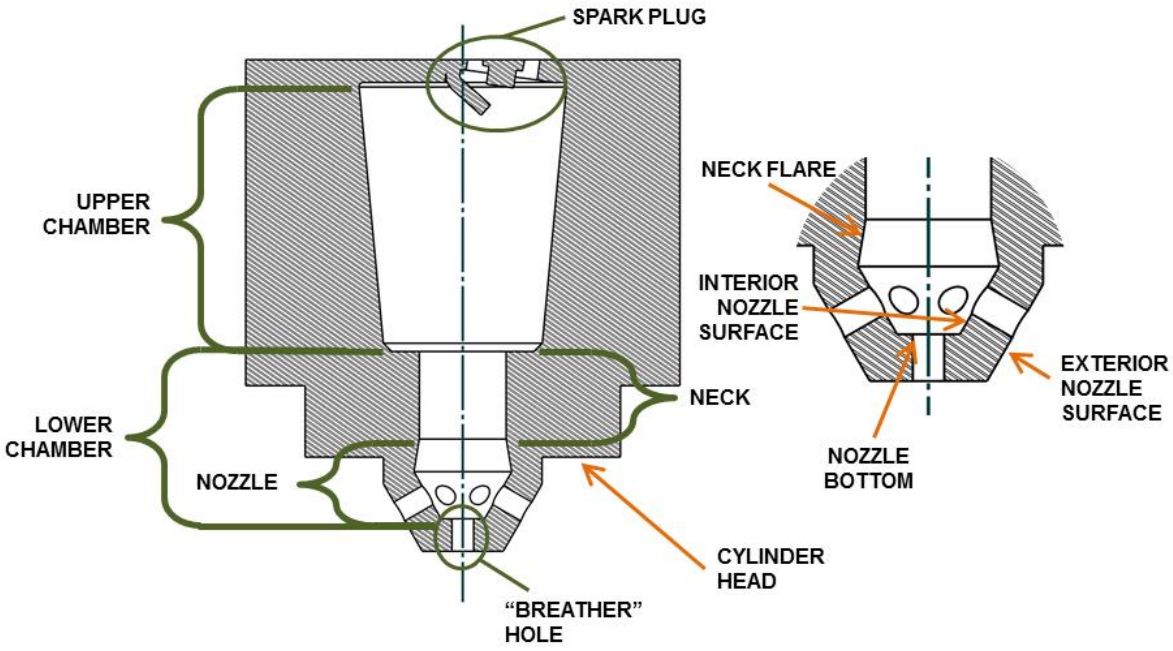

Figure 9-3 Generic pre-chamber cavity geometry (exterior surfaces above the cylinder head surface are not representative of the engine hardware)

The TJI geometries utilized in the simulations documented below are all variations of the pre-chamber geometry shown in Figure 9-3. While the geometry in the main combustion chamber of the simulations is fixed by the engine used in the project, there was some freedom to modify the design of the pre-chamber. Packaging constraints have led to the basic design shown above with

only a limited number of geometric parameters altered from simulation to simulation. It was identified early in the project that the geometry of the upper chamber would largely be dictated by what would fit into the space in and above the cylinder head vacated by the original engine's diesel direct injector. This, coupled with the desire for a cavity that provided a pre-chamber to main chamber volume ratio of about 2-3%, meant that this part of the geometry did not change from simulation to simulation. Space is also limited in the region where the TJI protrudes through the cylinder head into the engine's traditional combustion chamber. For this reason, the exterior geometry of the nozzle, its outer diameter, and the distance that it intrudes into the main chamber also remained unchanged from case to case. A rendering of the CAD model that was created and maintained throughout the effort to generate the fluid domain inputs for the simplified mixing CFD simulations is shown in Figure 9-4. The figure displays the three components that bound the volume. These are the TJI pre-chamber, the bowled piston of the series 50 engine, and a very simplified, flat, cylinder head and sleeve. The image also shows theoretical jet trajectories, the red cones, of which six are shown. This image was generated before making determinations for how many orifice holes to include in the TJI nozzle. In the simulations that follow, all the pre-chamber nozzles have between 8-12 orifices.

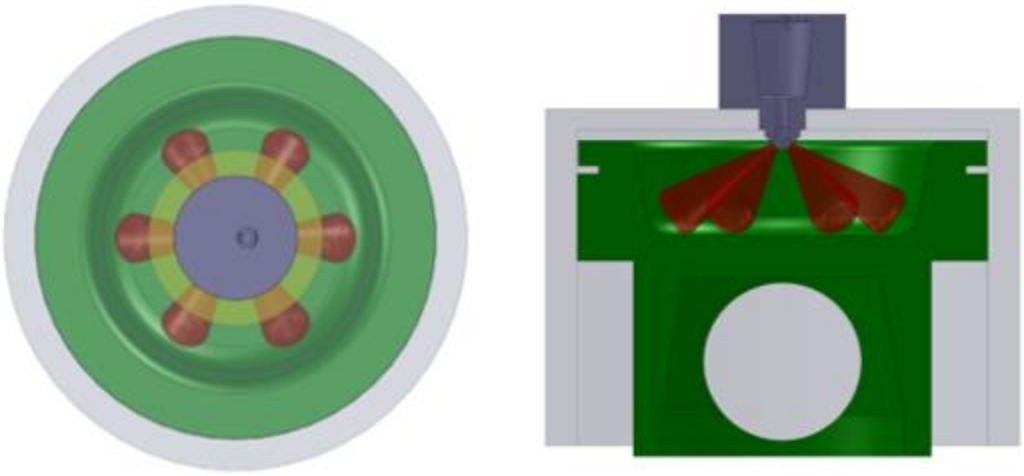

Figure 9-4 Rendered view of the simplified CAD model of the cylinder, piston, and TJI pre-chamber with cones drawn to mock potential jet directories (Note: the nozzle in this model has only 6 orifices, simulations presented below have 8, 9, or 12 orifices)

Two types of nozzle configurations are present in the simulations below, those that include an extra orifice in the bottom of the nozzle, the "breather hole, and those that do not. With or without the extra hole, all of the nozzles used in the simplified mixing simulations have eight radial orifices equally spaced around the centerline of the pre-chamber. The orientation of the radial orifice centerlines relative to the vertical axis of the pre-chamber is 40°. This angle was selected in the following manner. First, the CAD model shown in Figure 9-4 was configured with the piston at its top dead center position was used to determine the angle which produced the greatest distance between the center of the TJI nozzle and the wall of the bowled piston, which was 55° from the vertical centerline of the pre-chamber—where 0° would be a line straight down into the face of the piston. Second, 15° was subtracted from the 55° angle to compensate for the upward deflection that the jets will experience due to the flow induced by the upward motion of the piston.

In the simulations without the breather hole, the eight orifices in the nozzle all have a diameter of 1.63 mm. In the simulations with the breather hole, the individual orifice diameters are reduced to 1.5 mm so that the total combined cross-sectional area of the orifices for each nozzle

configuration remains the same. The orifices pass through a 3 mm thick wall in all but one case below. Figure 9-5 shows the geometry used for the simulation that has been named Case 1. The dimensions in this diagram are common to all of the cases considered here as the variations in the various designs focused on the effects of the neck geometry and the inclusion or exclusion of the ninth breather hole orifice.

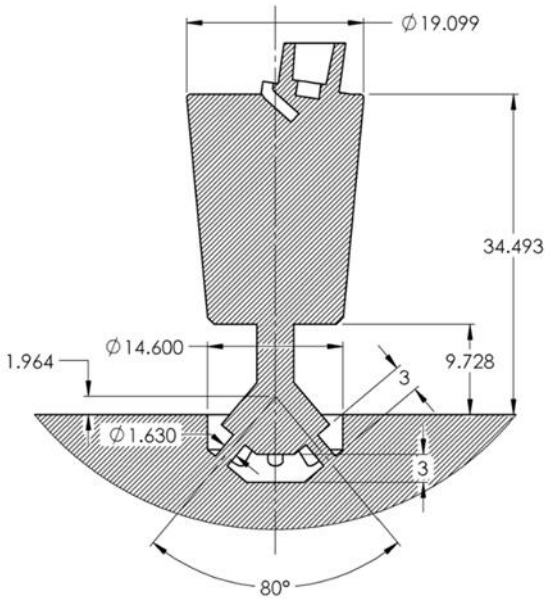

Figure 9-5 Simulation geometry, Case 1, with the dimensions of the fixed elements of TJI pre-chamber geometry shown (dimensions are in mm, and aside from the spark plug, the geometry is axisymmetric)

9.2 Simulation Setups

The content of this section provides overviews of the three simulations that have been set up to support the research and development effort described above. Of the three presented, most of the data presented here was generated using the simplified mixing/scavenging simulation described first below. The second and third setups have been designed to provide the framework to add additional features and fidelity to the modeling of the system for any future simulation efforts in support of this particular TJI application.

Simplified Pre-chamber Mixing/Scavenging Simulation Framework

In the simplified simulations, there are no gas exchange processes or valve motions. The geometry is simply that of the cylinder, piston face, and pre-chamber. This geometry is shown in Figure 9-6 with the piston at bottom dead center, which was exported from a CAD assembly similar to that shown in Figure 9-4. The simulations begin with a quiescent, homogenous lean mixture of CH_4 and air (λ=2) at atmospheric pressure and 313 K. The piston moves in correspondence with an engine speed of 1500 rpm. The simulations have fuel artificially mapped into the simulation domain when the piston reaches 90° before top dead center. To accomplish this the gas within the simulation domain that intersects with a sphere centered on the top wall of the upper pre-chamber with a radius of 10.35 mm is altered to have a composition of pure methane gas at the mapping crank position. This mapping is shown in Figure 9-7. The size of the sphere was selected to provide the correct mass of additional fuel that needs to be introduced into the pre-chamber to result in an overall pre-chamber mixture slightly richer than stoichiometric at 30° before top dead center.

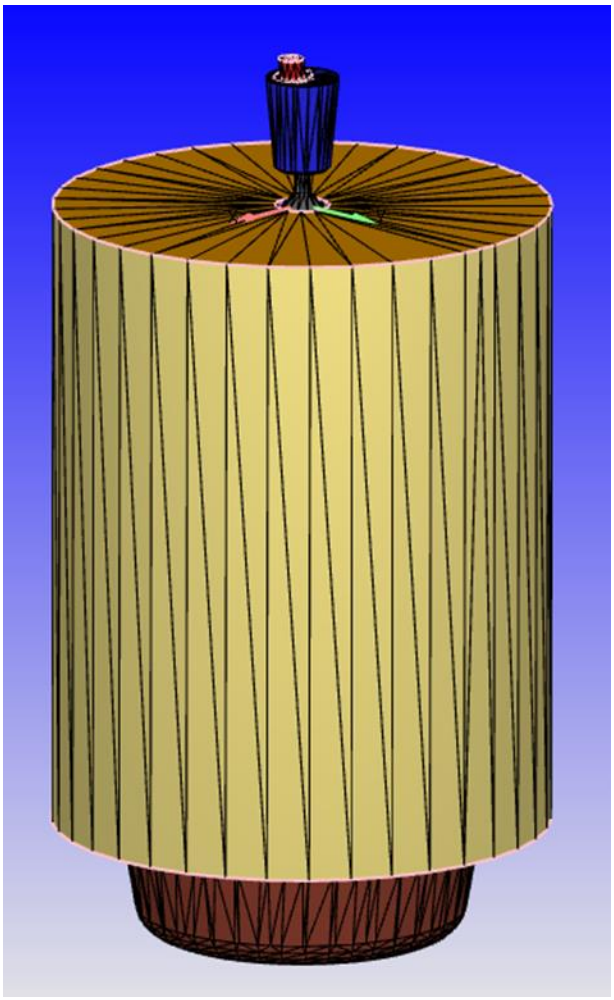

Figure 9-6 The geometry of the simplified mixing simulation consisting of a single cylinder with a pre-chamber as viewed in the Converge preprocessor software (the piston is positioned at bottom dead center here)

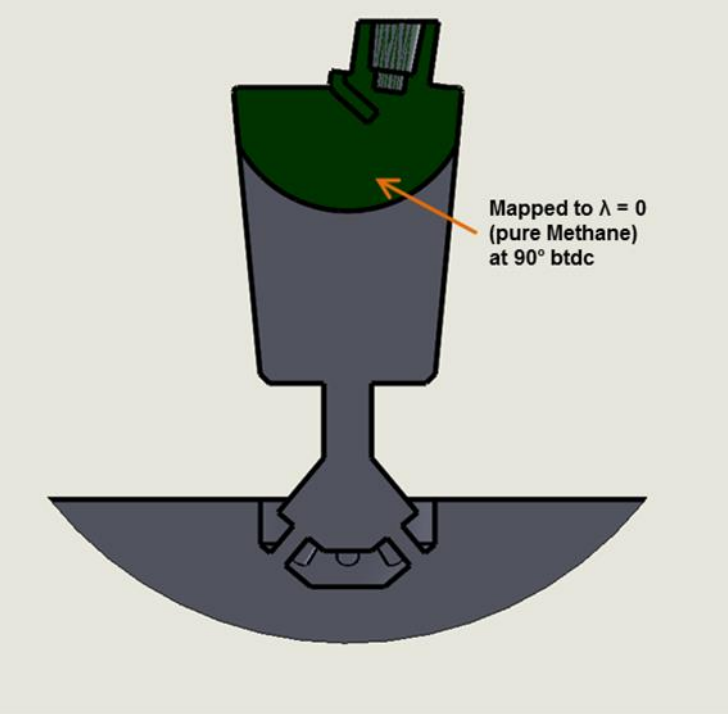

Figure 9-7 Diagram showing methane mapping strategy used for the simplified mixing simulations

This mapping procedure, of course, is not based on reality. In the actual system, auxiliary fuel will be provided through injection into the pre-chamber over a finite duration of time. Initial efforts to simulate this finite duration fueling were also developed, which will be discussed briefly in its own section below. However, to quickly generate informative data at the start of the project, the mapping simplification was employed to bypass the difficulties that defining and accurately modeling an auxiliary gas injection process presented. While the Converge CFD package is set up to conveniently handle the direct injection of liquid fuel and the sprays associated with it, the injection of gaseous fuels is less elegant. Despite the unrealistic qualities of the simplified simulations, two aspects of each design's geometry can be ascertained from the data they produce. The first is the degree to which the region of fuel in the pre-chamber gets mixed with the lean mixture coming into it through its nozzle during the remainder of the compression stroke, and the second is the pressure drops that certain aspects of the geometry create during the compression

stroke's forced flow into the pre-chamber.

Pre-chamber Auxiliary Fuel Injection

Two additional simulations were created in support of the TJI development that were intended to add additional fidelity to the simplified mixing simulations. Presently these two simulation setups are demonstrations of the potential framework that they provide for further simulation work in the future. The first of the two simulations presented is an extension of the simplified simulations described in the previous subsection to include methane injection into the pre-chamber cavity replacing the contrived methane mapping previously utilized. Two pre-chamber geometries were created to facilitate the simulations. These are shown in Figure 9-16 in a subsection below. Each includes fuel passages added to the top of the pre-chamber. The rest of the geometry and boundary conditions remain identical to the simplified simulations. To simulate the injection, the uppermost surface of the fuel passage was set as an inflow boundary condition with an elevated static pressure. In the simulations, a virtual boundary is defined at the exit of the added fuel passage into the pre-chamber. To simulate the injection event, this boundary is temporarily removed, which allows an inflow from the passage as its uppermost surface's boundary conditions provide inflow to maintain the static pressure at the boundary.

Basic Engine Model with Intake Gas Exchange Process and Simplified Combustion

The second more advanced simulation setup that was created included additional engine components, extending the simulation domain to include the intake and exhaust valves and air flow passages in the cylinder head. The fluid domain geometry generated for this simulation is shown in Figures 9-8 to 9-10. The geometry for the valves, piston face, and the bottom surface of the cylinder head that is exposed to the combustion chamber were reproduced using technical drawings provided by Omnitek. The intake and exhaust passages of the cylinder head are rough estimates of the actual casting inspired by hand measurements taken of the provided cylinder head

chunk shown in Figure 9-1. In the absence of a model from the manufacturer for this complex geometry, lofted profiles between the cross-sections of the start and end of the passage were deemed sufficient starting points. An expanded foam casting of the intake passage of the sawn sample cylinder head was made and subsequently scanned using the engineering college's blue light 3D scanner. The 3D model produced by the scan is shown in Figure 9-11. Incorporation of this geometry and a similar exercise for the exhaust side of the cylinder head remains a potential activity in the future to improve the fidelity of the model.

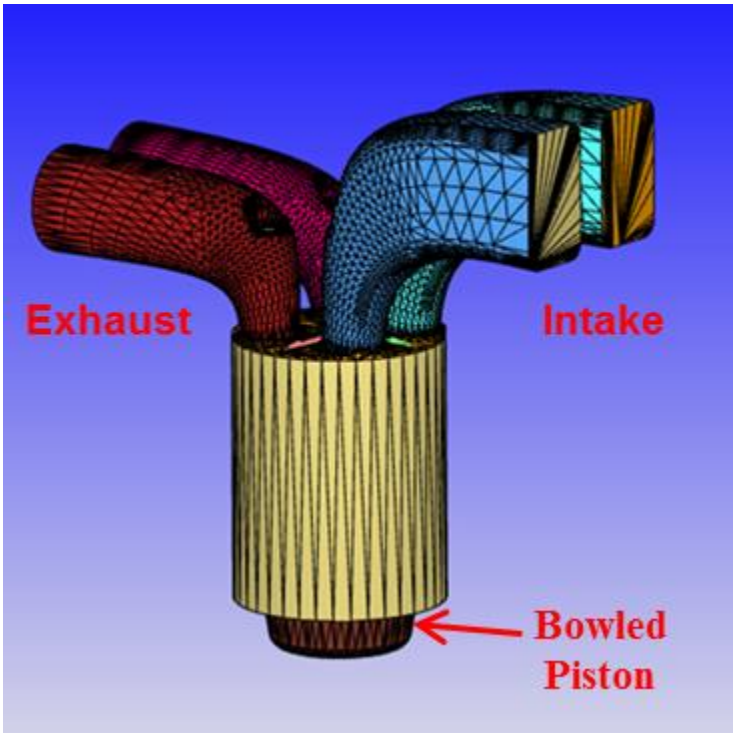

Figure 9-8 The geometry used for the single-cylinder engine model captured being viewed in the CFD preprocessor software (shown with the piston at bottom dead center)

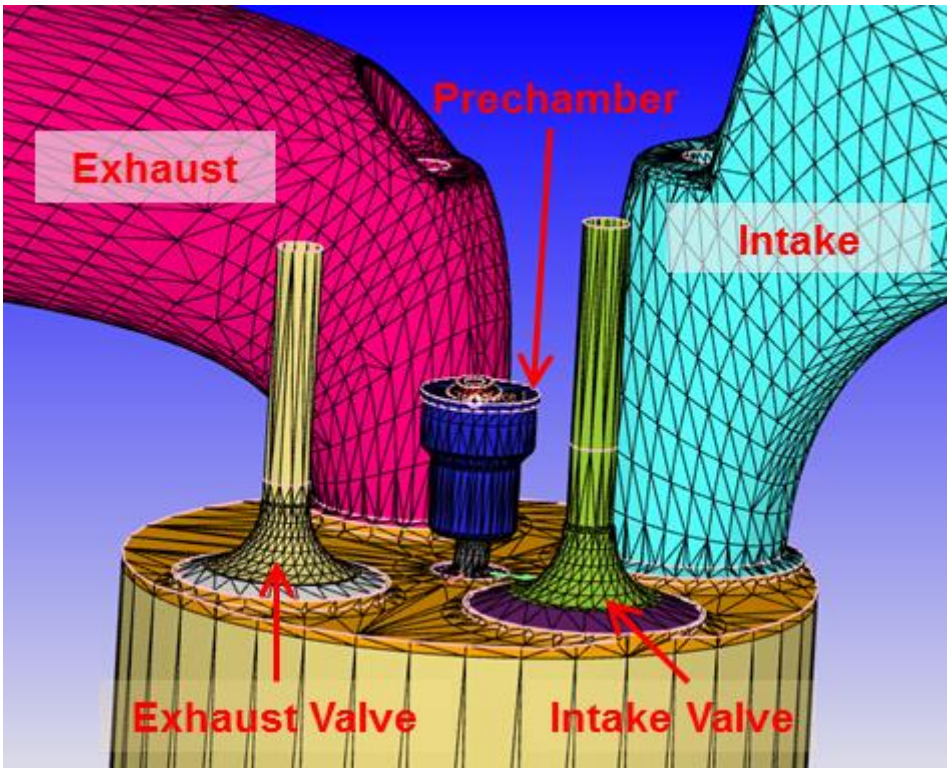

Figure 9-9 A view with one of the intake and exhaust passages each removed to reveal the geometry of an intake and exhaust valve as well as the centrally located pre-chamber

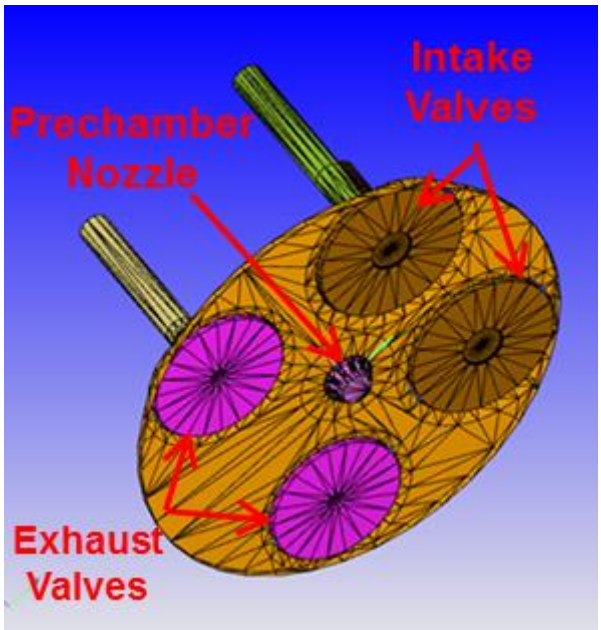

Figure 9-10 A view with the cylinder wall removed showing the increased detail of the top of the combustion chamber

Figure 9-11 Scan results of the positive body casting of the intake port made from the sample cylinder head pictured in Figure 9-1

The simulation is capable of simulating full four-stroke cycles. Valve timing and lift profiles were measured by Omnitek on an assembled engine using a dial indicator placed on the intake and exhaust valve rockers while the engine was turned over by hand in increments of two crank angle degrees at a time. This setup is shown in the photographs of Figure 9-12. Since the dial gages did not directly measure valve lift at their placed locations, the readings they produced were normalized and then scaled to the maximum valve lift of each valve type, which was taken from a Detroit Diesel service manual for the engine. The resulting valve lift profiles are shown in Figure 9-13 and are what is used in the engine simulation.

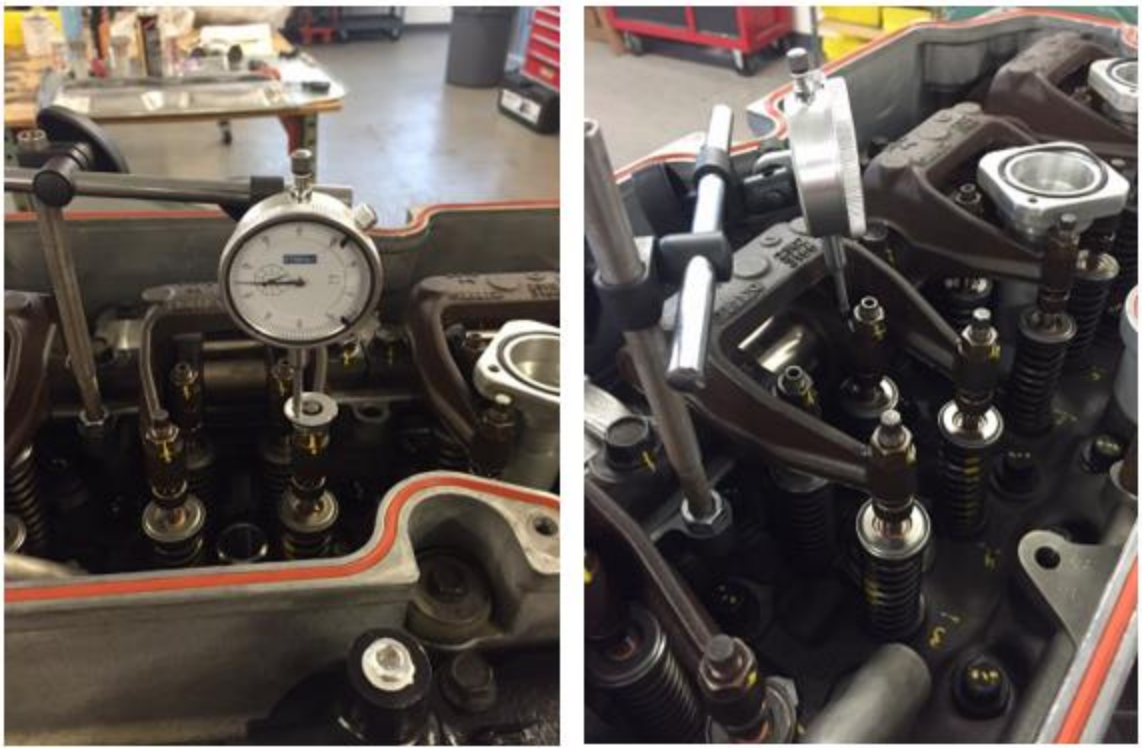

Figure 9-12 Photographs of the gauging setup used to measure the intake (left) and exhaust (right) valve lift profiles

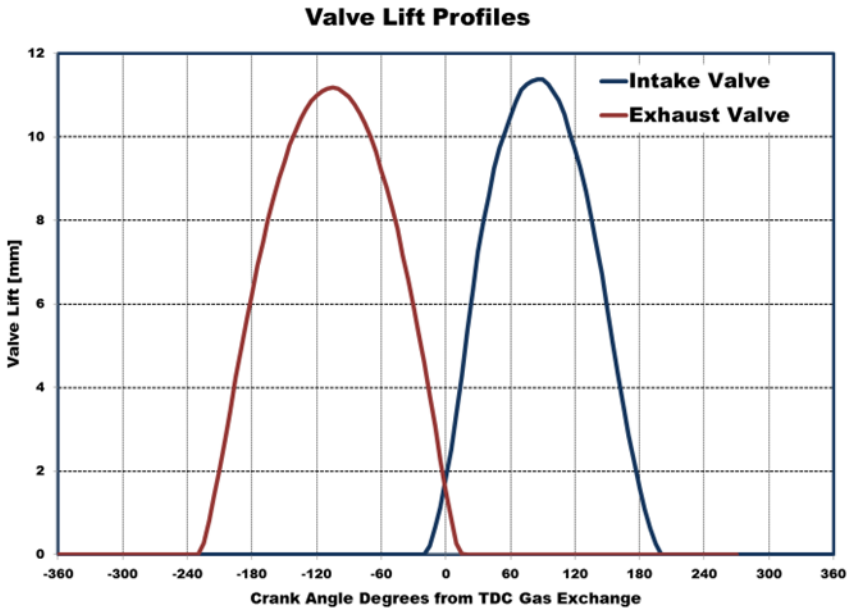

Figure 9-13 The valve lift profiles used in the engine simulation (only the intake lift was required for the simulation presented)

9.3 The Pre-chamber Geometries Evaluated

A total of 13 TJI geometries were generated for the performed simulations. These geometries are summarized in Table 9-1 and Figures 9-14 to 9-16. All of the dimensions given in the figures are in mm. Each geometry is referred to as a case, numbered in the order they were generated. In the figures documenting the results of the simulations, cases will be referenced using C1 for Case 1 and so on. Cases 9 and 10 were concepts that were created but never run. As such, they are not included in the table or subsequent results. Specification of their omission is made only to explain the gap in the case numbering instead of relabeling the higher-numbered cases.

Table 9-1 Summary of TJI geometries generated for CFD analysis

Simulation	Throat Diameter [mm]	Breather Hole	Notes
Case 1	4.0	No	
Case 2	8.0	No	
Case 3	8.0	Yes	
Case 4	See Notes	No	Throat converges to a diameter of 2.5 mm before diverging back to 8.0 mm
Case 5	6.0	No	
Case 6	6.0	Yes	
Case 7	5.0	No	
Case 8	See Notes	No	Throat is slanted 20° from vertical, for a 5.0 mm horizontal diameter at the top of the neck flare, a diameter of 4.7 mm results
Case 11	5.5	No	
Case 12	5.5	No	Same as Case 11 but with the lower pre-chamber geometry simplified to a single drilled bore
Case 13	5.5	No	Same as Case 12 but with the exterior of the nozzle modified to maintain orifice centerline lengths of 3.0 mm
Case 14	5.5	No	Geometry is identical to case 12, except a small fueling passage is added
Case 15	5.5	No	Geometry is identical to case 12, except a full fueling passage is added

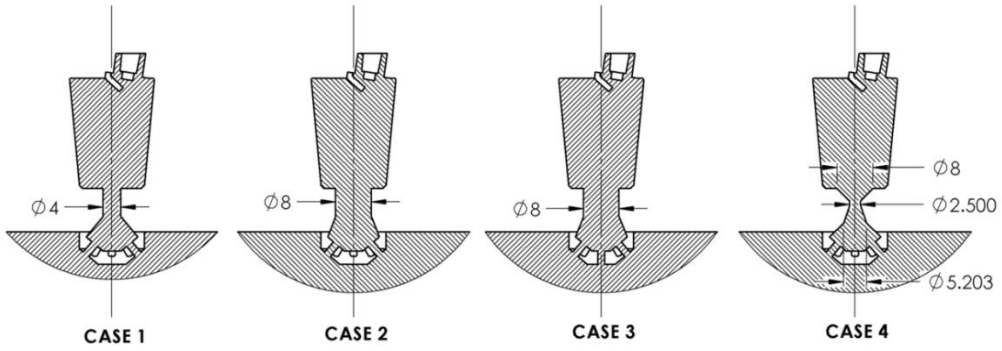

Figure 9-14 Cross-sections of pre-chamber geometries for simulation cases 1-4 (case 3 has a breather hole, and case 4 has a converging and diverging throat)

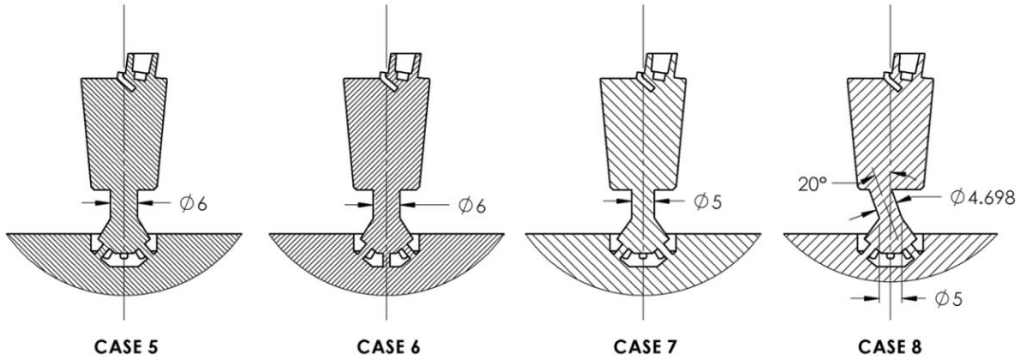

Figure 9-15 Cross-sections of the pre-chamber geometries of cases 5-8 (case 6 has a breather hole, and case 8 has a slanted throat)

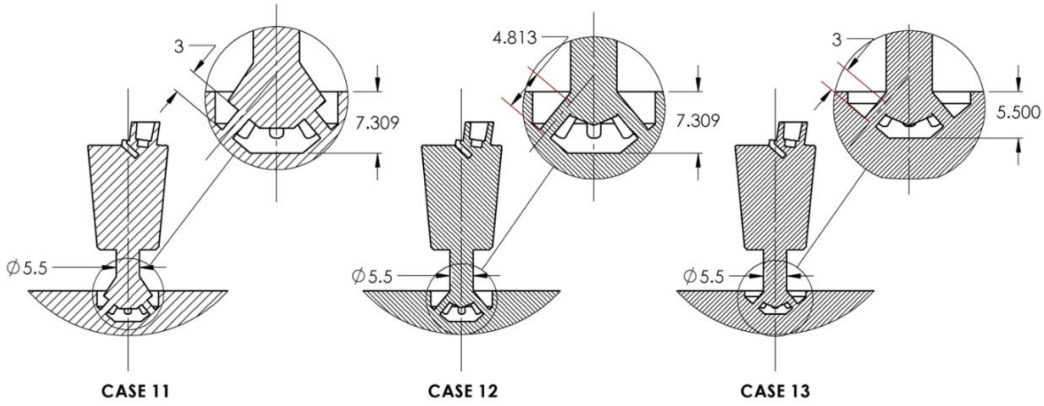

Figure 9-16 Cross-sections of the pre-chamber and nozzle geometries used in cases 11-13 (cases 12 and 13 include simplifications to the neck and nozzle interior targeting manufacturing, note case 12 has longer orifice passages than the rest of the cases)

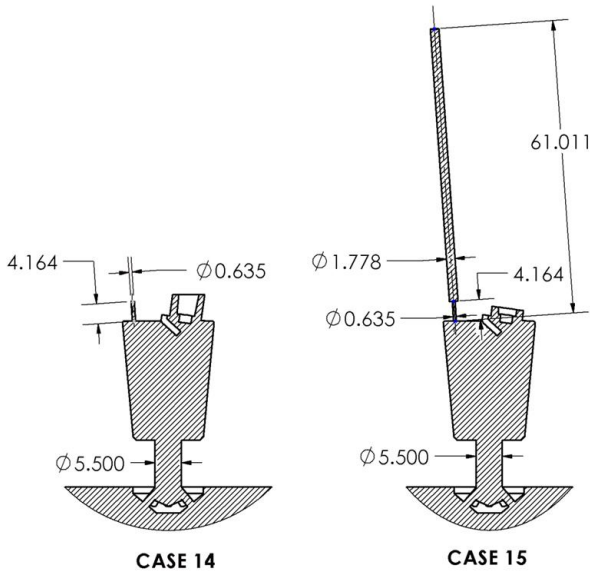

Figure 9-17 Geometries with auxiliary fuel passages included, only the simplified case, case 14, was simulated

The simulated cases fall into one of five groups. The first group examines the effects of the diameter of the pre-chamber throat on the mixing performance and pressure differential between the main and pre-chambers for pre-chambers with cylindrical throats that follow the centerline of the pre-chamber. This comparison utilizes cases 1, 2, 5, 7, and 11, all of which have the eight-orifice configuration and axisymmetric throat geometry. The second group of simulations examines the effects of adding the ninth breather hole orifice to the nozzle. Two cases, numbers 3 and 6, were designed to be compared to cases 2 and 5, respectively, to observe the effect of the breather hole. The third group of simulations compares the simple cylindrical throat utilized in the majority of the cases to that of a converging and diverging throat, case 4, and a geometry with a throat that is slanted at an angle to the centerline of the pre-chamber which passes into one side of the upper pre-chamber rather than its center, case 8. These two cases are compared to case 11.

The fourth group of simulations, which includes cases 11, 12, and 13, was generated with the concerns of pre-chamber fabrication in mind. In all of the cases before and including case 11, the

lower pre-chamber expands out to a larger diameter, the flare labeled in Figure 9-3, creating a relatively complicated shape to machine. Cases 12 and 13 simplify this geometry to that of a blindly drilled bore using a drill with a 135° tip. The purpose of these cases was to determine if these modifications adversely affected the function of the pre-chamber observed in case 11. The only difference between cases 12 and 13 is their exterior nozzle surfaces. In case 12, the nozzle exterior is the same as the previous cases run before it with the flare in the lower pre-chamber removed. The elimination of the flare results in orifices that are longer than 3 mm, which is the length common among all the other cases, which is why this case is referred to as the long orifice case in the figures below. Case 13 addresses this by bringing the exterior surface of the TJI nozzle closer to the pre-chamber centerline resulting in orifices that are 3 mm long over their centerlines. Thus, the protrusion of the nozzle into the main chamber is less for case 13 than in the other cases.

The fifth group of cases, 14 and 15, was generated to support the incorporation of the process of finite-duration fuel injection into the simulations. Case 14 is a simplified scenario. It does not include the long narrow passage through which auxiliary fuel must pass to reach the pre-chamber. The utility of this case is that it could be run quickly without a significant computational burden. Case 15 adds the complication of the long passage the fuel must pass through to reach the pre-chamber from the top of the TJI assembly. Case 15 was not successfully run. It is included here to show direction for potential future work. This setup challenged the Converge solver that was available at the time when this work was performed due to the inclusion of features with a great disparity in size[1]. In this case, the long narrow passage requires a grid much finer than the rest of

[1] This issue effected simulations for large heavy-duty diesel engine selective catalytic reduction systems that the author has had experience attempting to simulate with the software. In these systems, very large volumes are found adjacent to regions that contain mixing components which include many small features, perforated plates or guiding vanes as an example. Convergent was

the simulation domain to resolve the flow within it. This was an issue when the domain was decomposed for parallel processing as its algorithm could not effectively distribute areas with highly refined meshes, thus eliminating the advantage of parallel processing. This is because the domain breakdown was limited to dimensions twice that of the base grid dimension used in the discretization, which traps groups of cells in highly refined areas together on the same processor. Thus, the progress of the computation is always dependent on one or two highly loaded processors that receive these heavily refined blocks[2].

9.4 Simulation Results for the Simplified Mixing Experiments

In the figures that follow, the following data is presented. For each group of simulations, contour plots of local λ within the pre-chamber at various crank positions are displayed. The data displayed in these plots is taken from and displayed on a plane in which the cylinder, pre-chamber, and spark plug's centerlines lie. While the simulations contain λ values between 0 and 2, the color bar for these figures is limited to a range of 0.75 to 1.6 to provide contrast to the regions within the flammability limits of methane/air mixtures. Data is also given on the pressure differential or drop generated by the various geometries simulated. These pressure differentials are calculated by measuring the difference between the pressures in one of the three locations shown in Figure 9-18. The total pressure drop displayed below is the difference between the pressure measured within the main chamber and the pressure within the upper pre-chamber. The pressure drop attributed to the throat is the difference between the lower pre-chamber and upper pre-chamber pressures.

---

aware of this issue for these types of systems and versions 3 and above of the software include improved parallelization methods.

[2] More complicated analysis can be done for each specific case where there is a large disparity in feature sizes in order to optimize the computational speed of the simulations for a given number of processors. If overall processor count is not an issue, then a good rule of thumb is to size the base grid small enough that the smallest features can be resolved using three levels of refinement. The penalty of increasing the overall cell count can then be addressed by using more processors.

Finally, the mean λ of the mixture within a small sphere located at the spark electrode is also measured for the simulations to help further evaluate the mixing qualities displayed in the contour plots that are provided.

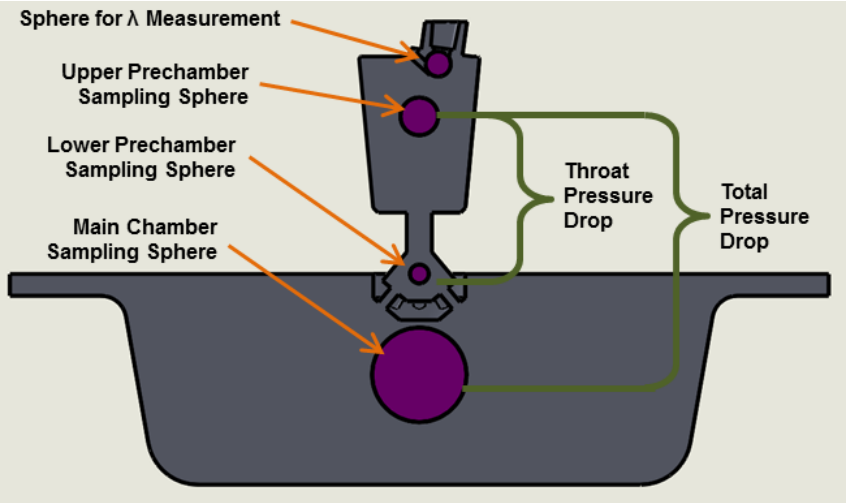

Figure 9-18 Pressure and λ sampling locations on the cross-section of the simulation's fluid domain with the piston approaching top dead center

Evaluation of Throat Diameter and Shape

Figure 9-18 shows contour plots of λ for cases 1, 7, 11, 5, and 2. These images demonstrate the ability of each design to mix the mapped methane region placed in the pre-chamber with the incoming λ = 2 mixture that is being forced in by the compressing piston. In general, the cases that show larger areas of blue-green, indicative of mixtures near λ = 1 earlier in the process, are the better performers. With that in mind, cases 7 and 11 generate the best mixing as they both possess the largest green swaths around the spark electrodes, where initial mixing is the most important, at around 30° before top dead center, which may be close to the eventual spark timing for the engine. It is also important to emphasize that the results displayed for the cases shown in Figure 9-19 should not be analyzed independently since they are produced from a contrived scenario but need to instead be evaluated in mutual comparison.

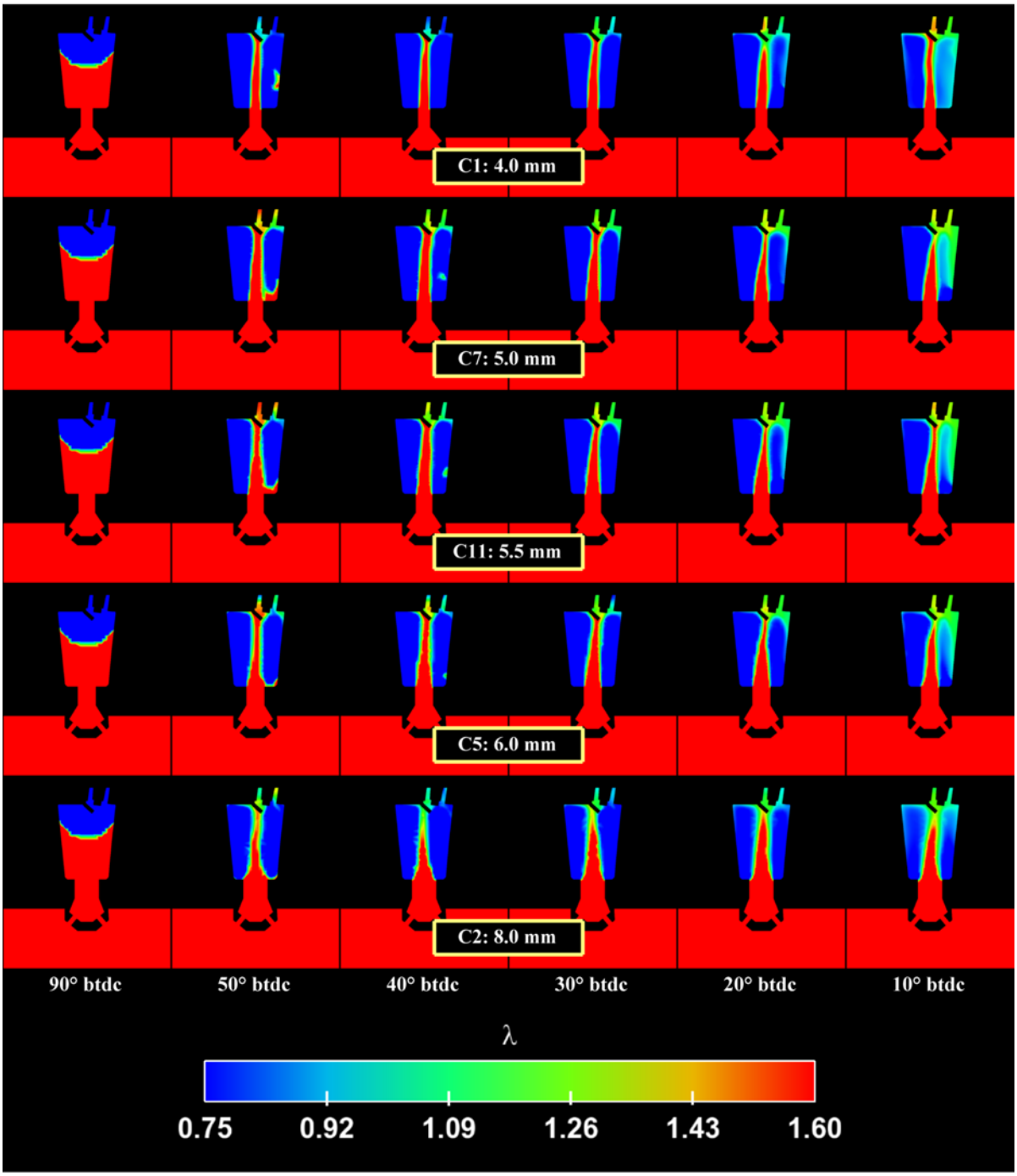

Figure 9-19 Comparison of the effects of pre-chamber throat diameter on mixing in the pre-chamber showing λ (cases 1, 2, 5, 7, and 11)

In Figure 9-20, the average value of λ in the sphere designated in Figure 9-18 around the pre-chamber's spark electrodes is plotted against the engine's crank position. The metric of

performance evaluated for the cases in this plot is whether or not the design achieves a steady value quickly and how wide this steady region is centered around 30 ° before top dead center. Because of the simplifications used in the setup, the final value of λ isn't as meaningful compared to how quickly and steadily a case maintains its final mixed value. From this plot, the geometries used in cases 7, 5, and 11 all have similar performance. They reach near to their final value quickly and remain steadily there for an extended duration. Case 1, the geometry with the smallest neck diameter, also increases quickly, and does not produce a great deal of oscillation. Case 1 may in fact exhibit the best mixing performance of the cases examined since the λ value around the spark plug electrodes follows the trend of the overall mixture ratio of the pre-chamber, which by virtue of the fuel mapping scheme used should be unity at 30°, less than unity prior to 30°, and greater than unity after. In general, all of the cases exhibit an upward slope for λ, which should be expected as inflow from the main chamber is a diluted mixture of λ = 2. Cases 2 and 5 have the largest neck diameters. Both of these cases have slower responses and exhibit larger fluctuations around the spark plug as the piston moves through the region when the spark is likely to be fired, which is undesirable.

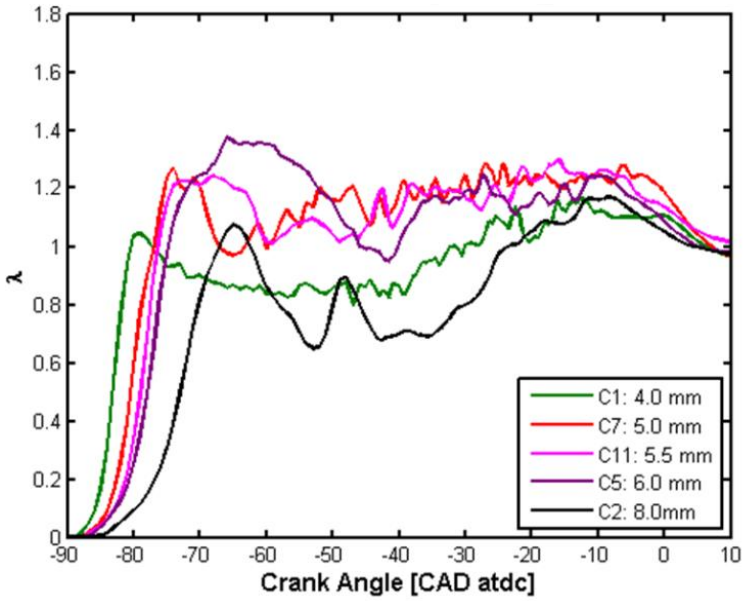

Figure 9-20 A plot of the volume-averaged value of λ within the sphere around the spark plug electrodes is shown in Figure 9-18

The two plots displayed in Figure 9-21 display pressure data measured within the sampling spheres shown in Figure 9-18. The plot on the left side of the figure shows the overall pressure drop experienced by gases traveling from the main chamber of the engine all the way to the upper section of the pre-chamber as a function of crank angle. The plot on the right gives the fraction of this total pressure drop that occurs moving from inside the nozzle of the pre-chamber through the pre-chamber throat to the upper portion of the chamber. The trends of the overall pressure drop and the share of the drop belonging to the passage through the throat follow expectations, with both drops increasing in magnitude as the diameter of the throat is reduced. It is desirable to have the bulk of the pressure loss of the incoming or outgoing flows in the pre-chamber occur at the nozzle orifices as they are what produce the turbulent jets. Also important from a scavenging perspective is to have the pressure drop be low enough that the pre-chamber is not too difficult to fill or purge. Thus, it is desirable for the throat to have a low share of the overall pressure drop, yielding smaller overall pressure drops. Of the cases presented, Case 4 is the only case that shows

a significant throat pressure drop.

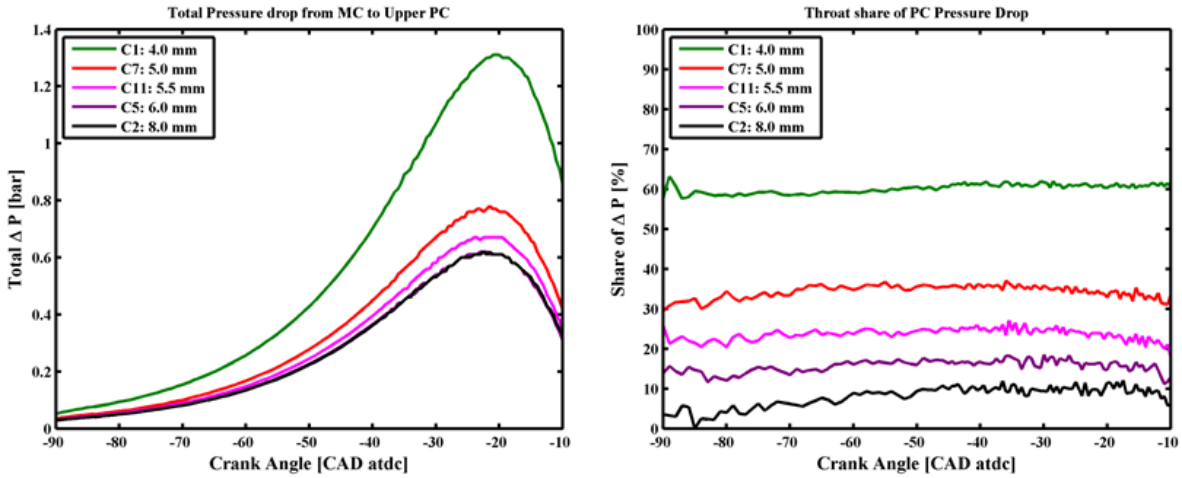

Figure 9-21 Pressure drops of the throat configurations, total pressure drop from the main chamber to the upper pre-chamber (left), and the share of the total pressure drop attributed to the throat section of the pre-chamber

As the chronological numbering of the test cases should suggest, the results of cases 1, 2, 5, and 7 directed to the creation of case 11, which has a 5.5 mm throat diameter. This is the throat diameter that has been suggested for initial designs of the TJI pre-chamber for physical testing. It demonstrates good mixing in the simulations while not generating too large of pressure loss for the incoming and eventually outgoing flows.

Evaluation of the Breather Hole

As mentioned above in the section describing the geometries of the various cases presented, a second nozzle orifice configuration utilizing nine holes, one of which was located on the bottom face of the nozzle and referred to as a breather hole, was included in some of the cases. The purpose of the breather hole is to assist with mixing in the pre-chamber with the idea that the vertical hole provides a simpler more direct path for gas being forced upwards by the compressing piston to enter the pre-chamber. Two cases were run using the breather hole orifice configuration, cases 3 and 6. They are compared to their regular eight orifice counterparts, cases 2 and 5, in Figure 9-22. The pressure drops of these four cases are also compared in Figure 9-23, with the overall pressure

drop shown on the left of the figure and the magnitude of the pressure drop across the nozzle orifices on the right. The contour plots do not suggest that there is any advantage of having the ninth hole included for mixing. Also, it is not surprising that the plots indicate that keeping the total cross-sectional orifice area equivalent between the eight and nine orifice configurations leads to higher pressure loss when the nine slightly smaller orifice diameters are used. The conclusion drawn from these cases has been that the breather hole doesn't provide any useful contribution to mixing within the pre-chamber and should not be included in future designs.

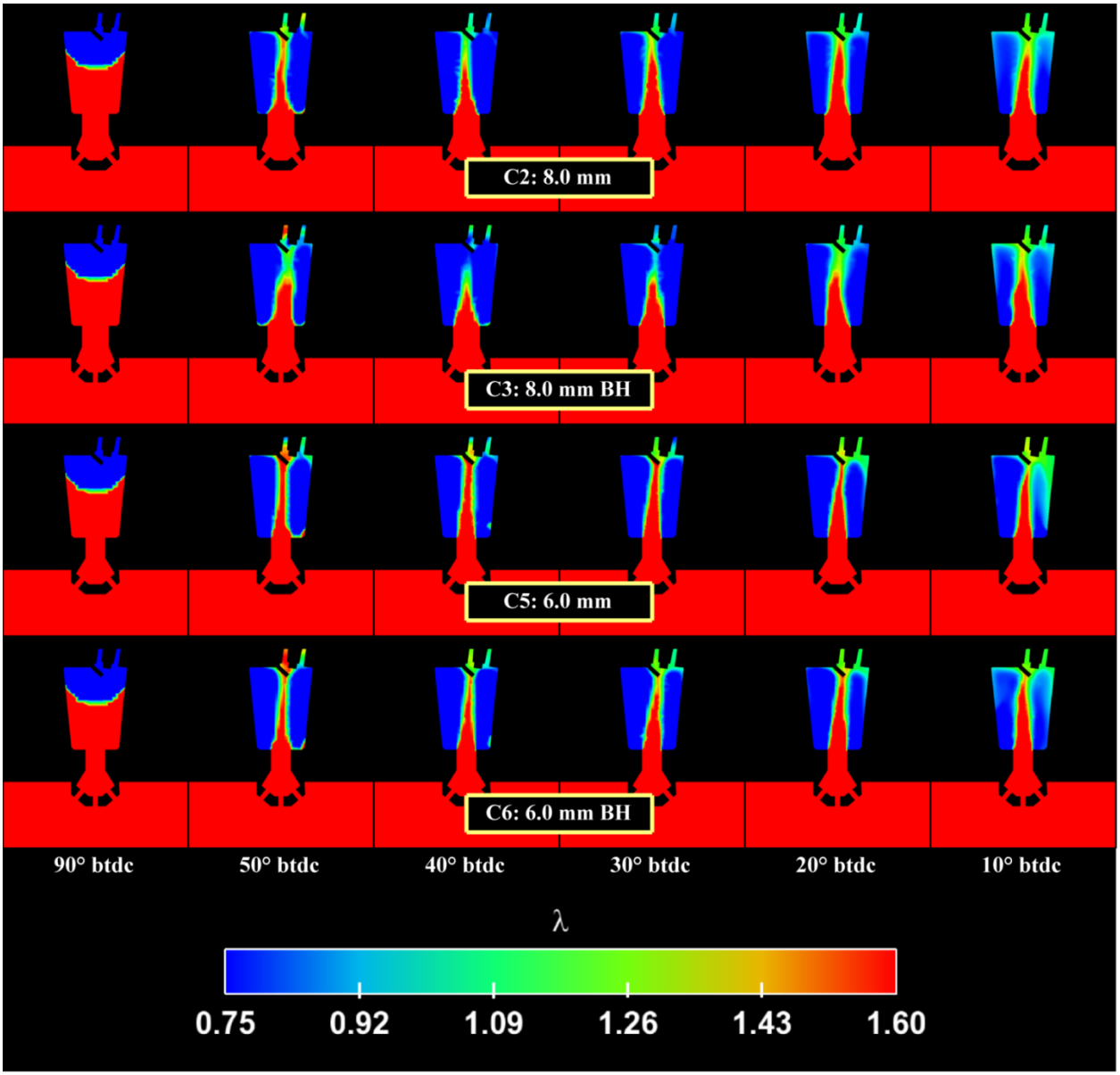

Figure 9-22 Contours of λ shown to compare the mixing performance of breather (cases 3 and 6) and non-breather hole (cases 2 and 5) nozzle orifice configurations

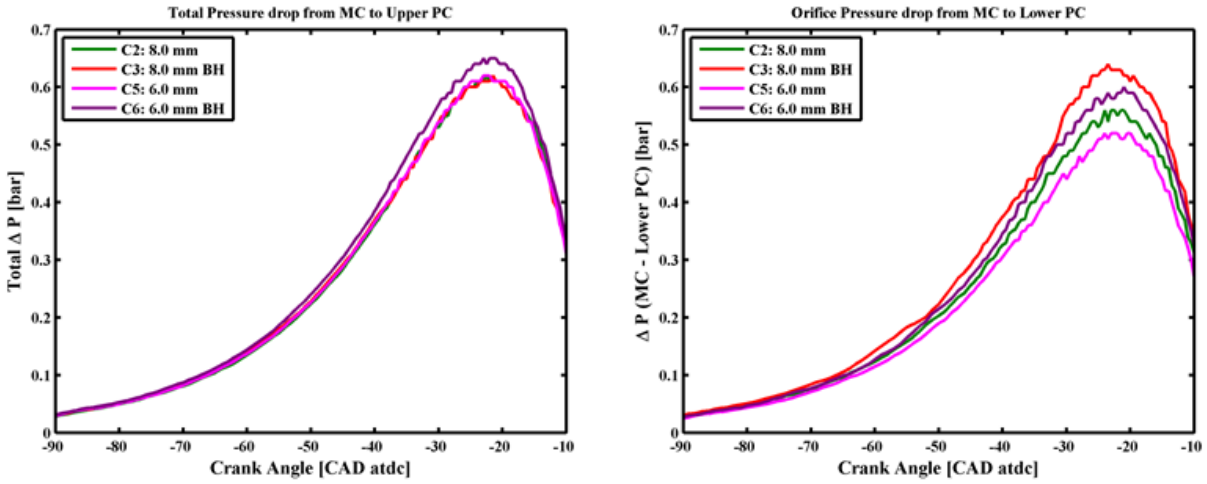

Figure 9-23 Pressure drops for breather (BH) and no-breather hole configurations, total pressure drops from the main chamber to the upper pre-chamber (left) and pressure drop across the nozzle orifices (right)

Evaluation of Alternative Throat Geometry

Two cases were also run with throats that were not simple constant radius cylinders. Case 4 was run using a converging and then diverging axisymmetric profile for the throat with the idea that it might improve mixing. Case 8 was run to see what happens when the incoming jet from the throat into the upper pre-chamber is directed to one side of the upper pre-chamber. Contour plots generated from these two nonstandard cases along with a regular case, case 11, for direct comparison are given in Figure 9-24. Pressure drops from the main chamber to the upper pre-chamber are shown in Figure 9-25. The results in the two figures demonstrate that the throat in case 4 is too restrictive and mixes poorly. Case 8 is a forebearer of potential design modifications to the throat if higher fidelity simulations in the future that include auxiliary gas injection demonstrate that there is a stratification of fuel to one side of the pre-chamber. Here, case 8 is slanted towards the injection side of the upper pre-chamber. The slant is disadvantageous in this contrived fueling scenario with methane equally distributed to both sides of the chamber. It is included to evaluate its effect on pressure drop where it shows only a slight increase over the

straight-throated case, and this increase is likely a result of the smaller diameter of the throat (4.7 mm to 5.5 mm) required to package the slant into the available space in the injector cavity.

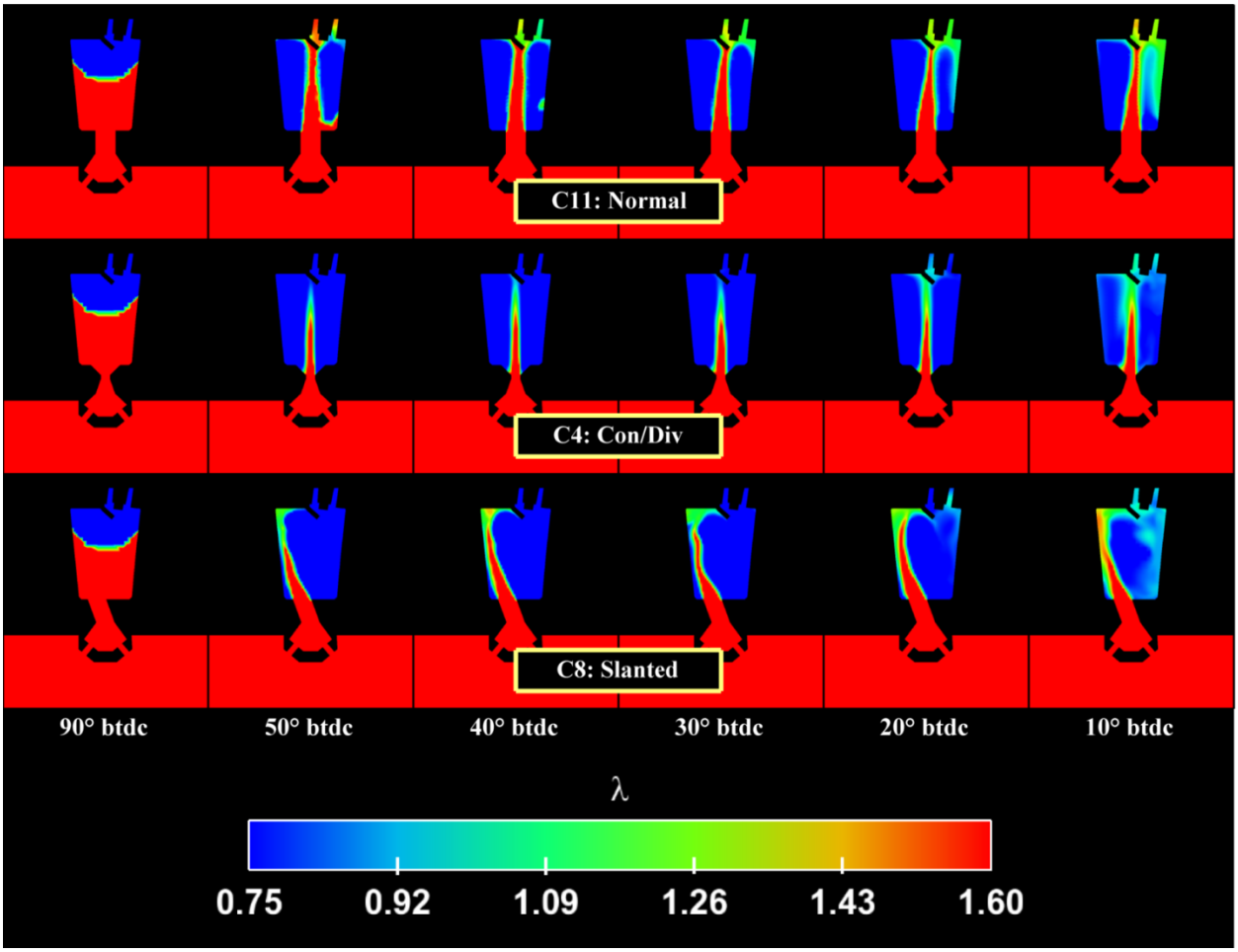

Figure 9-24 Contours of λ comparing the mixing performance of the non-standard throat geometries (case 11 having a standard straight throat; case 4, a converging and diverging throat: and case 8, a throat slanted in the direction of the fueling port)

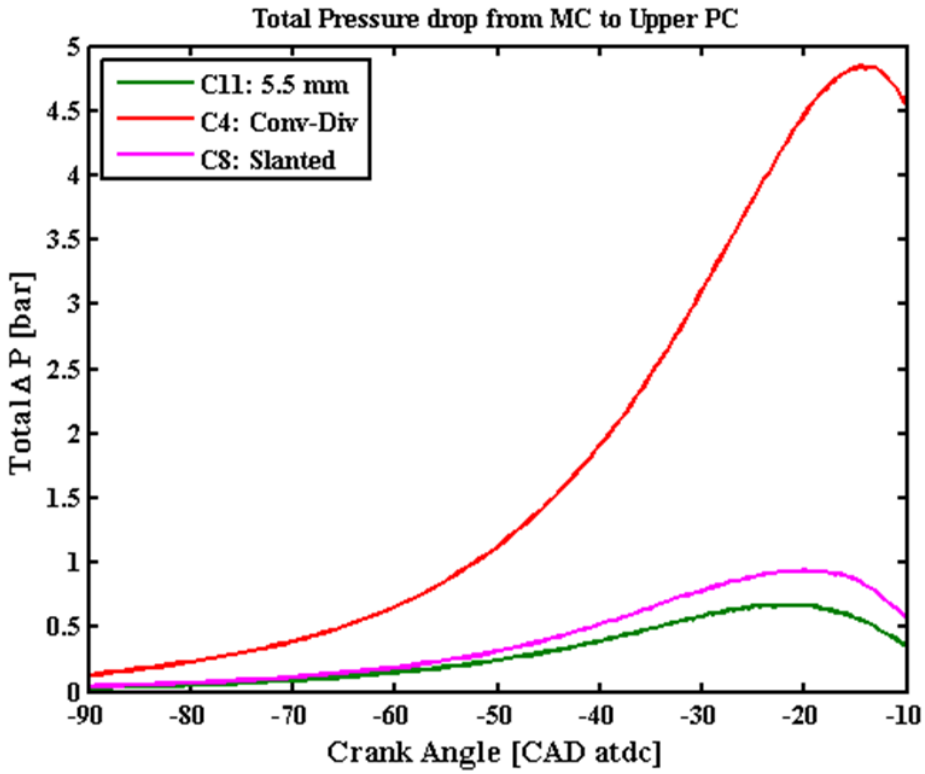

Figure 9-25 Pressure drops for the non-standard throat configurations (cases 4 and 8) compared to a normal straight throat (case 11)

Lower Pre-chamber Simplification for Manufacturing Considerations

As the chronological nature of the case numbering indicates along with the results of the group comparisons provided in the previous subsections, the 5.5 mm diameter throat was selected to be the basis for the first physical prototype for the project. With the real prospect of fabricating pre-chambers based on case 11 in mind, two more cases were simulated to determine if the design of the lower pre-chamber near the nozzle could be simplified to make manufacturing of the TJI pre-chamber simpler. The two new cases, numbers 12 and 13, replace the flare from the throat to the nozzle cavity, which would require a multi-component assembly that would have to be welded together, with a simple drilled bore. Results of these simulations compared to the case 11 design, which includes the original complicated flare design, are shown in the λ contour plots given in Figure 9-26. These results indicate that simplifying the geometry does not generate any ill effects

on the mixing performance of the designs.

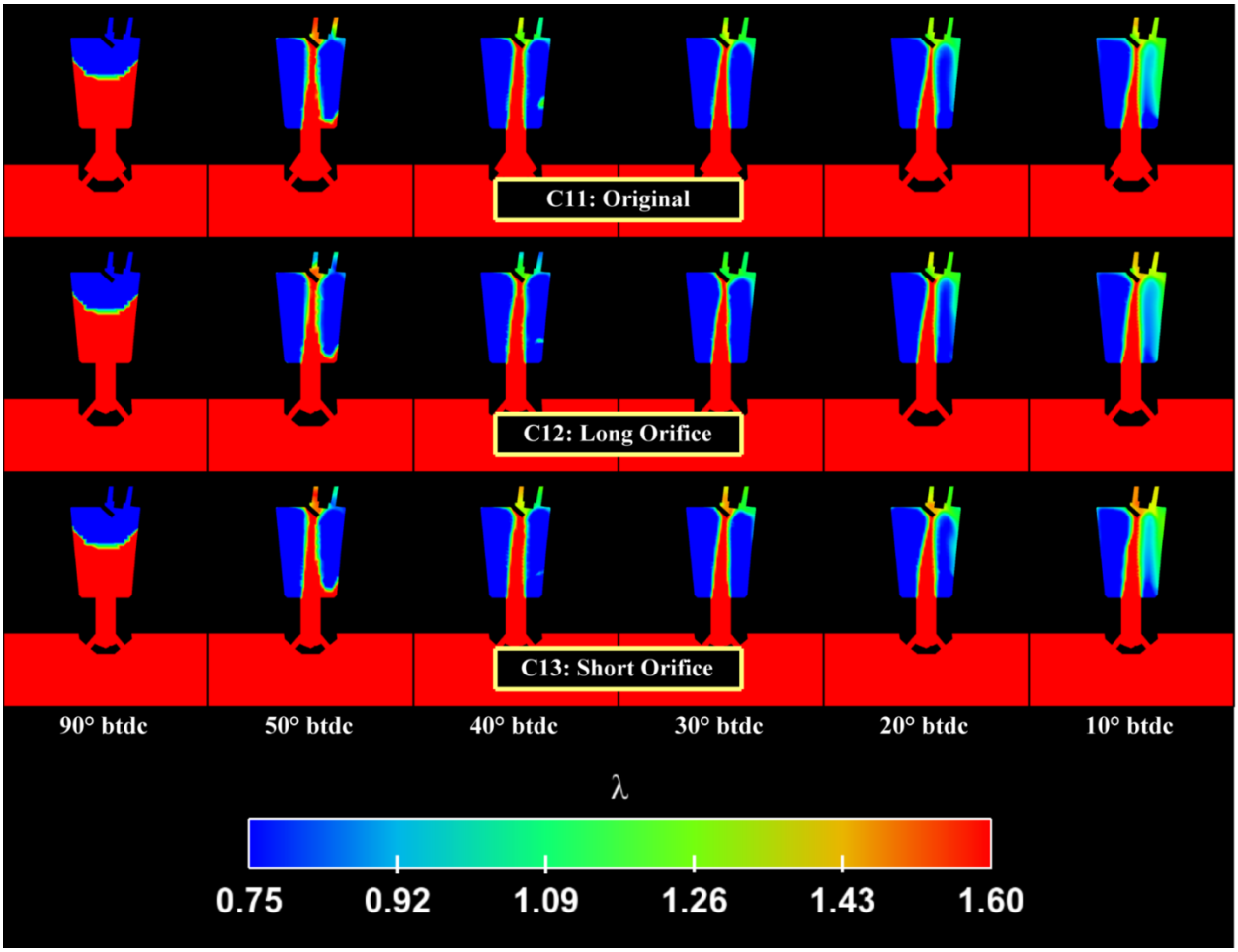

Figure 9-26 Contours of λ comparing the mixing performance of the 5.5 mm throat diameter cases that include modifications to simplify manufacturing

Also, of interest is whether the simplification alters the pressure losses experienced by gases being forced into the upper chamber. Figure 9-27 shows these pressure results and demonstrates that the simpler designs perform better without the flare. This figure also demonstrates that the effects of the orifice length on the pressure drop are insignificant. This set of simulations indicates that the design simplifications should be incorporated into the initial physical prototypes of the TJI system

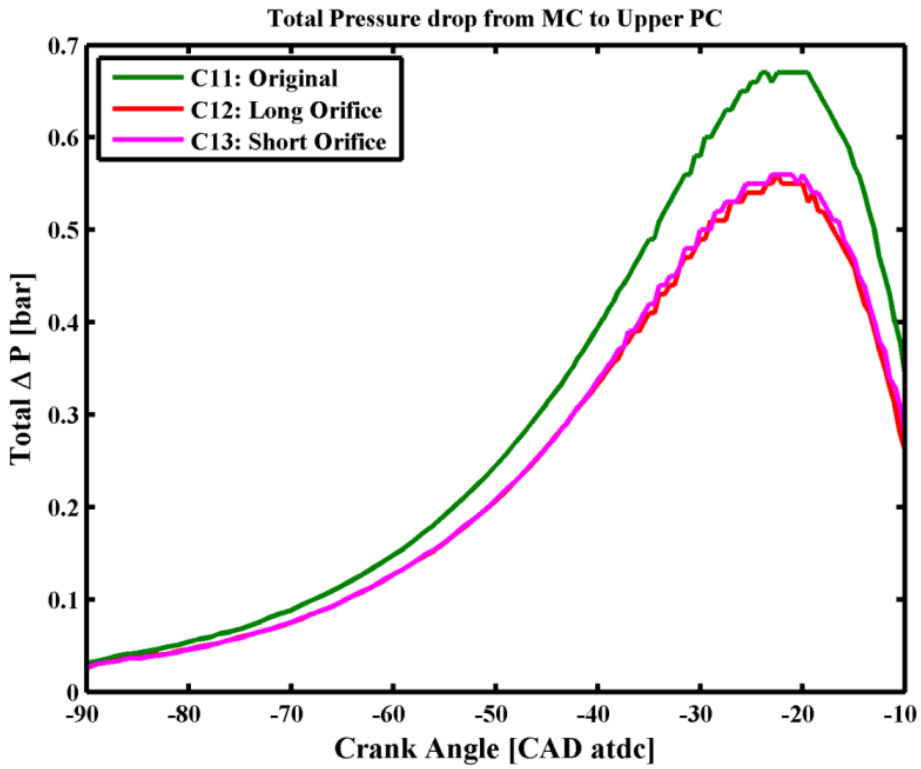

Figure 9-27 The total pressure drop from the main chamber to the upper pre-chamber for the 5.5 mm diameter throat cases (11-13)

9.5 Pre-chamber Fuel Injection Results

Case 14 was set up and run to explore methods for simulating the addition of fuel into the pre-chamber through the TJI's auxiliary fuel passage. Results from case 14, which has a truncated passageway, are shown in Figure 9-28. In this case, the top of the small fuel passage is set as an inflow boundary held at an elevated pressure (well above what is expected to be provided by the fuel system). In the simulation, the passage is disconnected from the rest of the domain until 90° before top dead center at which point pure methane is allowed to flow out of the passage until 30° before top dead center. With such a high pressure, the flow rate of methane is very high, and the pre-chamber fills with methane very quickly. This is why only the first 14° of the injection is shown, as after this point, nothing discernable can be seen in the very rich pre-chamber mixture that is present until top dead center is reached, which is too late for the spark. The purpose of case

15 was to add more complete detail of the geometry that the auxiliary fuel must pass through. As stated above, this more complicated case has been left as a potential area for future work. At the time that these simulations were created, information about the fuel system was not available. Experimental data and specifications for a realistic fuel system will add additional fidelity to these simulations. At this point, however, the simulation of case 14 is limited to confirming what should be intuitive based on the design of the TJI system, which is that fuel addition will not be a symmetric process. It is this prospect that generated interest in the slanted throat case examined above. If further numeric investigations are continued in the future, refinement of this simulation is suggested to allow for more accurate pre-chamber mixing simulations.

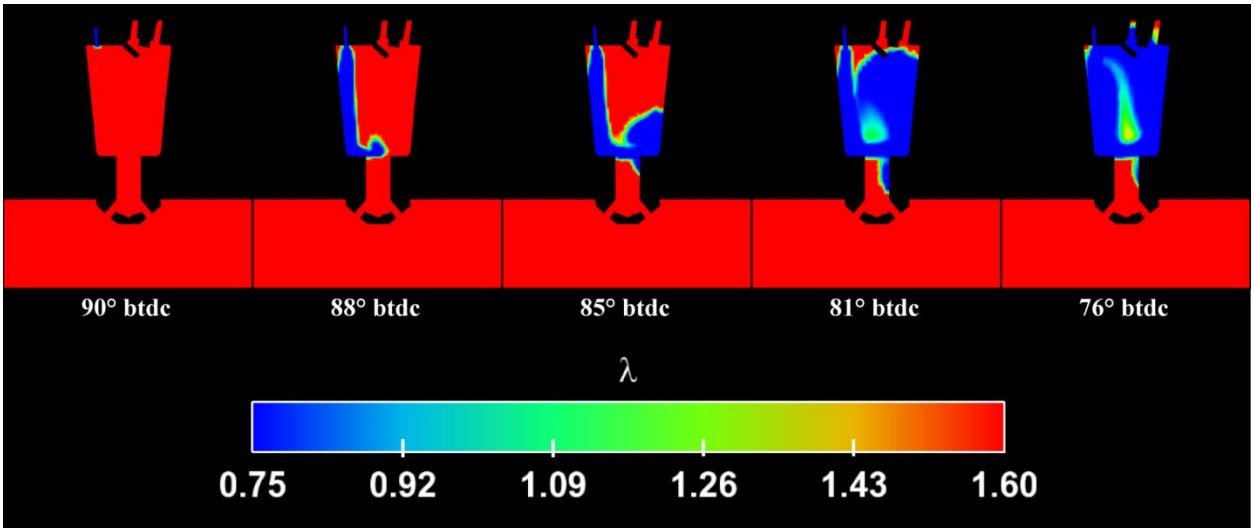

Figure 9-28 Contours of λ for the simplified simulation with methane auxiliary fuel injection (case 14)

9.6 Results for Initial Engine Simulation

Results from a run of the CFD engine model are provided in this section to demonstrate its functionality. Much like the simulation with auxiliary fueling, the work has been done to set up the simulation framework, and it has been left as future work to improve its fidelity and utilize it as a tool to evaluate or understand the behavior of proposed TJI systems for the engine. The pre-chamber included in this simulation is identical to that of case 8, but its nozzle has 12 equally

spaced orifices. The results shown here are for the engine running at 1800 rpm. The model was initialized 15 crank angle degrees prior to top dead center of the gas exchange. At the start of the simulation, the fluid everywhere was quiescent. Mixture composition and temperatures varied depending on region at initialization. In the intake passages, the composition and temperature matched those of the inlet boundary conditions. In the exhaust and combustion chambers, the mixture composition was that of a completely burned mixture of air and methane with $\lambda = 2.0$ at 1200K and at the pressure specified at the exhaust outlet boundaries. The inlet boundaries of the model have a specified pressure applied at them of 305 kPa absolute. The composition of the fluid that crossed this boundary was a methane and air mixture of $\lambda = 2.0$ and a temperature of 400 K. The inlet pressure and temperature were elevated from atmospheric conditions because the engine is turbocharged. A pressure of 104 kPa absolute was specified on the exhaust outlet boundaries of the model to provide some exhaust system backpressure.

Intake and Compression

Figure 9-29 shows the velocity contours of the flow field a short time after the simulation was initialized, which is at the tail end of the exhaust stroke. The plane in this figure and the next cuts through the simulation domain along the center axis of the exhaust valve. The timing of this figure is within the valve overlap of the engine. As the exhaust valve closes, the intake valve begins to open. Figure 9-30 displays velocity contours at a point at the beginning of the intake stroke. In this figure, the exhaust valve is closed and the intake valve begins approaching its maximum lift. Finally, Figure 9-31 shows a plane through the centerline of the piston and pre-chamber axis. This figure is of the velocity contours during the second half of the compression stroke and displays the inflow that is pushed into the pre-chamber during the compression through the orifices in the nozzle.

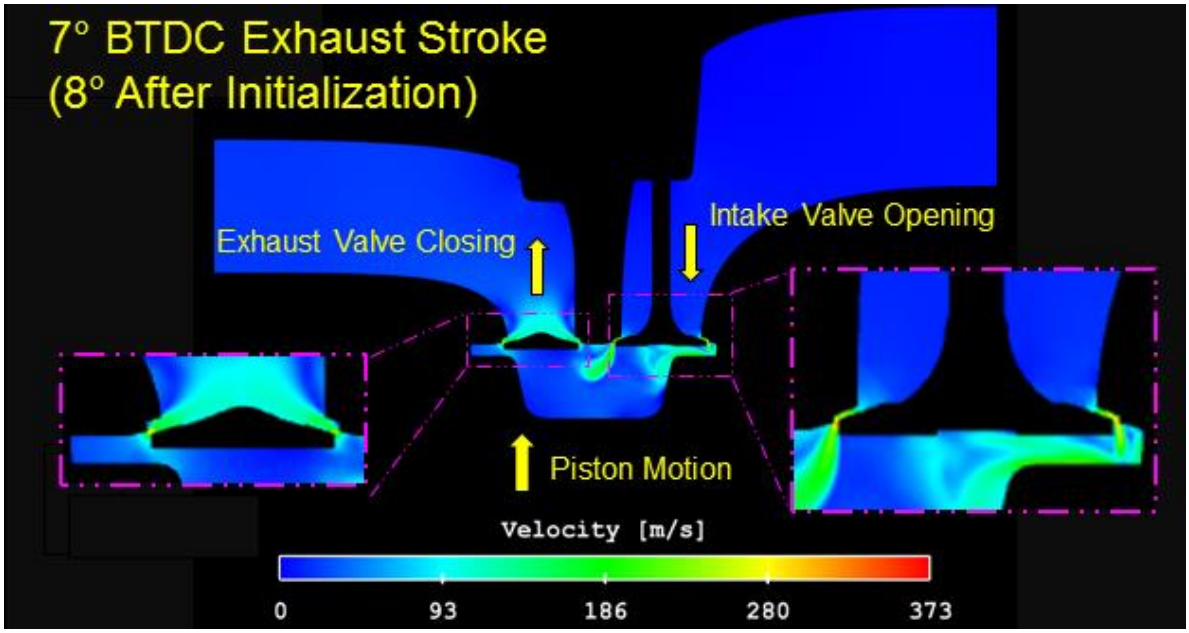

Figure 9-29 Velocity contours on a plane running through the axis of one of the intake valves just after the initialization of the simulation

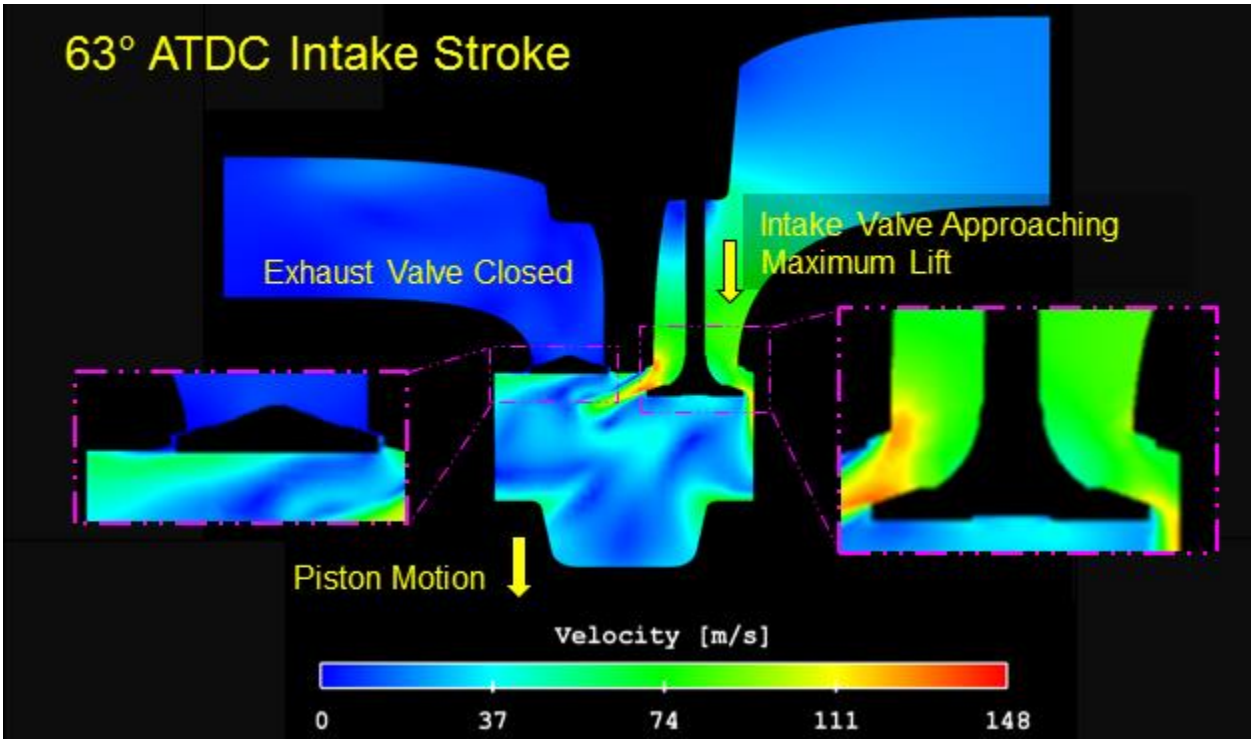

Figure 9-30 Velocity contours on a plane running through the axis of one of the intake valves during the intake stroke

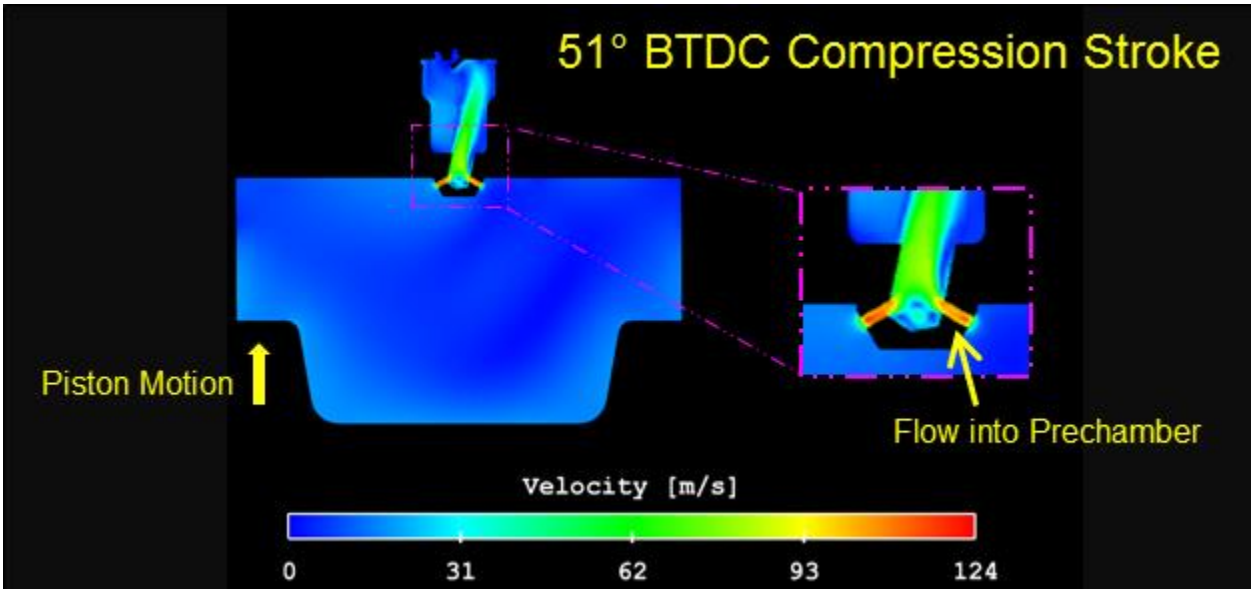

Figure 9-31 Velocity contours on a plane running through the center plane of the cylinder and pre-chamber showing flow into the pre-chamber through the nozzle orifices

Simplified Combustion Modeling

Combustion was modeled with a single reaction step chemistry model, which without doubt does not accurately model the combustion. Pre-chamber fuel stratification was achieved by mapping a stoichiometric mixture into the engine model's pre-chamber at the timing of the spark. Integration of the auxiliary fueling methods discussed above is expected in any potential future work to improve the model over this contrived condition. Plots of the temperature contours taken on the centerline of the combustion chambers are shown in Figure 9-32. These images show the TJI combustion process from spark kernel formation through to the emission of hot jets into the engine's main combustion chamber. Additional visualization of the flame front is given in Figure 9-33. This figure repeats the three times given in Figure 9-32, but displays a temperature iso-surface, representing the approximate location of the propagating flame front.

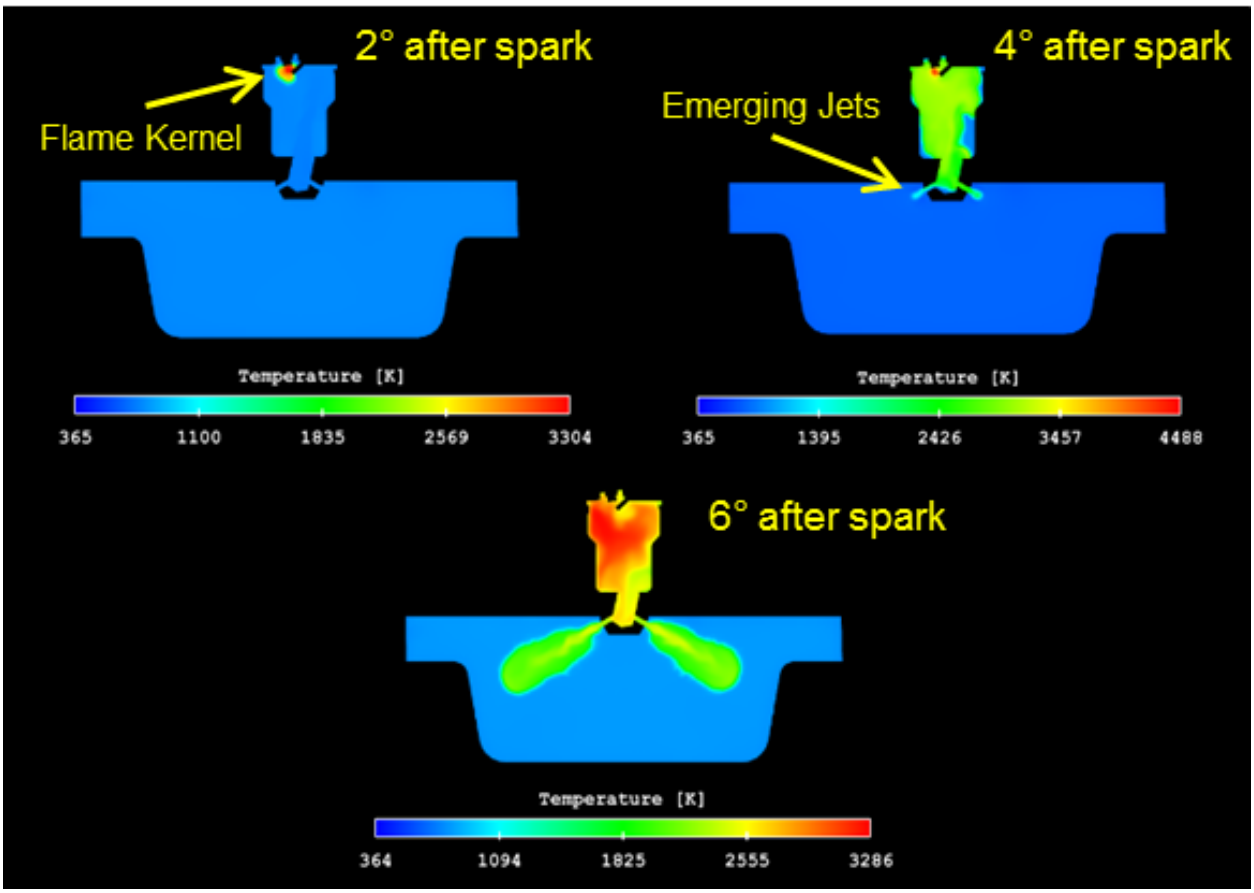

Figure 9-32 Temperature contours on a plane coincident with the centerline of the cylinder and the centerline of two opposing orifices showing pre-chamber combustion and hot jet formation

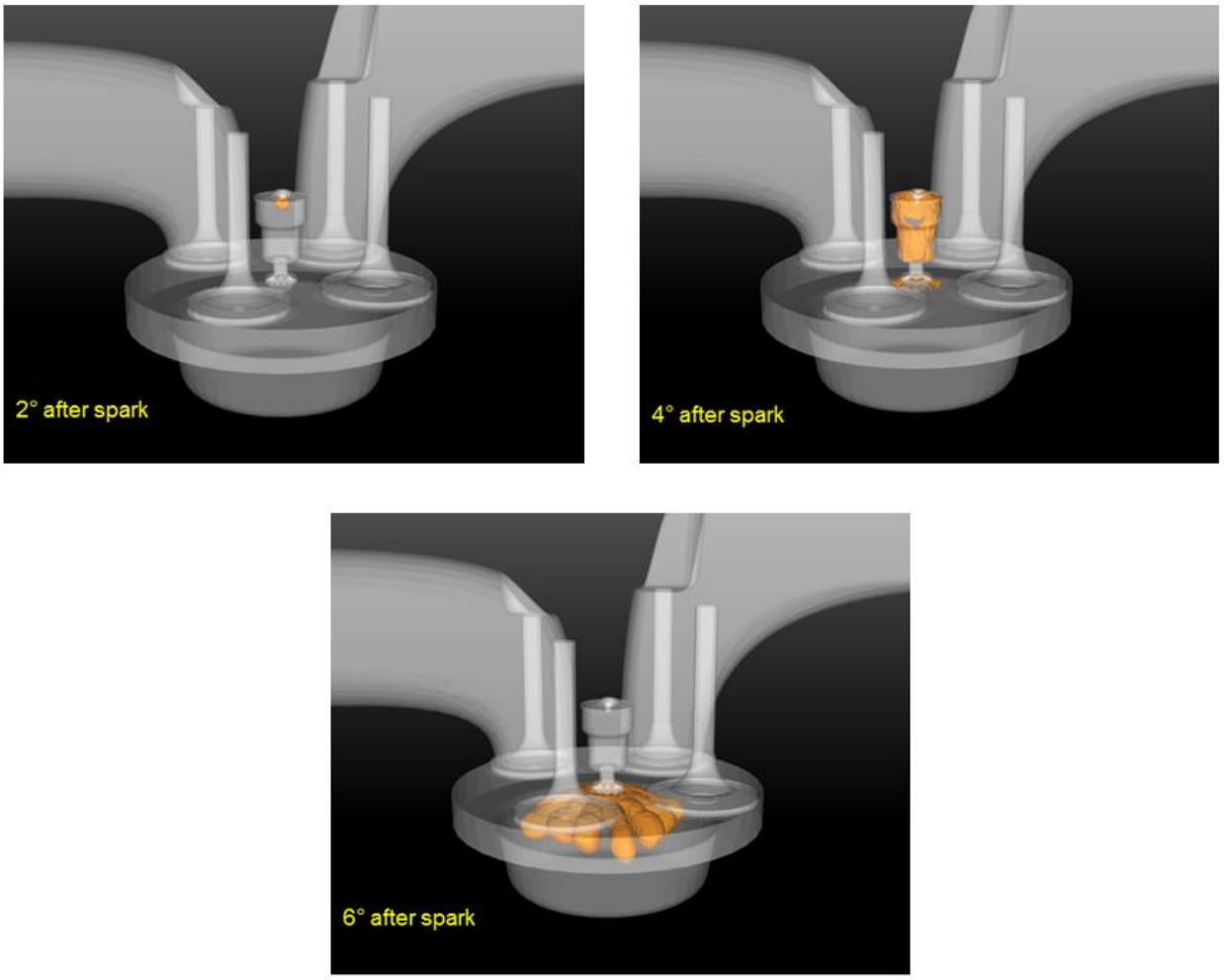

Figure 9-33 Three-dimensional flame front visualization of flame propagation in the example engine simulation

While in its current state, the simulation does not provide useful results, with a more appropriate and detailed chemical mechanism—for which there are multiple available, see [114] for a review of methane-air mechanisms in context to applications using CFD—and data from physical engine testing to better inform boundary conditions at the intake and exhaust, the simulation can serve as a tool to evaluate the overall combustion performance and behavior of the TJI system and be used to conduct virtual experiments relevant to fueling strategies, spark timing, and orifice/nozzle design.

9.7 Summary of the Computational Modelling of a Turbulent Jet Ignition System for a Converted Natural Gas Engine

Three simulation setups that were created to support the early development efforts for a turbulent jet ignition system for use in a converted heavy-duty natural gas engine are described above. Of these three, most of the results presented came from a simplified mixing simulation that was analyzed with the intent of making design recommendations for the pre-chambers being made in a subsequent physical prototyping phase in the development. The two additional simulations, one for modeling fuel injection into the TJI pre-chamber and the other for a more complete engine model are demonstrated with brief projections of their potential usefulness in future development efforts. A summary of the findings of the activities described above are as follows:

- The geometry of the lower pre-chamber affects the mixing performance within the upper pre-chamber or the chamber topologies examined.
- The performance metrics considered in the mixing simulations, upper chamber mixing and flow restriction through the lower pre-chamber, lead to the recommended selection of a 5.5 mm diameter lower pre-chamber throat for initial physical prototypes.
- Simulations of pre-chamber geometries simplified for manufacturing indicate that the simplifications should be adopted and that the changes should improve their performance.
- Initial results from simulations with fuel injection into the pre-chamber indicate that if continued simulation efforts are undertaken, investigations into the stratification of the fueling as the result of the localized injection location are warranted.
- A preliminary engine simulation has been set up and demonstrated with statements of its present shortcomings. Should modeling efforts continue in the future, integration of a detailed chemical mechanism and improved boundary condition data generated from physical engine testing, this simulation can be used to evaluate the combustion

performance of the TJI system and be used to investigate items such as spark timing, injection timing, nozzle and orifice design, etc.

CHAPTER 10: SUMMARY AND CONCLUDING REMARKS

Since the chapters above that included research results each contained a summarizing section at their culmination, the conclusions made in these chapters will not be repeated here. Instead, this section will provide specific answers to the research questions provided in Section 1.4 above and highlight a subset of the experimental and modeling objectives listed in Sections 1.5 and 1.6 to be followed by a discussion of the possibilities for future research related to the topics covered in this dissertation.

10.1 Experimental and Modeling Objectives of Note

The following discusses several topics listed in the experimental or modeling objectives. They were selected because either the activity they pertain to resulted in a useful result that was not the focus of the research being conducted or there was work performed that can be passed on to other researchers using similar tools.

Develop data acquisition capabilities and data analysis routines for the dynamometer test stand.

Custom data acquisition software was written by the author in support of the engine test stand utilizing MATLAB and its Ni-DAQmx toolbox. This software includes a simplified graphical user interface for the test stand user and several scripts for post-processing and analyzing the data. This suite includes the routines to perform the combustion analysis presented in Chapter 4. A repository for this software is provided in Appendix A.

Mount a Fuji Imvac-34EI single-cylinder engine with the necessary instrumentation for engine testing and combustion analysis to the dynamometer.

This is described in Chapter 3. Perhaps the thing that warrants the most review from this experience is the identification of the coupling used to connect the engine's output shaft to the dynamometer. A small single-cylinder four-stroke engine is its own little beast when it comes to vibration and torque pulsation. The test engine absolutely ate couplings. Until the Quadra-flex

coupling was identified, engine testing only lasted seconds. While the coupling wasn't indestructible, many hours of testing were completed before the elastomeric member in the coupling was replaced more as a precaution than out of absolute necessity.

Develop the framework for efficiently implementing CONVERGE software at Michigan State University High-Performance Computing Center.

The simulations that were run for the research covered here typically took multiple days of computation time to complete, running on anywhere from 40 to 200 processors in parallel on the high-performance computer (HPCC) provided by Michigan State's Institute for Cyber-Enabled Research. This shared resource environment requires users to set up and schedule their computational jobs. While this is not directly evident in the dissertation, a good deal of effort was put into developing tools and workflow processes to run Converge successfully and efficiently on the HPCC. While these tools did not influence the research outcomes per se, they were instrumental in facilitating them as the increased throughput they provided allowed for more simulations to be run and/or simulations to be run with more refined computational meshes. An explanation of the infrastructure that was created and a guide for how to use it is provided in Appendix B, and the details for the code repository for the scripts necessary for its implementation are given in Appendix A.

Develop post-processing tools to aid in the task of analyzing CFD-generated data.

Similar to the last objective, quite a bit of work was done to automate the generation of the images in Chapters 6-9 using the post-processing software Ensight, which is currently a module available with ANSYS. The repository with the supporting source code is specified in Appendix A.

10.2 Answers to the Research Questions

Will replacing a standard inductive coil ignition system with a plasma-enhanced ignition system extend the lean operating limit of a spark-ignited internal combustion engine?

Data from both the small metal engine testing and the automotive scale optical engine testing demonstrate an extension of the lean operating limit of both engines. The optical engine's limit was extended from $\lambda = 1.35$ to $\lambda = 1.45$. For the small displacement metal engine, which would not provide stable running with any mixture lean of stochiometric, stable combustion, at least by the looser standards that should be applied to an engine this size, could be maintained out to $\lambda = 1.1$ at all speeds and out to $\lambda = 1.2$ at higher rpm.

What effects does the plasma-enhanced ignition system have on engine-out emissions?

Emissions measurements are presented in Chapter 4 for the small displacement single-cylinder engine. The enhanced system generally resulted in higher engine-out NOx and CO_2 and lower HC emissions. The increased levels of CO_2 and lower levels of HC emissions are indicative of more complete combustion being achieved. An increase in NOx emissions is likely a direct result of increased combustion temperatures with the plasma system, but the literature suggests that there is room to speculate that there is potential that if the plasma has non-equilibrium effects it may provide additional means of NOx formation that of the Zeldovich mechanism.

How well can the operation of a Turbulent Jet Ignition system be modeled using RANS CFD modeling and detailed chemistry?

Chapter 6 compares specific RCM TJI experiments matched to companion CFD simulations with the same conditions. A comparison of optical data collected from the physical test to filed data generated by the CFD simulations suggests adequate agreement regarding jet penetration and flame front propagation with the main chamber of the RCM. Main chamber pressure comparison also indicates agreement between simulation and physical test except for a deviation at the end of the combustion event where the simulations reach a higher peak pressure, which has been

identified to likely be a result of the simulations' lack of crevice volume, which are appreciable in the RCM in the configuration tested, accounting for the higher total heat release that the difference in pressure presents.

What is the effect of orifice size on the TJI combustion process?

The size of the orifice in the nozzle of the TJI system has a significant effect on the rate of combustion in the main chamber. The parameter sweep of orifice diameters detailed in the first half of Chapter 8 demonstrated that by increasing the restriction between the pre-chamber and the main chamber, the velocity of the jet produced increased thereby increasing the amount of turbulence generated in the main chamber by the shear flow of the jet. Thus, the general trend was observed that as orifice size decreased, the durations of the main chamber were reduced. This was true up to a limit at which point the additional jet velocity is offset by the reduction of the diameter of the jet and/or from increased heat loss to the orifice walls.

How does pre-chamber spark location affect the TJI combustion process?

Results of simulations detailed in the second half of Chapter 8 indicate that combustion should be initiated in the prechamber as far from the exit of the chamber as possible as faster burns were achieved in the main combustion chamber thigh higher, which is further from the orifice, in the pre-chamber the ignition source was placed. Two factors could be driving this result. The first is that by requiring the flame front to transverse the full chamber, a greater amount of pressure is built up in the chamber which drives a higher velocity jet into the main chamber. The second, albeit less likely, is that there is a benefit provided by the cold jet, which precedes the hot jet into the main chamber for a longer duration the further through the pre-chamber the flame front has to travel, possibly adding turbulence to the main prior to the emergence of the hot jets.

What additional insights into the TJI can be gained from the three-dimensional field data generated from the simulation that is absent from data generated experimentally?

The CFD simulations provide a view into the combustion in the TJI pre-chamber, which is not typically optically accessible. Another example is that jet velocity could be measured over the course of the combustion event. In contrast in the TJI RCM experiments, only the initial jet velocity could be inferred via the rate at which the jet tip penetrated the main chamber. The simulations also demonstrated the existence and behavior of the cold jet that precedes the hot jet in the main combustion chamber, a topic suggested for potential further research below.

10.3 Recommendations and Ideas for Future Work

The following is a list of potential ideas inspired by the research described above that could be future topics of research. The lists are divided between physical experiments and computational modeling. Pertaining to the small engine plasma-enhanced ignition testing the following ideas are provided:

- There is plenty of room for improvement to the small engine test stand that was built for the plasma ignition research covered above which could facilitate more investigation into either the plasma-enhanced ignition system or the implementation of the TJI into a small-scale engine. Adding actual electronic engine control would be the first major step. This would allow for engine loads other than the maximum WOT condition the research above pursued.
- A better understanding of the RF plasma discharge that the system used in this research produced could be undertaken. The first question to seek an answer to is whether or not the discharge created any non-equilibrium effects or if the system was just a train of multiple sparks that were all basic breakdowns that were in complete thermodynamic equilibrium.
- Evaluation of the miniaturization of the RF system could be pursued. The absurdity of

testing an ignition module that the author could not easily lift on his own on an engine used as the powerplant on hand-launched UAVs should rightfully be called into question.

As for modeling efforts for the TJI in the RCM, the following are suggested:

- An examination of the effect of spark location on TJI pre-chambers with auxiliary fuel could be undertaken to determine whether it follows the same trend as the unfueled experiments covered here.
- Additional experiments could be run on spark location by including horizontal bias to the ignition location instead of just vertical bias. Having the source away from the centerline of the prechamber is a very realistic possibility due to packaging constraints that could be encountered in practical implementations of the TJI. It will also be interesting to see if there are any gains in the main chamber burn durations as a little more distance is added between the ignition source and the pre-chamber exit.
- The author would love to address the ignition delay observed in the high location case from the spark location research. This effort would focus on determining if the phenomenon was physically plausible or if it was a computational quirk or error.
- Research could examine the cold jet phenomenon and its effects on combustion. Contrived simulations could be staged to gauge its effects on main chamber combustion. How much does its presence aid in the main chamber combustion? Does the cold jet of a pre-chamber with auxiliary fuel behave differently than an unfueled pre-chamber?

And finally, for the engine simulations covered in Chapter 9:

- The engine simulation could be validated against physical engine test data that should now exist, making it a valid platform for conducting virtual experiments.
- Better information about the engine's fuel system and/or the incorporation of a feasible

fueling system into the model would allow higher-fidelity simulations to be run, examining the scavenging, pre-chamber mixture preparation, and ignitability that the simplified simulations covered here.

- Adding realistic fueling and a chemical mechanism with more detail and appropriateness for the engine's conditions would allow the simulation to examine and optimize the TJI nozzle design for the engine.

BIBLIOGRAPHY

[1] *Annual Energy Outlook 2020*. 2020, U.S. Energy Information Administration Office of Energy Analysis. p. 162.

[2] *High-Efficiency, Dilute Gasoline Engine (HEDGE)*. 2020 [cited 2020 07/06/20]; Available from: https://www.swri.org/consortia/high-efficiency-dilute-gasoline-engine-hedge.

[3] *Advanced Combustion Strategies*. 2020 [cited 2020 07/06/20]; Available from: https://www.energy.gov/eere/vehicles/advanced-combustion-strategies.

[4] *USCAR: Who We Are*. 2020 [cited 2020 07/06/20]; Available from: https://www.uscar.org/guest/about/.

[5] *2019/2020 Worldwide Emissions Standards: Passenger Cars and Light Duty Vehicles*. 2016: Delphi.

[6] Paul Hemmersbaugh, P.W. *Trump Administration issues new regulations reducing stringency of automobile fuel economy and greenhouse gas emissions standards for 2021-2026*. 2020 [cited 2020 07/06/20]; Available from: https://www.linkedin.com/pulse/trump-administration-issues-new-regulations-reducing-gas-paul/?trackingId=Tl3Ve7dhRqewfPQXKzqvYg%3D%3D.

[7] *Final Rollback of Corporate Average Fuel Economy Standards & Greenhouse Gas Standards for Passenger Cars and Light Duty Trucks*. 2020 [cited 2020 07/06/20]; Available from: https://eelp.law.harvard.edu/wp-content/uploads/EELP-Car-Rules-Backgrounder-Final-Updated.pdf.

[8] *Cost, effectiveness, and deployment of fuel economy technologies for light-duty vehicles*. 2015, Washington, D.C.: National Academies Press.

[9] Davis, S.C., Robert G. Boundy, *Transportation Energy Data Book: Edition 38*. 2020, Oak Ridge National Laboratory.

[10] Lambert, C.K., *Current state of the art and future needs for automotive exhaust catalysis.* Nature Catalysis, 2019. **2**(7): p. 554-557.

[11] Toulson, E., H.J. Schock, and W.P. Attard, *A Review of Pre-Chamber Initiated Jet Ignition Combustion Systems*. 2010, SAE International.

[12] Davis, S.C., S.W. Diegel, and R.G. Boundy, *Transportation Energy Data Book: Edition 34*. 2015, Center for Transportation Analysis Energy and Transportation Science Division.

[13] Najt, P.M. and D.E. Foster, *Compression-Ignited Homogeneous Charge Combustion*. 1983, SAE International.

[14] Zhang, S., et al., *Improvement in the combustion mode transition for a spark ignition engine capable of homogeneous charge compression ignition.* Proceedings of the Institution of Mechanical Engineers, Part D: Journal of Automobile Engineering, 2015.

[15] Atkins, M.J. and C.R. Koch, *The effect of fuel octane and dilutent on homogeneous charge compression ignition combustion.* Proceedings of the Institution of Mechanical Engineers, Part D: Journal of Automobile Engineering, 2005. **219**(5): p. 665-675.

[16] Aleiferis, P.G., et al., *The effect of axial charge stratification and exhaust gases on combustion 'development' in a homogeneous charge compression ignition engine.* Proceedings of the Institution of Mechanical Engineers, Part D: Journal of Automobile Engineering, 2008. **222**(11): p. 2171-2183.

[17] Pucher, G.R., et al., *Alternative Combustion Systems for Piston Engines Involving Homogeneous Charge Compression Ignition Concepts - A Review of Studies Using Methanol, Gasoline and Diesel Fuel*. 1996, SAE International.

[18] Marriott, C.D. and R.D. Reitz, *Experimental Investigation of Direct Injection-Gasoline for Premixed Compression Ignited Combustion Phasing Control*. 2002, SAE International.

[19] Ortmann, R., et al., *Methods and Analysis of Fuel Injection, Mixture Preparation and Charge Stratification in Different Direct Injected SI Engines*. 2001, SAE International.

[20] Solomon, A.S. and G.A. Szekely, *Combustion Characteristics of a Reverse-Tumble Wall-Controlled Direct-Injection Stratified-Charge Engine*. 2003, SAE International.

[21] Park, C., et al., *Effect of a split-injection strategy on the performance of stratified lean combustion for a gasoline direct-injection engine.* Proceedings of the Institution of Mechanical Engineers, Part D: Journal of Automobile Engineering, 2011. **225**(10): p. 1415-1426.

[22] Nakashima, T., et al., *A Study of Stratified Charge Combustion Characteristics in New Concept Direct Injection SI Gasoline Engine*. 2001, SAE International.

[23] Li, B.-Z., et al., *Development of a direct-injection stratified-charge methanol engine.* Proceedings of the Institution of Mechanical Engineers, Part D: Journal of Automobile Engineering, 2008. **222**(11): p. 2121-2129.

[24] Chintala, N., et al., *Measurements of combustion efficiency in nonequilibrium RF plasma-ignited flows.* Combustion and Flame, 2006. **144**(4): p. 744-756.

[25] Kim, W., M. Godfrey Mungal, and M.A. Cappelli, *The role of in situ reforming in plasma enhanced ultra lean premixed methane/air flames.* Combustion and Flame, 2009. **157**: p. 374-383.

[26] Cathey, C.D., et al., *Nanosecond Plasma Ignition for Improved Performance of an Internal Combustion Engine.* Plasma Science, IEEE Transactions on, 2007. **35**(6): p. 1664-1668.

[27] Gussak, L.A., *High Chemical Activity of Incomplete Combustion Products and a Method of Prechamber Torch Ignition for Avalanch Activation of Combustion in Internal Combustion Engines.* SAE Transactions, 1975. **84**: p. 2421-2445.

[28] Boretti, A., R. Paudel, and A. Tempia, *Experimental and computational analysis of the combustion evolution in direct-injection spark-controlled jet ignition engines fuelled with gaseous fuels.* Proceedings of the Institution of Mechanical Engineers, Part D: Journal of Automobile Engineering, 2010. **224**(9): p. 1241-1261.

[29] Boretti, A., H. Watson, and A. Tempia, *Computational analysis of the lean-burn direct-injection jet ignition hydrogen engine.* Proceedings of the Institution of Mechanical Engineers, Part D: Journal of Automobile Engineering, 2010. **224**(2): p. 261-269.

[30] Lutsey, N., *Regulatory and technology lead-time: The case of US automobile greenhouse gas emission standards.* Transport Policy, 2012. **21**: p. 179-190.

[31] Bradley, D., *Chapter 2 - Fundamentals of Lean Combustion*, in *Lean Combustion*, D. Dunn-Rankin, Editor. 2008, Academic Press: Burlington. p. 19-II.

[32] Michael J. Moran, H.N.S., *Fundamentals of Engineering Thermodynamics*. 5 ed. 2004, United States of America: John Wiley & Sons, Inc.

[33] Heywood, J.B., *Internal Combustion Engine Fundamentals*. 1988, United States of America: McGraw-Hill. 930.

[34] J. Warnatz, U.M., R.W.Dibble, *Combustion: Physical and Chemical Fundamentals, Modeling and Simulation, Experiments, Pollutant Formation*. 4 ed. 2006, Germany: Springer.

[35] Glarborg, P., J.A. Miller, and R.J. Kee, *Kinetic modeling and sensitivity analysis of nitrogen oxide formation in well-stirred reactors.* Combustion and Flame, 1986. **65**(2): p. 177-202.

[36] Tully, E.J. and J.B. Heywood, *Lean-Burn Characteristics of a Gasoline Engine Enriched with Hydrogen Plasmatron Fuel Reformer*. 2003, SAE International.

[37] Shelef, M. and R.W. McCabe, *Twenty-five years after introduction of automotive catalysts: what next?* Catalysis Today, 2000. **62**(1): p. 35-50.

[38] Calnan, P., et al., *The Influence of Dilution Composition and Temperature Upon a Stratified Charge Spark Ignition Engine*. 2000, SAE International.

[39] Yang, J., T. Culp, and T. Kenney, *Development of a Gasoline Engine System Using HCCI Technology - The Concept and the Test Results*. 2002, SAE International.

[40] Starikovskii, A.Y., *Plasma supported combustion.* Proceedings of the Combustion Institute, 2005. **30**(2): p. 2405-2417.

[41] Starikovskaia, S.M., *Plasma assisted ignition and combustion.* Journal of Physics D: Applied Physics, 2006. **39**(16): p. R265-R299.

[42] Leonov, S.B. and D.A. Yarantsev, *Plasma-induced ignition and plasma-assisted combustion in high-speed flow*. Plasma Sources Science and Technology, 2007. **16**(1): p. 132-138.

[43] Hemawan, K.W., et al., *Microwave plasma-assisted premixed flame combustion.* Appl. Phys. Lett., 2006. **89**(14): p. 141501.

[44] Wang, F., et al., *Transient Plasma Ignition of Quiescent and Flowing Air/fuel Mixtures.* IEEE Trans. on Plasma Science, 2005. **33**: p. 844-849.

[45] Lawton, J. and F.J. Weinberg, *Electrical Aspects of Combustion*. 1969: Clarendon, Oxford.

[46] Jaggers, H.C. and A. von Engel, *The effect of electric fields on the burning velocity of various flames.* Combustion and Flame, 1971. **16**: p. 275-285.

[47] Carleton, F.B., I.M. Vince, and F.J. Weinberg, *Energy and radical losses from plasma jet igniters to solid surfaces.* Proceedings of the Combustion Institute, 1982. **19**: p. 1523-1531.

[48] Lee, A. and F.J. Weinberg, *A novel ignition device for the internal combustion engine.* Nature (London, United Kingdom), 1984. **311**(5988): p. 738-40.

[49] Weinberg, F.J., et al., *Ignition by plasma jet.* Nature, 1978. **272**: p. 341-343.

[50] Bromberg, L., et al., *Plasma Catalytic Reforming of Methane.* Inter. J. of Hydrogen Energy, 1999. **24**: p. 1131-1137.

[51] Kalra, C.S., A. Gutsol, and A. Fridman, *Gliding arc discharge as a source of intermediate plasma for methane partial oxidation.* IEEE Transactions on Plasma Science, 2005. **33**(1): p. 32-41.

[52] Lou, G., et al., *Ignition of Premixed Hydrocarbon-Air Flows by Repetitively Pulsed, Nanosecond Pulse Duration Plasma.* Proceedings of the Combustion Institute, 2007. **31**(2): p. 3327-3334.

[53] Kim, W., et al. *Flame stabilization enhancement and NOx production using ultra short repetitively pulsed plasma discharge*. in *44th AIAA Aerospace Sciences Meeting and Exhibit, AIAA-2006-560*. 2006.

[54] Ombrello, T., Y. Ju, and A. Fridman, *Kinetic Ignition Enhancement of Diffusion Flames by Nonequilibrium Magnetic Gliding Arc Plasma.* AIAA J., 2008. **46**(10): p. 2424-2433.

[55] Kim, W., et al., *Plasma-Discharge Stabilization of Jet Diffusion Flames.* IEEE Transactions on Plasma Science, 2006. **34**(6): p. 2545-2551.

[56] Leonov, A.B., et al. *Plasma-assisted ignition and flameholding in high-speed flow*. in *44th AIAA Aerospace Sciences Meeting, AIAA-2006-563*. 2006. Reno, Nevada.

[57] Kitagawa, T., et al., *Ignition characteristics of methane and hydrogen using a plasma torch in supersonic flow*. Journal of Propulsion and Power, 2003. **19**(5): p. 853-858.

[58] Matveev, I., et al. *Non-Equilibrium Plasma Igniters and Pilots for Aerospace Applications*. in *43rd AIAA Aerospace Sciences Meeting and Exhibit, AIAA Paper 2005-1191*. 2005. Reno.

[59] Kimura, I., *Effectiveness of Plasma Torches for Ignition and Flameholding in Scramjet.* Journal of Propulsion and Power, 1992. **8**(4).

[60] Matveev, I., *Plasma Assisted Combustion, Gasification, and Pollution Control: Volume I. Methods of plasma generation for PAC*. 1st ed, ed. I. Matveev. Vol. 1. 2013, Denver, Co: Outskirts Press, Inc. 538.

[61] Matveev, I.B. and L.A. Rosocha, *Guest Editorial Classification of Plasma Systems for Plasma-Assisted Combustion.* Plasma Science, IEEE Transactions on, 2010. **38**(12): p. 3257-3264.

[62] Bittencourt, J.A., *Fundamentals of plasma physics 3rd ed.* 3 ed. 2003: Springer.

[63] Meichsner, J., *Low Temperature Plasmas.* Plasma Physics, 2005. **670**: p. 95.

[64] Tropina, A.A., et al., *Comparative Analysis of Engine Ignition Systems.* Plasma Science, IEEE Transactions on, 2009. **37**(12): p. 2286-2292.

[65] Mariani, A., F. Foucher, and B. Moreau, *The Effects of a Radio Frequency Ignition System on the Efficiency and the Exhaust Emissions of a Spark-Ignition Engine.* SAE Technical Paper Series, 2013-24-0053, 2013.

[66] Ricardo, H.R., *Recent Work on the Internal Combustion Engine.* SAE Transactions, 1922. **17**.

[67] Attard, W.P. and P. Parsons, *A Normally Aspirated Spark Initiated Combustion System Capable of High Load, High Efficiency and Near Zero NOx Emissions in a Modern Vehicle Powertrain.* SAE Int. J. Engines, 2010. **3**(2): p. 269-287.

[68] Attard, W.P., et al., *A New Combustion System Achieving High Drive Cycle Fuel Economy Improvements in a Modern Vehicle Powertrain*. 2011, SAE International.

[69] Attard, W.P. and H. Blaxill, *A Single Fuel Pre-Chamber Jet Ignition Powertrain Achieving High Load, High Efficiency and Near Zero NOx Emissions.* SAE Int. J. Engines, 2011. **5**(3): p. 734-746.

[70] Gussak, L.A., V.P. Karpov, and Y.V. Tikhonov, *The Application of Lag-Process in Prechamber Engines.* SAE Transactions, 1979. **88**: p. 2355-2380.

[71] Yamaguchi, S., N. Ohiwa, and T. Hasegawa, *Ignition and burning process in a divided chamber bomb.* Combustion and Flame, 1985. **59**(2): p. 177-187.

[72] Glasson, N., et al., *Development of the HAJI System for a Multi-Cylinder Spark Ignition Engine*. 1996, SAE International.

[73] Lumsden, G. and H.C. Watson, *Optimum Control of an S.I. Engine with a λ=5 Capability*. 1995, SAE International.

[74] Attard, W.P., J. Kohn, and P. Parsons, *Ignition Energy Development for a Spark Initiated Combustion System Capable of High Load, High Efficiency and Near Zero NOx Emissions.* SAE Int. J. Engines, 2010. **3**(2): p. 481-496.

[75] Attard, W.P. and P. Parsons, *Flame Kernel Development for a Spark Initiated Pre-Chamber Combustion System Capable of High Load, High Efficiency and Near Zero NOx Emissions.* SAE Int. J. Engines, 2010. **3**(2): p. 408-427.

[76] Attard, W.P., et al., *Knock Limit Extension with a Gasoline Fueled Pre-Chamber Jet Igniter in a Modern Vehicle Powertrain.* SAE Int. J. Engines, 2012. **5**(3): p. 1201-1215.

[77] Anderson, E.K., et al., *Experimental Study of a Pre-Chamber Jet Igniter in a Turbocharged Rotax 914 Aircraft Engine*. 2013, SAE International.

[78] Attard, W.P. and H. Blaxill, *A Gasoline Fueled Pre-Chamber Jet Ignition Combustion System at Unthrottled Conditions.* SAE Int. J. Engines, 2012. **5**(2): p. 315-329.

[79] Attard, W.P. and H. Blaxill, *A Lean Burn Gasoline Fueled Pre-Chamber Jet Ignition Combustion System Achieving High Efficiency and Low NOx at Part Load*. 2012, SAE International.

[80] Millo, F., et al. *Experimental and Numerical Investigation of a Passive Pre-Chamber Jet Ignition Single-Cylinder Engine*. in *15th International Conference on Engines & Vehicles*. 2021.

[81] Sanal, S., et al. *A Numerical Study on the Effect of a Pre-Chamber Initiated Turbulent Jet on Main Chamber Combustion*. in *WCX SAE World Congress Experience*. 2022.

[82] Zhong, L., et al., *Effects of Orifice Configuration on the Flame Propagation and Mechanism of Jet Ignition under Elevated Temperature and Pressure.* SAE International Journal of Engines, 2021. **15**(5): p. 631-649.

[83] Atis, C. and H. Schock, *Comparison of Excess Air (Lean) vs EGR Diluted Operation in a Pre-Chamber Air/Fuel Scavenged Dual Mode, Turbulent Jet Ignition Engine at High Dilution Rate (~40%).* SAE International Journal of Advances and Current Practices in Mobility, 2021. **3**(4): p. 1569-1584.

[84] Tolou, S. and H. Schock, *Experiments and modeling of a dual-mode, turbulent jet ignition engine.* International Journal of Engine Research, 2020. **21**(6): p. 966-986.

[85] Vedula, R.T., *Optical investigations and efficiency measurements of a dual-mode turbulent jet ignition engine under lean and high-EGR near-stoichiometric conditions*. 2016, Michigan State University: United States -- Michigan. p. 113.

[86] Schock, H., *Michigan State University, High-Efficiency, High Dilute Active Turbulent Jet Engine Enabled by Mechanical Prechamber Air Control*. 2023, 32nd Aachen Colloquium on Sustainable Mobility: Aachen, Germany.

[87] Gholamisheeri, M., S. Givler, and E. Toulson, *Large eddy simulation of a homogeneously charged turbulent jet ignition system.* International Journal of Engine Research, 2019. **20**(2): p. 181-193.

[88] Validi, A., H. Schock, and F. Jaberi, *Turbulent jet ignition assisted combustion in a rapid compression machine.* Combustion and Flame, 2017. **186**: p. 65-82.

[89] Ombrello, T., et al., *Flame propagation enhancement by plasma excitation of oxygen. Part I: Effects of O3.* Combustion and Flame, 2010. **157**(10): p. 1906-1915.

[90] Chintala, N., et al., *Nonthermal Ignition of Premixed Hydrocarbon-Air Flows by Nonequilibrium Radio Frequency Plasma.* Journal of Propulsion and Power, 2005. **21**(4): p. 583-590.

[91] Singleton, D., S.J. Pendleton, and M.A. Gundersen, *The role of non-thermal transient plasma for enhanced flame ignition in C 2 H 4 –air*. Journal of Physics D: Applied Physics, 2011. **44**(2): p. 022001.

[92] Mittal, M., et al., *A Study of Fuel Impingement Analysis on In-Cylinder Surfaces in a Direct-Injection Spark-Ignition Engine with Gasoline and Ethanol-Gasoline Blended Fuels.* SAE Technical Paper Series, 2010-01-2153, 2010(2010-01-2153).

[93] Withrow, L. and F. Bowditch, *Flame Photographs of Autoignition Induced by Combustion-Chamber Deposits.* SAE Technical Paper Series, 520265, 1952.

[94] Rao, X., I.B. Matveev, and T. Lee, *Nitric Oxide Formation in a Premixed Flame With High-Level Plasma Energy Coupling.* IEEE TRANSACTIONS ON PLASMA SCIENCE, 2009. **37**(12): p. 2303.

[95] Allen, C., et al., *Ignition behavior and surrogate modeling of JP-8 and of camelina and tallow hydrotreated renewable jet fuels at low temperatures.* Combustion and Flame, 2013. **160**(2): p. 232-239.

[96] Allen, C., et al., *Application of a novel charge preparation approach to testing the autoignition characteristics of JP-8 and camelina hydroprocessed renewable jet fuel in a rapid compression machine.* Combustion and Flame, 2012. **159**(9): p. 2780-2788.

[97] Gentz, G., et al., *A study of the influence of orifice diameter on a turbulent jet ignition system through combustion visualization and performance characterization in a rapid compression machine.* Applied Thermal Engineering, 2015. **81**: p. 399-411.

[98] Gentz, G., et al., *Combustion Visualization, Performance, and CFD Modeling of a Pre-Chamber Turbulent Jet Ignition System in a Rapid Compression Machine.* SAE Int. J. Engines, 2015. **8**(2): p. 538-546.

[99] Richards, K.S., P., and Pomraning, E., *CONVERGE*. 2014, Convergent Science, Inc.: Middleton, WI.

[100] Issa, R.I., *Solution of the implicitly discretised fluid flow equations by operator-splitting.* Journal of Computational Physics, 1986. **62**(1): p. 40-65.

[101] Pope, S.B., *Turbulent Flows*. 2000: Cambridge University Press, UK.

[102] Senecal, P.K., et al., *A New Parallel Cut-Cell Cartesian CFD Code for Rapid Grid Generation Applied to In-Cylinder Diesel Engine Simulations*. 2007, SAE International.

[103] Béchet, E., J.C. Cuilliere, and F. Trochu, *Generation of a finite element MESH from stereolithography (STL) files.* Computer-Aided Design, 2002. **34**(1): p. 1-17.

[104] Senecal, P.K., et al., *Multi-Dimensional Modeling of Direct-Injection Diesel Spray Liquid Length and Flame Lift-off Length using CFD and Parallel Detailed Chemistry*. 2003, SAE International.

[105] Mechanical and Aerospace Engineering (Combustion Research), U.o.C.a.S.D. *Chemical-Kinetic Mechanisms for Combustion Applications*. August 2014; Available from: http://combustion.ucsd.edu.

[106] Pomraning, E., K. Richards, and P.K. Senecal, *Modeling Turbulent Combustion Using a RANS Model, Detailed Chemistry, and Adaptive Mesh Refinement*. 2014, SAE International.

[107] Launder, B.E. and D.B. Spalding, *The numerical computation of turbulent flows.* Computer Methods in Applied Mechanics and Engineering, 1974. **3**(2): p. 269-289.

[108] Amsden, A.A., *KIVA-3V: A Block-Structured KIVA Program for Engines with Vertical or Canted Valves*. 1997, Los Alamos National Laboratory.

[109] Toulson, E., et al., *Visualization of Propane and Natural Gas Spark Ignition and Turbulent Jet Ignition Combustion.* SAE Int. J. Engines, 2012. **5**(4): p. 1821-1835.

[110] Wilcox, D.C., *Turbulence Modeling for CFD*. 3rd ed. 2006: DCW Industries, Inc. 522.

[111] Kuo, K.K.-y. and R. Acharya, *Fundamentals of Turbulent and Multiphase Combustion*. 1 ed. 2012: Wiley. 912.

[112] Thelen, B.C., G. Gentz, and E. Toulson, *Computational Study of a Turbulent Jet Ignition System for Lean Burn Operation in a Rapid Compression Machine*. 2015, SAE International.

[113] *DETROIT DIESEL SERIES 50®: FUEL-EFFICIENT AND COST-EFFECTIVE*. 2024 [cited 2024 04/02/24]; Available from: https://www.demanddetroit.com/engines/legacy-engines/series-50/.

[114] Zettervall, N., C. Fureby, and E.J.K. Nilsson, *Evaluation of Chemical Kinetic Mechanisms for Methane Combustion: A Review from a CFD Perspective.* Fuels, 2021. **2**(2): p. 210-240.

APPENDIX A: ONLINE CODE REPOSITORIES

Several online code repositories have been set up to store and distribute some of the computer code developed during the research activities documented above. The repositories are hosted on GitHub, viewable to the public, and listed under the user name thelenb8. There are five repositories in total. At the time of writing, very little documentation beyond the additional appendix that exists here, but that may change as time passes, particularly if updates to the code are being made in the future. Table A-1 provides a summary of the five repositories.

Table A-1 Summary of GitHub Repositories

Repository Name	Description of Content	Programming Language	URL
EnsightTools	Tools for scripting CEI Ensight CFD post-processing software	Python 2	github.com/thelenb8/EnsightTools
Auto_Submit	Scripts for use on the MSU HPCC to use the Auto_Submint scheme to run Converge simulations in repeated four-hour chunks efficiently	BASH	github.com/thelenb8/Auto_Submit
MSU_Python	Tools for data plotting and managing Converge data on MSU HPCC	Python 3	github.com/thelenb8/MSU_Python
MSU_Engine_MATLAB	Code written in support of the small engine test stand covered above	MATLAB	github.com/thelenb8/MSU_Engine_MATLAB
MSU_MATLAB_Tools	Various tools that were developed to support the research presented above	MATLAB	github.com/thelenb8/MSU_MATLAB_Tools

The three most useful are the Auto_Submit, EnsightTools, and MSU_Python packages as these are the most recently developed or updated. A guide to Auto_Submit is provided in Appendix B

below, which is a suite of scripts for the automation of Converge job submissions on the MSU HPCC. EnsightTools contains a Python package that was developed to automate the repetitive tasks that accompany processing many sets of CFD data. Finally, documentation for the MSU_Python repository is not included here but can be found within the repository itself.

APPENDIX B: GUIDE TO THE AUTO SUBMISSION HPCC CONVERGE TOOL

B.1 Disclaimer

It is important to note that the author only possesses the experience gained as a user of the high-performance computing (HPC) hosted by the Institute of Cyber Enhanced Research (ICER) at Michigan State University and no formal training in computer science/engineering beyond the programming classes the undergraduate mechanical engineering curriculum at MSU required. All of what is conveyed below was either self-taught or provided through repeated visits to ICER's help hours. As such, there is a high probability that the language or concepts used and described below will not match the common lexicon in the computer science field or Linux community.

Any discussion about the ICER HPC provided below is meant only to describe the system enough to instruct a user of the Converge CFD package on how to run the software efficiently on hardware outside of any buy-in resources they may or may not have access to. If the reader is interested in accurate and up-to-date information or better definitions of the HPC, please visit ICER's website (https://icer.msu.edu) and/or contact ICER (https://icer.msu.edu/contact)

B.2 Motivation and Background

The following is a brief statement for the motivation of the Auto Submit scheme described in this appendix within the context that the reader understands how the ICER HPC and Converge work. The HPC has a lot of computing processors. The vast majority of these are reserved and belong to various research groups/individuals. The only way to have a job run on one of these processors is to request job run times that are four hours or less. A Converge simulation is not likely to finish in four hours. If combustion is involved, several days of run time will likely be required. Instead of the prospective user submitting jobs every four hours themselves, the scheme and code described here will allow the user to submit the first four-hour job and provided the simulation runs well, the code will automatically manage the simulation and continually submit

new jobs before the conclusion of the active job.

Description of the ICER HPC

For users, particularly those without a computer background, the HPC can be seen as a giant collection of computers networked together that all run Linux operating systems. These computers can be accessed remotely and used to run computations for their research. These computing resources are shared with everyone who has access to the system at the university.

The computing hardware making up the HPC is organized as follows:

- The cluster is the largest subcollection of hardware. A cluster consists of groups of nodes with identical processors and is typically named after its processor type and either the year it went online or the year its processor was manufactured. I am not sure which.
- The node is a collection of processors that share the same physical unit along with the memory they have access to and any other accessories they may have. While this may not be strictly true at present, years ago, each node was a single server blade. This is also the unit that research groups purchase. All of the nodes that are currently active have a single multi-core processor.
- The core is the smallest unit, which is an individual computational processing unit. Each node will have multiple cores, and the specific number of cores in a node will depend on the specific cluster to which it belongs.
- For example, the cluster named intel16 contains a total of 378 nodes. Each node has an Intel Xeon processor with 40 cores. The typical node in this cluster has 115 GB of memory.
- Every node is either a public node or a reserved node. The reserved nodes were purchased with buy-in funds provided by the research groups that own them. The owners of reserved nodes are guaranteed access to the hardware within four hours of submitting a job to the

scheduler.

The last bullet in the list above is the lynchpin for what is covered here. Notice the distinction that the owners of the reserved hardware are not guaranteed immediate access to their nodes. They could be required to wait up to four hours for a job they have submitted to run (provided that the resource is not already in use by someone within their group). The reason for this possible four-hour delay is that the HPC does not want hardware not in use by its owner group to sit idle. Instead, it is made available to public (non-group) users provided those jobs do not request more than four hours of walltime. It is this idle reserved hardware that the scheme below takes advantage of. At the moment this is being written, the ICER dashboard (https://icer.msu.edu/dashboard) indicates that 97% of the public nodes are in use, which is probably all of the public nodes that are operational. Only 60% of the reserve nodes are active. The takeaway from those numbers is that there is a vast sea of idle cores of reserved nodes just waiting for a four-hour job.

B.3 Running Converge on the HPC

The purpose of this section is to describe the workflow the author believes to be typical for users of Converge on the MSU HPC to put the Auto Submit scripts into context. The following is an outline summary of the workflow:

1. The simulation is set up using Converge Studio, which generates a directory of input and data files.
    a. A common alternative for steps 1-3 is to copy a new simulation from an existing simulation already on the HPC with the user modifying the input text files to alter the simulation.
2. The input files exported from Converge Studio are transferred to the HPC into their own directory.
3. The user logs into the HPC, then into one of the development nodes, and finally, navigates

to the directory where the recently uploaded files have been placed.

4. A job script is written (typically a copy of a previously used script) which contains the following:
    a. SLURM, the job scheduler, resource requests
    b. Code to load Converge software module
    c. Code calling a Converge executable
5. The job script is submitted to SLURM using sbatch <job-script> from within the directory containing the input files referred to as the simulation directory going forward.
6. The job gets put into a queue, and the scheduler waits for the hardware required to become available.
7. The job runs, and either the simulation runs to completion, something causes Converge to crash or not run (something wrong with the input files), or the walltime requested has expired.
8. If the simulation is not complete, the inputs.in file is modified to restart the simulation from the latest restart file, restart<####>.rst.
9. Another job is submitted (it can use the same job script), and the process returns to 6.
10. When the simulation has reached its conclusion, the binary output files located in the subdirectory created by Converge and labeled output in the simulation directory are processed for whichever post-processing software is to be used.
    a. This can be done using the command line on a development node, but a single processor job is a better choice.
    b. If the simulation does not run in a single session or if the user had to start from a restart file that was not the latest available at the time, then there will be multiple

output files for the same output write step within the outputs directory. If output step 10 has three files written for it, only the file that was written most recently should be kept, and the rest should be discarded before converting the output binaries to formats for post-processing.

11. Text output <name>.out and <name><restart_number>.out are combined if restart files were used during the run so that there is a single, for example, thermo.out file that covers the entire simulation duration.
12. Ideally, the entire simulation directory, output binaries, inputs, and text output are downloaded to a local computer or network drive that is not part of the HPC.
    a. It is good practice to run the simulations on HPC's scratch drive to avoid filling up the user's home drive, which has limited space.
    b. The only caveat is that data on the scratch drive gets deleted some number of days after it was created; so the data needs to be saved elsewhere before this occurs.
13. Post-processing of the converted output files is completed with whichever software the user chooses, and any data from the text output is plotted using MATLAB or Python.

An example of a simple job is shown in Figure B-1. The first block of code consists of SLURM directives that request the resources for the job and set some configurable settings for the job execution. Here, 120 processor cores are requested for four hours of walltime. The next block of code loads the Converge software module onto the cores running the job followed by the open mpi version of the Converge solver that matches the Converge version loaded above it. The last line of code prints data about the job to the output. These will be the last lines of the *.SLURMout file that the execution of the job creates in the directory. The point of showing this code is to emphasize that this script gets executed on one of the cores used by the job, and it executes line by line in

sequence. If Converge does not exit before the walltime for the job expires, then the last line of code does not get executed.

```
#!/bin/bash --login
#SBATCH --job-name=CHANGE2DIR-W.qsub
#SBATCH --time=04:00:00
#SBATCH --ntasks=120
#SBATCH --cpus-per-task=1
#SBATCH --mem-per-cpu=2G
#SBATCH --output=%x-%j.SLURMout
#SBATCH --mail-type=ALL
#SBATCH --mail-user=thelenb8@msu.edu

# Load converge and change into working directory
cd ${SLURM_SUBMIT_DIR}
module load CONVERGE

mpirun -np ${num_pros} /opt/software/CONVERGE/2.4.27/1_x86_64/bin/converge-2.4.27-ompi -S

scontrol show job ${SLURM_JOBID}
```

Figure B-1 Example Sbatch job script for Converge without using Auto_Submit

When Converge runs, it advances in discrete time steps, which are either user-specified or are limited based on whichever CFL like condition limits its size. Between every time step, the input files in the simulation directory are reread. During this rereading, the current time and the simulation end time that is listed in inputs.in are compared. If the current time is greater than the end time, then the simulation exits. If not it continues. It is the rereading process that Auto_Submit takes advantage of to get Converge to exit and allow lines of code below the call to Converge to be executed.

B.4 The Auto Submit Scheme

Auto Submit is a directory of BASH scripts that were written in order to create job scripts that would run Converge simulations in a series of four-hour jobs. Auto Submit is designed with the intent that the user only submits the first four-hour job request, and then all of the following submittals are done automatically by the job scripts. Each job submits the next job at its conclusion.

If Converge and the job scripts run without issue and the simulation hasn't reached its desired end time, then the automation process is as follows:

1. The job is initiated

2. Data about the submission is written to a file in the directory name LOG
    a. This LOG file is important and should not be modified; some of the scripts will look for information in it. Its absence or misunderstood modification will result in the process's failure.
3. Before Converge is called, a countdown is initiated as a background process
4. Converge is called and begins to execute
5. When the countdown expires, scripts execute in the background to modify the end time variable in inputs.in to be 1e-08 seconds
6. When Converge completes its current time step, the inputs are reread, and the solver will believe that the simulation is complete when it compares itself to the new end time number; so it exits cleanly
7. A script is run to modify inputs.in to prepare the file for the next job, which includes the following:
    a. The end time is set back to the original end time for the simulation
    b. The restart flag is set to 1
    c. The restart number is set to match the latest restart file in the simulation directory
    d. The flag for using an initialization map is set to OFF
8. Additional information is written to the LOG file
9. A new job script is created and submitted
10. The job script concludes by printing job information to the screen output that gets written to <job_name><job_number>.SLURMout

The process described is the ideal case where everything works. Multiple things can go awry. The flow of logic in the actual is slightly more complicated. A diagram of the logic for the

automated job script is provided inFigure B-2. The most common fault is that Converge will fail to run at all. This occurs when the input files are not set up properly. When this happens, Converge exits, and the job script continues its execution. There are checks to ensure that Converge has made progress before another job is submitted. If it didn't, the user is alerted with an e-mail that Converge failed the process of automatically submitting jobs is terminated. Converge can also fail because of other errors unrelated to a poor setup. The result is the same as bad inputs. Failure will be reported.

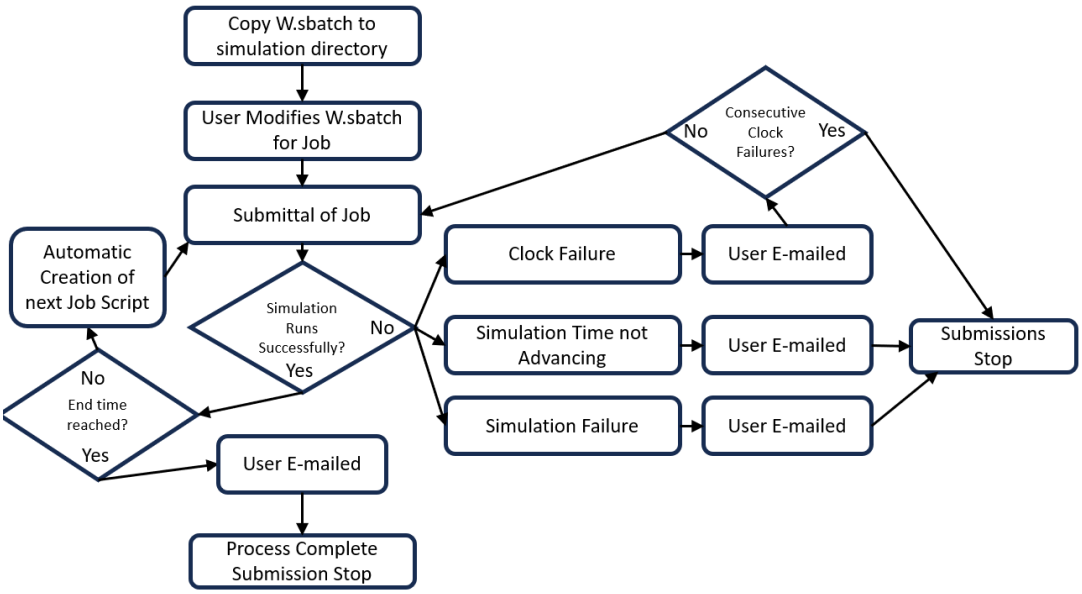

Figure B-2 Diagrm of the Auto_Submit scheme's logic

A second less common issue that comes up is that the countdown clock does not leave enough time for Converge to complete its current time step (typically only occurs if there is some ridiculous level of embedding that chokes the parallel balancing is present, an example is while an energy source is active to simulate a spark plug discharge). There is a second countdown clock that starts when the first expires. If this second clock expires, a script will run that will kill the process that is running Converge. The process is killed to return control of the job to the main script so another submission can be made. Having Converge killed in this manner is not ideal; the

reasons for this are manifold and are beyond the scope of this explanation. If the script at the end of the second countdown clock is being executed more than once every so often, it indicates that the user needs to address the conditions causing it to be invoked. This may include adjusting the resources requested or modifying some of the settings in the simulation's input files. As such, if this second clock expires in consecutive job submissions, then the user is e-mailed, and the automatic job submission is terminated.

Finally, the scripts check to see if the simulation has run to completion. If this is the case, the user is e-mailed that the simulation has been run to completion successfully, and additional jobs are not submitted.

Implementing Auto Submit

Using Auto Submit requires the prerequisites discussed in the next section to be in place. To run the scheme, a copy of the file W.sbatch, a job submission script provided in the Auto Submit directory, must be copied to the simulation directory and modified to match the needs of the user and simulation it is to be used for. This new version of W.sbatch should be submitted as the first job. A file named LOG will be created when the first job starts. It will contain information about all of the job submittals. There are fields in the LOG file that no longer have data entered into them. Instead, there are N/A even for data that seems like it should be readily available. These are legacy fields from the original Auto Submit implementation which was created to work with Converge version 2 and a previous job scheduler. Updates to Converge restart files and the transition to SLURM on the HPC “broke” the code used to provide the data to these fields. Where the information was not critical to process, effort was not made to update the code to return it to functionality.

Prerequisites for Running the Auto Submit Scripts

In order for Auto Submit to work, the user will need to transfer the script files to a directory

within their home directory on HPC. The user then needs to modify their .bashrc file so that the directory within which these files are stored is appended to the environment variable **PATH**. The individual files themselves will also need to have their permissions changed using the **chmod** command so that they can be executed. Once these two tasks are accomplished, the example job script included in the directory with the script files can be copied to simulation folders, modified as needed, and used to execute the Auto Submit scheme.

Since the author does not know the level of familiarity the reader has the concepts used in the two prequisite steps. Specific instructions will be provided here.

Modifying .bashrc

The .bashrc file is located in a user's home directory. When a user logs into the HPC, .bashrc is a script that runs. There are many reasons to add lines to or modify this file. As stated above, modifying it allows a user to add the Auto Submit directory to the system's path, which will allow the contents of the directory to be executed when called without the need to call the full path for each script.

The steps for making this modification are as follows:

1. Log into the HPC
2. Log into a development node, for example logging into intel16 with:
    a. intel16
3. Using the nano editor, open .bashrc, from the command line
    a. nano ~/.bashrc
4. Use the arrow keys to navigate to the end of the file
5. Add this line, replacing the contents of < > with your own user name
    a. PATH=/mnt/home/<username>/<path for Auto Submit>:$PATH
6. Exit the nano editor by pressing **Ctrl+X**

7. The dialog at the bottom of the screen will ask if you want to save the modified buffer, press Y
8. The .bashrc file will be updated, but to take effect you must log out and back into a node. If you followed step 2, then you can exit the development node and enter back into the same or different development node
    a. exit
    b. intel16
9. The changes should now be in effect
10. You can check your **PATH** variable by typing the following into the command prompt
    a. echo $PATH
11. The first path in the list should be your path in step 5

Changing permissions

For a script to be executable, its permissions must be set accordingly. On a Linux system, each file has a different permission for the owner of the file, anyone within the same group as the owner, and anyone who can access the file. These are referred to as owner, group, and public. For each category, the permissions can be set to one of three options: read, write, or execute. In order for the file to run as a script, the owner's permission at the very least must be set to execute. Generally speaking, however, nobody will care about these files that you have in your home directory, it is okay to set all three groups' permissions to execute. Permissions are modified using the chmod command. The syntax for the command is chmod <permission code> <filename>. To set just the owner's permission to execute and the others to read, the permission code is 144. To set them all to execute, the code is 777. While the author believes that 144 is sufficient, he has always used 777.

Here are step-by-step instructions for changing the permissions for all of the script files in the

Auto Submit folder:

1. Navigate to the Auto Submit folder
2. Type the following command into the terminal to change all of the permissions for the script files, which all have the .sh extension
    a. chmod 777 *.sh

Here the *, the expansion character, means the command above expands into chmod 777 Clean_up.sh followed by chmod 777 Command_Kill.sh and so on for all of the files that end with the characters .sh

Using the Auto_Submit Routine

The use of the Auto_Submit routine is not exactly trivial. An instructional video may be posted in the repository to supplement the brief explanation of the routine provided here. For now, an outline of the process is provided below. Within the directory where the script files have been copied, there should be a file named W.sbatch. This script runs the routine an example of which is shown inFigure B-3. This script needs to be located in the Converge directory of the job that is being run with the modifications detailed in the instructions below incorporated. It is advised to keep an untarnished copy of this file in the Auto_Submit directory in the event that modifications render one of your active copies unusable. It should also be stated that it is not out of the question that Converge will update its input file structure in the future, which will break the routine unless some of the scripts are updated to accommodate the changes.

The following is the description of the work flow associated with Auto_Submit routine:

1. Copy the W.sbatch script to the directory that has the Converge inputs files
2. Modify W.sbatch for the specific case
    a. Lines 2-9 are the job resource requests
    b. Some of these will need to change and some will not

c. Explanations for what is included here and what should be changed
    i. Line 2: [Change] This is the job name that the scheduler will display when a user requests to see their queue (powertool command ‘qs’)
    ii. Line 3: [Change]This is the wall time request for the job, currently set at four hours
    iii. Line 4: [Change] This is the number of processors that the job will request
    iv. Line 5: I cannot remember why, but this number needs to be 1
    v. Line 6: [Change] This is the amount of memory that each processor will have available to it while the job runs
    vi. Line 7: This merges some of the screen output into one file that will appear in the converge directory while and after the job runs
    vii. Line 8: [Change] This instructs the scheduler to send you e-mails for activity related to the job. I believe you will receive a job start and job end e-mail.
    viii. Line 9: [Change] This is the e-mail address that the messages will be sent to. I am not certain, but it may need to be the e-mail your HPCC/ICER account is associated with

3. Other lines that must be updated
    a. Line 22: [Change] You must load the correct version of Converge that you wish to run
    b. Line 30: [Change] You must know the correct command to call to run the version of Converge that you want to run
4. Submit W.sbatch

5. The first run will create a file named LOG in the directory
6. Information for the first submission will be written to the log
7. One of the following behaviors will result from the first submission
    a. The job is successful, a new W-[#].sbatch file is created and submitted to the scheduler; so the simulation continues to proceed
    b. The job fails
        i. Converge fails to close out as it should, instead one of the timers has stepped in and killed the Converge process that was running, the user is e-mailed, and Auto_Submit will attempt to run the simulation again. If this happens twice, the process terminates
        ii. The Converge simulation fails to run because the simulation is not set up correctly, the user is e-mailed, and the process terminates
8. If the job is successful, W-[#].batch runs, and steps 5-7 continue until something fails or the simulation reaches its end time or crank angle
9. When the simulation reaches its completed state, the user is e-mailed, and the process terminates

W.Sbatch

Finally for reference, the following is an explanation of the code in W.sbatch as displayed in Figure B-3, a diagram showing the coding logic is provided in Figure B-4:

Line 1: line at the top of every job script that denotes that the script is written in BASH and logs the user into the network

Lines 2-9: Job resource requests

Line 14: Sets the job kill countdown clock

Line 17-18: Code to determine the number of processors that were requested (this was added

so that processor count information only needs to be entered once)

Line 21: Changes the working directory to the directory from which W.sbatch was submitted

Line 22: Loads the Converge module

Line 24: Call to watchdog_calc.sh to determine how long to let the simulation in real-time before the code “requests” Converge to stop and exit

Line 26: If it does not exist already, the file ‘LOG’ is created in the directory. Information for this job submission is written to ‘LOG’

Line 28: The watchdog timer is activated as a background process

Line 30: This is the function call to Converge

Line 32: If Converge exits cleanly, this line pauses everything for 45 seconds to make sure that all the input files in the directory are available

Line 34: Clean up routine is run, which kills any active processes like the watchdog or reaper clocks, determines how the submission ended, and writes the info to ‘LOG’

Line 36: Completes writing data about the previous submission to ‘LOG’

Line 38: Runs the script that resets all of the input files, makes a new submission file, and submits the job to the scheduler

Line 40: This is the final output to write to the <Job_Name>-<Job ID>.SLURMout file that the job creates in the simulation directory

W.sbatch

```
#!/bin/bash --login
#SBATCH --job-name=CHANGE2DIR-W.qsub
#SBATCH --time=04:00:00
#SBATCH --ntasks=120
#SBATCH --cpus-per-task=1
#SBATCH --mem-per-cpu=2G
#SBATCH --output=%x-%j.SLURMout
#SBATCH --mail-type=ALL
#SBATCH --mail-user=thelenb8@msu.edu



# Set the reaper clock
reaper_clock=15 # minutes

# Calculate the number of processors to use with Converge.
num_pros=`scontrol show job ${SLURM JOBID} | grep NumTasks | cut -d ' ' -f 6 | cut -d =
-f 2`
echo "The simulation is using ${num_pros} processors."

# Load converge and change into working directory
cd ${SLURM_SUBMIT_DIR}
module load CONVERGE

watchdog_time=`watchdog calc.sh ${SLURM JOBID} ${reaper clock}`

log_write_1.sh ${SLURM_JOBID} ${watchdog_time}

watchdog.sh ${watchdog_time} ${reaper_clock} &

mpirun -np ${num_pros} /opt/software/CONVERGE/2.4.27/1_x86_64/bin/converge-2.4.27-ompi -s

sleep 45

Clean_Up.sh

log_write_2.sh ${SLURM_JOBID}

Next_Submission.sh ${SLURM_JOBID}

scontrol show job ${SLURM_JOBID}
```

Figure B-3 An example W.sbatch script

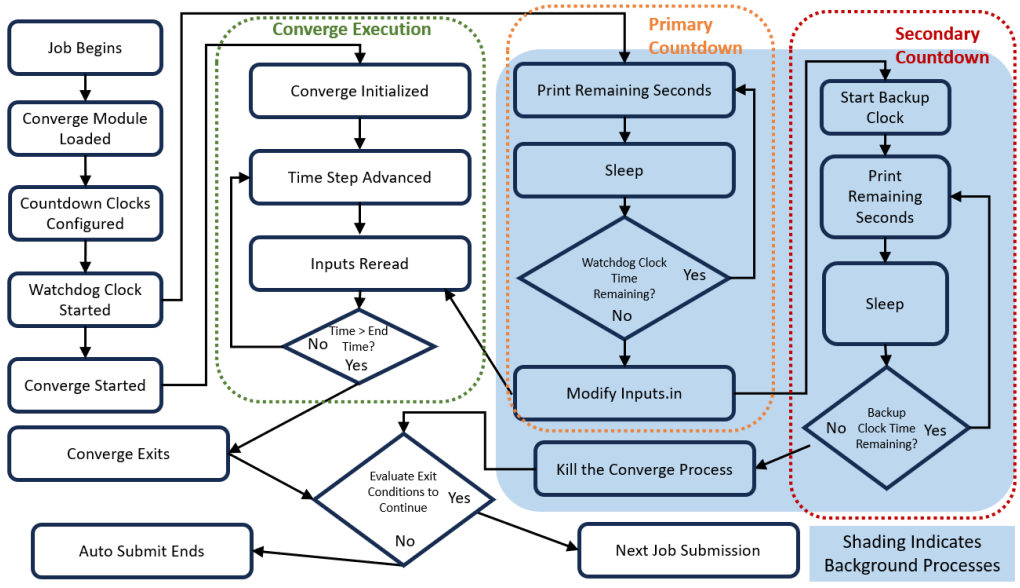

Figure B-4 Logic diagram for W.sbatch

APPENDIX C: GT POWER MODELLING OF THE FUJI IMVAC 34 EI ENGINE

Modeling of the Fuji Imvac EI-34 Single Cylinder 4-Stroke Gasoline Engine with GT Power

ABSTRACT

A GT-Power model of a small 33.5 cc, four-stroke, gasoline, single-cylinder engine is developed. Discussion of the engine geometry relevant to the model is given and a break down of the individual GT-Power elements used explored. A three dimensional flow component is also modeled using GEM3D and incorporated into the GT-Power model. The data produced by the model is compared to dynamometer test data for the engine collected in the author's previous work. Finally, the effects of exhaust system modifications made to the engine during the previous dynamometer testing are investigated.

INTRODUCTION

The following paper describes the work performed by the author to complete the requirements of the course ME 445: Automotive Powertrain Design's final project for the spring 2013 Semester at Michigan State University. The course introduces students to different aspects of powertrain design and heavily incorporates the use of Gamma Technologies GT-Suite software for the purpose of simulation of such systems. GT-Suite is a computer aided design application that is popular in the automotive industry. The class mainly focused on the use of GT-Power module to set up one-dimensional models of reciprocating piston internal combustion engines. The software package, however, included access to other modules such as GT-VTrain, GT-Fuel, GT-cool, GT-Drive, GT-Crank which each provide environments for the simulation and design of valve trains, fuel systems, coolant systems, drive cycles, and analysis of crankshafts respectively. While none of these modules were used in the simulation developed in this paper, a tool that is also a part of GT-Suite called GEM3D was used to discretize a three-dimensional body into a one-dimensional equivalent model appropriate for use in GT-Power.

The engine that has been modeled is a Fuji Imvac EI-34 single cylinder, four-stroke gasoline engine. This engine was selected because the author has performed engine dynamometer testing with this engine as part of his graduate work in the recent past. The Fuji engine was marketed as a power plant for remote control aircraft before it was recently discontinued. Given its market, it is no surprise that it is also used by the United States Air Force as the engine for a small unmanned aerial vehicle. This engine was chosen by the Air Force Office of Scientific Research as the test engine for a project they funded at Michigan State with the purpose of investigating the effects of using plasma enhanced ignition systems. While the results of this research are beyond the scope of this paper, the work did result in baseline measurements of the engine with its standard ignition coil which will be utilized in this paper as a comparison to the GT-Power model that was developed.

The remainder of this paper includes a description of the measurements taken of the engine's components and geometry, the elements of the GT-Power model that was developed, the use of the GEM3D software to discretize the engine's muffler, and the assumptions made in the modeling process. The results generated by the GT-Power model are compared to data collected during the plasma project mentioned above. These engine test points were all gathered with the engine operating at wide open throttle (WOT) with stoichiometric air fuel ratio at engine speeds of 4000, 5000, and 6000 revs/min. Finally, the GT-Power model is used to investigate the effects that the size of components that were installed after the engine's stock exhaust to house exhaust gas sensors as part of the instrumentation used to perform testing with the engine have on the performance of the engine.

SUMMARY OF ENGINE AND ITS COMPONENTS RELEVEANT TO THE GT-POWER SIMULATION

A picture from Fuji's website showing the Imvac EI-34 is shown below in Figure 1. A summary of key features and specifications for the engine is given in Table 1. The Fuji engine has a displacement of 33.5 cc, a bore of 39, a stroke of 28 mm, and a compression ratio of 8.6. The advertised maximum

torque and power output for the engine is 1.76 N-m and 1.18 kW respectively. The single cylinder four-stroke engine is air-cooled and carbureted. The same basic engine is also sold under the Subaru Robin brand name as an engine for utility equipment. The major components of the Subaru engine are identical to those of the Fuji engine with the exception of differences in protective housing, output shaft hardware, ignition system, and carburetor. The engine used for testing was originally a Subaru engine, but the carburetor from the Fuji engine replaced the Subaru's original. This was because the Fuji's carburetor has air fuel ratio adjustments while the Subaru's does not. The rest of the engine is identical using the same cylinder head, crank train, valves, cam, etc. The Subaru's magneto ignition system was also replaced with the Fuji's electronic, battery powered ignition system. The Subaru engine is discussed here mainly because there is literature available regarding the service and maintenance of the engine published by Subaru Robin. Any dimensions not measured directly by the author were taken from this service manual.

Figure 5. The Fuji Imvac EI-34 Engine

Table 2. Summary of Subaru Robin EH035 Engine Specifications

Type		Air-Cooled, 4-Cycle, Single-Cylinder, Horizontal P.T.O. Shaft, Gasoline Engine
Bore x Stroke		39 x 28 mm (1.54 x 1.10 in.)
Piston Displacement		33.5 cm3 (2.04 cu.in.)
Compression Ratio		8.6
Output	Continuous	0.81 kW (1.10 HP) /7000 r.p.m.
	Max.	1.18 kW (1.60 HP) /7000 r.p.m.
Max. Torque		1.76 N•m (0.18 kgf•m) /5000 r.p.m.
Cooling system		Forced Air Cooling
Valve Arrangement		Overhead Valve
Lubrication		Forced Lubrication
Lubricant		Automotive Oil SAE #20, #30 or 10W-30
Fuel Consumption Ratio		340 g/kW•h (at continous rated output)
Spark Plug		NGK CMR6A (M10 x 1.0)
Dry Weight		3.5 kg (7.72 lb.)
Dimensions (L x W x H)		191 mm x 234 mm x 246 mm

The components of main interest in regards to the GT-Power model that was constructed for this paper consist of all of the components that are involved in the case exchange process (intake, exhaust, cylinder geometry, valves, etc.) and the geometry of the components that dictate the motion of the piston (the piston rod length, swept displacement, and compression ratio). Details of the crank case, cooling system, piston ring kit, and lubrication are not considered by the model. The following sections describe each of the relevant components by dividing them into the following groups: intake, cylinder, and exhaust.

Intake Components

The engine has a very simple intake system. The first component intake air encounters is the carburetor. There is both a throttle and choke plate integrated into the carburetor with the choke plate visible in Figure 1. The carburetor has a rounded intake and then a subtle Venturi in front of the throttle. A molded plastic component, which will be referred to as the intake runner, serves as a standoff between the carburetor and the cylinder head which contains a passage into the cylinder head that has a slight taper. The intake passage in the cast cylinder head has a constant diameter which meets at a mitered corner with the intake valve passage located above the engine's cylinder. Figure 2 shows photographs of the intake runner and the carburetor as well as a cylinder head that has been cut away to show the head's intake passage. The dimensions of these components are summarized in Table 2.

Figure 2. Carburetor and Intake Runner Standoff as viewed from outlet side (left) and Cutaway of a Cylinder Head to show Intake Passage (right)

Table 3. Summary of Intake Component Dimensions

Component	Dimension [Inches]	
Carburetor	Inlet Diameter	0.737
	Length	1.125
Intake Runner	Inlet Diameter	0.39
	Outlet Diameter	0.345
	Length	1.533
Cylinder Head Intake Passage	Inlet/Outlet Diameter	0.453
	Length	0.956

Exhaust Components

The engine's exhaust flows out of the cylinder head through a circular passage into the engine's muffler. The muffler is a sheet metal box with a single baffle containing a pattern of six holes placed in between its intake port and exhaust pipe. More details regarding the exhaust muffler will be given in the modeling section below. The muffler is the final component in the stock engine's exhaust, but in order to utilize an exhaust gas sensor to measure the air fuel ratio at which the engine operates, additional components were added after the muffler. These components are simply two steel tubes. A small tube is welded onto the exhaust pipe which in turn extends to a large diameter pipe of significant length. This large tube contains the exhaust gas sensors. The end of the tube has a cap welded onto with an orifice drilled into it to allow the exhaust gas to escape. Figure 3 contains an image of the exhaust side of the engine in its test setup and Figure 4 shows a cutaway of the cylinder head showing the exhaust passage in the cylinder head. Finally Table 3 summarizes the important dimensions of each of the components mentioned above.

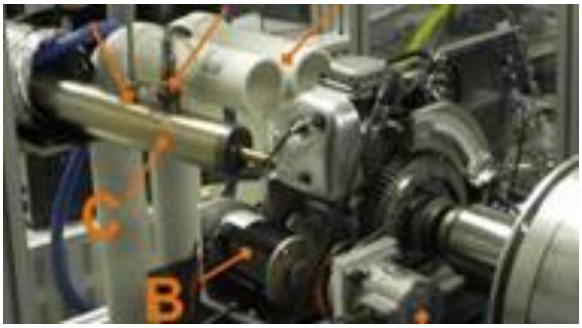

Figure 3. The exhaust side of the engine test setup, the extended exhaust components are labeled C

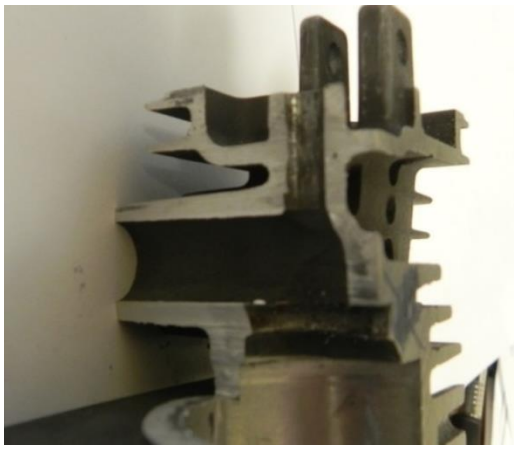

Figure 4. Cutaway of a Cylinder Head to show Exhaust Passage

Table 4. Summary of Exhaust Component Dimensions

Component	Dimension [Inches]	
Exhaust Passage	Inlet Diameter	0.485
	Length	1.2
Muffler	Height (approx)	3
	Width (approx)	3
	Depth (approx)	1.5
Exhaust Extension	Small Pipe Diameter	0.5
	Small Pipe Length	1.9
	Large Pipe Diameter	2
	Large Pipe Length	12
	Final Orifice Diameter	0.346

Cylinder Components

A list of components and dimensions necessary to the definition of the cylinder geometry is given in Table 4. The top land of the piston is flat and the engine's two valves are located overhead of the cylinder and lift directly downward into the cylinder. The valves

are standard looking poppet valves and the diameters given below are measured at the widest section of the valve. The measurement of valve lift and timing by the author is described in the next section. It is important to note that the maximum valve lift is the same for both the exhaust and intake valves.

Table 5. Cylinder Geometry Dimensions

Bore	1.535 in
Stroke	1.102 in
Swept Displacement	33.5 cc
Compression Ratio	8.6
Rod Length	1.993 in
TDC Clearance Height	0.117 in
Intake Valve Diameter	0.568 in
Exhaust Valve Diameter	0.502 in
Maximum Valve Lift	0.112 in

Valve Lift and Timing

While the maximum valve lift was published in the Subaru service manual, a valve lift profile was not. The valve lift was measured manually with a dial gage. Pictures of the setup are shown below in Figures 6 and 7. The cam is located just above the engine's crank shaft of the back side of the engine. Followers ride on the cam and actuate push rods that run up two channels in the engine's cylinder head to two rocker arms located atop the cylinder head. The cam, cam gear, and cam followers are shown in Figure 5 below with the bottoms of the pushrods visible in each of the top corners of the cavity in which the cam sits. The two followers and pushrods are interchangeable and the cam profile is clearly symmetric.

The measurements of valve lift were taken by removing the head cover on the top of the engine and removing the rocker arms that actuate the valves. The engine was clamped to a flat table and a dial gage was positioned to rest on the top of the push rod where the valve rocker had been. An angle indicator was secured to the engine's output shaft. A complete sweep of the engine's cam was completed recording pushrod displacement in increments of 5 crank angle degrees over the active region of the cam. Since the cam is symmetric and the followers identical, the measurements only had to be taken for one of the valves and then mirrored about the top dead center of the gas exchange. The "cylinder decompression" system that the engine features to assist in the pull starting of the engine added complication to the measurement. The cam has a small crescent shaped weight that protrudes above the cam at slow speeds of rotation that lifts the exhaust valve early in the compression stroke of the engine. It also affects the intake valve during the exhaust stroke, but its purpose is to relieve the torque required to turn the engine during starting by lowering the peak pressure of the compression stroke. At operating speeds, the counterweight is forced below the cam surface by centrifugal forces. As a result of this protrusion, the measurement had to be taken while turning the crank in the opposite direction that the engine runs as the decompression protrusion happens to get pressed below the cam surface by the followers when the engine is turned in its reverse direction.

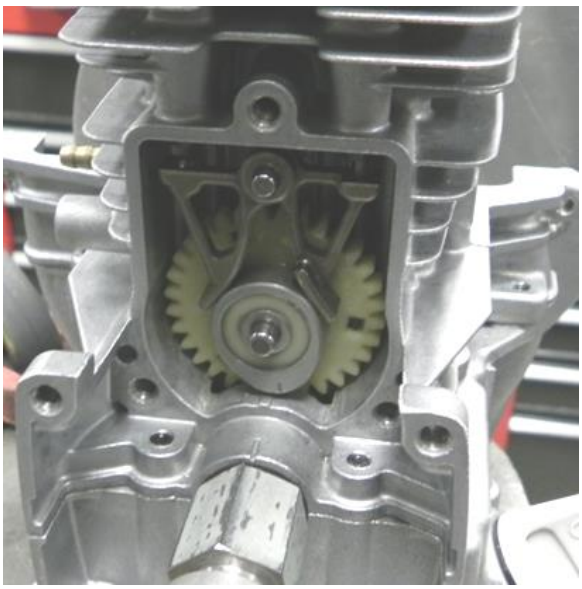

Figure 5. A view of the rear side of the engine with the cover over the cam gear removed

Figure 6. The setup for measuring pushrod displacement with the dial gage positioned to measure TDC

Figure 7. An up close picture showing the dial gage resting on the top of the engine's pushrod

After a table of pushrod displacement as a function of crank angle was compiled for the exhaust valve, top dead center was established using a positive stop method near the middle of the piston stroke by inserting the dial gage through the spark plug hole into the cylinder. An offset was then established between the crank angle indicator's zero and the actual top dead center of the engine. Using the maximum valve lift published in the Subaru manual and the largest pushrod displacement, the ratio between the two was established and table of valve lift as a function of crank angle was generated. A plot of this lift is shown in Figure 8 below.

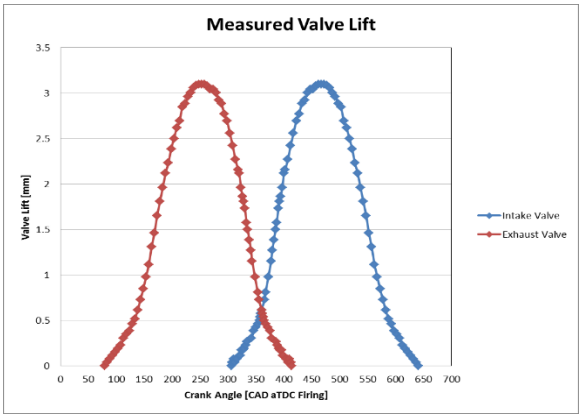

Figure 8. Valve lift as a function of crank angle referenced to TDC firing

GT-Power Model

The model map developed in GT-Power is shown below in Figure 9. The discussion of this model will be broken down in the same manner as that of the engine in the previous sections into intake, cylinder, and exhaust.

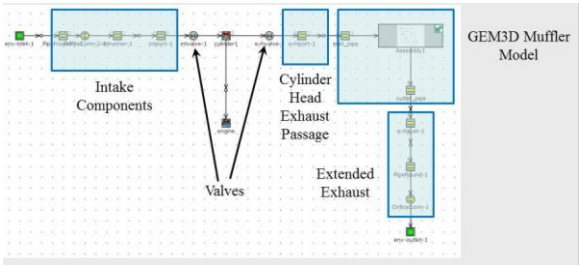

Figure 9. Screen capture of the model map developed in GT-Power

Intake Components

As mentioned above, the intake consists of a carburetor, intake runner, and cylinder head passage. Since the air fuel ratio is to be specified for each run, no attempt to model the carburetor as a fuel metering device was made. Instead the environment from which the intake gas is supplied has been set as a stoichiometric mixture of Indolene and air at atmospheric pressure and room temperature. The carburetor is modeled in GT-Power as a single round

pipe followed by an orifice element that allows the model to be adjusted by changing the orifice diameter to account for the effects of the throttle and Venturi nozzle in the carburetor. Although test points used in this paper are all at WOT, the orifice still helps account for the presence of the open plate in the flow. Finally the intake runner and inlet passage are also modeled as round pipes. A summary of the GT-Power elements and their important specifications used to model the intake is shown in Table 5.

Table 6. Summary of GT-Power elements used to model the intake side of the engine

Engine Component	GT-Power Model Elements	Key Model Attributes	
Carburetor	Round Pipe	Diameter	0.737 in
		Length	1.125 in
		Wall Temperature	350 K
	Orifice Connection	Hole Diameter	0.549 in
		Number of Holes	1
		Discharge Coefficents	default
Intake Runner	Round Pipe	Inlet Diameter	0.380 in
		Outlet Diameter	0.340 in
		Length	1.533 in
		Wall Temperature	350 K
Cylinder Head Intake Passage	Round Pipe	Diameter	0.453 in
		Length	0.463 in
		Wall Temperature	450 K

Exhaust Components

The portion of the GT-Power map that comprises the exhaust system of the engine begins with a round pipe which models the cylinder passage. This pipe connects to components of the muffler that was discretized using GT-Suite's GEM3D module. A more detailed discussion of the muffler is given in the following subsection. In Figure 9, the map shows a sub assembly connected to an inlet pipe on one side and an outlet pipe on the other, these three graphical icons comprise the muffler. Beyond the muffler, there are two more round pipes and an orifice which model the exhaust extension welded onto the muffler. No attempt was made to account for the presence of the exhaust gas sensors in these pipes. The end environment is air at atmospheric pressure and room temperature. A summary of the GT-Power elements and their specifications used to model the exhaust is given in Table 6.

Table 7. Summary of GT-Power Elements used to model the exhaust side of the engine

Engine Component	GT-Power Model Elements	Key Model Attributes	
Cylinder Head Exhaust Passage	Round Pipe	Diameter	0.485 in
		Length	1.104 in
		Wall Temperature	550 K
Muffler	Round Pipe (Muffler Inlet)	Diameter	0.483 in
		Length	0.106 in
		Wall Temperature	600 K
	GEM 3D Discretization		
	Round Pipe (Muffler Outlet)	Diameter	0.348 in
		Length	.0598 in
		Wall Temperature	600 K
Extended Exhaust	Round Pipe	Diameter	0.346 in
		Length	0.598 in
		Wall Temperature	600 K
	Round Pipe	Diameter	2.0 in
		Length	12 in
		Wall Temperature	550 K
	Orifice Connection	Hole Diameter	0.364 in
		Number of Holes	1
		Discharge Coefficents	default

Modeling and Discretization of the Engine Muffler

The modeling of the engine's muffler was by far the most time consuming element in the development of the GT-Power model. Since the muffler has more complicated geometry than a round or square pipe or passage, it was incorporated into the GT-Power model by using GEM3D. GEM3D is part of GT-Suite and is a tool that allows users to import or create complicated three-dimensional models of flow components in a graphical environment and manipulate the models to a state from which GEM3D can discretize the volume into a network of equivalent one-dimensional components that can be imported into GT-Power.

A surface model of the muffler's main chamber (basically the muffler without the baffle, inlet, and outlet ports) was created with a separate CAD software package, this surface is shown in Figure 10, and exported as a .STL formatted file. The geometry was then imported into GEM3D and converted into a GEM Mesh component. Within GEM3D, the muffler's baffle was created and six holes created through it. Inlet and outlet ports were created by inserting round pipes into the model and assigning each as either an inlet or an outlet. The complete GEM3D model is shown in Figure 11. This model was then discretized and converted into a one-dimensional equivalent model. A preview of the discretization is shown in Figure 12**.** Each cube is a separate discrete volume. The equivalent one-

dimensional model is shown in Figure 13. This diagram is not meant to show any specific detail of the model, rather its purpose is to indicate the massive and complicated web of one-dimensional elements that the GEM3D conversion produces.

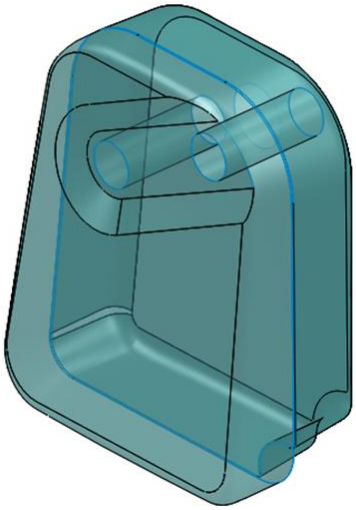

Figure 10. SolidWorks surface model of the main volume of the muffler

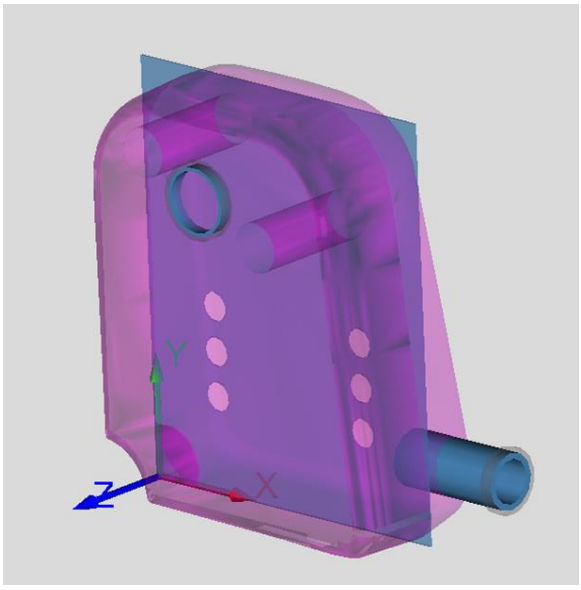

Figure 11. Complete muffler model in GEM3D including inlet, outlet, baffle, and baffle holes

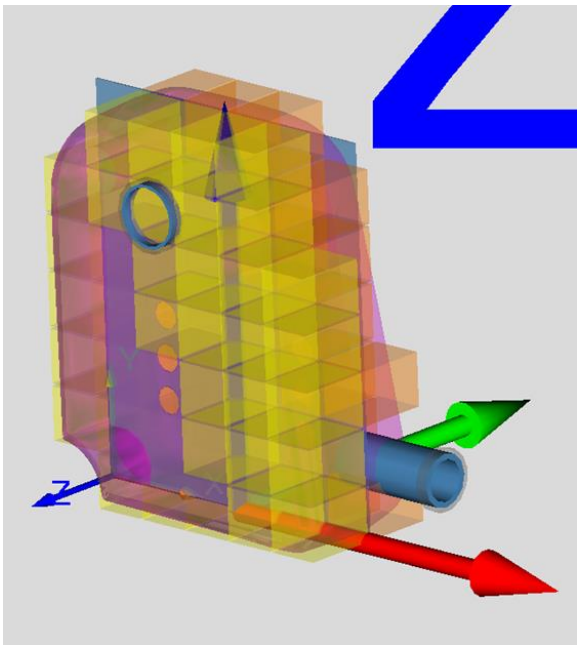

Figure 12. Discretization preview given by GEM3D of the engine muffler, each cube is a separate discrete volume considered by the software

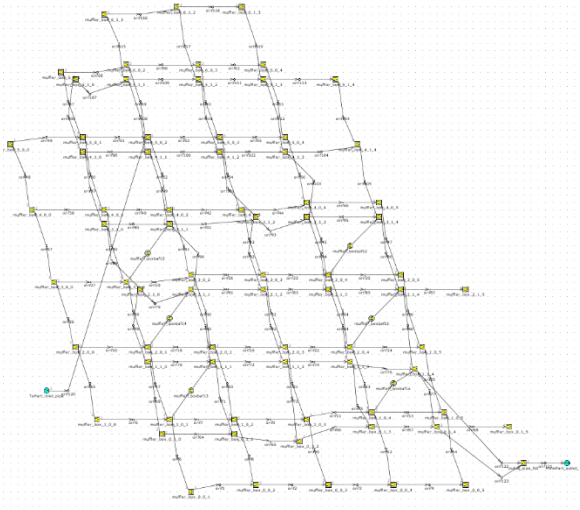

Figure 13. The muffler's equivalent model composed of one-dimensional GT-Power elements (note the complexity)

While the description of the creation of the muffler model using GEM3D is brief, the modeling process was not as easy as may appear. Placing components in GEM3D is not simple a drag and drop operation and the use of GEM Mesh elements is nuanced. Guidance was necessary and sought from Gamma Technologies' Support in order to complete the conversion of the muffler model.

Cylinder Components and Combustion

The dimensions used for the cylinder geometry are the same as those given in Table 4 above. The data collected for valve lift was inserted into the model's lift table, and given time constraints, a flow table was not experimentally obtained specifically for the engine's valves. Instead a flow table copied from a GT-Power tutorial of a single cylinder engine with poppet valves was used. The flow table is a tabulation of discharge coefficients as a function of the non-dimensional lift divided by valve reference diameter. Given this non-dimensionalization, the imported table serves as a good starting point for modeling the engine's valves. Finally, combustion is modeled using GT-Power's default Weibe function for spark ignition combustion. The timing of combustion is specified by the 50% burn crank angle location and the 10-90% burn duration. Mass fraction burn data was calculated for the engine tests and the necessary crank angle locations and durations taken from plots such as that shown in Figure 14 for the 4000 revs/min case.

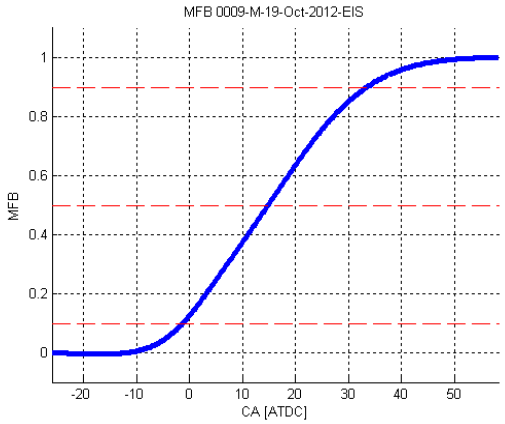

Figure 14. Experimental mass fraction burn data for 4000 revs/min operating speed

Model Results and Comparison to Real Engine Data

PV diagrams generated in GT-Power are compared to experimental diagrams in Figures 15, 16, and 17. The IMEP of the GT-Power model is consistently higher than the IMEP recorded during experimentation with the engine by about an entire bar for every operating speed. The peak pressures do no match, and the pumping loops show some deviation. There are several major reasons for this. First and foremost, the model makes no attempt at modeling heat loss. Heat transfer is a major factor in small scale engines like the Fuji. In addition the engine is air cooled and there was no data collected regarding specific engine head temperatures beyond a measure to determine if the engine had reached a steady temperature for data collection during experiments. The temperatures of all the surfaces were set using best estimates based on previous simulations. Also, it is evident that the standard Wiebe function with GT-Power's default parameters does not match the combustion in the actual engine. Finally, some tuning of the intake and exhaust sections of the model could be done to more closely match the pumping losses of the real engine.

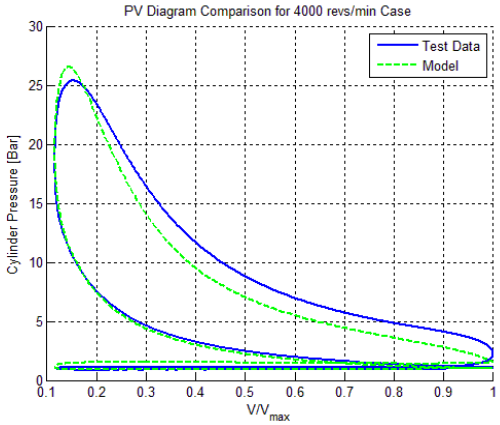

Figure 15. PV diagram comparison for 4000 revs/min WOT

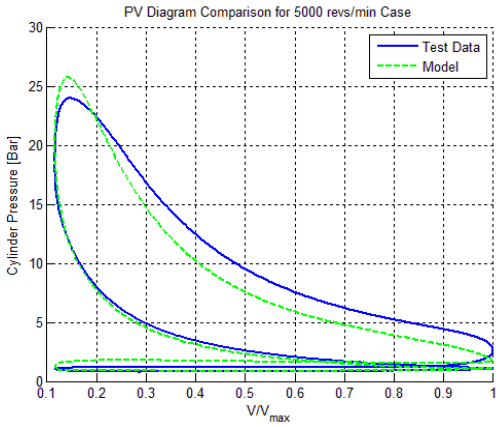

Figure 16. PV diagram comparison for 5000 revs/min WOT

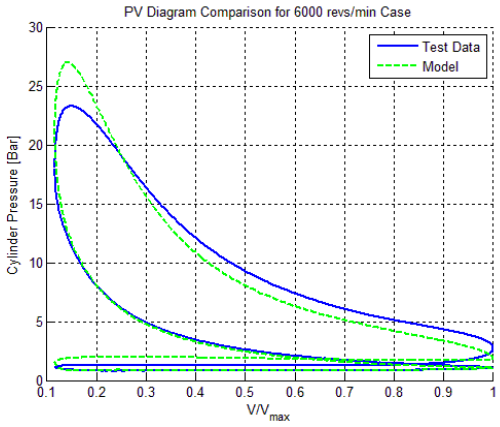

Figure 17. PV diagram comparison for 6000 revs/min WOT

While the model's fidelity leaves something to be desired, the model is close enough to the real engine that it can be used to answer a question concerning the added exhaust extension. When the engine was being tested prior to the undertaking of the modeling presented in this paper, the exhaust extension was installed without any analysis as to its effects to the tuning of the engine. The author has feared looking foolish in the event that he completely ruined the tuning of the engine and intended to use the model to investigate the effect of the extended exhaust. In order to accomplish this, a parameter sweep was set up for different exhaust extension lengths at a single operating speed. A plot of the volumetric efficiency as a function of the exhaust length is shown in Figure 18. There is only a spread in the volumetric efficiency of about one tenth of a percent in the plot which indicates that the extension does not adversely affect the engine's performance.

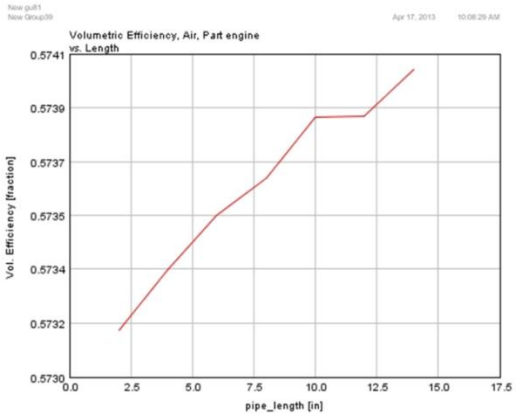

Figure 18. Plot of volumetric efficiency vs. exhaust extension pipe length at 5000 revs/min (Note: maximum/minimum y-axis values of 0.5741/0.5730)

SUMMARY/CONCLUSIONS

A GT-Power model was successfully developed for the small, single cylinder, four-stroke, gasoline Fuji Imvac EI-34 engine. While the data produced by the model did not match the experimental data obtained for the engine well, it was similar enough to test whether the engine's extended exhaust disrupted the performance of the engine, indicating that it did not. From the stand point of an academic exercise, the work performed extended the author's understanding of the tools included in GT-Suite including GEM3D. The process also indicates the directions that need to be pursued in order to produce a more accurate model including proper modeling of the engine's combustion, heat loss, and valve discharge data specific to the geometry in question.

ACKNOWLEDGMENTS

The author would like to acknowledge the effort of the course's instructor Dr. Schock for putting together an interesting course that allowed his students to gain the practical skill of running GT-Power. The efforts of Ravi Vedula and Cheng Chao is also appreciated in regards to the support of the students in the course.